

The  
University  
Of  
Sheffield.

# Aerodynamics, Stability and Shape Optimisation of Unmanned Combat Air Vehicles

Joe Coppin, MEng

Supervised by Professor Ning Qin

Department of Mechanical Engineering  
University of Sheffield

This thesis submitted to the University of Sheffield in partial fulfillment of  
the requirement for the degree of *Doctor of Philosophy*

September 2014



# Abstract

---

Unmanned Combat Air Vehicles have been proposed for future military roles. The shape of these vehicles is driven by stealth requirements and is often aerodynamically compromised. This results in designs which struggle to meet their take-off lift requirements without experiencing flow separations and unacceptable instabilities in the pitch or yaw axis. This work aims to better understand the aerodynamics of these vehicles as well as develop methods to generate improved designs.

An in depth RANS analysis has been completed for the Boeing 1303 UCAV concept with validation from QinetiQ 5m and ARA transonic wind tunnels. Two flow solvers and various turbulence models have been used. Longitudinal and directional stability have been investigated, looking at total and spanwise forces, pressure distributions and flow visualisation. The effects of modelling assumptions has also been studied. This has helped to better understand the underlying flowfield and has given some indication as to how the design may be improved.

A novel design methodology has been developed and applied to the 1303 UCAV aiming to minimise drag at cruise while ensuring the leading edge flow remains attached at take-off. This is based on an a sequential quadratic programming (SQP) optimiser where objective function ( $C_D$ ) is calculated with an in house solver MERLIN and the gradients are calculated in an efficient manner using a discrete adjoint solver adjoint-MERLIN. High lift constraints were applied based on Lan's Quasi-Vortex-Lattice Method with an experimentally derived limit on attainable leading edge thrust. The geometry was parametrised with Bézier-Bernstein polynomials combined with the Class Shape Transformation method for improved geometrical control near the leading edge. Various designs were produced giving some indication of the trade-off between cruise and high lift performance as well as limitations to the method. The method has proved to be good for generating balanced designs however higher lift designs suffer from lower surface separation at cruise.



# Acknowledgements

---

I appreciate and wish to thank my supervisor Prof. Ning Qin for his patience and support throughout my PhD project. I would also like to thank Prof. Trevor Birch from DSTL for his help guiding the project, and for allowing me to gain invaluable experience through visits to DSTL and various wind tunnel facilities. Frequent discussions with Dr. Raj Nangia have provided me with inspiration and given direction to the project for which I am also very grateful.

The project was jointly funded by the EPSRC and DSTL through an industrial CASE award.



# Table of Contents

---

<b>Abstract</b>	<b>iii</b>
<b>Acknowledgements</b>	<b>v</b>
<b>Table of Contents</b>	<b>x</b>
<b>Nomenclature</b>	<b>xvii</b>
<b>1 Introduction</b>	<b>1</b>
1.1 Motivations . . . . .	1
1.2 Aims and Objectives . . . . .	2
1.3 Thesis Outline . . . . .	2
<b>2 Background and Literature Review</b>	<b>3</b>
2.1 Advantages of Unmanned Combat Air Vehicles . . . . .	3
2.1.1 Typical UCAV Mission . . . . .	3
2.1.2 Advantages of Unmanned Aircraft . . . . .	4
2.1.3 Advantages of Low Observable Designs . . . . .	5
2.2 Low Observable Design Features . . . . .	6
2.2.1 Radar . . . . .	6
2.2.1.1 Planform Alignment . . . . .	6
2.2.1.2 Materials . . . . .	7
2.2.1.3 Internal Stores Carriage . . . . .	7
2.2.1.4 Intakes and Nozzles . . . . .	8
2.2.1.5 Equipment . . . . .	8
2.2.1.6 Mission Planning . . . . .	8
2.2.2 Infra Red . . . . .	8
2.2.3 Visual . . . . .	9
2.2.4 Acoustics . . . . .	9
2.3 Key Performance Indicators . . . . .	9
2.3.1 Take-off . . . . .	9
2.3.2 Cruise . . . . .	10
2.3.3 Loiter . . . . .	11
2.3.4 Dash . . . . .	11
2.4 Planform Selection . . . . .	12

2.4.1	Shape . . . . .	12
2.4.2	Propulsion Considerations . . . . .	12
2.4.3	Planform Sweep Angles . . . . .	14
2.5	Aerofoil Aerodynamics . . . . .	15
2.5.1	High Lift . . . . .	16
2.5.1.1	Canonical Pressure Distribution . . . . .	16
2.5.1.2	Maximum Lift Aerofoils . . . . .	18
2.5.2	Supercritical . . . . .	19
2.6	Wing Aerodynamics . . . . .	21
2.6.1	Swept Wings . . . . .	21
2.6.2	Slender Wings . . . . .	22
2.7	Design Methods and Optimisation . . . . .	25
2.7.1	Design Process . . . . .	25
2.7.2	Conceptual Design . . . . .	25
2.7.3	Detailed Wing Design . . . . .	25
2.7.3.1	Genetic Algorithms . . . . .	26
2.7.3.2	Response surface methods . . . . .	26
2.7.3.3	Gradient based methods . . . . .	27
2.8	1303 UCAV . . . . .	27
<b>3</b>	<b>Computational Methodology</b>	<b>31</b>
3.1	Optimisation Design Process . . . . .	31
3.1.1	Sequential Quadratic Programming . . . . .	32
3.1.2	Aerodynamic Objective and Constraint Functions . . . . .	33
3.1.3	Optimiser Set Up . . . . .	35
3.2	Flow Solver . . . . .	36
3.2.1	Introduction . . . . .	36
3.2.2	Governing Equations . . . . .	36
3.2.3	Primitive Variables & Non-dimensionalisation . . . . .	38
3.2.4	Turbulence Models . . . . .	39
3.2.4.1	Baldwin-Lomax Model . . . . .	40
3.2.4.2	$k - \omega$ Model . . . . .	42
3.2.5	Spacial Discretisation . . . . .	42
3.2.5.1	The Finite-Volume Method . . . . .	43
3.2.6	Time Integration . . . . .	44
3.2.6.1	Explicit Formulation . . . . .	44
3.2.6.2	CFL Condition and Time Step . . . . .	44
3.2.6.3	Implicit Formulation . . . . .	45
3.2.7	Calculation of the Flux Vector . . . . .	46
3.2.7.1	Inviscid Components . . . . .	46
3.2.7.2	Osher's Approximate Riemann Solver . . . . .	46
3.2.7.3	MUSCL Scheme . . . . .	48
3.2.7.4	Viscous Components . . . . .	49
3.2.7.5	Flux Jacobian . . . . .	50
3.2.8	Boundary Conditions . . . . .	50



	3.2.8.1	Slip Wall . . . . .	51
	3.2.8.2	Viscous Wall . . . . .	51
	3.2.8.3	Symmetry . . . . .	52
	3.2.8.4	Pole . . . . .	52
	3.2.8.5	Farfield . . . . .	52
	3.2.8.6	Interface . . . . .	54
	3.2.9	Implicit Solver . . . . .	54
3.3		Vortex Lattice Method . . . . .	50
	3.3.1	Classical Approach . . . . .	50
	3.3.2	Compressibility Corrections . . . . .	52
	3.3.3	Leading Edge Thrust . . . . .	52
	3.3.4	Quasi Vortex Lattice Method . . . . .	54
	3.3.5	Vortex and Control Point Locations . . . . .	55
	3.3.6	Force Calculation . . . . .	57
	3.3.7	Specified Lift Calculation . . . . .	57
3.4		Empirical High Lift Constraint . . . . .	58
	3.4.1	Simple Sweep Theory and Normal Section Parameters . . . . .	58
	3.4.2	Limiting Pressure and Leading Edge Thrust $C_{p,lim} = C_{p,vac}$ . . . . .	59
	3.4.3	Equivalent Mach Number . . . . .	61
	3.4.4	Curve Fit Formulae for $C_{p,lim}$ . . . . .	61
	3.4.5	Application of Carlson's Procedure in the Constraint Function . . . . .	63
3.4		Adjoint Solver . . . . .	72
	3.4.1	Background . . . . .	72
	3.4.2	Quasi-Analytical Methods . . . . .	72
	3.4.2.1	Direct Differentiation . . . . .	73
	3.4.2.2	Adjoint Method . . . . .	73
3.6		Geometry Parametrisation . . . . .	68
	3.6.1	Aerofoil Parameterisation . . . . .	68
	3.6.1.1	Bernstein Polynomial Basis Functions . . . . .	68
	3.6.1.2	Class Shape Transformation (CST) . . . . .	70
	3.6.2	Aerofoil perturbation with constant area . . . . .	70
	3.6.3	Wing Parametrisation . . . . .	73
	3.6.3.1	Camber, Aerofoil or Thickness . . . . .	73
	3.6.3.2	Twist . . . . .	73
	3.6.3.3	Interpolation . . . . .	73
	3.6.4	Volume grid . . . . .	74
	3.6.5	Angle of Incidence . . . . .	74
<b>4</b>		<b>Aerodynamic Investigations</b>	<b>77</b>
	4.1	Geometry . . . . .	77
	4.2	CFD Procedure . . . . .	80
	4.2.1	Flow conditions . . . . .	80
	4.2.2	Mesh . . . . .	80
	4.2.3	Convergence . . . . .	82
	4.3	Longitudinal Results . . . . .	82

4.3.1	Total Forces . . . . .	82
4.3.2	QinetiQ and ARA Test Comparisons with Corresponding RANS results . . . . .	85
4.3.2.1	Drag . . . . .	85
4.3.2.2	Pitching Moment . . . . .	86
4.3.3	Spanwise Forces . . . . .	86
4.3.4	Pressure Distributions . . . . .	90
4.3.5	Flow Visualisation and Pitchup . . . . .	92
4.3.6	Comparisons with the Cobalt Solver . . . . .	94
4.3.7	Cruise Results . . . . .	97
4.4	Lateral Results . . . . .	99
4.4.1	Directional Stability . . . . .	99
4.4.2	Pitching Moment . . . . .	101
4.4.3	Spanwise Forces with Sideslip . . . . .	104
4.4.4	Flow Visualisation . . . . .	104
4.5	Discussion . . . . .	110
<b>5</b>	<b>UCAV Wing Optimisation</b>	<b>113</b>
5.1	Geometry and Mesh . . . . .	113
5.1.1	Geometry . . . . .	113
5.1.2	Mesh . . . . .	113
5.2	Design Points . . . . .	115
5.3	Design Variables . . . . .	116
5.4	Optimiser convergence . . . . .	118
5.5	Designed wings . . . . .	118
5.5.1	Geometry . . . . .	119
5.5.1.1	Cruise Design . . . . .	119
5.5.1.2	High Lift Camber Designs . . . . .	119
5.5.1.3	High Lift Camber and Thickness Design . . . . .	119
5.5.1.4	Euler $C_p$ Slices: Cruise . . . . .	122
5.5.2	RANS evaluation . . . . .	125
5.5.2.1	Total Forces . . . . .	125
5.5.2.2	$M = 0.8$ Flowfields . . . . .	128
5.5.2.3	$M = 0.25$ Flowfields . . . . .	134
5.6	Discussion . . . . .	140
<b>6</b>	<b>Conclusions</b>	<b>143</b>
6.1	Achievements . . . . .	143
6.2	Further Work . . . . .	144
	<b>Bibliography</b>	<b>147</b>

# List of Figures

---

1	Coordinate Systems . . . . .	xx
2.1	Typical Mission . . . . .	4
2.2	RCS for X-Band Illumination at 9GHz from head on for (a) F-18E Super Hornet, (b) Northrup Grumman X-47B and (c) Generic 40° Swept UCAV (adapted from [3])	7
2.3	Comparison of fuselage and fins for a conventional (F-18A) vs low RCS (F-22) aircraft . . . . .	7
2.4	UCAV Planforms . . . . .	12
2.5	Various Stealthy Aircraft . . . . .	13
2.6	Typical Flow Features In A Short, Convoluted Duct [18] . . . . .	14
2.7	Aerofoil geometrical parameters . . . . .	16
2.8	Separation loci for a family of canonical pressure distributions at different Reynolds numbers [19] . . . . .	17
2.9	Canonical pressure distributions for two Liebeck Aerofoils with laminar rooftops designed for $Re = 5 \times 10^6$ . . . . .	18
2.10	Whitcomb's integral (1966) supercritical aerofoil [23] . . . . .	19
2.11	Generalised pressure distributions [23] . . . . .	20
2.12	Schematic flowfield of a supercritical aerofoil [23] . . . . .	20
2.13	Slender Wing Non-linear Lift . . . . .	22
2.14	Rounded Leading Edge Slender Wings [30] . . . . .	23
2.15	1303 UCAV plan [54] . . . . .	28
3.1	Optimiser process . . . . .	34
3.2	A typical cell in MERLIN . . . . .	43
3.3	Osher and Soloman Integration Path (P Variant) . . . . .	47
3.4	Computational stencil for calculation of inviscid and viscous flux . . . . .	48
3.5	Schematic of dual control volume approach . . . . .	50
3.6	Halo cell numbering . . . . .	51
3.7	Vortex Lattice Layout . . . . .	51
3.8	Biot–Savart law for a vortex line . . . . .	52
3.9	Aerofoil pressure distribution and thin aerofoil solution . . . . .	53
3.10	VLM and QVLM singularity parameter vs analytical solution for a parabolic camber aerofoil . . . . .	54

3.11	Grid, $C_p$ distribution and spanwise forces for the Warren 12 planform . . . . .	56
3.12	Various aerodynamic and geometrical parameters . . . . .	58
3.13	Integration of truncated pressure distributions [80] . . . . .	60
3.14	Effect on attained leading edge thrust $C_t$ of various geometrical parameters[80] . . . . .	61
3.15	$C_{p,lim}$ vs $M_n$ [80] . . . . .	62
3.16	Twist applied at the second crank . . . . .	68
3.17	Bernstein polynomial basis functions $S_{r,n}$ with different values of $n$ . . . . .	69
3.18	Basis functions with class shape transformation $CS_{r,n}$ . . . . .	69
3.19	Example upper/lower surface movement for a Clark Y aerofoil with 8 design variables . . . . .	72
3.20	Example thickness distribution modification for a Clark Y aerofoil with 6 design variables . . . . .	72
3.21	Volume grid $y$ sensitivity (red <i>+tive</i> blue <i>-tive</i> ) and corresponding grid movement . . . . .	75
4.1	1303 Geometry . . . . .	78
4.2	Various geometrical parameters for the 1303 UCAV . . . . .	79
4.3	Pressure tap locations . . . . .	79
4.4	1303 multiblock mesh. Red lines indicate block boundaries, every 2 <sup>nd</sup> grid line shown. . . . .	81
4.5	MERLIN convergence for 1303 UCAV at $M = 0.25$ , $\alpha = 11.9^\circ$ . . . . .	82
4.6	Mach 0.25 total forces . . . . .	83
4.7	Axial force vs $C_L^2$ . . . . .	84
4.8	Various Wind Tunnel and Solver Comparisons . . . . .	85
4.9	QVLM compared with MERLIN RANS result $\alpha = 4.57^\circ$ . . . . .	87
4.10	$C_l$ , $C_x$ , $C_m$ , $C_{p,min}$ vs spanwise coordinate $z/b$ . . . . .	88
4.11	Chordwise centre of pressure location vs spanwise coordinate $z/b$ . . . . .	89
4.12	1303 Pressure distributions: MERLIN (blue lines) and QinetiQ Run17 (red dots) . . . . .	91
4.13	1303 coloured $C_p$ distributions and skin friction lines . . . . .	93
4.13	1303 coloured $C_p$ distributions and skin friction lines ( <i>cont.</i> ) . . . . .	94
4.14	1303 experimental oil flow visualisation $\beta = 0^\circ$ . . . . .	95
4.15	Code and turbulence model comparisons . . . . .	96
4.16	Mach 0.8 total forces . . . . .	98
4.17	Overset mesh used in Cobalt . . . . .	100
4.18	1303 UCAV Directional Stability $C_{n\beta}$ vs $\alpha$ . . . . .	102
4.19	1303 UCAV Pitching Moment $C_M$ vs $\alpha$ at different sideslip angles $\beta$ . . . . .	103
4.20	Spanwise forces for leading and trailing wings $\alpha = 5$ . . . . .	105
4.21	Spanwise forces for leading and trailing wings $\alpha = 8$ . . . . .	106
4.22	Spanwise forces for leading and trailing wings $\alpha = 11$ . . . . .	107
4.23	Coloured $C_p$ distribution and skin friction lines at various incidence and sideslip angles . . . . .	108
4.23	Coloured $C_p$ distribution and skin friction lines at various incidence and sideslip angles ( <i>cont.</i> ) . . . . .	109
4.24	Coloured $C_p$ distribution and streamlines at slices normal to the leading edge $\alpha = 11^\circ, \beta = 10^\circ$ . . . . .	110

---

5.1	Original and optimisation geometry comparison . . . . .	114
5.2	Computational meshes . . . . .	114
5.3	Design variable sections . . . . .	116
5.4	Design Variable Examples . . . . .	116
5.5	Optimiser convergence . . . . .	117
5.6	Objective vs constants for various designs . . . . .	118
5.7	Designed wings . . . . .	120
5.7	Designed wings <i>Cont.</i> . . . . .	121
5.7	Designed wings <i>Cont.</i> . . . . .	122
5.8	Aerofoils . . . . .	123
5.9	Euler $C_p$ distributions at cruise . . . . .	124
5.10	Designed wings total forces $M = 0.25$ . . . . .	126
5.11	Designed wings total forces $M = 0.8$ . . . . .	127
5.12	Lower surface separation on designed wings at low incidence, $M = 0.8$ . . . . .	128
5.13	Planar wing $M = 0.8$ coloured $C_p$ distributions and skin friction lines . . . . .	129
5.14	$C_L0.4C$ $M = 0.8$ coloured $C_p$ distributions and skin friction lines . . . . .	130
5.15	$C_L0.5C$ $M = 0.8$ coloured $C_p$ distributions and skin friction lines . . . . .	131
5.16	$C_L0.5CT$ $M = 0.8$ coloured $C_p$ distributions and skin friction lines . . . . .	132
5.17	$C_L0.6C$ $M = 0.8$ coloured $C_p$ distributions and skin friction lines . . . . .	133
5.18	Planar wing $M = 0.25$ coloured $C_p$ distributions and skin friction lines . . . . .	135
5.19	$C_L0.4C$ $M = 0.25$ coloured $C_p$ distributions and skin friction lines . . . . .	136
5.20	$C_L0.5C$ $M = 0.25$ coloured $C_p$ distributions and skin friction lines . . . . .	137
5.21	$C_L0.5CT$ $M = 0.25$ coloured $C_p$ distributions and skin friction lines . . . . .	138
5.22	$C_L0.6C$ $M = 0.25$ coloured $C_p$ distributions and skin friction lines . . . . .	139



# List of Tables

---

1	Aircraft 6 Force and Moment Coefficients Body Axis . . . . .	xx
2.1	Comparison of a family of UCAVs . . . . .	15
3.1	Non-dimensionalisation of variables in MERLIN . . . . .	39
3.2	Osher and Solomon flux formulae: P variant . . . . .	48
3.3	Farfield boundary rules . . . . .	53
3.4	Exponents for Carlson's $C_{p,lim}$ Formulae . . . . .	62
4.1	1303 wind tunnel model (1:10.8 scale) reference values . . . . .	78
4.2	1303 Flow conditions . . . . .	80
4.3	Mesh Refinement Results . . . . .	82
4.4	$\alpha = 0^\circ$ $C_D$ various numerical and wind tunnel results . . . . .	85
5.1	Squared 1303 planform dimensions . . . . .	114
5.2	1303 Vehicle scale flow conditions ( $\bar{c} = 5.4m$ ) . . . . .	115
5.3	Summary of design variables . . . . .	117
5.4	Designed wings . . . . .	117





# Nomenclature

---

## Symbols

$x, y, z$	coordinates in the x,y,z directions
$u, v, w$	velocity components in the x,y,z directions
$t$	time
$\Omega$	fluid element
$V$	cell volume
$S$	cell surface
<b>Q</b>	vector of conservative variables
<b>P</b>	vector of primitive variables
<b>F</b>	vector of fluxes
<b>S</b>	vector of source terms
<b>R</b>	residual vector
$Re$	Reynolds number
$\rho$	fluid density
$p$	static pressure
$\gamma$	ratio of specific heats
$E$	total energy
$e$	specific internal energy
$\tau$	fluid shear stress
$S$	strain rate
$\mu$	molecular viscosity
$\mu_t$	turbulent viscosity
$k$	turbulent kinetic energy
$\omega$	specific dissipation rate
$T$	static temperature
$q$	heat flux
$\ell$	mixing length
$\omega$	vorticity

$y^+$	dimensionless wall distance
$\xi, \eta, \zeta$	$i, j, k$ direction face metric terms
$\lambda$	Lagrange multiplier
$\beta$	design variable
$F(\beta)$	objective function
$C(\beta)$	constraint function
$u$	upper constraint bound
$l$	lower constraint bound
$\Gamma$	vortex strength
$K_t$	attained leading edge thrust parameter
$t/c$	thickness to chord ratio
$r/c$	leading edge radius to chord ratio
$\eta$	position of maximum thickness
$r_{in}$	leading edge bluntness parameter
$C_L$	wing lift coefficient
$C_D$	wing drag coefficient
$C_M$	wing moment coefficient
$C_X$	wing x direction force coefficient
$C_Y$	wing y direction force coefficient
$C_T$	wing thrust coefficient
$C_\ell$	aerofoil lift coefficient
$C_d$	aerofoil drag coefficient
$C_m$	aerofoil moment coefficient
$C_x$	aerofoil x direction force coefficient
$C_y$	aerofoil y direction force coefficient
$C_t$	aerofoil thrust coefficient
$\Lambda$	wing sweep angle
$\theta_t$	wing geometric twist
$c$	chord
$b$	wingspan
$\alpha$	angle of incidence
$\beta$	sideslip angle

## Acronyms

AFRL	Air Force Research Laboratory
AR	Aspect Ratio
ARA	Aircraft Research Association
AVT	Applied Vehicle Technology

BILU	Block Incomplete Lower Upper
BWB	Blended Wing Body
CAD	Computer Aided Design
CDO	Conceptual Design Optimisation
CFD	Computational Fluid Dynamics
CFL	Courant-Friedrichs-Lewy
CST	Class Shape Transformation
DES	Detached Eddy Simulation
DSTL	Defence Science and Technology Laboratory
DSTO	Defence Science and Technology Organisation
GA	Genetic Algorithm
IR	Infra Red
ISTAR	Intelligence, Surveillance, Target Acquisition, and Reconnaissance
LO	Low Observable
MPI	Message Passing Interface
MUSCL	Monotone Upstream-centred Scheme for Conservation Laws
NACA	National Advisory Committee for Aeronautics
NAG	National Algorithms Group
NASA	National Aeronautics and Space Administration
NATO	North Atlantic Treaty Organization
PIV	Particle Image Velocimetry
QVLM	Quasi-Vortex-Lattice Method
RANS	Reynolds Averaged Navier-Stokes
RCS	Radar Cross Section
RHS	Right Hand Side
RSM	Response Surface Model
SQP	Sequential Quadratic Programming
TTCP	The Technical Cooperation Program
TWT	Transonic Wind Tunnel
UAV	Unmanned Air Vehicle
UCAV	Unmanned Combat Air Vehicle
VLM	Vortex-Lattice Method

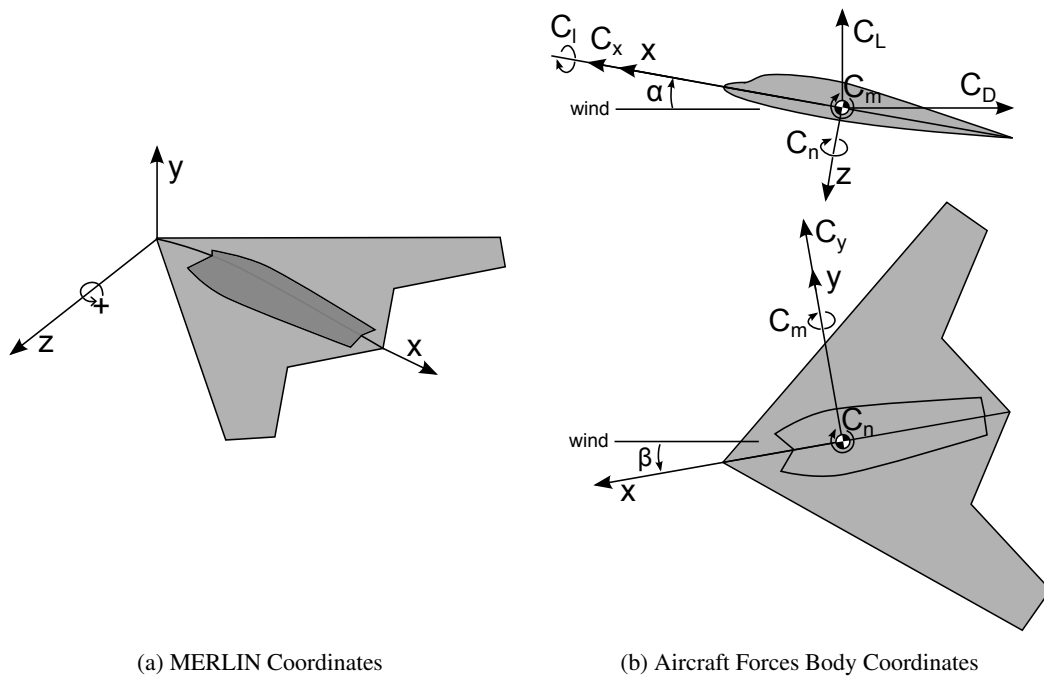


Figure 1: Coordinate Systems

Axis		Force	+tive	Moment	+tive		
$x$	$l$	$C_x$	Axial Force	Forward	$C_l$	Rolling Moment	Roll Right
$y$	$m$	$C_y$	Side Force	Right	$C_m$	Pitching Moment	Nose Up
$z$	$n$	$C_z$	Normal Force	Down	$C_n$	Yawing Moment	Nose Right

Table 1: Aircraft 6 Force and Moment Coefficients Body Axis

# *Chapter 1*

## Introduction

---

### 1.1 Motivations

Unmanned Combat Air Vehicles (UCAVs) are becoming increasingly popular in the UK and wider world defence scene. Current operational UAVs are generally ISTAR (Intelligence, Surveillance, Target Acquisition, and Reconnaissance) platforms which tend to be fairly conventional designs. Some of these aircraft have been adapted to carry weapons, however they cannot operate in a high threat environment due to a lack of stealth features. There are currently several stealthy UCAV concepts being developed in various countries including BAE Taranis in the UK, Dassault nEUROn in France and a Northrop Grumman's naval X-47B in the USA. These designs are broadly similar, with geometric features chosen for stealth reasons. They are all tailless flying wing concepts with moderately swept ( $40^\circ \leq \Lambda \leq 55^\circ$ ) edge aligned wings and obscured propulsion systems. These wings exhibit mixed (attached/separated) flows at moderate incidence angles and hence struggle to generate enough lift at take-off or landing while remaining controllable.

There has been much work on aerodynamic design and optimisation but this has mainly focused on civil type aircraft. This has not tended to be transferred to the military world, as military aircraft rarely fly 'on-design'. Designers have been more concerned with the aircraft performing acceptably across the flight envelope. Now, with unmanned aircraft there is a desire for increased persistence leading to subsonic designs where the detailed shape of the wing becomes much more important.

Stealth as well as trim requirements dictate that high lift devices are prohibited and hence the wings are required to work acceptably in all parts of the flight envelope, meaning compromises for the design at any specific point. Developing improved methodologies for the generation of improved designs for these wings is the main motivation for this work.

### 1.2 Aims

There are two main aims of this work. The first aim is to improve our understanding of low observable UCAV aerodynamics and their prediction using CFD techniques. The second aim is to understand the issues and trade-offs involved in the design of UCAV wings and in doing so produce improved designs for the 1303 UCAV.

### 1.3 Objectives

To achieve the first aim, high quality RANS calculations will be performed for the 1303 UCAV configuration. These will be run for representative take-off and cruise conditions. Two CFD codes will be compared as well as a range of turbulence models, geometric assumptions and mesh resolutions. The flowfield will be examined in detail with comparisons made with wind experiments where possible. Both longitudinal and lateral stability will be assessed and the flow features responsible for nonlinearities discussed.

The second aim will be achieved by developing a high fidelity optimisation methodology for the design of UCAV wings, aiming to improve the low speed high lift capability as well as the transonic performance. The process will be based on a gradient based SQP optimiser where the objective is to minimise drag in the cruise configuration. The objective will be calculated by an in house CFD code MERLIN in Euler mode and the associated gradients will be efficiently calculated using a previously developed adjoint solver. A constraint will be developed for the take-off / high lift condition based on a vortex lattice method combined with empirical curve fit formulae which place limits on achievable local leading edge thrust levels. A large number of design variables is preferable to obtain a sufficiently large design space and the parameterisation scheme must be differentiable for integration into the adjoint solver. The design method will be used to design a family of UCAV wings with different high lift constraints to assess the trade off with cruise performance. The limitations of the methodology for designing high lift wings will be discussed as well as the limitations of the particular planform being studied.

### 1.4 Thesis Outline

Chapter 2 covers in detail, background to the UCAV aerodynamic design problem as well as a literature review of work on UCAV relevant aerodynamics and more broadly on aerodynamic optimisation. Chapter 3 covers the computational methodology used in this work. This includes a detailed description of the RANS flow solver, vortex lattice method and empirical high lift constraint, optimiser, adjoint method as well as details of the geometry parameterisation and mesh movement procedure. Chapter 4 is a detailed investigation into the aerodynamics of the 1303 UCAV including low and high speed calculations, and an in-depth analysis of the flowfield and comparisons with experimental data. The investigation includes both longitudinal and directional stability and uses a number of flowfield visualisation techniques to improve our understanding of the flow. Furthermore, these calculations are used to validate the empirical high lift constraint which is used for design in the subsequent chapter. Chapter 5 describes the aerodynamic optimisation subject to high lift constraints of the 1303 UCAV as well as a detailed evaluation of the designs using the previously described RANS flow solver. Finally Chapter 6 draws conclusions on the above work and makes suggestions for future investigations.

## Chapter 2

# Background and Literature Review

---

This chapter covers two main areas. The first is some background on unmanned combat aircraft design. The second is a literature review on design methods and optimisation.

An unmanned combat air vehicle or UCAV is a military aircraft with no pilot that can carry weapons. As with most modern military aircraft, there is an increasing desire for the aircraft to be survivable and hence they are designed to be stealthy, i.e. avoid detection by various sensors. Early UAV designs have tended to have conventional planform shapes which are aerodynamically efficient and easy to design but are easily detectable by radar and vulnerable to air defence weapons. Technologies such as remote sensors, communication and autonomy are maturing, which allows many of the missions currently undertaken by manned aircraft to be completed by UAVs with reduced risk and cost thus driving the development for improved designs. For this reason, a new class of UCAV planform shapes are being developed that makes use of edge aligned geometries to reduce the radar signature.

### 2.1 Advantages of Unmanned Combat Air Vehicles

This section outlines the key benefits of using UCAVs for combat missions, many of which are currently carried out by manned aircraft. This is given in the context of a generic UCAV mission defined below.

#### 2.1.1 Typical UCAV Mission

A typical UCAV mission is defined which provides a basis for discussing the advantages and disadvantages of various UCAV geometries as well as forming a criterion for judging various designs. Figure 2.1 shows various numbered stages in the UCAV mission. A discussion on how the shape or design of the aircraft impacts the performance in various regards at each stage is given in the following sections. The phases are

1. Take-off - the aircraft would operate out of an airfield in some friendly territory. The runway length and distance to some threshold altitude would be limited. This is particularly important for carrier operations.
2. Climb - the aircraft would climb to its cruising altitude, nominally the edge of the stratosphere ( $\sim 11,000m$ ). A high rate of climb and small fuel requirement would be desirable.

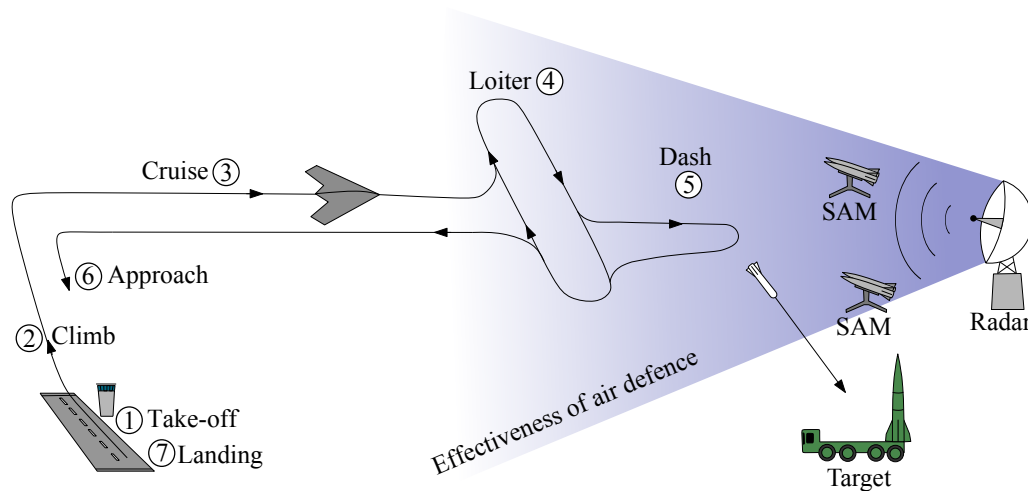


Figure 2.1: Typical Mission

3. Cruise - the aircraft would cruise to its loiter location. This is at a speed just below the drag rise Mach number. A long range and fast cruise desirable.
4. Loiter - The aircraft would loiter, possibly at a lower altitude, in an area were it could utilise sensors and possibly deploy a weapon. Here a long endurance is important.
5. Dash - the aircraft would fly towards its target as quickly as possible to deploy weapons and/or gather intelligence. The maximum speed is important.
6. Approach - during the approach the aircraft will lose altitude to land.
7. Landing - the aircraft must be able to slow itself to the landing speed. After touchdown it must come to rest before the end of the runway.

### 2.1.2 Advantages of Unmanned Aircraft

Unmanned aircraft offer various financial, operational and strategic advantages over manned aircraft. Some points are elaborated upon below.

**Reduced pilot training costs.** The cost of maintaining a traditional fast jet pilot is extremely high. This is largely due to the amount of flying hours required to train and maintain the skill level of a pilot and the support crew and maintenance costs associated with this activity. With an unmanned aircraft, the operator can undertake much of the training on a simulator at a vastly reduced cost. The operator also does not have to remain as physically fit as an equivalent fast jet pilot as they are not subject to the same fatiguing environment of a cockpit including g-forces, vibrations, noise and altitude/pressurisation effects. Fewer pilots may also be required because one operator can potentially operate multiple UAVs when a high degree of autonomy is employed.

**Increased persistence.** No pilot on board removes the constraint that a pilot can only operate an aircraft for a limited period. This is particularly evident if air to air refuelling is used. The aircraft can be present at a particular location for an increased duration either for surveillance or to serve as a deterrent.



**Cockpit not required.** The aircraft design and manufacture can be simplified as compared to manned aircraft as no provision for a cockpit and associated hardware is required. This allows greater flexibility in the design and thus a simpler, cheaper and potentially better performance aircraft can be realised.

Unmanned aircraft can be remotely piloted or even autonomous but for the legal use of weapons, human intervention is currently required to authorise their use. In the MOD Doctrine[1] it states that there is no current plan to develop systems that operate without a human in the loop.

### 2.1.3 Advantages of Low Observable Designs

Low observable aircraft have various advantages for military roles compared with traditional designs. Primarily they offer improved survivability. This obviously depends upon the air defence capability of the enemy. This discussion assumes the enemy has relatively developed air defences as in the above scenario Figure 2.1. The advantages are:

**Effectively reduces the range of enemy air defences.** This means that the aircraft can operate much closer to its targets in phases 3-5 and fly deeper into enemy territory. With a reduced distance to the targets, sensors become more effective and the requirement for stand off weapons is reduced.

**Less likely to be taken down by a surprise attack.** It is much more difficult for ground to air defences to attack the aircraft. This is particularly true for portable ground to air systems which are likely to have much less sophisticated targeting systems.

**Element of surprise.** The aircraft will not be detected until it is closer to its target, giving less time for the enemy to prepare for an attack.

There are also disadvantages associated with current low observable aircraft designs for both the designers and operators of the aircraft.

**Aircraft shape is largely driven by signature requirements.** Traditionally, the shape of an aircraft is determined by aerodynamic and structural requirements. This is particularly true for civil aircraft. With modern low observable military aircraft, the shape is heavily constrained by radar and infra red signature requirements. The result is an aircraft that needs a lower wing loading in order to generate enough lift at low speed which results in large and costly vehicles. This will be particularly detrimental during the take-off/ landing phases.

**Small payload capacity.** Due to signature as well as stability and control requirements, ordinance must be stored inside the aircraft in weapons bays. This significantly reduces the volume available compared with traditional aircraft with external pylons, which also puts pressure on planform size due to packing constraints.

## 2.2 Low Observable Design Features

For an aircraft to remain undetected or to reduce the effectiveness of guided weapons, it must be difficult to detect by various sensors. These include ground and air based radars, infra red sensors as well as visual and acoustic detection.

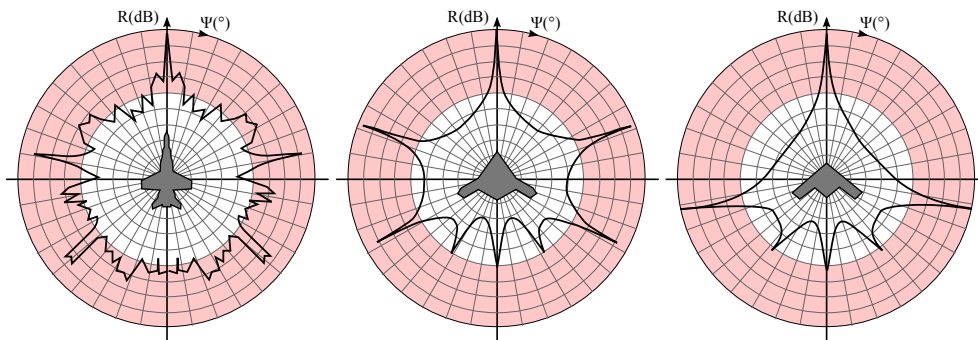


Figure 2.2: RCS for X-Band Illumination at 9GHz from head on for (a) F-18E Super Hornet, (b) Northrup Grumman X-47B and (c) Generic 40° Swept UCAV (adapted from [3])

## 2.2.1 Radar

Radar (short for radio detection and ranging) systems work by emitting radio waves from a directed antenna and ‘listening’ for signals back from aircraft. There are various types of radar that have different arrangements of radio sources and detectors although the most common, especially for air based systems, is the monostatic radar [2] where the source and detector are both on board an aircraft.

### 2.2.1.1 Planform Alignment

The main mechanism by which radar energy gets back to the detector is reflection, known as specular return. This occurs when any surface is perpendicular to the radar system. For an aircraft with curved and or vertical surfaces, this will occur much of the time and the returns will be strong. The signature can be managed by reducing the number of angles from which the reflections occur. This is achieved through ‘planform alignment’ so that features such as the wing leading and trailing edges and control surface hinge lines are aligned in a particular direction. An example is shown in Figure 2.2 of three aircraft, a conventional fighter (F-18A) and two feature aligned UCAVs. The feature aligned planforms have much lower broadband responses (must be close to or below background levels to remain undetected) and the reflections are managed into spikes. The minimum number of planform angles would be 3 for a delta planform although it is undesirable to have a spike at the front or rear as then you cannot fly directly towards or away from a threat. Therefore four spikes are preferred. Curved edges are also avoided as they tend to scatter radar signals. Concave angles close to 90° such as wing body junctions should also be avoided as they reflect the incident radio waves back to their source.

Vertical surfaces such as fins or fuselage sides will reflect a large amount of radio energy horizontally back to the source. Some aircraft have dual fins tilted outwards or a ‘V’ tail, which offers a compromise between low observability and directional stability, important if the aircraft must be manoeuvrable. chines are extensions added to fuselage sides to deflect incident radio waves either upwards or towards the ground. A comparison of two body cross sections is given in Figure 2.3 one with chines and a twin fins (LO design) compared with a conventional design. An even better solution for reducing RCS is to omit fins and separate fuselages altogether resulting in the flying wing concepts discussed in this thesis.

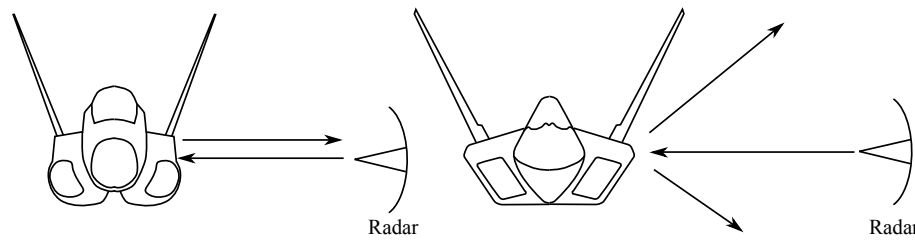


Figure 2.3: Comparison of fuselage and fins for a conventional (F-18A) vs low RCS (F-22) aircraft

Another mechanism for radar signals to be directed back to the source is through radiation of surface currents. When an aircraft's skin is energised by incident radio signals, currents build up in the skin and radiate from discontinuities such as control surface hinges or bay doors and trailing edges. This can again be managed by aligning these features with the main planform RCS spikes.

#### 2.2.1.2 Materials

Material selection and structural design can also be used to reduce RCS. Radar absorbent materials (RAM) will absorb radar electromagnetic energy and convert it to heat which is then radiated through the skin. The internal structures can also be designed to deflect radar away from its source. This does not place hard constraints on the possible aerofoil shapes although a smaller leading edge radius seems to be preferred. The resulting low observable structure including RAM will be much heavier than that not designed for low RCS.

#### 2.2.1.3 Internal Stores Carriage

For the same reasons discussed above, the complex shapes associated with external weapons and stores carried on pylons scatter a lot of radar energy and therefore they must be carried internally to minimise RCS. This requires a larger volume and allows for less flexibility in the design.

#### 2.2.1.4 Intakes and Nozzles

The position and geometry of the engine inlets and nozzles are important for controlling RCS. Radar energy entering these cavities gets reflected around and can be scattered back towards its source. To reduce RCS, the intakes can be placed on top of the aircraft, obscuring them from view from ground sources of radar. Two dimensional (high aspect ratio) nozzles can be used to obscure the LP turbine from outside view at most angles. Current intake designs for low observable aircraft include intakes with grills (F-117) and edge aligned intakes including W shaped inlets (B2, nEUROn) and V shaped inlets (X-47b, BAE Taranis). The x47b UCAV demonstrator has a diverterless bump inlet, a bump on the forebody just before the intake which diverts the majority of the boundary layer around the inlet as well as obscuring the intake cavity from outside view.

Within the aircraft, convoluted ducts are used to obscure the engine faces from the outside. There are limits on how short these can be to avoid flow separation and hence the total propulsion length is often quite long. As planforms are heavily constrained by planform alignment constraints, the resultant aircraft will have to be large in order to accommodate the propulsion system.

#### 2.2.1.5 Equipment

A large contributor to RCS are the cavities, which house the sensors as well as the sensors themselves. For example, in traditional fighter aircraft, the radar is mounted on the front bulkhead with a radar transparent cowling in front. The bulkhead itself would reflect a large amount of radar as well as the radar antenna radiating absorbed energy. The problem can be reduced with cowling made from band pass materials that only allow a specific frequency of electromagnetic radiation to pass through as well as mounting the equipment in accordance with the edge aligned principle.

#### 2.2.1.6 Mission Planning

All of the above techniques can only go so far in avoiding detection. The mission must also be planned with observability in mind. The mission trajectory can be planned in order to direct the known RCS spikes and vulnerabilities away from any known detectors. This includes avoiding operation of the radar in an active mode (sending out radio signals) which gives away the aircraft's location unless it absolutely necessary.

#### 2.2.2 Infra Red

Many short range air defence systems use infra-red (IR) as a means of identifying and tracking their targets. The main source of the IR radiation for obvious reasons is the engine. For this reason the engine can be obscured from view using convoluted ducts as well as 2-D nozzles consistent with reducing the RCS discussed above. High bypass turbofan engines are used to cool the exhaust and bleed air from the engine is used to cool hot components of the aircraft which may be visible from the outside. This means that a non-optimal bypass ratio is often be used resulting in a higher fuel consumption. Convoluted ducts, non-optimal intake and nozzle designs and the use of bleed air further reduce engine performance.

The aircraft skin can also be designed to reduce IR signature. This will mainly involve selection of materials and surface coatings to minimise reflections from the sun and ensure radiation from the skin is close to background levels. In order to avoid aerodynamic heating issues at airframe edges, stealth aircraft usually fly at subsonic speeds.

#### 2.2.3 Visual

Visual detection can also be important, especially if the aircraft cannot be detected by other sensors. To minimise the visual signature, the colour of the aircraft is important with blue/grey colours being preferred. Contrails and soot are also a source of visual detection and can be minimised by quickly mixing the engine plume with the freestream air. This will however deteriorate engine performance.

#### 2.2.4 Acoustics

Finally, the acoustic signature can be reduced by minimising engine and airframe noise. Engine noise can be reduced by embedding the engine within the airframe. Slowing the exhaust (consistent with having a high bypass engine) to reduce the shear flow in the exhaust jet will reduce noise. Flying at subsonic speeds will eliminate the sonic booms associated with supersonic aircraft although this means the aircraft can now be heard from the front.

## 2.3 Key Performance Indicators

This section outlines some conceptual design fundamentals relating to aerodynamic performance that are important in the design of a new UCAV.

### 2.3.1 Take-off

The take-off distance is an important design consideration for low observable aircraft as, with no high lift devices, the maximum lift the wing can produce under take-off conditions may be relatively low. Furthermore potential airfields may have short runways. Assuming the thrust and weight remain constant during the ground run and neglecting drag and rolling resistance (which result in 10 - 20% longer distances) the ground run distance for a lift-off speed of  $1.2V_s$  (stall speed) is [4]

$$d = \frac{1.44(W/S)}{\rho C_{L,max}(T/W)} \quad (2.1)$$

From this we see that for a short ground run we require a low wing loading ( $W/S$ ), a high thrust-to-weight ratio ( $T/W$ ) and a high maximum lift coefficient  $C_{L,max}$ . The ground run  $d$  is inversely proportional to the maximum lift and thus the ground run distance is extremely sensitive to a low  $C_{L,max}$ . In order to compensate for this, a low wing loading and high thrust will be required resulting in a large and costly vehicle. The full take off distance calculation requires integration of a differential equation in which the thrust, drag, rolling resistance, weight and lift are all functions of the speed. The calculation also usually includes rotation as well as the climb to a threshold altitude.

The  $C_{L,max}$  for take-off is not simply at the stall angle for the wing. It will be the highest usable  $C_L$  in the take-off configuration constrained by stability and control aspects and tailscrape incidence with a safety margin applied and is likely to be significantly lower than the wing stall angle.

The US Air Force military specifications[5] for piloted aircraft specifies that the take-off speed must be  $V_{takeoff} \geq 1.1V_s$ , the stall speed. For the initial climb, the requirement is  $V_{climb} \geq 1.2V_s$ . This corresponds to a required lift coefficient margin of  $C_{L,max} \geq C_{L,takeoff}1.1^2$  and  $C_{L,max} \geq C_{L,climb}1.2^2$  respectively.  $C_{L,max}$  will be determined by the maximum usable incidence, beyond which the aircraft can no longer be controlled. It may be possible to relax these specifications for some unmanned aircraft due to improved flight control systems and potentially reduced safety requirements although no requirements for military UAVs were found.

### 2.3.2 Cruise

Cruise performance is determined by the aircraft's range  $R$  and cruise speed  $V$  or Mach number  $M$ . The range is calculated using the Breguet range equation (2.2), which estimates a distance  $R$  given the Mach number  $M$ , speed of sound  $a$ , the specific fuel consumption  $sfc$ , the lift to drag ratio  $L/D$  and the weight at the beginning and end of the cruise  $W_0$  and  $W_1$ .

$$R = \frac{aM}{sfc} \frac{L}{D} \ln \left( \frac{W_0}{W_1} \right) \quad (2.2)$$

For the purposes of this thesis, we will assume that  $sfc$  has a value of  $1 \text{ kg/decaN/hr}$  and the fuel fraction available for cruise is 30% of the MTOW giving  $W_0/W_1 = 1.3$ . The range now depends upon the speed and the lift to drag ratio. To get the longest range,  $M^{L/D}$  should be maximised.

A high speed cruise is preferable for obvious reasons but the aircraft will be limited to subsonic airspeeds for the reasons discussed above. Speeds too close to  $M_\infty = 1$  will have an excessive drag penalty due to transonic drag divergence. This drag divergence Mach number depends upon the wing sweep and aerofoil design and wing loading. A nominal cruise speed of  $M_\infty = 0.8$  is assumed in this work.

The lift to drag ratio determines the range for a particular flight condition. Wing aspect ratio is extremely important here as it will determine the induced drag. The drag coefficient can be estimated by equation (2.3)

$$C_D = C_{D0} + \frac{C_L^2}{\pi e AR} \quad (2.3)$$

where  $C_{D0}$  is the zero lift drag coefficient,  $C_L$  is the lift coefficient,  $AR$  is the wing aspect ratio and  $e$  is the span efficiency factor which depends upon the spanwise lift distribution. The theoretical maximum value for  $e$  is 1 for an elliptical lift distribution and will be lower than this for any other distribution. Under transonic conditions, Qin *et al.* [6] showed that an elliptical distribution does not necessarily have the lowest overall drag due to wave drag contributions. For a swept wing BWB airliner, of three distributions tested, a mixed triangular / elliptical distribution was found to be best. Furthermore for flying wing aircraft trim and also structural weight can also considerations when selecting a lift distribution.

The wing loading  $W/s$  of the aircraft will determine the required lift coefficient  $C_L$  and therefore the induced drag generated by the wing. Lower wing loadings result in lower induced drag values but the viscous drag contribution will increase due to an increase in wetted area. For an aircraft which is purely designed for cruise, the optimum wing loading can be chosen for cruise. On a UCAV with limited provision for high lift devices, it is likely to be lower due to take-off requirements. A simple analysis can be used to estimate the lift coefficient at which the highest lift to drag ratio occurs. Equation (2.3) can be differentiated to find the stationary point giving the following expression for  $C_L$

$$C_{L|L/D_{max}} = \sqrt{\pi e AR C_{D0}} \quad (2.4)$$

### 2.3.3 Loiter

The time available for an aircraft to loiter  $t$  is calculated very similarly to the range calculation above. The time is given by equation (2.5), identical to (2.2) apart from the speed is now omitted.

$$t = \frac{1}{sfc} \frac{L}{D} \ln \left( \frac{W_0}{W_1} \right) \quad (2.5)$$

The loiter speed is selected to maximise the product  $\frac{1}{sfc} \frac{L}{D}$  and is likely to be lower than the cruise speed. For this reason, delaying the transonic drag rise is less important and hence the detailed wing shape is less critical and going to be driven by the cruise requirements. Similar to the above analysis for the best  $L/D$ , it can be shown that the best endurance is achieved at  $L^3/D^2$  [7]. Again assuming the drag polar of equation (2.3) and constant  $sfc$  the best endurance is found at a lift coefficient of

$$C_{L|L^3/D^2_{max}} = \sqrt{3\pi e AR C_{D0}} \quad (2.6)$$

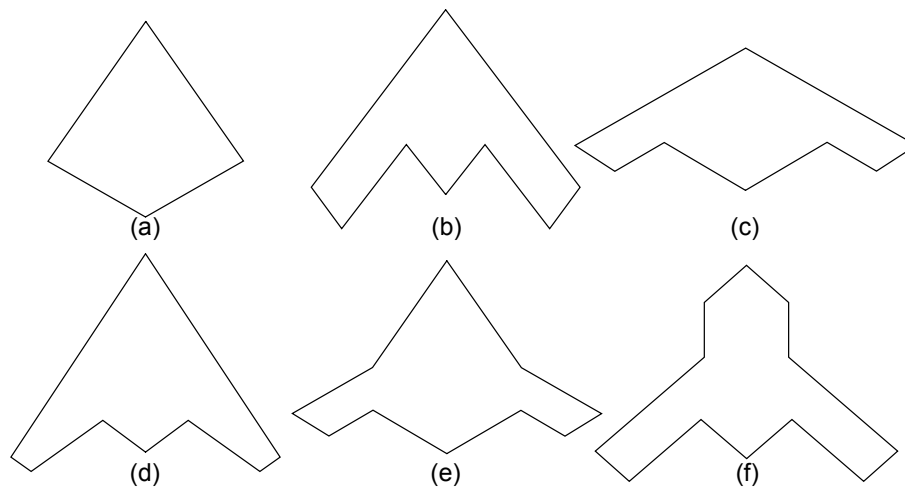


Figure 2.4: UCAV Planforms

which is clearly going to give a higher lift coefficient than the best cruise speed and hence a lower speed will be required.

### 2.3.4 Dash

The dash phase of the flight will involve flying at high speed towards a target in order to release weapons. The dash is likely to be at a high subsonic Mach number and it is important that the aircraft remains controllable throughout, including increased ‘g’ turns.

## 2.4 Planform Selection

### 2.4.1 Shape

There are numerous examples of planform shapes for military aircraft. These include rectangular, elliptical, tapered, swept and delta wing planforms. Stealthy aircraft have edge aligned planforms which can be diamond shaped, lambda wings or more complex shapes (example B2) as long as the sweep angles  $\pm\Lambda$  conform to the intended radar return angles of the aircraft. This results in planform shapes which have large chord variations and/or discontinuous leading/trailing edges selected for stealth reasons. The selection of a particular planform shape for a given mission depends upon stealth, aerodynamic performance as well as structural and packaging requirements and is essentially a trade-off of these factors.

Figure 2.4 shows a number of planforms (current concepts), each with a small number of planform angles. (a), (d), (e) and (f) each have four return angles. (b) and (c) have two and are essentially the same apart from the sweep angle. This does not necessarily mean that (b) and (c) would be the most survivable. The RCS would have to be evaluated with respect to a particular mission and threat scenario.

### 2.4.2 Propulsion Considerations

The propulsion system for a stealthy aircraft should be designed to minimise the infra-red, radar and acoustic signature. There are various low observable features found on current aircraft and



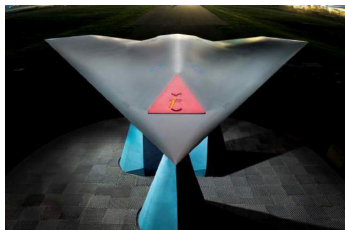
(a) General Atomics MQ-1 Predator[8]



(b) BAE Systems Mantis[9]



(c) BAE Systems Corax[10]



(d) BAE Systems Taranis[11]



(e) Dassault nEUROn[12]



(f) Northrop Grumman X-47A[13]



(g) Northrop Grumman X-47B[14]



(h) Boeing X-45A[15]



(i) Lockheed F-117[16]



(j) Northrop Grumman B-2[17]

Figure 2.5: Various Stealthy Aircraft



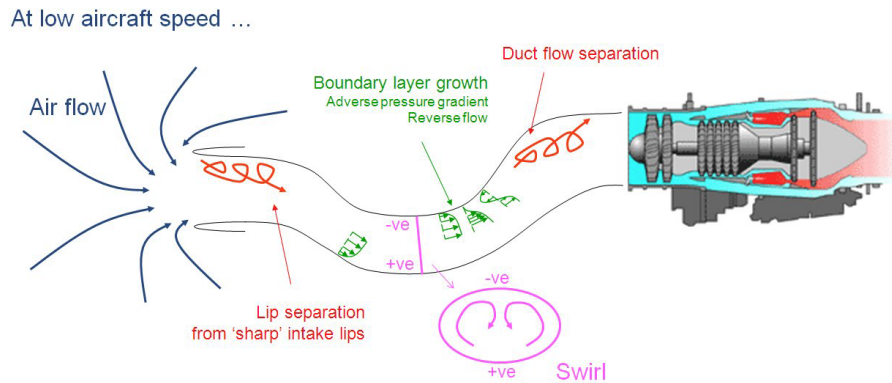


Figure 2.6: Typical Flow Features In A Short, Convoluted Duct [18]

future concepts. One key principle is to obscure the engine faces (compressor and turbine) from view from the outside. The intake and nozzle can be placed on top of the aircraft to make it less visible from the ground. This is seen on almost all stealthy UCAV concepts. Further obscuration is achieved by incorporating convoluted S shaped ducts as shown in Figure 2.6 used on both the intake and exhaust. The flow however cannot negotiate tight turns without incurring total pressure losses due to flow separation. This puts constraints on the minimum length of the ducts and hence the propulsion system can become quite long. When incorporated in a stealthy edge aligned planform, this can drive the size of the vehicle, which may become very large. Planforms (e) and (f) and to a lesser extent (d) in Figure 2.4 are attempts at de-coupling the propulsion length from the wingspan at the expense of increasing the number of planform angles. The ducts should be carefully designed to minimise losses and flow control devices can be employed to help the flow negotiate bends and allow shorter duct lengths.

### 2.4.3 Planform Sweep Angles

For any UCAV planform the sweep angle/s can be varied to produce a family of similar UCAV shapes. Changing the sweep will significantly affect the radar signature, aerodynamics and packaging and thus the resulting size and cost of the vehicle. Table 2.1 shows a comparison of 5 similar UCAVs differing only in their sweep angles. Several attributes are qualitatively compared to demonstrate the trade-offs when selecting a particular shape.

A small wingspan would be beneficial for logistical reasons such as airfield size and storage as well as reducing the structural weight. This also affects the aspect ratio which determines the induced drag where a large aspect ratio is preferred. For a cruise lift coefficient of  $C_L = 0.2$ , the lift to induced drag ratio ( $e = 1$  assumed) varies by a factor of almost five between the  $20^\circ$  and  $60^\circ$  planforms. This is not truly representative of the actual performance as the viscous drag is not considered. Viscous drag would be similar in each case due to equal wetted areas. Sweeping the wing has the effect of reducing the maximum attached flow lift coefficient at low speed. This is because an aerofoil on a swept wing cannot sustain such a high sectional lift, as well as the three dimensional effects degrading the wing's performance. When the wing becomes highly swept ( $\Lambda > 55^\circ$ ), some of the high lift performance is regained due to enhanced lift from the leading edge vortices. At transonic and supersonic speeds, a high sweep angle may be beneficial for reducing

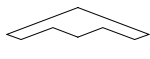
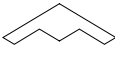



					
Sweep Angle $\Lambda$	20°	30°	40°	50°	60°
Wing Span $b/\sqrt{S}$	2.4	1.9	1.6	1.3	1.1
Aspect Ratio $AR$	11.4	7.2	4.9	3.5	2.4
$L/D_i$ @ $C_L = 0.2$	179	113	78	55	38
Range / Endurance	highest				lowest
$C_{L,max}$	highest		lowest		better
$c_{root}/\sqrt{S}$	0.95	1.2	1.5	1.7	2
Propulsion Length	shortest				longest
RCS	worst				best

Table 2.1: Comparison of a family of UCAVs

wave drag and in the case of supersonic flight, aerodynamic heating. A large root chord is preferred for incorporating the propulsion system. Finally for reducing radar cross section a high sweep is generally preferred.

Trading off these factors for various planforms is a difficult and involved process because each aspect must be considered. In order to reduce the problem to one where it is possible to consider many planforms, simplified models are used which reduce the aerodynamic, structural, packaging and RCS models to simple physics based relationships, database / curve fit models and rules of thumb. The problem with this approach for an LO aircraft is that, many of the assumptions are no longer accurate or valid but can end up driving the design of the vehicle, leading to poor design decisions. One critical area which requires improvement is high lift predictions for take-off and landing. This is not only difficult and time consuming to predict, but can be dramatically improved with detailed shape design.

Table 2.1 shows a family of UCAVs with different sweep angles ranging from  $\Lambda = 20^\circ$  to  $60^\circ$ . A simplistic analysis of some of the above factors is given. The designs considered in this work are in the  $\Lambda = 50^\circ$  category which offer a compromise between range, propulsion length and RCS. This category is also less well understood aerodynamically as there is often a mixed attached/separated flowfield at high lift.

## 2.5 Aerofoil Aerodynamics

The selection of aerofoil sections for a flying wing UCAV is certainly going to have a significant impact upon the performance across the flight envelope. Unlike conventional aircraft, there is only very limited provision for flaps and high lift devices. This is partly for RCS reasons but also because on a flying wing, there is relatively a low control authority in pitch and hence large pitching moments generated by high lift devices cannot be tolerated. For this reason, the (single element) aerofoils have to be able to sustain a high lift for take-off as well as having reasonable performance at cruise, loiter and dash phases of the flight. A brief review of different specialised aerofoils is given below. A UCAV will have to have aerofoils with a combination of several of these characteristics.

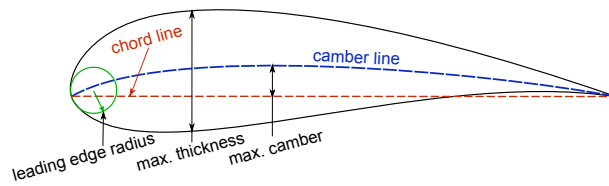


Figure 2.7: Aerofoil geometrical parameters

### 2.5.1 High Lift

There are 4 basic aerofoil parameters which strongly influence the maximum lift for most conventional aerofoil sections. Shown graphically in Figure 2.7 these are:

- (a) Thickness to chord ratio  $t/c$

Thicker aerofoil sections will have a higher  $C_{l,max}$ , mainly due to the associated increases in leading edge radius. Once an aerofoil becomes too thick, the maximum lift reduces as the stall mechanism moves from leading edge to trailing edge stall. A thick aerofoil will also decrease the drag divergence Mach number.

- (b) Leading edge radius  $r_i/c$

A large leading edge radius is good for producing a high  $C_{l,max}$  as the leading edge suction peak will be reduced and hence adverse pressure gradient will be less severe on the upper surface of the aerofoil. A large leading edge radius is particularly important if the aerofoil has to work over a wide range of incidences.

- (c) Camber  $y_c/c$

Addition of camber almost always has a beneficial effect on  $C_{l,max}$ . This is most apparent on thin aerofoils or aerofoils with a small leading edge radius. Camber has the effect of 'spreading' the chordwise loading and thus reducing adverse pressure gradients. It also shifts the lift curve upwards and hence can be used to modify the spanwise lift distribution of a wing in a similar way to geometric twist. This is known as aerodynamic twist.

- (d) Maximum thickness position  $\eta$

Similar to the effect of leading edge radius, a forward movement of maximum thickness position is beneficial for a high  $C_{l,max}$ .

#### 2.5.1.1 Canonical Pressure Distribution

In configuration aerodynamics, a different definition of pressure coefficient was introduced by A.M.O Smith [19] known as the canonical pressure coefficient  $\bar{C}_p$ . This gives a more intuitive understanding when comparing different aerofoils and looking at separation criteria. The canonical pressure distribution is

$$\bar{C}_p = 1 - \left( \frac{U}{U_0} \right)^2 \quad (2.7)$$

where  $U_0$  is the velocity at the edge of the boundary layer just before the compression occurs. This can be obtained from the surface pressure using Bernoulli's equation and the value of  $C_p$  at the suction peak such that

$$U_0 = \sqrt{1 - C_{p0}} \quad (2.8)$$

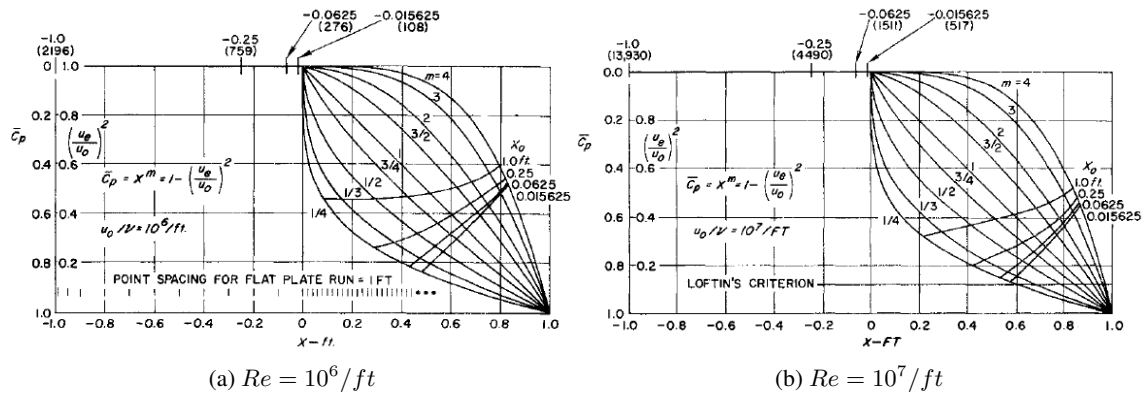


Figure 2.8: Separation loci for a family of canonical pressure distributions at different Reynolds numbers [19]

In this definition, the canonical pressure just before the compression is  $\bar{C}_p = 0$  and the stagnation pressure is at  $\bar{C}_p = 1$ . The canonical pressure therefore gives an indication of the relative momentum of the flow throughout the compression and hence is much more meaningful in separation analysis.

Figure 2.8 shows some canonical pressure distributions for flat plates of various lengths, followed by a compression at  $x = 0$ . The pressure distributions for these compressions are of the form  $\bar{C}_p = x^m$  with different exponents  $m$ . The pressure distributions were then fed into the Cebeci-Smith method to find the loci of separation which are shown by the perpendicular lines for different leading flat plate lengths. The figures show that in each case the best pressure recovery (highest  $C_p$  before separation) was achieved using a concave pressure distribution. Furthermore a short flat plate length and a high Reynolds number is preferable which essentially reduces the boundary layer thickness before the compression. Smith suggests that for initial approximations, the canonical pressure coefficient at which separation occurs is a function of the incoming boundary layer momentum thickness Reynolds number  $R_\theta$  and the shape of the compression curve  $\bar{C}_p(x)$ . This means that the flow is just as likely to separate in a compression from  $100m/s$  to  $50m/s$  as a compression from  $10m/s$  to  $5m/s$ , providing the shape of the compression is the same.

Loftin and von Doenhoff [20] studied many thin aerofoils and arrived at a separation criteria of  $\bar{C}_p = 0.88$ . This is marked on Figure 2.8(b) and coincides very well with the separation point for the  $m = 1/4$  profile with a flat plate length of  $1/64ft$  which closely matches the conditions found on many thin aerofoils.

### 2.5.1.2 Maximum Lift Aerofoils

Stratford developed a mathematical expression (see [21]) for estimating the point of separation in an arbitrary decelerating flow. He used this to derive a further expression for a pressure distribution which has a constant margin against flow separation. If the margin is set to zero, the limiting case is obtained where the flow is about to separate everywhere but the compression is completed in the shortest distance. For a given pressure rise and length, Stratford's solution also gives the minimum drag.

For application to aerofoil design, the problem is re-formed to find the pressure distribution which has the highest mean suction across the chord with no flow separation. Comparing pressure

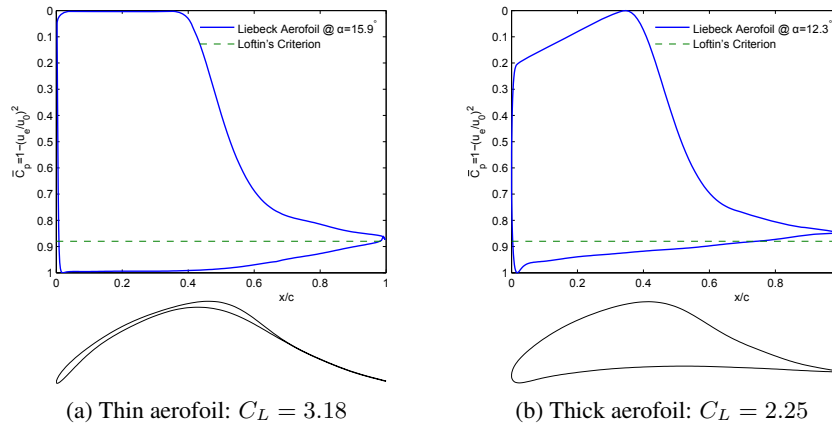


Figure 2.9: Canonical pressure distributions for two Liebeck Aerofoils with laminar rooftops designed for  $Re = 5 \times 10^6$

distributions for various rooftop ( $-C_p$ ) values, followed by Stratford compressions (to  $C_p = 0.2$ , a typical dumping velocity), it was observed that as the pressure peak is increased, a longer compression is required. An optimum exists where the  $C_p(x/c)$  curve encloses the maximum area and hence produces the most lift. The optimum value of  $C_p$  depends upon the incoming boundary layer and hence the Reynolds number. It should be noted that a laminar boundary layer before compression is beneficial because it produces lower  $R_\theta$  values which permits a quicker compression.

Liebeck applied this to aerofoil design [22]. This requires a lower surface pressure distribution as well as an inverse design method to find the corresponding aerofoil geometry. Two examples of Liebeck aerofoils are shown in Figure 2.9 with their corresponding canonical pressure distributions. The thinner aerofoil (a) has a constant rooftop  $C_p$  followed by a Stratford compression on the upper surface. The lower surface is as cambered as possible to generate the maximum possible lower surface lift. This results in an extremely thin and cambered aerofoil with a lift coefficient of  $C_L = 3.18$ . This aerofoil is unsuitable for most aircraft applications due to a small cross sectional area and extremely poor off design performance. The second design (b) initially has a mild negative pressure gradient on the suction side in order to promote laminar flow, followed by a Stratford compression. It is designed so that transition occurs just before the compression. The lower surface now has an approximately linear expansion from the leading edge stagnation point to the trailing edge, which results in a much thicker aerofoil with a lower lift coefficient of  $C_L = 2.25$ . This however would be much more suitable for real world applications.

### 2.5.2 Supercritical Aerofoils

Early supersonic aircraft found it extremely difficult pass through the sound barrier due to the significant drag rise experienced at transonic speeds. In the early 1960's Dr Richard Whitcomb developed an aerofoil concept which attempted to remedy this problem by shaping the aerofoil such that the flow would re-compress isentropically or with a significantly weaker shock. During the subsequent decades, significant effort was put into the development of these aerofoils which delay the transonic drag rise behaviour but also retain good low speed high lift characteristics [23].

An additional benefit with these aerofoils is that, an aircraft can cruise much closer to the speed of sound without incurring a drag penalty – a feature which is exploited in almost all current civil aircraft.

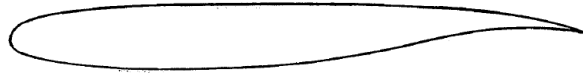


Figure 2.10: Whitcomb's integral (1966) supercritical aerofoil [23]

As shown in the example in Figure 2.10, this classification of aerofoil is characterised by a fairly large leading edge radius, a flat top and substantial aft camber. In broad terms, supercritical aerofoils aim to accelerate the flow to a little above sonic velocity and then gradually decelerate the flow before the shock occurs, weakening the resulting shock and hence reducing losses. Another common feature of supercritical aerofoils is aft camber. This boosts the amount of lift by compressing the flow before the trailing edge resulting in higher lower surface pressures. This is shown in Figures 2.11 (a) and (b).

It is a little counter-intuitive that a large leading edge radius should improve transonic behaviour of an aerofoil. This phenomena is explained graphically in Figure 2.12 showing the expansion waves generated around the leading edge. These (theoretically infinite number of) waves reflect off the sonic line as compression waves, slowing the flow and thus allowing some positive upper surface curvature to keep the flow velocity constant or gradually decelerating. The larger the leading edge radius, the stronger these disturbances will be, giving a stronger effect. This is what makes transonic aerofoil design is difficult as shape changes can have far reaching and unexpected consequences. The aim is to design an aerofoil in which the disturbances are sufficient to return the flow to subsonic speeds before a shock occurs.

In the early (pre CFD) days, supercritical aerofoil design was done using rules of thumb and significant testing. Advances in numerical prediction techniques has allowed optimisation to be performed producing improved designs. One problem with highly optimised single point aerofoils is that, although the performance may be locally very good, experience has shown that off design the performance can drop off quicker than that of other designs. For real world aircraft, the freestream conditions are continuously changing during the flight and cannot be precisely measured. Furthermore as the fuel load changes, the weight and aeroelastic shape of the aircraft will also change meaning that the benefits of such an aerofoil could not be realised. Multi-point optimisation has been suggested to improve this deficiency as shown in references [24] for aerofoils or [25] for wings. The resulting designs show benefits over those from single point methods. However, the solution still tends to give better performance at the considered points. Huyse [26] developed a more robust approach to aerofoil design which uses a probabilistic approach for design. This way a range of flight conditions and possible surface shapes can be taken into account for the design, resulting in better overall performance throughout the flight with none of the 'local' shaping features which can be produced with the above single point or to a lesser extent multi point methods.

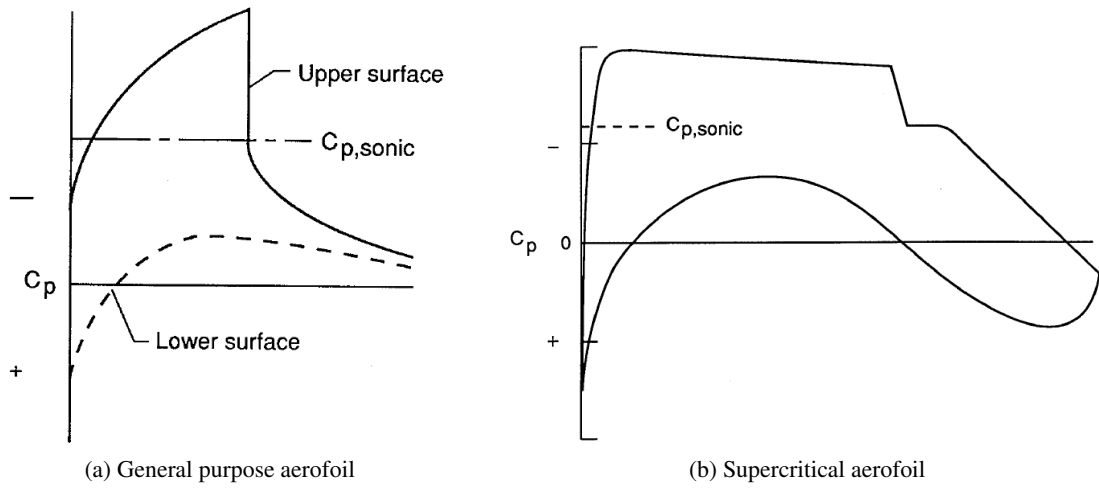


Figure 2.11: Generalised pressure distributions [23]

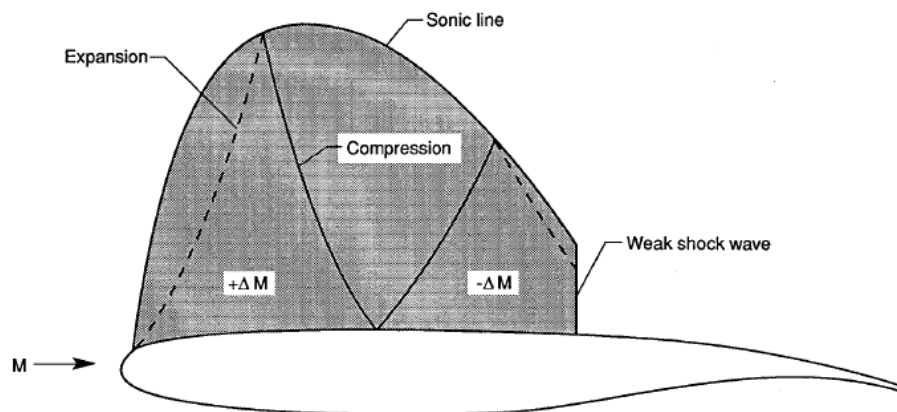


Figure 2.12: Schematic flowfield of a supercritical aerofoil [23]

## 2.6 Wing Aerodynamics

### 2.6.1 Swept Wings

Wing sweep is used on many (civil and military) aircraft for reducing the effects of compressibility at transonic speeds. On a swept wing, the surface curvature is rotated relative to the incoming flow and hence the velocity component normal to curvature direction is reduced. In simple sweep theory, the incoming velocity vector is broken down into two components. One normal and one tangential to the wing sweep direction  $\Lambda$ . Curvature in the tangential direction is small compared with that in the normal direction and hence can be ignored. The remaining (normal) velocity component is lower than that of the freestream flow and hence the effective Mach number is reduced by the factor

$$M_n = M_\infty \cos \Lambda \quad (2.9)$$

From this equation, aerodynamic advantage is obvious. However, there are several other implications. With increased sweep, structural weight will be increased due to the additional torsional load. Aero-structural design is required in order to maximise any potential benefits. There are also stability and control implications with wing sweep adding to the dihedral effect.

Another important implication of sweep is that the lift distribution becomes biased to the wingtips. This causes undesirable stall characteristics because the tips will stall first. This can cause pitch-up as the tips are behind the aircraft's centre of gravity or strong rolling or yawing moments if one wingtip experiences stall first. On early swept wing aircraft, modifications such as fences, notches or vortex generators were made to remedy this problem by delaying separation. Wing shaping e.g. washout can also be used to design out this characteristic.

For flying wing aircraft, sweep is beneficial for trimming as the aircraft as washout produces a nose up moment. It also has the benefit of increasing the moment arm for the control surfaces and therefore improving their effectiveness.

### 2.6.2 Slender Wings

Modern military fighters e.g. Typhoon and F-22 are designed for supersonic cruise and manoeuvre requirements. These highly swept wings are designed to lie behind the Mach cone at the cruise condition hence reducing drag. The wings are also thin, with small leading edge radii and make use of leading edge vortices in order to meet high g manoeuvre requirements. A detailed review of the evolution of slender wing aircraft was given by Polhamus [27]. An example of a slender wing flowfield is shown in the sketch by Hummel (Figure 2.13 [28]). The wing has a very small leading edge radius causing the flow to separate. A primary vortex is formed which follows the wing leading edge. A suction peak is present below the vortex generating additional 'vortex' lift. Also shown in the sketch is a secondary vortex caused by separation of the spanwise flow induced by the primary vortex due to the adverse pressure gradient here. Again this generates some additional lift. Polhamus developed an expression for the amount of additional vortex lift generated relating to the loss in leading edge thrust known as the leading edge suction analogy.

$$C_L = K_p \cos^2 \alpha + K_v \sin^2 \alpha \cos \alpha \quad (2.10)$$



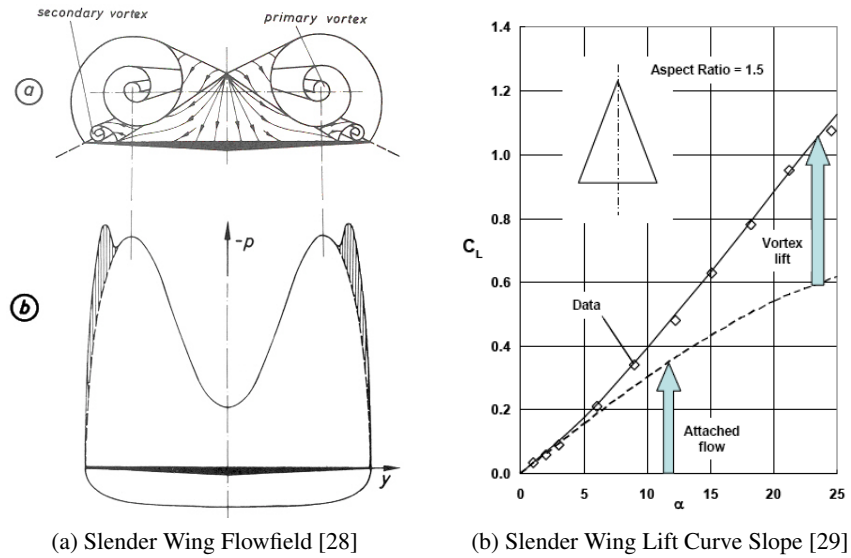


Figure 2.13: Slender Wing Non-linear Lift

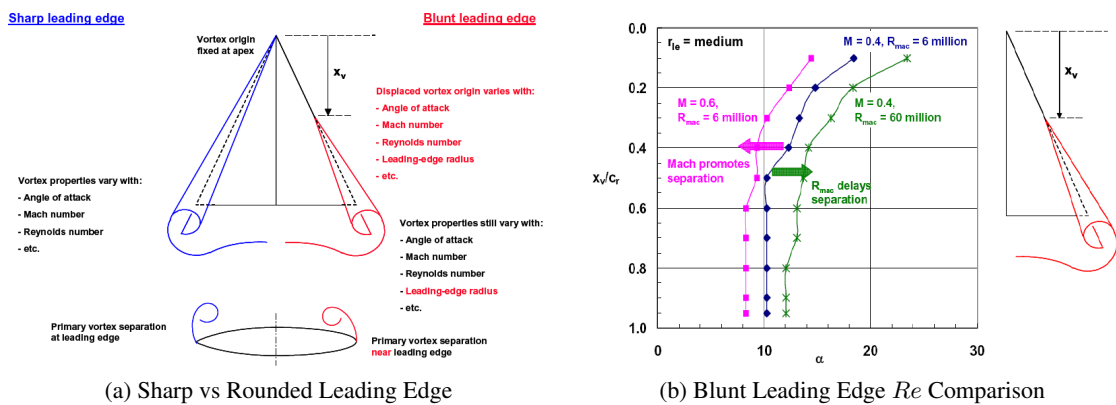


Figure 2.14: Rounded Leading Edge Slender Wings [30]

Here  $K_p$  is normal force curve slope and  $K_v$  is a similar term relating to the attached flow wing leading edge suction that determines the vortex lift increment. Both are a function of the planform and can be determined using simple attached flow methods, e.g. vortex lattice. An example of the applicability of this expression is shown in Figure 2.13[29], which shows good agreement with experimental results for an  $AR = 1.5$  slender wing. The method does not always give accurate results, particularly if some ‘higher order’ effects are present such as longitudinal curvature or vortex breakdown.

More recent requirements place a greater emphasis on range and endurance for military aircraft leading to concepts designed for high subsonic cruise. These wings can be described as semi slender because aerodynamically they exhibit characteristics of slender and higher aspect ratio wings. In order to achieve efficient cruise, blunt leading edge aerofoils are used and therefore an extent of attached flow is maintained.

A comparison of the separated flowfields of sharp and blunt leading edged wings is shown in Figure 2.14 [30]. On the blunt leading edged wing the vortex origin is displaced downstream by a distance  $x_v$ , which varies with angle of attack, Mach and Reynolds numbers, and the leading edge radius. At low incidences the wing would exhibit attached flow behaviour because the flow would be mostly attached. At higher incidences the wing would exhibit similar behaviour to the sharp leading edged wing as the separation origin approaches the apex. There are two reasons for this progression. The primary reason is that with slender wings, the upwash (induced angle of attack) increases in the chordwise direction towards the trailing edge. This means that at any positive incidence angle, the tip experiences a higher local incidence than the root and hence is more likely to be separated. Secondly, the leading edge radius and hence local Reynolds number are usually lower at the tip further promoting early separation.

Another important characteristic of blunt leading edge separations is that the strength of the resulting vortex tends to be weaker than that of an equivalent sharp leading edged wing. Examples of this is shown in Reference [31]. This is thought to be because the smooth surface separation has different flow physics than that of a sharp leading edge separation and the surface curvature in the vicinity of the vortex origin effects the flow.

Further factors affecting the separation characteristics are the Mach and Reynolds numbers (see [32]) as well as factors such as attachment line transition (see ref [33]) which affect both the separation position and nature of the resulting vortex.

In order to obtain a design for such a wing, all of these aspects should be properly accounted for in the analysis used for the design method. As we are still far from fully understanding the flow on these wings, this cannot be achieved and hence reduced order and empirically based models are used in this work to obtain improved designs.

## 2.7 Design Methods and Optimisation

### 2.7.1 Design Process

The design process for a typical aircraft would consist of three distinct phases, conceptual design where the basic configuration of the aircraft would be decided upon, preliminary design where a more detailed description of the aircraft would be developed including the surface definition and finally detailed design where each component is designed and tested. For a particular concept, as the project progresses through these phases, the amount of investment in the project and hence risk are increased. It is important therefore to try and make the best decisions as early as possible.

### 2.7.2 Conceptual Design

Typically at the conceptual design phase, aerodynamics may be accounted for using simple methods, either simple physical relationships or data sheet methods. When designs move away from traditional aircraft configurations or the most important factors cannot be easily estimated with these methods, designers look towards higher fidelity methods to obtain data. Recent advances in aerodynamic prediction capabilities and available computing resources means that this has become a practical possibility.

For UCAV conceptual design, a number of concepts would be evaluated with respect to the lifetime costs associated with meeting various mission requirements. Such requirements may be payload, sensors, range, take-off distance, climb rate, observability targets, etc. This would usually include sizing the aircraft, i.e. scaling various components in order to obtain the required wing area and internal volume. Examples of conceptual design studies were presented by Woolvin from DSTL who compared and sized various UCAV configurations [34] and sized the 1303 UCAV [35].

Woolvin's investigations make use of 'rubber' components which can be scaled in order to produce the required size, volume or power output, etc. The components were also packaged so that they do not overlap. Aerodynamics is handled through simple curve fit relationships with maximum usable incidence explicitly specified. The aircraft is then sized and configured by an optimisation routine looking for a configuration with the minimum basic empty mass (BEM). Woolvin concluded that the aircraft size and hence cost is extremely sensitive to the maximum usable incidence. For the 1303 investigation, maximum usable incidence was based upon data from the QinetiQ low speed wind tunnel test [36]. This is for a planar wing design, not designed for high lift performance, and hence this limitation pushed up size of the design. This highlights the need to bring more detailed design (aspects from the preliminary design phase), into the concept design phase.

### 2.7.3 Detailed Wing Design

Aerodynamic prediction capabilities have become increasingly fast and accurate in recent years due to improved algorithms and availability of computing resources. Despite this, with the large number of design variables required for a full aircraft configurations, the computational burden is still extremely high. Various design methods have been used including genetic algorithms, response surface methods and gradient based methods. Here some examples found in the literature will be briefly discussed.

### 2.7.3.1 Genetic Algorithms

Genetic algorithms are a class of evolution theory inspired optimisation methods. The algorithm begins with a population of randomly generated designs and calculates the objective or fitness function for each one. Favourable designs are kept and the poor designs are discarded. At the next design iteration, new designs are formed by breeding the surviving designs. Mutations are also introduced which allows for random design changes to occur. The method is regarded as a global optimisation method because after many iterations, much of the design space should have been explored. Constraints are typically introduced through penalty functions. Although this method makes a thorough search of the design space, it is also extremely expensive with many calls to the objective function required. This limits its use to relatively low numbers of design variables and cheap to evaluate objectives even if large computing resources are available. An example of UCAV design using a genetic algorithm is given in Reference [37], where a UCAV is designed for cruise drag and a low RCS as calculated by the flo22 potential flow solver and POFACETS, an electro optics prediction tool. The design variables were the sweep angles and taper ratios of each spanwise section and there were 4 aerofoils defined using Bezier curve control points. Due to the multi-objective nature of the problem, a Pareto set was produced reflecting different combinations of aerodynamic vs RCS performance. The study clearly shows the power of this technique for aerodynamic design although if the fidelity of the objective functions was increased, the computing requirement would quickly become difficult to handle. Other examples of genetic algorithms for aerodynamic design are found in References [38–40].

### 2.7.3.2 Response surface methods

Response surface methods offer another global technique for locating optimum designs within a multi-dimensional design space. With these techniques the design space is sampled using a design of experiments technique. A popular choice is Latin-hypercube sampling which ensures samples lie on unique axis aligned planes. The objective function is then modelled using a ‘surrogate model’ or response surface. There are many options available including linear, polynomial, radial basis function methods and Kriging, offering various levels of simplicity and fidelity. Once a surrogate model has been produced, the optimum can be found either directly or using another optimisation routine depending on the choice of surrogate model. For higher order surrogate models where the optimum cannot be directly calculated, a popular choice is to use a genetic algorithm. This method is useful, especially if the objective function is noisy and a more robust optimum is required. Extensions to the above method include successive refinement techniques where after the initial optimum has been found, more samples are placed in the vicinity of the predicted optimum location to gain a more accurate estimate. There are many examples of response surface methods being used for aerodynamic design including reference [41] at Sheffield for transonic aerofoil design or [42] for full wing design.

### 2.7.3.3 Gradient based methods

The final class of optimisation methods discussed here are gradient based methods. These methods use gradient information to successively reduce the objective function at each design iteration. They are considered to be local optimisation methods because they may not find the global optimum in the design space if it is not directly downhill from the starting point. Despite this they are the most

efficient methods for problems with large numbers of variables, especially if efficient methods are used for gradient computations. A discussion of the methods for aerodynamic gradient evaluation including adjoint methods is given in Chapter 3. Currently the most efficient method and the one used in this work is the adjoint method. The adjoint method for aerodynamic optimisation was demonstrated in the 1980's by Jameson [43], and for the first time allowed large scale aerodynamic optimisation problems to be tackled on available computing hardware. Early examples of its use for full aircraft configurations include optimisation of a Reno racing aircraft wing [44], optimisation of a business jet [45] and of a supersonic transport aircraft [46].

At Cranfield/Sheffield universities, a discrete adjoint solver was developed [47] for both Euler and Navier-Stokes solutions which has been extensively used in the current work. The solver has been used to optimise an aerofoil, the ONERA M6 Wing [48] and a BWB transport aircraft [49]. Shock control bumps have also been optimised on the M6 wing and BWB transport aircraft [50] with this method.

Currently almost all major aerospace companies have adjoint solvers including notably the Tau code [51] from DLR, which is extensively used at Airbus and provides a viscous adjoint capability on 3D unstructured meshes [52] as well as the Edge code from FOI.

The adjoint approach has also been applied to the design of high-lift single and multi element aerofoils in viscous flow by Kirn *et al.* [53] and Nemec *et al.* [24]. Nemec generated a multi-objective Pareto front using both the adjoint approach and a genetic algorithm (GA). Both methods generated similar sets of solutions although the adjoint approach drove to a lower minimum and was more efficient.

## 2.8 1303 UCAV

The 1303 UCAV shown in Figure 2.15 is an evolution of the 1301 concept which was developed by AFRL and Boeing through a downselection of many potential configurations. This process is discussed in detail in Reference [54]. The 1301 was initially selected because of the long subsonic range / mission radius, available options for controls and longitudinal balance considerations. It subsequently evolved into the 1303 concept to align it with modified requirements. The changes included reduction of the leading edge sweep to  $47^\circ$ , increasing the trailing edge sweep to  $\pm 30^\circ$ , removing the trailing edge discontinuities for continuous mouldline technology, addition of an asymmetric fuselage and modification to the lower fuselage.

As well as the original planar wing, an alternative design was produced using the AFRL/Boeing 3DOpt tool primarily to improve cruise and dash performance. Both models were tested in the Boeing Polysonic Wind Tunnel (PSWT) at Mach numbers from 0.45 to 1.4. Common results are only presented for Mach 0.8 and 1.2 with both wings, showing that the optimised wing only has a reduced drag at lift coefficients above 0.3 and the pitch break is slightly delayed by around  $\Delta C_L = 0.8$ . No indication is given however of the effect on pitchup at low speed.

The planar wing variation of the 1303 has also been extensively studied in the UK with low speed wind tunnel tests in the QinetiQ 5m wind tunnel [36] at Mach 0.25 and the ARA Transonic Wind tunnel [55] at Mach numbers from 0.35 to 1.2. These have been extensively used for CFD validations as well as preliminary design work.

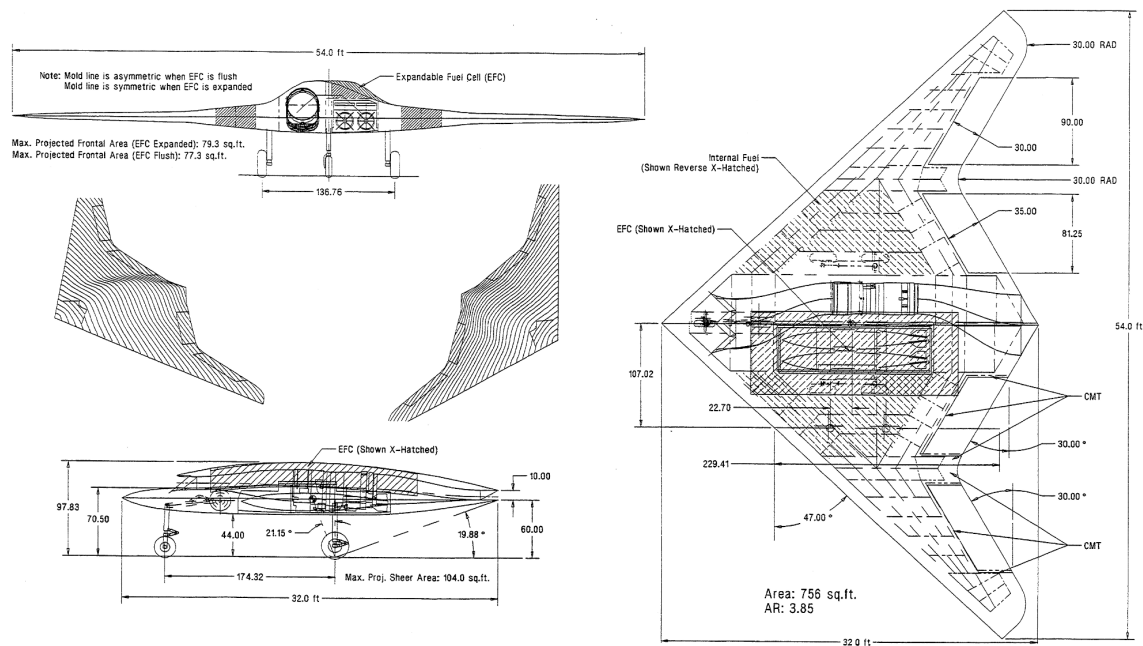


Figure 2.15: 1303 UCAV plan [54]

A conceptual design study by Woolvin [34] on the 1303 geometry used the Conceptual Design and Optimisation (CDO) program, an in house code at DSTL, to investigate the sensitivity of vehicle weight to various criteria including the aerodynamic performance of the wing. It was concluded that as well as the mission range fuel requirement, the maximum usable incidence limitation would drive the design and restricting this would result in a significantly larger and costlier vehicle. This conclusion has led to the need to be able to both predict this incidence limitation accurately for candidate designs as well as design improved wings to increase it.

The 1303 UCAV has also been the subject of a number of CFD investigations [56–66] using Reynolds averaged Navier-Stokes (RANS) solutions and comparing with the low speed QinetiQ 5m wind tunnel results. There is a fairly significant spread of results between different RANS codes, due to mesh types, turbulence models and geometry idealisation.

Investigations were made by Petterson [57, 58] at DSTL using the Cobalt RANS solver on a range of meshes, with and without the sting and using various turbulence models. Petterson states that at higher incidence angles it was clear that the wake from the sting mount was interfering with the aircraft wake which affected the flowfield causing a slightly later pitch break. Different turbulence models gave a relatively modest scatter of results with the most significant differences being at high incidence angles when large regions of separated flow are present.

A paper summarising the results from the TTCP consortium 1303 case [56] compared results of several RANS calculations based on the QinetiQ test case, including the above DSTL results. They found that most parties captured the trend of the results correctly although important features like the onset of pitch divergence and the zero lift drag varied amongst the codes. One interesting point to note is that a larger mesh size did not necessarily improve the quality of results. The best match in terms of drag coefficient was achieved by AFRL using the AVUS code and  $k - \omega$  turbulence model on a 5.7 million cell unstructured mesh with a prismatic boundary layer region.

Some codes, notably Fluent (DSTO) and Cobalt (DSTL) gave a fairly large over prediction for the drag at low incidence. The pitch divergence incidence also varied between the codes within the range  $6^\circ \leq \alpha \leq 8^\circ$ . Additionally the incidence for the high lift pitching moment recovery was predicted very differently, with DSTL's Cobalt result being closest to the experiment.

Arthur *et al.* [61–63, 67] studied the 1303 case with a transition prediction method. At low incidences there appears to be large regions of laminar flow (as much as 75% $c$ ) which may account for the over prediction of drag in the results using a fully turbulent assumption. In [67], at low incidence, the drag goes from an over prediction (fully turbulent  $k - \omega$ ) to being well predicted with the  $k - \omega +$  transition model. Results from another publication [62] show a varying degree of success predicting drag with  $k - \omega +$  transition performing much better than  $k - g +$  transition model. Unfortunately the transition model does not seem to improve the prediction of the low incidence pitching moment with all the models giving effectively the same result. At  $\alpha = 11.7^\circ$  (post pitchup) the SST or SARC (fully turbulent) models give the best predictions for the pitching moment. There are too few data points to properly determine which model best predicts the onset of pitchup most accurately. At moderate incidence angles ( $\alpha = 5.89^\circ$ , ARA Mach 0.35 conditions), the numerical prediction of transition location is very close to the leading edge. The author notes that at this incidence, the predicted  $C_p$  distributions are better with the transition models than the fully turbulent results. The transition models used in the study do not predict attachment line transition and therefore the flow is assumed to be laminar at the attachment line. At higher incidences (close to pitchup) this may be an over simplification if transition has occurred in the attachment line. An obvious extension is to study the case with a method capable of predicting attachment line transition.

Sherer *et al.* [64] have performed DES calculations for the 1303 with the sharp leading edge geometry. Flowfield comparisons between water tunnel PIV results and the DES results are given. These are not directly comparable with the above as the leading edge geometry is different. The results however show very good agreement between the calculation and experimental flowfields although no comparison of integrated forces is presented.

QinetiQ have applied their CODAS design method [68] to the 1303 UCAV. The CODAS tool uses a gradient based optimiser and the SAUNA flow solver in Euler mode to calculate objectives and constraints. Gradients of these functions are calculated using finite differences. The author cites significant difficulties obtaining accurate gradients as the mesh was coarse and the meshes were regenerated for each calculation introducing significant noise. The finite difference method for computing gradients is also extremely expensive as the number of variables is increased. Despite these difficulties, a design was produced, raising the pitchup  $C_L$  to 0.45-0.5 with a modest drag penalty.

A camber and twist design has also been done by Nangia and Palmer [69]. A lifting surface panel code was used with limitations placed on the local leading edge thrust. Candidate designs were formed using the method of Lagrange multipliers by finding the mildest camber/twist surface which satisfies both a leading edge thrust constraint and optionally a pitching moment constraint. These designs do not necessarily constitute good high speed designs as it is a fairly crude assumption that a design that is as close as possible to the planar wing will perform well transonically. This work has inspired aspects of the design method used in this work.

Investigations have also been made into deployable Rao vortex flaps on the 1303 configuration to improve the high lift behaviour of this wing by Atkinson [70] and Chung[71]. Their calculations showed that the flap reduced the drag at high incidence  $> 8.5^\circ$ [70] and  $> 11^\circ$ [71] and smoothed out the pitching moment curve but did not have a large effect on when pitchup occurred.



## Chapter 3

# Computational Methodology

---

This chapter introduces the various computational methods developed and used in this work. This includes details about the optimiser that was used, the Reynolds Averaged Navier-Stokes solver MERLIN, the adjoint solver adjoint-MERLIN, geometry parametrisation, the quasi-vortex-lattice method and empirical high lift constraint. It includes some relevant background theory and derivation of the methods. Some of the codes used are commercial software, but most have been developed within the department or by the author for this work.

### 3.1 Optimisation Design Process

An optimisation algorithm is concerned with finding minima of the objective function  $F$  through suitable modifications to the design variables  $\beta$ . An aerodynamic cost function for real world aerodynamic problems involves non-linearities. These arise due to compressibility or viscous effects and prevent direct solutions from being obtained.

Aerodynamic objective functions are generally expensive to compute. Furthermore, large numbers of design variables are required in order to get a sufficiently large design space. For global methods such as response surface methods or genetic algorithms, this makes the number of computations required considerable and the computational requirement can become too high. This is the reason why gradient based methods are employed, especially if efficient methods can be used to calculate the objective function gradients.

For many aerodynamic design problems, we also wish to use constraint functions denoted by  $C$ . These tend to be either inequality or equality constraints. The optimisation problem can be summarised

$$\text{Minimise: } F(\beta) \quad \text{Subject to: } l \leq \begin{pmatrix} \beta \\ C(\beta) \end{pmatrix} \leq u \quad (3.1)$$

where  $\beta$  is the vector of design variables,  $F(\beta)$  is the objective function and  $C(\beta)$  is a vector of constraints.  $u$  and  $l$  are vectors containing the upper and lower variable bounds and constant function bounds. For equality constraints,  $u$  and  $l$  are set to the same value.

As the objective and constraint functions are expensive to compute, it is desirable to find the most efficient algorithm possible to solve the problem. Mathematicians have put significant effort in

developing many types of gradient based optimisers over the years. Amongst the most efficient and robust are those based upon sequential quadratic programming which makes them a popular choice for engineering problems.

### 3.1.1 Sequential Quadratic Programming

Sequential quadratic programming (SQP) optimisers are a class of gradient based algorithms designed to minimise smooth non-linear objective functions subject to an arbitrary number of (possibly nonlinear) constraints. They are a popular choice for engineering applications because they are generally efficient, stable and can handle many industrially relevant problems. For the UCAV optimisation problem, a commercial SQP optimiser from the National Algorithms Group (NAG) Fortran library, E04UCF [72] is used, which is a well developed routine with many advanced features and customisation options. The user has to supply Fortran compatible subroutines which calculate the objective and constant functions as well as their gradients and a configuration file to specify various options.

The optimisation problem (3.1) is solved iteratively by approximating the real problem with a simpler sub problem at each major iteration. The idea is that the solution of the sub problem brings the current design closer to the real optimum. At each iteration, the SQP algorithm calculates the variables at the next iteration  $\beta^{k+1}$  in the following manner. Firstly the Lagrangian is defined

$$\mathcal{L}(\beta, \lambda) = F(\beta) - \lambda^T C(\beta) \quad (3.2)$$

where  $\lambda$  is an as yet undefined Lagrange multiplier. The optimiser calculates the step  $d$  from the solution of a quadratic sub-problem subject to linearised constraints

$$\begin{aligned} \text{Minimise: } & \nabla \mathcal{L}(\beta^k, \lambda^k)^T d(\beta) + \frac{1}{2} d(\beta)^T \nabla_{\beta\beta}^2 \mathcal{L}(\beta^k, \lambda^k)^T d(\beta) \\ & \beta \in \mathbb{R}^n \\ \text{Subject to: } & l \leq C(\beta^k) + \nabla C(\beta^k)^T d(\beta) \leq u \end{aligned} \quad (3.3)$$

This problem contains the Hessian of the Lagrangian ( $\nabla_{\beta\beta}^2 \mathcal{L}$ ), which is unknown and cannot be directly calculated. Equation (3.3) is solved using a quasi-Newton method where the Lagrangian is successively approximated using the BFGS algorithm. The solution yields the search direction  $d$  as well as giving the search direction for the Lagrange multiplier  $\xi$ . A line search consisting of minor iterations is then performed to calculate the step size  $\alpha$ . A new set of design variables and the Lagrange multiplier is then be calculated with the following Newton iteration

$$\begin{pmatrix} \beta^{k+1} \\ \lambda^{k+1} \end{pmatrix} = \begin{pmatrix} \beta^k \\ \lambda^k \end{pmatrix} + \alpha \begin{pmatrix} d \\ \xi \end{pmatrix} \quad (3.4)$$

This presentation of the algorithm procedure has glossed over many of the finer points and subtleties included in the NAG routine E04UCF. Slack variables are used which allow the constraints to be applied without discontinuities. Various checks and tolerances are applied to ensure that the optimiser is always reducing the objective and governing the convergence of the inner and outer problems. This will have a large effect upon the number of calls made to the objective and constraint functions and hence will determine how efficient or stable the algorithm will be.

Unfeasible designs are permitted throughout the optimisation. This generally accelerates optimiser convergence but if the optimisation is terminated too early, the current design may not be usable due to violations to the constraints. This feature is particularly useful for designs constrained by the high lift performance which will initially be far from being feasible.

There is also an option within the E04UCF routine which triggers it to automatically calculate objective or constraint gradients through finite differences. This is only really suitable for functions that are cheap to evaluate as for each element in the gradient vector, several calls are made to the function as the routine tries to determine the optimum step size. This feature is not used as more efficient methods have been employed.

### 3.1.2 Aerodynamic Objective and Constraint Functions

Ultimately the aim of the optimisation is to reduce the vehicle cost for a given mission profile. This objective function would obviously be extremely difficult if not impossible to formulate, therefore a simpler objective is to be based upon the conclusions from the previous conceptual design work. Woolvin[34] suggested that the most important aerodynamic parameters for the 1303 UCAV were related to the cruise fuel requirement and the high lift capability of the wing. The strategy used for designing the wing will therefore be to minimise the drag at cruise, constrained by the high lift performance which addresses the above issues.

Initially considering only the cruise condition, we wish to minimise the drag  $C_D$ . The wing however must also generate enough aerodynamic lift to balance the weight. Therefore  $C_L \geq C_{L,cruise} = W/(1/2\rho u^2 S)$ . The aircraft should also be designed to be in trim about the centre of gravity ( $C_{M,c.g} = 0$ ) so no control deflections are required and hence there will be no trim drag penalty. The design is also subject to some design variable constraints to prevent extreme designs. The constraints are summarised similar to the above notation

$$\text{Minimise: } C_D(\beta) \quad \text{Subject to: } \begin{pmatrix} l \\ C_{L,cruise} \\ 0 \end{pmatrix} \leq \begin{pmatrix} \beta \\ C_L(\beta) \\ C_M(\beta) \end{pmatrix} \leq \begin{pmatrix} u \\ \infty \\ 0 \end{pmatrix} \quad (3.5)$$

The objective, and constraints at cruise are calculated using the MERLIN solver in Euler mode. The solver is described in detail in a subsequent section. Also required by the optimiser as discussed are the gradients of these functions with respect to the design variables. These are calculated using adjoint-MERLIN, a method which can efficiently calculate aerodynamic function gradients for arbitrary numbers of design variables. This is discussed in more detail in a subsequent section.

At take-off and landing, the aircraft needs to remain stable and controllable at relatively low speeds. This requires a high lift coefficient and for the aerodynamic moments (pitch, yaw and roll) to remain within controllable bounds. On the 1303 UCAV, the static margin is fairly low to minimise trim penalties but flow separation causes strong pitching moments. For this reason the design strategy is to avoid flow separation up to the design lift coefficient and hence keep the forces within the linear region. In order to avoid flow separation, a constraint is applied to the leading edge thrust factor  $K_t$ , an indication of how much leading edge thrust would be attained in a viscous flow regime. The leading edge thrust factor and details of its calculation are presented in a later section. For now, it is enough to know that  $K_t$  will be  $\geq 1$  for attached flows and  $< 1$  for separated

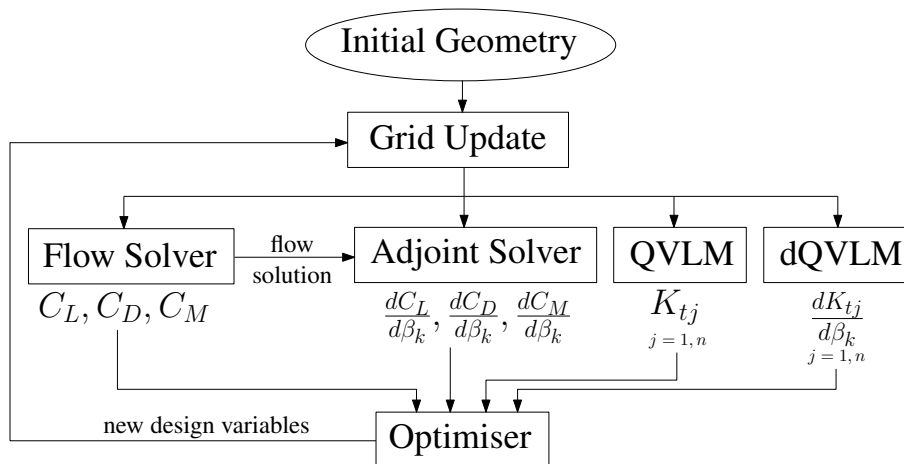


Figure 3.1: Optimisation process

flows. The constraint is

$$1 \leq K_{t,n} \leq \infty \quad (3.6)$$

which is applied at various spanwise stations labelled  $n$  along the wing.

### 3.1.3 Optimiser Set Up

Figure 3.1 shows how each of the programs used to calculate the objectives, constraints or their gradients interact with the optimiser in the design cycle. The original design is supplied in the form of an initial CFD grid containing the aircraft geometry as well as starting values for the design variables. The initial grid is simply that for a planar wing.

A program is then called which updates the grid according to the current design variables. The optimiser then calls the aerodynamic objective or constraint functions as required before updating the design variables at the next (major or minor) iteration.

The flow and adjoint solvers are always restarted with the solutions from the previous iteration. As the optimiser progresses, the time taken for solver convergence is dramatically reduced because successive solutions become more similar. Before the solution is copied to the restart folder, the convergence level is checked to make sure that it is going to be beneficial. The adjoint solver also requires the current flow solution before it can calculate the gradients. When the gradients are requested by the optimiser, the flow solver is first called to ensure that the solution is current and converged. If the solution is converged for the current grid, no iterations will be required. This is denoted by a sideways arrow in figure 3.1.

## 3.2 Flow Solver

This section describes the governing equations for the category of flows which we are concerned with and a description of how they are solved in the numerical flow solver MERLIN, an in house CFD code developed at both Cranfield and Sheffield universities. The solver has been validated against many test cases [73] and been used for various aerodynamic investigations [6, 41, 74]. The section includes a description of the fundamental equations, non-dimensionalisation of the variables, discretisation of the equations in space and time and the solution procedure.

### 3.2.1 Introduction

The Navier-Stokes equations were derived assuming the fluid can be considered a continuum, i.e. the effects of individual molecule movement is not important and that the stresses within the fluid arise from a combination of pressure and viscous forces caused by velocity gradients. For the purposes of this work, the fluid (air) is also assumed to be Newtonian, i.e. the shear stress is proportional to the velocity gradient.

### 3.2.2 Governing Equations

The compressible Navier-Stokes equations were derived by applying conservation laws of mass, momentum (Newton's second law) and energy (first law of thermodynamics) to an infinitely small fluid element  $\Omega$ . Written in the integral form, Equation (3.7) below states that the change of a conserved variable  $Q$  within the fluid element per unit time plus the net flux  $F$  across the elements boundary should equal the source term  $S$ , usually zero.

$$\frac{\partial}{\partial t} \int_{\Omega} \mathbf{Q} dV + \oint_{\partial\Omega} \mathbf{F} \cdot \mathbf{n} dS = \int_{\Omega} \mathbf{S} dV \quad (3.7)$$

A vector of 5 conserved variables is required to define the Navier-Stokes equations for a three dimensional compressible flow which can be written as

$$\mathbf{Q} = (\rho \quad \rho u \quad \rho v \quad \rho w \quad \rho E)^t \quad (3.8)$$

in which  $\rho$  is the density,  $u, v, w$  are velocity components and  $E$ , the total energy which is given by

$$E = e + \frac{1}{2}(u^2 + v^2 + w^2) \quad (3.9)$$

where the specific internal energy  $e$  is

$$e = \frac{1}{\gamma - 1} \frac{p}{\rho} \quad (3.10)$$

$p$  is the static pressure and  $\gamma$  is the ratio of specific heats ( $\gamma = 1.4$  for air).  $p$  is calculated using Boyle's law where  $R$  the gas constant is  $287 \text{ J/kgK}$  and  $T$  is the static temperature.

$$p = \rho RT \quad (3.11)$$

For convenience the flux vector,  $\mathbf{F}$  is split into inviscid and viscous components denoted by subscripts  $i$  and  $v$  and grouped into  $\mathbf{F}$ ,  $\mathbf{G}$  and  $\mathbf{H}$  components according to the cartesian direction in which

they act.

$$\mathbf{F} = \begin{bmatrix} \mathbf{F}^i - \mathbf{F}^v \\ \mathbf{G}^i - \mathbf{G}^v \\ \mathbf{H}^i - \mathbf{H}^v \end{bmatrix}$$

$$\mathbf{F}^i = \begin{bmatrix} \rho u \\ \rho u^2 + p \\ \rho uv \\ \rho uw \\ u(\rho E + p) \end{bmatrix}, \quad \mathbf{F}^v = \begin{bmatrix} 0 \\ \tau_{xx} \\ \tau_{xy} \\ \tau_{xz} \\ u\tau_{xx} + v\tau_{xy} + w\tau_{xz} - q_x \end{bmatrix}$$

$$\mathbf{G}^i = \begin{bmatrix} \rho v \\ \rho vu \\ \rho v^2 + p \\ \rho vw \\ v(\rho E + p) \end{bmatrix}, \quad \mathbf{G}^v = \begin{bmatrix} 0 \\ \tau_{yx} \\ \tau_{yy} \\ \tau_{yz} \\ u\tau_{yx} + v\tau_{yy} + w\tau_{yz} - q_y \end{bmatrix} \quad (3.12)$$

$$\mathbf{H}^i = \begin{bmatrix} \rho w \\ \rho wu \\ \rho wv \\ \rho w^2 + p \\ w(\rho E + p) \end{bmatrix}, \quad \mathbf{H}^v = \begin{bmatrix} 0 \\ \tau_{zx} \\ \tau_{zy} \\ \tau_{zz} \\ u\tau_{zx} + v\tau_{zy} + w\tau_{zz} - q_z \end{bmatrix}$$

In the flux vector, several auxiliary relations are required. The stress tensor  $\tau$  is given by

$$\tau_{ij} = 2\mu S_{ij} + \lambda \frac{\partial u_k}{\partial x_k} \delta_{ij} \quad (3.13)$$

$$\delta_{ij} = \begin{cases} 0, & \text{if } i \neq j \\ 1, & \text{if } i = j \end{cases}$$

where  $\delta_{ij}$  is the Kronecker symbol and the strain rate is given by

$$S_{ij} = \frac{1}{2} \left( \frac{\partial u_i}{\partial x_j} + \frac{\partial u_j}{\partial x_i} \right) \quad (3.14)$$

The second coefficient of viscosity  $\lambda$  is

$$\lambda = -\frac{2}{3}\mu \quad (3.15)$$

and with the thermal conductivity coefficient  $\kappa$ , the heat flux vector  $q$  is

$$q_i = \kappa \frac{\partial T}{\partial x_i} \quad (3.16)$$

Finally the molecular viscosity  $\mu$  depends only upon the temperature  $T$  and is given by the Sutherland formula

$$\frac{\mu}{\mu_{\infty}} = \left( \frac{T}{T_{\infty}} \right)^{3/2} \frac{\frac{110.4}{T_{\infty}} + 1}{\frac{110.4}{T_{\infty}} + \frac{T}{T_{\infty}}} \quad (3.17)$$

Variable	Non-dimensionalisation
$\rho$	$\rho^* = \rho/\rho_{\infty}$
$u$	$u^* = u/V_{\infty}$
$v$	$v^* = v/V_{\infty}$
$w$	$w^* = w/V_{\infty}$
$p$	$p^* = \frac{p}{p_{\infty}\gamma M_{\infty}^2}$
$\mu$	$\mu^* = \mu/\mu_{\infty}$
$T$	$T^* = T/T_{\infty}$

where:  $V = \sqrt{u^2 + v^2 + w^2}$   
 $M_{\infty} = V_{\infty}^2/\gamma RT_{\infty}$   
 $p_{\infty} = \rho_{\infty}RT_{\infty}$   
 $p_{\infty}\gamma M_{\infty}^2 = \rho_{\infty}V_{\infty}^2$

Table 3.1: Non-dimensionalisation of variables in MERLIN

### 3.2.3 Primitive Variables & Non-dimensionalisation

The flow solver MERLIN actually stores the primitive variables  $\mathbf{P}$  rather than  $\mathbf{Q}$  the conservative variables outlined above.  $\mathbf{P}$  is defined as

$$\mathbf{P} = (\rho \quad u \quad v \quad w \quad p)^t \quad (3.18)$$

The conservative variables  $\mathbf{Q}$  can readily be interchanged with the primitive variables  $\mathbf{P}$  through the following relation

$$\frac{\partial \mathbf{Q}}{\partial \mathbf{P}} = \begin{bmatrix} 1 & 0 & 0 & 0 & 0 \\ u & \rho & 0 & 0 & 0 \\ v & 0 & \rho & 0 & 0 \\ w & 0 & 0 & \rho & 0 \\ \frac{u^2+v^2+w^2}{2} & \rho u & \rho v & \rho w & \frac{1}{\gamma-1} \end{bmatrix} \quad (3.19)$$

and back via the inverse relation

$$\frac{\partial \mathbf{Q}^{-1}}{\partial \mathbf{P}} = \frac{\partial \mathbf{P}}{\partial \mathbf{Q}} = \begin{bmatrix} 1 & 0 & 0 & 0 & 0 \\ -u/\rho & -1/\rho & 0 & 0 & 0 \\ -u/\rho & 0 & -1/\rho & 0 & 0 \\ -u/\rho & 0 & 0 & -1/\rho & 0 \\ \gamma^{-1/2}(u^2 + v^2 + w^2) & -(\gamma - 1)u & -(\gamma - 1)v & -(\gamma - 1)w & \gamma - 1 \end{bmatrix} \quad (3.20)$$

The variables are also non-dimensionalised by their freestream values. This has advantages in computational accuracy as the variables will all be of a similar magnitude. The non-dimensionalisation is summarised in table 3.1. Note that the superscript \* is dropped in future sections.

### 3.2.4 Turbulence Models

The existence of turbulence in the flows with which we are concerned means that it is difficult to obtain a direct solution to the Navier-Stokes equations due to the large range of length scales present. In order to obtain a direct solution, length scales down to the Kolmogorov scale would need to be resolved by the computer demanding excessive mesh sizes and thus computational expense. This approach is only possible for extremely low Reynolds number flows and is known as DNS. To resolve this problem, the equations are 'Favre Averaged' by splitting the velocities into average ( $\bar{U}_i$ ) and fluctuating ( $u'_i$ ) components. Once re-arranged this gives rise to extra terms known as 'Reynolds stresses' ( $\rho u'_i u'_j$ ) as the units are consistent with stress terms. Auxiliary equations known as turbulence models are then used to model these terms and through the Boussinesq assumption the effects are added to the molecular viscosity as an additional turbulent viscosity such that  $\mu = \mu + \mu_t$ . Equation (3.13) then becomes

$$\tau_{ij} = 2\mu S_{ij} + \lambda \frac{\partial u_k}{\partial x_k} \delta_{ij} - \frac{2}{3} \rho k \delta_{ij} \quad (3.21)$$

#### 3.2.4.1 $k - \omega$ Model

Willcox'  $k - \omega$  model [75] adds two additional equations to (3.7) which solve for the turbulent kinetic energy  $k$  and the specific dissipation  $\omega$ . The main advantage of using additional equations is that history in the flow is taken account of and thus the applicability is extended to flows under adverse pressure gradients and regions of flow separation.

The additional conserved variables are

$$\mathbf{Q} = (\rho k, \rho \omega)^t \quad (3.22)$$

and the viscous and inviscid fluxes are

$$\mathbf{F}_i = \begin{bmatrix} \rho u_j k \\ \rho u_j \omega \end{bmatrix}, \quad \mathbf{F}_v = \begin{bmatrix} (\mu + \mu_t \sigma_k) \frac{dk}{dx_j} \\ (\mu + \mu_t \sigma_\omega) \frac{d\omega}{dx_j} \end{bmatrix} \quad (3.23)$$



The  $k - \omega$  model requires some non-zero source terms

$$\mathbf{S} = (S_k \quad S_\omega)^t$$

$$\begin{bmatrix} S_k \\ S_\omega \end{bmatrix} = \begin{bmatrix} \tau_{ij} \frac{du_i}{dx_j} - \beta^* \rho \omega k \\ \frac{\gamma \omega}{k} \tau_{ij} \frac{du_i}{dx_j} - \beta \rho \omega^2 \end{bmatrix} \quad (3.24)$$

and the closure coefficients are

$$\sigma_k = 0.5, \quad \sigma_\omega = 0.5, \quad \beta^* = 0.09, \quad \beta = 3/40, \quad \gamma = 5/9$$

Finally the turbulent viscosity is calculated as

$$\mu_t = \frac{\rho k}{\omega} \quad (3.25)$$

### 3.2.5 Spatial Discretisation

There are many numerical formulations for solving the Navier-Stokes equations. The finite-volume method is currently the most popular for CFD codes and is used in this work as it has several advantages over other approaches. These include:

- Ease of application, especially to complex geometries and on unstructured meshes
- Arbitrary polyhedral cells can be employed (geometric flexibility)
- Mass, momentum and energy are conserved in each cell as well as in the whole domain
- Boundary conditions are simple to implement
- Stable solutions can be obtained
- Low memory overhead for large problems
- Efficient solutions are possible

The main disadvantages of this method are that schemes can be quite diffusive, especially if low order numerics are used and if the computational mesh is coarse or stretched.

#### 3.2.5.1 The Finite-Volume Method

The basis of the finite-volume method is that the integral equation (3.7) is applied to a large number of finite control volumes, defined by a computational mesh. Flowfield variables are stored at each elements cell centre, representing cell averaged values. Equation (3.7) then can be simplified to

$$V_i \frac{\partial \mathbf{Q}_i}{\partial t} = -\mathbf{R}_i + \mathbf{S}_i V_i \quad (3.26)$$

where  $\mathbf{R}_i$  is the residual vector,  $V_i$  is the cells volume,  $\mathbf{Q}_i$  is the vector of average flow variables and  $\mathbf{S}_i$  is the source term. The residual vector physically is the volume imbalance of the conserved variables in a cell per unit time for example in the continuity equation this is mass per unit time. The residual is calculated by adding up contributions from each face as follows:

$$\mathbf{R}_i = \sum_{faces} \mathbf{F}_i \cdot \mathbf{n} S \quad (3.27)$$

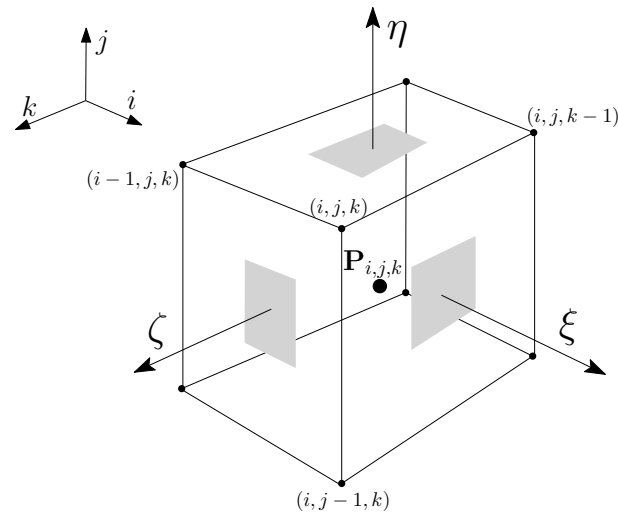


Figure 3.2: A typical cell in MERLIN

Here, the flux vector  $\mathbf{F}_i$  was defined in (3.12),  $\mathbf{n}$  is the face unit normal vector and  $S$  is the face surface area. As the flowfield variables in a finite-volume are stored at each cells centroid the fluxes need to be evaluated at the cell faces. This requires special attention and is described in section 3.2.7. The source terms are straightforward to calculate as they are specified at the cell centres.

The cells in MERLIN are arranged in a structured multiblock manner meaning that the (hexahedral) cells are grouped into structured blocks ordered by  $i$ ,  $j$  and  $k$  co-ordinates respectively. The solver works on each block in turn, or in parallel, treating block interfaces as boundary conditions. The multiblock approach is less flexible on complex geometries compared to unstructured codes, but it has advantages in memory requirements, speed and accuracy. One main advantage is that for an implicit solver, when large matrix inversions are required, due to the ordering of cells, a sparse banded matrix is obtained which can be efficiently solved.

### 3.2.6 Time Integration

For the purposes of aerodynamic shape optimisation we are only concerned with a steady state result of Equation (3.7). In space the viscous Navier-Stokes equations are of a mixed hyperbolic/elliptic type for transonic flows which means it is difficult to obtain a direct solution if the time term is dropped. In order to obtain a steady state result, the equations are marched in time until the unsteady term approaches zero. Introducing some nomenclature, terms on the right hand side of Equation (3.37) are grouped such that

$$\mathbf{RHS} = -\mathbf{R}_i + \mathbf{S}_i V_i$$

then the left hand side term of equation (3.37) can be replaced by a difference approximation to define how the solution variables will evolve over time.

### 3.2.6.1 Explicit Formulation

The simplest approximation for the left hand side of (3.37) is to replace the partial derivative with forward difference approximation and use the **RHS** at the current time such that

$$V_i \frac{Q^{n+1} - Q^n}{\Delta t} = \mathbf{RHS}(Q^n) \quad (3.28)$$

This can be rearranged to give an update of the flow variables  $Q$  at the new time step  $n + 1$ .

$$Q^{n+1} = Q^n + \mathbf{RHS}(Q^n) \frac{\Delta t}{V_i} \quad (3.29)$$

The problem is then reduced to calculating the **RHS** term which can be done explicitly from the current data stored about the flowfield. This formulation is simple and cheap to compute the flow variables at the next iteration but the stability of such a scheme only permits small time steps. This can make solution convergence very slow.

### 3.2.6.2 CFL Condition and Time Step

For an explicit method, it can be shown that the stability depends upon the Courant-Friedrichs-Lewy or CFL condition which for a 1D conservation equation is

$$\text{CFL} = \frac{a\Delta t}{\Delta x} \leq 1 \quad \text{or} \quad \Delta t \leq \frac{\Delta x}{a} \quad (3.30)$$

where  $a$  is the wave speed and  $\Delta x$  is the grid spacing. As shown, the maximum time step is proportional to grid spacing, so for a viscous, high Reynolds number calculation with small cells in the boundary layer, the time step must be extremely small. In MERLIN, this concept is extended for a 3D viscous flow such that the time step becomes

$$\Delta t = \frac{\text{CFL}}{|\mathbf{V}\xi| + |\mathbf{V}\eta| + |\mathbf{V}\zeta| + a(\|\xi\| + \|\eta\| + \|\zeta\|) + \frac{2\gamma\mu}{\rho Re Pr V} (\|\xi\|^2 + \|\eta\|^2 + \|\zeta\|^2)} \quad (3.31)$$

here  $\mathbf{V}$  is the velocity vector,  $a$  is the speed of sound,  $Re$  is the Reynolds number and  $Pr$  is the Prandtl number.  $\xi$ ,  $\eta$  and  $\zeta$  are the cell face normal vectors. For a time accurate solution,  $\Delta t$  for the each cell would have to be the lowest value in the whole domain. We are not however concerned with a time accurate solution and thus for many problems, local time stepping can be employed to accelerate convergence. Note that this may not always be suitable because incorrect steady state solutions can be obtained.

### 3.2.6.3 Implicit Formulation

In order to remove the restriction that the CFL number must be less than unity, an implicit formulation is used where the **RHS** in equation (3.43) at the current time step is changed for the **RHS** at the new time step  $n + 1$ . Equation (3.37) then becomes

$$V_i \frac{Q^{n+1} - Q^n}{\Delta t} = \mathbf{RHS}(Q^{n+1}) \quad (3.32)$$

The value of  $\mathbf{RHS}(\mathbf{Q}^{n+1})$  can not be directly calculated as with the explicit method because we do not have the values of the flow at time level  $n + 1$ . The  $\mathbf{RHS}$  is therefore linearised such that

$$\mathbf{RHS}(\mathbf{Q}^{n+1}) = \mathbf{RHS}(\mathbf{Q}^n) + \frac{\partial \mathbf{RHS}(\mathbf{Q}^n)}{\partial \mathbf{Q}} {}^n \Delta \mathbf{Q} + \dots \text{higher order terms} \quad (3.33)$$

where

$${}^n \Delta \mathbf{Q} = \mathbf{Q}^{n+1} - \mathbf{Q}^n$$

With this linearisation, equation (3.43) becomes

$$\left[ \frac{V_i}{\Delta t} + \frac{\partial \mathbf{RHS}(\mathbf{Q}^n)}{\partial \mathbf{Q}} \right] {}^n \Delta \mathbf{Q} = \mathbf{RHS}(\mathbf{Q}^n) \quad (3.34)$$

In MERLIN, as discussed in section 3.2.3 the primitive variables are used so equation (3.45) combined with (3.19) to convert primitive to conservative variables becomes

$$\left[ \frac{V_i}{\Delta t} \frac{\partial \mathbf{Q}}{\partial \mathbf{P}} + \frac{\partial \mathbf{RHS}(\mathbf{Q}^n)}{\partial \mathbf{P}} \right] {}^n \Delta \mathbf{P} = \mathbf{RHS}(\mathbf{Q}^n) \quad (3.35)$$

The implicit update is then

$$\mathbf{P}^{n+1} = \mathbf{P}^n + \Delta \mathbf{P} \quad (3.36)$$

Equation 3.46 contains the Jacobian matrix  $\frac{\partial \mathbf{RHS}(\mathbf{Q}^n)}{\partial \mathbf{P}}$ , the vector of unknown flowfield variable updates  ${}^n \Delta \mathbf{P}$  and the  $\mathbf{RHS}$  vector as in the explicit method above. This forms a linear system of the form  $\mathbf{Ax} = \mathbf{b}$  which is solved for  ${}^n \Delta \mathbf{P}$  in order to apply 3.47

The Jacobian matrix  $\frac{\partial \mathbf{RHS}(\mathbf{Q}^n)}{\partial \mathbf{P}}$  contains information about how the  $\mathbf{RHS}$  vector changes with changes in the flowfield variables  $\mathbf{P}$ . In general this matrix contains, for each cell in the computational block, how each other cell in the block will affect the resulting flux or source term and therefore the matrix will contain  $(ni \times nj \times nk)^2$  elements. The terms in the matrix will contain contributions from differentiating the flux calculation and source terms w.r.t the flowfield variables. As the flux calculation depends upon the cells surrounding the current cell as defined by the computational stencil, the matrix is sparse and of a banded nature and thus is much less computationally demanding to solve. In fact, because for a converged solution the  $\mathbf{RHS}$  will approach zero, simplifications are permitted in the calculation of the Jacobian matrix thus making it cheaper to evaluate and the resulting system easier to solve. In MERLIN only a 1st order Jacobian is used reducing the problem to a septa-diagonal system where the 7 rows refer to the 6 elements surrounding the current element as well as the current element. The elements are labelled according to the compass points  $n, s, e, w$  front and back  $f, b$  and the centre point  $c$ .

### 3.2.7 Calculation of the Flux Vector

This section describes how the numerical flux is calculated at the cell boundaries. For the invicid components a Riemann solver by Osher and Soloman [76] is used as well a formally 3<sup>rd</sup> order MUSCL scheme for function reconstruction. This combination is particularly useful for this application as they are both differentiable, a useful property for calculation of the flux Jacobian which is used in both flow and adjoint solvers. The viscous components are calculated in a much simpler manner though central differences.

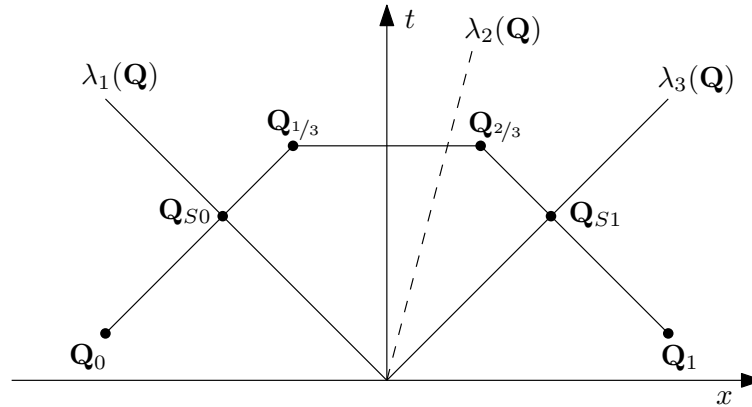


Figure 3.3: Osher and Soloman Integration Path (P Variant)

### 3.2.7.1 Inviscid Components

Calculation of the flux at element boundaries requires some special attention. This stems from characteristic theory which says that for a supersonic flow (hyperbolic system), information can only travel downstream whereas for a subsonic flow, information can travel in both directions. The flux calculation in the CFD code must reflect this, only using information from upstream for supersonic flow regions and both for subsonic regions. If a discontinuity, e.g. a shock, is present the flux calculation may have to consider both subsonic and supersonic states simultaneously. This problem is known as a Riemann problem and a Riemann solver must be used to calculate the resulting flux at the boundary.

### 3.2.7.2 Osher's Approximate Riemann Solver

Osher's Approximate Riemann solver assumes splitting of the flux vector  $\mathbf{F}(\mathbf{Q})$  into terms relating to information propagating in the upwind and downwind directions. The scheme is applied in 1D space between the left and right states,  $\mathbf{F}_L$  and  $\mathbf{F}_R$ . The flux can be written

$$\mathbf{F}(\mathbf{Q}) = \mathbf{F}^+(\mathbf{Q}) + \mathbf{F}^-(\mathbf{Q}) \quad (3.37)$$

the flux at the face  $i + 1/2$  can be written in the following mathematically equivalent form

$$\mathbf{F}_{i+1/2} = \frac{1}{2} \left[ \mathbf{F}(\mathbf{Q}_L) + \mathbf{F}(\mathbf{Q}_R) - \int_{\mathbf{Q}_L}^{\mathbf{Q}_R} \left| \frac{d\mathbf{F}}{d\mathbf{Q}} \right| d\mathbf{Q} \right] \quad (3.38)$$

which depends upon the left and right states as well as the integral of the flux Jacobian in phase space between the two states. This integral depends upon the integration path chosen and hence is approximate. In the P variant (physical variant as opposed to Osher's original variant) of the solver, the flux Jacobian is integrated in physical space along a path perpendicular to the characteristics of the flow as shown in Figure 3.3. To calculate the values  $\mathbf{F}_{1/3}$  and  $\mathbf{F}_{2/3}$ , the Riemann invariants are

set equal yielding 10 equations and 10 unknown values which can easily be solved.

$$\begin{aligned}
\left(u^* + \frac{2a}{\gamma-1}\right)_0 &= \left(u^* + \frac{2a}{\gamma-1}\right)_{1/3} & u_{1/3}^* &= u_{2/3}^* & \left(u^* - \frac{2a}{\gamma-1}\right)_1 &= \left(u^* - \frac{2a}{\gamma-1}\right)_{2/3} \\
\left(\frac{p^*}{\rho^* \gamma}\right)_0 &= \left(\frac{p^*}{\rho^* \gamma}\right)_{1/3} & p_{1/3}^* &= p_{2/3}^* & \left(\frac{p^*}{\rho^* \gamma}\right)_1 &= \left(\frac{p^*}{\rho^* \gamma}\right)_{2/3} \\
v_0^* &= v_{1/3}^* & & & v_0^* &= v_{1/3}^* \\
w_0^* &= w_{1/3}^* & & & w_0^* &= w_{1/3}^*
\end{aligned} \tag{3.39}$$

The variables at the sonic points  $S_0$  and  $S_1$  are calculated using the sonic condition such that  $u^* + \frac{2a}{\gamma-1} = 0$  and  $u^* - \frac{2a}{\gamma-1} = 0$ . With the values known at the intersection points, the flux at  $i + 1/2$  can be calculated according to the relations in table 3.2

	$u_0 - a_0 \geq 0$ $u_1 + a_1 \geq 0$	$u_0 - a_0 \geq 0$ $u_1 + a_1 \leq 0$	$u_0 - a_0 \leq 0$ $u_1 + a_1 \geq 0$	$u_0 - a_0 \leq 0$ $u_1 + a_1 \leq 0$
$u^* \geq 0$ $u^* - a_{1/3} \geq 0$	$\mathbf{F}_0$	$\mathbf{F}_0 + \mathbf{F}_1 + \mathbf{F}_{S1}$	$\mathbf{F}_{S1}$	$\mathbf{F}_{S0} - \mathbf{F}_{S1} + \mathbf{F}_1$
$u^* \geq 0$ $u^* - a_{1/3} \leq 0$	$\mathbf{F}_0 - \mathbf{F}_{S0} + \mathbf{F}_{1/3}$	$\mathbf{F}_0 - \mathbf{F}_{S0} + \mathbf{F}_{1/3} - \mathbf{F}_{S1} + \mathbf{F}_1$	$\mathbf{F}_{1/3}$	$\mathbf{F}_1 + \mathbf{F}_{1/3} - \mathbf{F}_{S1}$
$u^* \leq 0$ $u^* + a_{2/3} \geq 0$	$\mathbf{F}_0 - \mathbf{F}_{S0} + \mathbf{F}_{2/3}$	$\mathbf{F}_0 - \mathbf{F}_{S0} + \mathbf{F}_{2/3} - \mathbf{F}_{S1} + \mathbf{F}_1$	$\mathbf{F}_{2/3}$	$\mathbf{F}_{2/3} + \mathbf{F}_{S1} - \mathbf{F}_1$
$u^* \geq 0$ $u^* - a_{1/3} \geq 0$	$\mathbf{F}_0 - \mathbf{F}_{S0} + \mathbf{F}_{S1}$	$\mathbf{F}_0 - \mathbf{F}_{S0} + \mathbf{F}_1$	$\mathbf{F}_{S1}$	$\mathbf{F}_1$

Table 3.2: Osher and Solomon flux formulae: P variant

Using  $\mathbf{F}_L = \mathbf{F}_i$  and  $\mathbf{F}_R = \mathbf{F}_{i+1}$ , i.e. a 1st order accurate scheme, the velocity normal to the face  $i + 1/2$ ,  $u$  is evaluated and the flux at the intermediate and sonic points can be calculated from equations (3.50). For example if  $u_0 - a_0 \geq 0$ ,  $u_1 + a_1 \geq 0$ ,  $u^* \geq 0$  and  $u^* - a_{1/3} \leq 0$  then the flux at the face would be  $\mathbf{F}_{i+1/2} = \mathbf{F}_0 - \mathbf{F}_{S0} + \mathbf{F}_{2/3}$ .

### 3.2.7.3 MUSCL Scheme

For improved accuracy of the solution, a higher order scheme is used to calculate evaluate  $\mathbf{F}_L$  and  $\mathbf{F}_R$  at the cell interface. A MUSCL (Monotone Upstream-centred Scheme for Convection Laws) scheme used in this work, which is suitable for flows containing discontinuities such as shocks and shear layers. A flux limiter is used that avoids unwanted oscillations caused by the numerical scheme. The variables are calculated according to

$$\begin{aligned}
\mathbf{P}_L &= \mathbf{P}_i + 1/4s_i [(1 - s_i\kappa)(\mathbf{P}_i - \mathbf{P}_{i-1}) + (1 + s_i\kappa)(\mathbf{P}_{i+1} - \mathbf{P}_i)] \\
\mathbf{P}_R &= \mathbf{P}_{i+1} + 1/4s_i [(1 + s_{i+1}\kappa)(\mathbf{P}_{i+1} - \mathbf{P}_{i-1}) + (1 - s_{i+1}\kappa)(\mathbf{P}_{i+2} - \mathbf{P}_{i+1})]
\end{aligned} \tag{3.40}$$

here  $\kappa = 1/3$  makes the scheme formally 3rd order in space and the flux limiter terms  $s_i$  and  $s_{i+1}$  are calculated by

$$s_i = \frac{2(P_{i+1} - P_i)(P_i - P_{i-1}) + \varepsilon}{(P_{i+1} - P_i)^2 + (P_i - P_{i-1})^2 + \varepsilon} \tag{3.41}$$

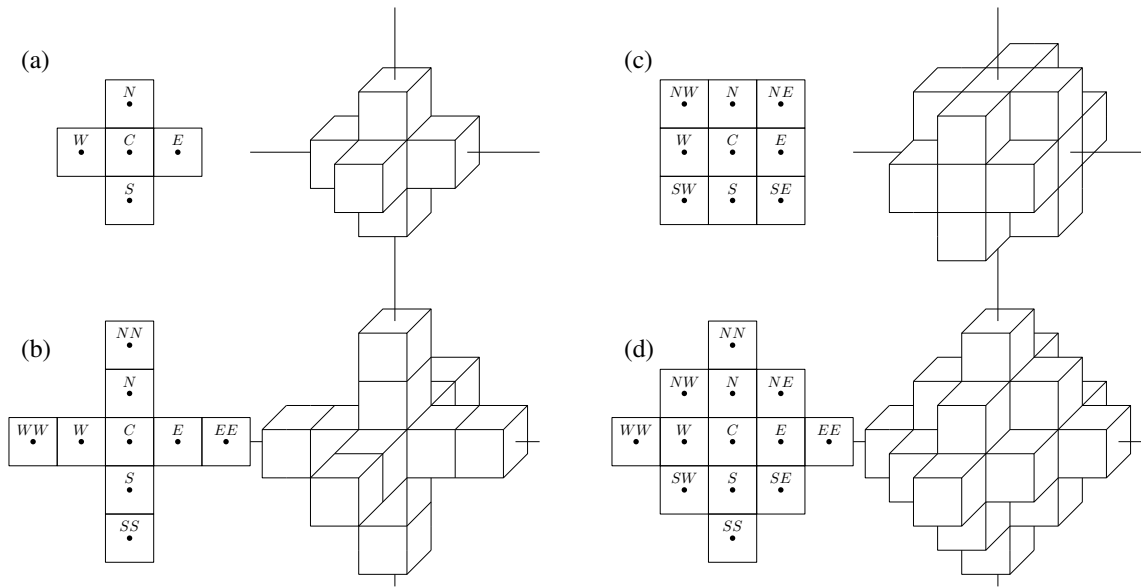


Figure 3.4: Computational stencil for calculation of inviscid and viscous flux

where the term  $\varepsilon$  is a small number which prevents the denominator from becoming zero and hence crashing the code. In regions where the flow is smooth i.e. no discontinuity exists, the term  $s_i \approx 1$  and the limiter has no effect on Equation (3.51). When discontinuities exist,  $s_i$  will be close to zero and Equation (3.51) will approach

$$\begin{aligned}\mathbf{P}_L &= \mathbf{P}_i + 0 \\ \mathbf{P}_R &= \mathbf{P}_{i+1} + 0\end{aligned}\quad (3.42)$$

i.e. the 1st order accurate flux expression described above.

Many other flux schemes are available for evaluating the flux at cell boundaries although this particular combination is preferred because it can be differentiated exactly for the flux Jacobian in the implicit solver and more importantly for the adjoint solver.

#### 3.2.7.4 Viscous Components

For the viscous terms in the flux vector, inter cell fluxes are simply calculated using centred-difference discretisation but the velocity and temperature gradients are also required. For this, Gauss' theorem and a dual volume approach are used. The dual volume approach defines a new cell volume centred around the face centre  $i + 1/2$  as shown in Figure 3.5. From the Gauss theorem

$$\int_{\Omega} \nabla \mathbf{F} \, dV = \oint_{d\Omega} \mathbf{F} \cdot \mathbf{n} \, dS \quad (3.43)$$

which can be written for a hexahedral cell as

$$\nabla \mathbf{F} = \frac{1}{V} \sum_{l=1}^6 \mathbf{F} \cdot \mathbf{n} \, S_l \quad (3.44)$$

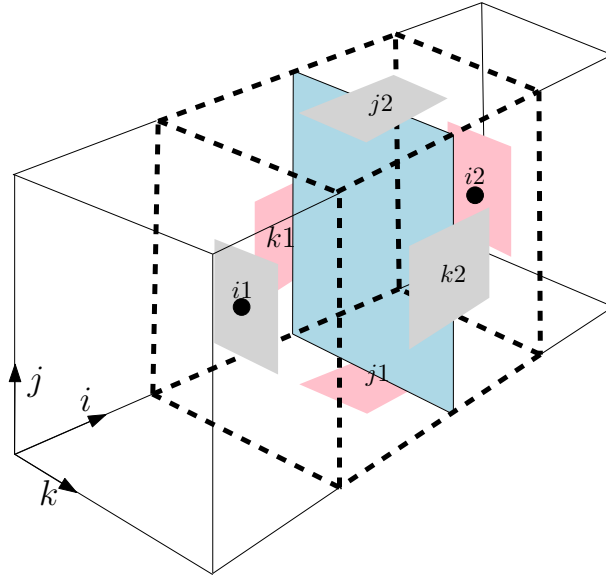


Figure 3.5: Schematic of dual control volume approach

The three components of temperature gradient for example can then be calculated by

$$\nabla T = \frac{1}{V} [T_{i2}\xi_{i2} + T_{j2}\eta_{j2} + T_{k2}\zeta_{k2} - T_{i1}\xi_{i1} - T_{j1}\eta_{j1} - T_{k1}\zeta_{k1}] = \left( \frac{\partial T}{\partial x}, \frac{\partial T}{\partial y}, \frac{\partial T}{\partial z} \right) \quad (3.45)$$

where the dual volume face centred values are an average of the four surrounding cells, for example

$$T_{k2} = 1/4(T_{i,j,k} + T_{i+1,j,k} + T_{i,j,k+1} + T_{i+1,j,k+1}) \quad (3.46)$$

and the metric term is the average of the metric terms for the two adjacent faces

$$\zeta_{k2} = 1/2(\zeta_{i,j,k} + \zeta_{i+1,j,k}) \quad (3.47)$$

### 3.2.7.5 Flux Jacobian

As discussed previously, the implicit solver requires calculation of the flux Jacobian term  $\frac{\partial \mathbf{R}}{\partial \mathbf{P}}$ . This is achieved through differentiation of Table 3.2 and the MUSCL scheme for convective terms and the central scheme for viscous terms. In the flow solver, a simplified 1<sup>st</sup> order Jacobian is used because in the limit of a converged solution, the flow Residual term diminishes to zero and as such this simplification does not affect the final result. Whilst possibly slowing the convergence rate of the numerical scheme, this has advantages in the reduced memory requirements and less bands in the resulting matrix making it more efficient to solve. In the adjoint code, the full high order Jacobian is required. However it is not stored but multiplied element by element with the adjoint vector when required. For full details of the calculation of the flux Jacobian see Reference [47].

### 3.2.8 Boundary Conditions

The boundary conditions in MERLIN are implemented with two layers of halo cells. The values in these halo cells are specified or extrapolated from within the domain as appropriate to enforce



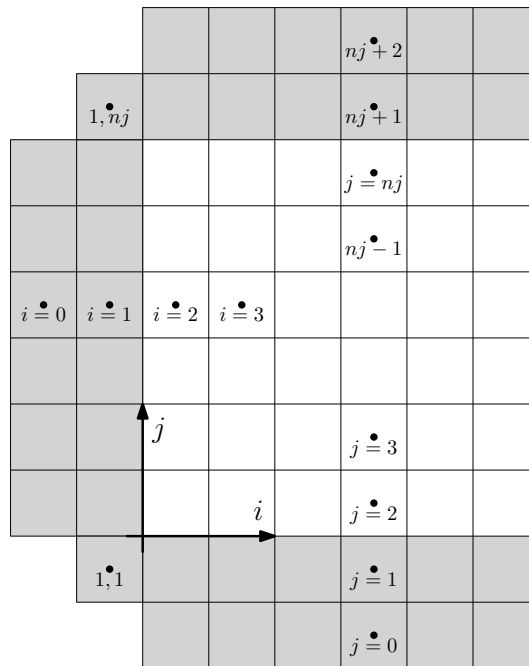


Figure 3.6: Halo cell numbering

the correct boundary condition. This way the MUSCL scheme described previously does see the boundaries and can be used without modification up to the domain or block boundaries. In this work, slip and no slip walls are used as well as symmetry, pole, farfield and internal boundary conditions. The cells are labelled as shown in Figure 3.6. In this description of the boundary conditions the numbering assumes the boundary is at the lower index such that the 1<sup>st</sup> halo cell is numbered 1 and the 2<sup>nd</sup> halo cell is labelled 0. The 1<sup>st</sup> cell inside the domain is labelled 2 and the 2<sup>nd</sup> 3.

### 3.2.8.1 Slip Wall

The slip wall boundary condition is used in Euler calculations to simulate a solid surface. The boundary condition essentially enforces flow tangency at the wall by ensuring zero normal pressure and density gradients, zero normal velocity and zero tangential velocity gradients. The velocity components are resolved such that  $\bar{U}$  is the surface normal velocity and  $\bar{V}$  and  $\bar{W}$  are the parallel velocity components. The primitive variables in the halo cells are set as follows.

$$\begin{aligned}
 \rho_1 &= \rho_2 & \rho_0 &= \rho_2 \\
 \bar{U}_1 &= -\bar{U}_2 & \bar{U}_0 &= -\bar{U}_3 \\
 \bar{V}_1 &= \bar{V}_2 & \bar{V}_0 &= \bar{V}_3 \\
 \bar{W}_1 &= \bar{W}_2 & \bar{W}_0 &= \bar{W}_3 \\
 p_1 &= p_2 & p_0 &= p_3
 \end{aligned} \tag{3.48}$$

### 3.2.8.2 Viscous Wall

The viscous, no slip wall boundary condition ensures zero velocity at the wall by specifying velocities in the adjacent cells in the opposite direction to that inside the domain. The boundary condition is also adiabatic because the normal pressure and density gradients are zero and hence the normal temperature gradient is also zero. For turbulent flows a boundary condition is also required for the turbulence model parameters  $k$  and  $\omega$ . As the velocity is zero at the wall, the turbulent kinetic energy  $k$  is also zero. The boundary condition is

$$\begin{aligned}
 \rho_1 &= \rho_2 & \rho_0 &= \rho_2 \\
 u_1 &= -u_2 & u_0 &= -u_3 \\
 v_1 &= -v_2 & v_0 &= -v_3 \\
 w_1 &= -w_2 & w_0 &= -w_3 \\
 p_1 &= p_2 & p_0 &= p_3 \\
 k_1 &= -k_2 & k_0 &= -k_3
 \end{aligned} \tag{3.49}$$

and  $\omega$  is calculated using Menter's formula

$$\omega_1 = \frac{60\mu_1}{\rho_1 C_{\omega 2} \delta y^2} \tag{3.50}$$

The flux calculated at the face on a wall boundary is in fact explicitly specified so an exact value is obtained, this means that the second halo cell is actually not used.

### 3.2.8.3 Symmetry

The symmetry boundary is commonly used to model half of a symmetrical geometry significantly reducing the grid size. The symmetry boundary should be on one side of the domain (parallel to the freestream) and planar. For the primitive variables, this boundary condition is identical to the slip wall but the turbulence model variables are now mirrored from within the domain

$$\begin{aligned}
 k_1 &= k_2 & k_0 &= k_3 \\
 \omega_1 &= \omega_2 & \omega_0 &= \omega_3
 \end{aligned} \tag{3.51}$$

### 3.2.8.4 Pole

A pole or singularity boundary condition is used when a block face is collapsed onto a single line. This may occur at the sharp nose of an aircraft or in this work it is used at the wingtip. The values in the halo cells are extrapolated from within the domain although as with the wall boundary conditions, the fluxes here are explicitly stated here and will be zero. The boundary condition for each of the 5 or 7 variables is

$$\phi_1 = 2\phi_2 - \phi_3 \quad , \quad \phi_0 = 2\phi_1 - \phi_2 \tag{3.52}$$

## 3.2.8.5 Farfield

The farfield is the most complex boundary condition used as it actually selects one of four boundary conditions depending upon the local flow conditions at the boundary. These are selected depending upon whether the normal velocity component is into or out of the domain and whether it is subsonic or supersonic. To determine this the Riemann invariants at the boundary (subscript  $b$ ), the Riemann invariants extrapolated from within the domain (subscript  $e$ ), and in the freestream (subscript  $\infty$ ) are set equal. This gives an expression for  $\bar{U}_b$ , the normal velocity (out of the domain) and the wave speed  $a_b$ . The Riemann invariants are calculated

$$R_+ = \bar{U} + \frac{2a}{\gamma - 1} \quad , \quad R_- = \bar{U} - \frac{2a}{\gamma - 1} \quad (3.53)$$

and then the boundary values of  $\bar{U}$  and  $a$  are

$$\bar{U}_b = \frac{1}{2}(R_e + R_\infty) \quad , \quad a_b = \frac{\gamma - 1}{4}(R_e - R_\infty) \quad (3.54)$$

The appropriate boundary condition is selected according to the following rules (table 3.3)

	$ \bar{U}_b  > a_b$	$ \bar{U}_b  \leq a_b$
$\bar{U}_b < 0$	(1) Supersonic inlet	(3) Subsonic inlet
$\bar{U}_b \geq 0$	(2) Supersonic outflow	(4) Subsonic outflow

Table 3.3: Farfield boundary rules

1. **Supersonic Inlet** For the supersonic inlet condition, since no information is exiting the domain, the halo cells can simply be set to the freestream values

$$\phi_1 = \phi_\infty \quad , \quad \phi_0 = \phi_\infty \quad (3.55)$$

2. **Supersonic Outlet** Similarly at a supersonic outlet, no information will be entering the domain so the halo cell values are taken from inside the domain

$$\phi_1 = \phi_2 \quad , \quad \phi_0 = \phi_2 \quad (3.56)$$

3. **Subsonic Inlet** For the subsonic inlet, the boundary values for the remaining variables are set to freestream values.

$$\bar{V}_b = \bar{V}_\infty \quad , \quad \bar{W}_b = \bar{W}_\infty \quad , \quad s_b = s_\infty \quad (3.57)$$

With the entropy and speed of sound known, the density and pressure are calculated by.

$$\rho_b \left( \frac{a_b^2}{\gamma s_b} \right)^{\frac{1}{\gamma-1}} \quad , \quad p_b = \frac{\rho_b a_b^2}{\gamma} \quad (3.58)$$

The 1<sup>st</sup> halo cell then takes the boundary value and the second is calculated through linear extrapolation. For all flowfield variables

$$\phi_1 = \phi_b \quad , \quad \phi_0 = 2\phi_1 - \phi_2 \quad (3.59)$$

4. **Subsonic Outlet** Finally for the subsonic outlet, the boundary values for the remaining variables are extrapolated from within the domain

$$\bar{V}_b = \bar{V}_e \quad , \quad \bar{W}_b = \bar{W}_e \quad , \quad s_b = s_e \quad (3.60)$$

The halo cell values are then calculated in exactly the same manor as before using Equations (3.69) and (3.70).

### 3.2.8.6 Interface

The last boundary condition used is an interface which is used to pass data from one mesh block to another. Here the halo cell values are simply copied from the corresponding cells in the neighbouring block. For a cell in block 1 at  $i = 1$ , neighbouring block 2 at  $i = ni$  the boundary condition would be

$$\phi_1^1 = \phi_{ni}^2 \quad , \quad \phi_2^1 = \phi_{ni-1}^2 \quad (3.61)$$

Clearly the indexing of this needs to be suitable for the particular block orientations and is set out before the solver is run in the boundary condition file. The programming of this boundary condition is also made more complex for the MPI version of MERLIN because the data needs to be passed over the network.

### 3.2.9 Implicit Solver

To obtain a solution for Equation (3.46) a linear system of the form  $\mathbf{Ax} = \mathbf{b}$  must be solved. In this equation,  $\mathbf{A}$  is the previously described 1<sup>st</sup> order Jacobian matrix,  $\mathbf{x}$  is the unknown vector of flowfield variable updates at iteration  $n + 1$  and  $\mathbf{b}$  is the **RHS** vector as used in the explicit method. For the same reasons as simplifications are allowed in the Jacobian matrix, the linear system (3.46) does not need to be solved exactly because in the limit of a converged (steady state) solution the multiplying unknowns will approach zero.

The equation is solved block by block by inverting  $\mathbf{A}$  using an approximate LU decomposition method termed BILU(0) (Block Incomplete Lower Upper decomposition with no fill in).

In the BILU method the matrix  $\mathbf{A}$  is separated into upper and lower triangular matrices such that

$$\mathbf{A} \approx \mathbf{LU} \quad (3.62)$$

The triangular matrices  $\mathbf{U}$  and  $\mathbf{L}$  are easily inverted and the unknown vector  $\mathbf{x}$  can be calculated by

$$\mathbf{x} = \mathbf{U}^{-1}\mathbf{L}^{-1}\mathbf{A} \quad (3.63)$$

Once a solution to  $\mathbf{x}$  or  ${}^n\Delta\mathbf{P}$  has been obtained, the solution can be updated with Equation (3.47).

This concludes the description of the flow solver. Now a description of the ajoint solver is given which allows efficient computation of the objective function gradients.



### 3.3 Vortex Lattice Method

Vortex Lattice methods give a simple, efficient potential flow solution for the lift distribution on finite wings. The method is particularly useful because the leading edge thrust can be obtained directly from the solution for use in the constraint function. In full 3D methods a chordwise integration would need to be performed to calculate the leading edge thrust but the definition of leading edge thrust becomes more complex when the aerofoil is cambered. There are many limitations of vortex lattice methods. They assume attached flow, thickness effects are not modelled, compressibility can only crudely be accounted for and the wake is assumed to be flat. The advantage, despite these deficiencies and unlike Navier-Stokes models, is that the objective or constraint function will always remain smooth, well behaved and differentiable.

In this work Lan's quasi vortex lattice method has been implemented in Fortran and used. This is an extension to the classical approach which eliminates errors due to the leading edge singularity and hence calculates leading edge thrust more accurately. The classical approach is first described followed by a description of the quasi vortex lattice method.

#### 3.3.1 Classical Approach

The solution is obtained by applying a Neumann boundary condition [77] (Eq 3.65) to the wings camber surface (mid way between upper and lower surfaces) which states that the normal velocity is zero at the surface and solving for the unknown vorticity distribution. This is achieved by discretising the surface into a number of quadrilateral panels as shown in Figure 3.7a, each with a horse shoe vortex applied to it and a collocation point at which the boundary condition is applied. The leading 'bound' vortex for each panel is applied along the  $1/4$  chord line and two further vortex lines join the ends of the bound vortex to a point infinitely far downstream as shown in Figure 3.7b. The collocation point is located half way along the panels  $3/4$  chord line. For each panel, the coordinates  $(x, y, z)$  of each end of the bound vortex must be known as well as the location of the collocation point and the normal vector ( $\mathbf{n}$ ).

$$\nabla(\phi + \phi_\infty) \cdot \mathbf{n} = 0 \quad (3.65)$$

The boundary condition in a discretised form (Eq 3.66) is applied to each collocation point which forms a linear system of the form  $\mathbf{Ax} = \mathbf{b}$  and can be solved using standard solution methods, in this case a Gaussian elimination algorithm.

$$\mathbf{A}\mathbf{\Gamma} + \mathbf{b} = 0 \quad (3.66)$$

where

$$\mathbf{A} = \begin{bmatrix} a_{11} & a_{12} & \cdots & a_{1N} \\ a_{21} & \ddots & & \vdots \\ \vdots & & \ddots & \vdots \\ a_{N1} & \cdots & \cdots & a_{NN} \end{bmatrix}, \mathbf{\Gamma} = \begin{bmatrix} \Gamma_1 \\ \Gamma_2 \\ \vdots \\ \Gamma_N \end{bmatrix}, \mathbf{b} = \mathbf{Q}_\infty \cdot \begin{bmatrix} \mathbf{n}_1 \\ \mathbf{n}_2 \\ \vdots \\ \mathbf{n}_N \end{bmatrix}$$

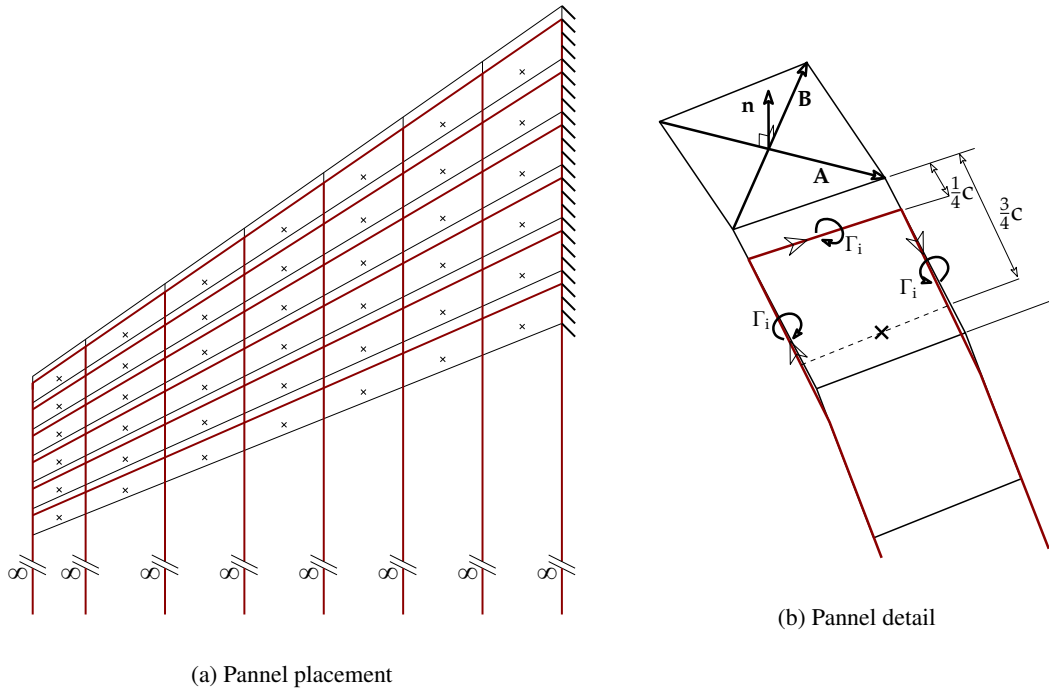


Figure 3.7: Vortex Lattice Layout

Each element of  $\mathbf{A}$  is calculated according to

$$a_{ij} = \mathbf{V}_{ij} \cdot \mathbf{n}_i \quad (3.67)$$

where  $i$  refers to collocation the points  $1 - N$  and  $j$  refers to the horseshoe vortices  $1 - N$ . The normal vectors are calculated through the cross product of the element diagonals

$$\mathbf{n}_k = \frac{\mathbf{A}_k \times \mathbf{B}_k}{|\mathbf{A}_k \times \mathbf{B}_k|} \quad (3.68)$$

and the induced velocities are calculated using 3 applications (bound vortex and two trailing vortices) of the Biot–Savart law (Eq 3.69) with unit vorticity in which the vectors  $\mathbf{r}_i$  are defined according to Figure 3.8.

$$\mathbf{V} = \frac{\Gamma}{4\pi} \frac{\mathbf{r}_1 \times \mathbf{r}_2}{|\mathbf{r}_1 \times \mathbf{r}_2|^2} \left[ \frac{\mathbf{r}_0 \cdot \mathbf{r}_1}{r_1} - \frac{\mathbf{r}_0 \cdot \mathbf{r}_2}{r_2} \right] \quad (3.69)$$

In order to reduce the computational cost, wing symmetry can be modelled by adding the influence of a wing located at  $-z$  to the corresponding influence coefficients in the influence matrix.

Once a solution has been obtained, the forces on each panel can be calculated according to the Kutta-Joukowski theorem.

$$\mathbf{F} = (\mathbf{V}_{eff} \times \Gamma_{ij})l \quad (3.70)$$

Assuming non-dimensionalised freestream conditions

$$\Delta L_{ij} \approx \Gamma_{ij} \Delta z_{ij} \quad (3.71)$$

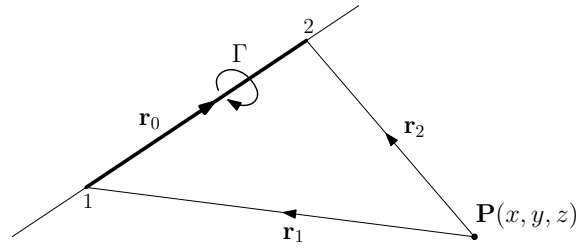


Figure 3.8: Biot–Savart law for a vortex line

The pressure difference between the upper and lower surfaces is

$$\Delta C_p = \frac{\Delta L_{ij}}{Q_\infty \Delta S_{ij}} = \frac{2\Delta L_{ij}}{\Delta S_{ij}} \quad (3.72)$$

To obtain the lift coefficient, the lift from each panel is summed over the wing and divided by the wing area.

$$C_L = \frac{2}{S} \sum_{i=1}^N \Gamma_i \Delta z \quad (3.73)$$

### 3.3.2 Compressibility Corrections

The above equations assume incompressible flow which becomes invalid for Mach numbers  $M_\infty > 0.25$ . The Prandtl-Glauert transformation improves accuracy for compressible flows by replacing the geometry in the influence coefficient calculation by an incompressible flow equivalent geometry. The Prandtl-Glauert factor  $\beta$  is defined as

$$\beta = \sqrt{1 - M^2} \quad (3.74)$$

and the geometry is then modified in the calculation of the influence coefficients such that

$$\begin{aligned} \mathbf{X}' &= \mathbf{X} \\ \mathbf{Y}' &= \beta \mathbf{Y} \\ \mathbf{Z}' &= \beta \mathbf{Z} \end{aligned} \quad (3.75)$$

The pressure coefficients also need to be modified according to the Prandtl-Glauert factor so that

$$C_p = C_{p0} / \beta \quad (3.76)$$

Using this simple correction the vortex lattice method can continue to give reasonable results up until shock waves begin to appear, usually around  $M_\infty > 0.7$ .

### 3.3.3 Leading Edge Thrust

The current solution predicts the chordwise lift distribution correctly but as shown in Figure 3.9 the force generated by the low pressure acting around the leading edge in the chordwise tangential direction is not yet accounted for. This force is known as the leading edge thrust. For a symmetrical aerofoil, it is equal to the axial force. The leading edge thrust for a 2D symmetrical aerofoil can be



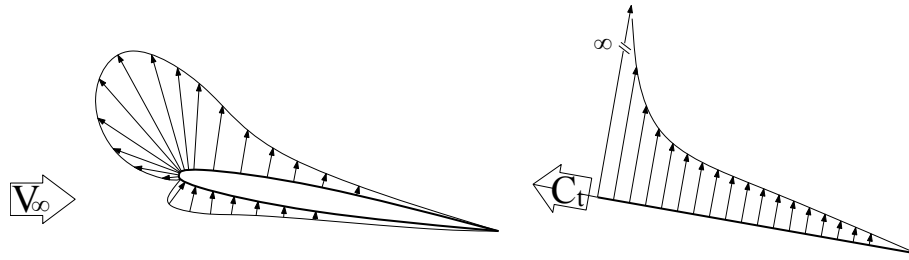


Figure 3.9: Aerofoil pressure distribution and thin aerofoil solution

easily calculated because we know that for inviscid, incompressible 2D flow, the drag will always be zero. The leading edge thrust makes up the difference between the integrated pressure force on the camber line and the drag force which must be zero. The thin aerofoil theory predicts the normal force coefficient to be

$$C_n = 2\pi\alpha \quad (3.77)$$

To have zero drag, the leading edge thrust must be

$$C_t = C_n \sin(\alpha) \approx 2\pi\alpha^2 \quad (3.78)$$

To find a more general expression for the leading edge thrust that can be applied to arbitrarily cambered aerofoils, we consider the pressure loading at the leading edge. The thin aerofoil/wing solution has a singularity at the leading edge so a singularity parameter is introduced which has a finite value

$$\lim_{x \rightarrow 0} sp_0 = C_p \sqrt{x} \quad (3.79)$$

To demonstrate the calculation of leading edge thrust through this approach, consider the analytical pressure distribution for the above symmetrical aerofoil

$$\Delta C_p = 2\gamma = 4\alpha \sqrt{\frac{1-x}{x}} \quad (3.80)$$

The singularity parameter at the leading edge for the symmetrical aerofoil when  $x \rightarrow 0$  is

$$sp_0 = 4\alpha \sqrt{\frac{1-x}{x}} \sqrt{x} = 4\alpha \quad (3.81)$$

Combining this with Equation(3.78) to eliminate  $\alpha$ , the leading edge thrust is

$$C_t = \frac{\pi}{8} sp_0^2 \quad (3.82)$$

This expression holds for any arbitrary camber line and can be extended for 3D wings. For a swept wing in compressible flow, the leading edge thrust is[78]

$$C_t = \frac{\pi}{8} sp_0^2 \frac{\sqrt{\beta^2 \cos^2 \Lambda_{le}}}{\cos \Lambda_{le}} \quad (3.83)$$

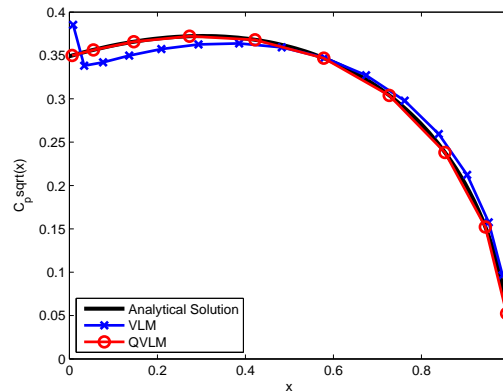


Figure 3.10: VLM and QVLM singularity parameter vs analytical solution for a parabolic camber aerofoil

The classical vortex lattice method cannot have a bound vortex or control point at the leading edge because a singularity exists there. The singularity parameter can be estimated through linear extrapolation from the two solution points closest to the leading edge. This is where the classical approach fails somewhat because as shown in figure 3.10 the solution becomes inaccurate near the leading edge. This is because square root and Cauchy type singularities are ignored in the method which creates numerical errors. Early wing optimisation attempts using the classical VLM to place limits on the leading edge thrust proved problematic because not only is  $C_t$  incorrectly calculated, the gradients with respect to the design variables ( $\partial C_t / \partial \beta_k$ ) have large errors and can even have the wrong sign! This caused the optimiser to diverge and output unrealistic designs. Hence an improved method was required.

### 3.3.4 Quasi Vortex Lattice Method

To overcome this difficulty, an extension to the above method was coded for this research, based on Lan's [79] method. The idea behind this modification is that through a change of variables and careful selection of control point locations, the singularities can be eliminated and hence the numerical solution is much more accurate and becomes mesh independent much more easily. The solution is also linearised using the small angle approximation which allows fixed lift calculations by combining planar and cambered wing solutions. Firstly the  $x$  coordinate is replaced by an angular parameter  $\theta$  using the following relation

$$x = (1 - \cos\theta)/2 \quad (3.84)$$

The calculation of the influence coefficients at the collocation point locations  $(x, y)$  (evaluation of Equation (3.69)), evaluated for a planar wing on the  $y=0$  plane with substitution of  $1/4\pi$  with

$c \sin\theta/8N$  consistent with Lan's modification now becomes

$$\begin{aligned}
 w(x, z) = & \frac{\gamma c}{8N} \sum_{k=1}^N \frac{G_1 \theta_k \gamma \theta_k \sin\theta_k}{(x_{1k} - x)(z_2 - z_1) - (x_{2k} - x_{1k})(z_1 - z)} \\
 & + \frac{\gamma c}{8N} \sum_{k=1}^N G_2 \theta_k \gamma \theta_k \sin\theta_k \\
 & - \frac{\gamma c}{8N} \sum_{k=1}^N G_3 \theta_k \gamma \theta_k \sin\theta_k
 \end{aligned} \tag{3.85}$$

where

$$\begin{aligned}
 G_1(x, z) = & \frac{(x_2 - x_1)(x_2 - x) + \beta^2(z_2 - z_1)(z_2 - z)}{[(x_2 - x)^2 + \beta^2(z_2 - z)^2]^{0.5}} \\
 & - \frac{(x_2 - x_1)(x_2 - x) + \beta^2(z_2 - z_1)(z_2 - z)}{[(x_1 - x)^2 + \beta^2(z_1 - z)^2]^{0.5}}
 \end{aligned} \tag{3.86}$$

$$G_2(x, z) = \frac{1}{z_1 - z} \left[ 1 - \frac{x_1 - x}{[(x_1 - x)^2 + \beta^2(z_1 - z)^2]^{0.5}} \right] \tag{3.87}$$

$$G_3(x, z) = \frac{1}{z_2 - z} \left[ 1 - \frac{x_2 - x}{[(x_2 - x)^2 + \beta^2(z_2 - z)^2]^{0.5}} \right] \tag{3.88}$$

and subscripts 1 and 2 indicate the inner and outer ends of the bound vortex and  $x$  and  $z$  are the coordinates of the control point in question.  $\gamma$  is the vortex density, related to the pressure coefficient by  $C_p = -2\gamma$ . It is also related to the discrete vortex strength (used above) by  $\Gamma = \gamma\Delta x$ . In order to account for the camber and twist on the wing, the boundary condition is changed to

$$b_i = \frac{\partial y_c}{\partial x} - \theta_t - \alpha_\infty \tag{3.89}$$

### 3.3.5 Vortex and Control Point Locations

Now that the square root singularities at the leading edge have been eliminated by the term  $\sin(\theta)$ , control points can be placed at the leading and trailing edges allowing both the leading edge thrust to be directly calculated (without extrapolation) and now the Kutta condition is exactly satisfied at the trailing edge. In the chordwise direction the vortex ( $k$ ) and control point ( $i$ ) locations are calculated using equal spacing in the  $\theta$  coordinate

$$\theta_k = \pi(2k - 1)/2N \quad k = 1, 2, \dots, N \tag{3.90}$$

$$\theta_i = \pi i/N \quad i = 0, 1, \dots, N \tag{3.91}$$

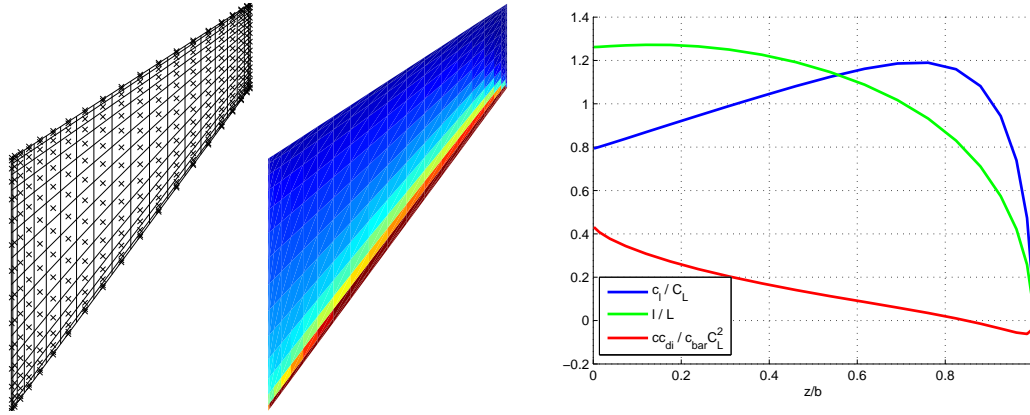


Figure 3.11: Grid,  $C_p$  distribution and spanwise forces for the Warren 12 planform

These are converted to the non-dimensional chordwise parameter  $\xi$  using Equation(3.84) and the  $x$  coordinate with

$$\xi_k = (1 - \cos(\theta_k))/2 \quad (3.92)$$

$$\xi_i = (1 - \cos(\theta_i))/2 \quad (3.93)$$

$$x_k = x_{le} + c\xi_k \quad (3.94)$$

$$x_i = x_{le} + c\xi_i \quad (3.95)$$

The equivalent relationships for vortex and control point spacing in the spanwise direction are

$$\phi_{z,k} = \pi k / M \quad k = 0, 1, \dots, M \quad (3.96)$$

$$\phi_{z,i} = \pi(2i - 1) / (2M) \quad i = 1, 2, \dots, M \quad (3.97)$$

$$z_k = b/2(1 - \cos(\phi_k))/2 \quad (3.98)$$

$$z_i = b/2(1 - \cos(\phi_i))/2 \quad (3.99)$$

If the planform has discontinuous leading or trailing edges such as those on a UCAV, the wing can be split into multiple spanwise sections, each with the above spacing. This refines the mesh at the discontinuities where the solution changes more rapidly. For the 1303 UCAV, 3 spanwise sections are used.

The quasi-vortex-lattice method becomes mesh independent for very low numbers of elements. For example Lan [79] shows the lift, pitching moment and leading edge thrust for a parabolic camber aerofoil can be correctly calculated with just two chordwise elements. Mesh independence for higher order camber shapes requires enough elements to capture the geometry correctly. For the 1303 case,  $15 \times 15$  elements for each of the spanwise sections gives mesh converted results for leading edge thrust when typical camber and twist were applied to the wing.

### 3.3.6 Force Calculation

The force integration for the QVLM is performed differently to the standard VLM. The sectional lift coefficient is evaluated using the midpoint trapezoidal rule

$$C_l = \frac{\pi}{N} \sum_{k=1}^N \gamma_k \sin(\theta_k) \quad (3.100)$$

Similarly the pitching moment and axial force can be calculated

$$C_m = \frac{\pi}{N\bar{c}} \sum_{k=1}^N \gamma_k \sin(\theta_k) x_k \quad (3.101)$$

$$C_a = \frac{\pi}{N} \sum_{k=1}^N \gamma_k \sin(\theta_k) \frac{-dy_c}{dx} \quad (3.102)$$

The leading edge thrust is also required. This is calculated firstly by evaluating Equation(3.85) at the leading edge control point and using the following relation to calculate the singularity parameter

$$sp_0 = 2 \frac{w_{le} - \frac{dy_c}{dx} + \theta_t + \alpha}{N(\tan^2 \Lambda + \beta^2)^{0.5}} \quad (3.103)$$

Equation(3.83) is then used to calculate the leading edge thrust. To calculate the sectional induced drag coefficient, the sectional forces above are summated in the streamwise direction

$$C_{di} = C_l \alpha - C_t + C_a; \quad (3.104)$$

Once the sectional forces are known, the total forces are calculated again using the midpoint trapezoidal rule.

$$C_L = \frac{b}{2S_w} \frac{\pi}{M} \sum_{i=1}^M C_{l,i} c_i \sin(\phi_i) \quad (3.105)$$

The pitching moment, axial force, drag and leading edge thrust coefficients can be calculated in exactly the same manner by substituting  $C_l$  with the appropriate variable. Alternatively the wing drag coefficient for the entire wing can be computed

$$C_{Di} = C_L \alpha - C_T + C_A \quad (3.106)$$

### 3.3.7 Specified Lift Calculation

In the optimiser constraint function, a solution is required at a fixed lift coefficient (take-off lift) regardless of the twist and camber applied to the wing. We can make use of the superposition principle to obtain a solution at a specified lift coefficient. Firstly, we use the above procedure to obtain two solutions, one for a planar wing at  $\alpha = 1$  radian and one for the twisted and cambered wing at  $\alpha = 0$ . Once the lift coefficients for these two solutions have been obtained, the lift curve

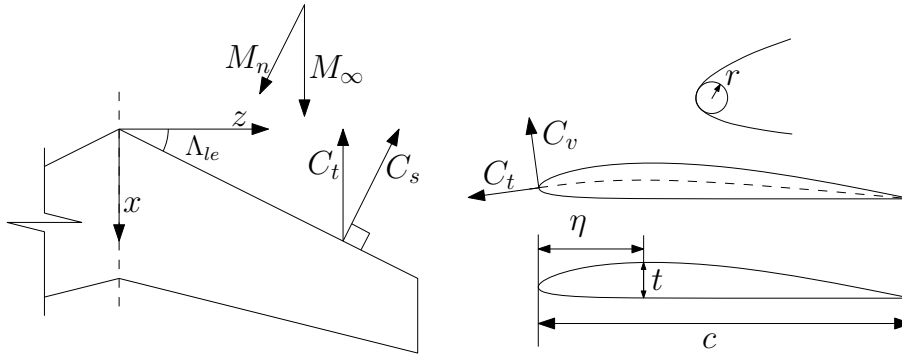


Figure 3.12: Various aerodynamic and geometrical parameters

slope and required incidence angle are

$$C_{L\alpha} = C_{L,planar}/1 \text{ rad} \quad (3.107)$$

$$\alpha_{req} = (C_{L,req} - C_{L,twist\&camber})/C_{L\alpha} \quad (3.108)$$

The solution is then reconstructed

$$\gamma = \gamma_{planar}\alpha_{req} + \gamma_{twist\&camber} \quad (3.109)$$

### 3.4 Empirical High Lift Constraint

On thin wings, flow separation is generally a result of a peaky pressure distribution in the region of the leading edge leading to strong adverse pressure gradients. The pressure levels at the leading edge are closely related to the strength of the singularity parameter and hence the leading edge thrust, which is accurately computed using the quasi-vortex-lattice method detailed in the previous section. This section describes and discusses the empirical constraint adapted for this work based on Carlson's [80] attained thrust parameter, an indication of whether the leading edge flow will remain attached. The method makes 2D assumptions and uses curve fit equations which may not be accurate for all flow conditions or aerofoil shapes but it allows extremely quick evaluation and is smooth, well behaved and suitable for gradient based optimisation algorithms.

#### 3.4.1 Simple Sweep Theory and Normal Section Parameters

Simple sweep theory gives a means of comparing aerofoil parameters and aerodynamic characteristics on swept wings with 2D section data or differently swept wings. The fundamental principle is that the flow can be de-constructed in two perpendicular planes, parallel and normal to the sweep direction. The flow parallel to the sweep experiences little or no curvature and hence the pressure changes are small in comparison to those in the normal direction and therefore can be ignored. In this work, of primary interest is the flow separation in the vicinity of the leading edge so the leading edge sweep angle  $\Lambda_{le}$  is considered. The velocity normal to the leading edge is

$$V_n = V_\infty \cos \Lambda_{le} \quad (3.110)$$

resulting in the normal Mach number

$$M_n = M_\infty \cos \Lambda_{le} \quad (3.111)$$

Traditionally wing sweep is used to delay the drag rise by effectively lowering the normal Mach number through this mechanism. Similarly the chord normal to the leading edge is

$$c_n = c \cos \Lambda_{le} \quad (3.112)$$

These are the primary reasons why both the lift curve slope  $C_{l\alpha}$  and maximum lift  $C_{l,max}$  of swept aerofoils is reduced because the effective dynamic pressure and chord have been reduced, reducing their load carrying capability. The section normal Reynolds is

$$Re_n = Re \frac{c_n}{\bar{c}} \frac{M_n}{M} \quad (3.113)$$

further promoting early flow separation due to a lower Reynolds number although this is an over simplification as we are not considering 3D phenomena such as attachment line transition. Also important is the thickness to chord ratio and leading edge radius given by

$$(t/c)_n = t/c \frac{1}{\cos \Lambda_{le}} \quad (3.114)$$

and

$$(r/c)_n = r/c \frac{1}{\cos^2 \Lambda_{le}} \quad (3.115)$$

Sweeping a wing results in an effectively thicker aerofoil with a larger leading edge radius which, for relatively thin wings, will have the effect of delaying separation. Likewise the effective camber will also be increased, but this will be accounted for by the vortex lattice solver. Not strictly a fundamental aerofoil parameter, Carlson uses the leading edge radius index defined as

$$r_{i,n} = \frac{(r/c)_n \eta}{(t/c)_n} \quad (3.116)$$

where  $\eta$  is the position of maximum thickness as a way of measuring the relative bluntness of an aerofoil and hence incorporating several of the above parameters into one which closely correlates with the onset of flow separation. Lastly the normal leading edge thrust is also required, calculated by

$$C_{t,n} = C_t \frac{c}{c_n} \frac{1}{\cos^2 \Lambda_{le}} \quad (3.117)$$

### 3.4.2 Limiting Pressure and Leading Edge Thrust $C_{p,lim} = C_{p,vac}$

In Carlson's method, a curve fit formula is conceived to compute the amount of attained leading edge thrust subject to a limiting pressure coefficient equal to the vacuum pressure limit  $C_{p,vac} = -2/\gamma M_n^2$  (i.e. a perfect vacuum). The vacuum pressure limit is infinite when the Mach number is zero and places more severe limitations as  $M_n$  is increased. Experimentalists have found that aerofoils can achieve up to about 70% of  $C_{p,vac}$  [81]. Using this data, more realistic limitations

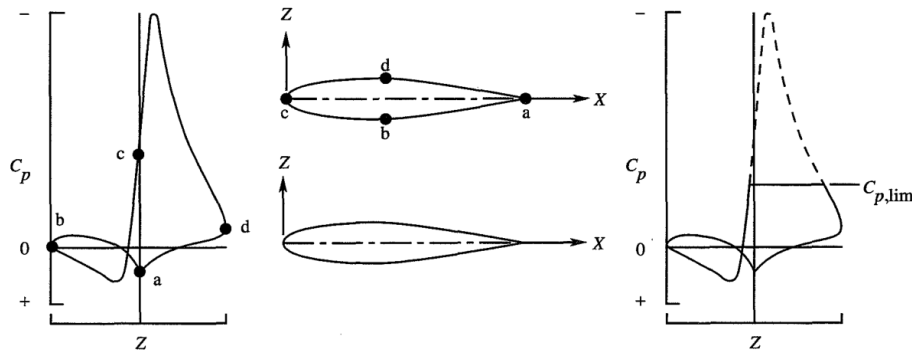


Figure 3.13: Integration of truncated pressure distributions [80]

can then be accounted for by computing an equivalent Mach number  $M_e$  where the limiting pressure  $C_{p,lim}$  is equal to the vacuum pressure limit  $C_{p,vac}$ . This is explained in the next section. The amount of attained leading edge thrust  $K_t$  is the ratio of the attained  $C_t^*$  and theoretical  $C_t$  (assuming no flow separation) leading edge thrust, i.e.

$$K_t = \frac{C_t^*}{C_t} \quad (3.118)$$

Data to form the curve fit relation was obtained by integrating various computed airfoil pressure distributions with the pressure truncated at  $C_{p,vac}$  as shown in figure 3.13. Carlson describes the process of finding the curve fit equation as “quite involved and was developed after significant trial and error” but the details are not presented. The relation is essentially a curve fit for data with Mach numbers ranging from 0 to 1.0, maximum thickness ratios from  $t/c = 0$  to 0.15, locations of maximum thickness  $\eta = 0.1$  to 0.5 and leading edge indices from 0 to 0.12. The equation is

$$\frac{K_t}{1 + (t/c)_n^{1.2}} = k \left\{ c_{t,n} \beta_n \left[ \frac{(t/c)_n (\eta/0.5)^{e_1}}{0.09} \right]^{e_2} \right\}^{e_3} \quad (3.119)$$

where

$$k = \{0.14[1.0 - (1.0 - \sqrt{r_{i,n}})M_n^5] + 0.11\sqrt{r_{i,n}}\} \times \left( \frac{1 - M_n}{M_n} \right)^{0.48(1+r_{i,n}^{0.3})} \quad (3.120)$$

$$e_1 = 0.4r_{i,n}^{0.16} - 0.7 \quad , \quad e_2 = 1.6r_{i,n}^{0.10} - 3.0 \quad , \quad e_3 = -0.32r_{i,n}^{0.10} - 0.3$$

$K_t$  values are limited to values less than 1 so the leading edge thrust does not exceed the theoretical values calculated in the lifting surface code. Notice in the formula, the constants  $t/c = 0.09$  and  $\eta = 0.5$  indicate that curve fit is centred about deviations to an airfoil with these parameters and hence is most accurate near this point. The 1303 UCAV with a NACA64a008 section is close to the centre of the valid range. Figure 3.14 shows how the attained leading edge thrust varies with various geometrical parameters according to Carlson’s formula. (a) shows how the leading edge thrust is greatly reduced for small leading edge radii. (b) shows that the attained thrust varies almost linearly with section thickness and (c) shows that a forward movement of the max thickness position allows



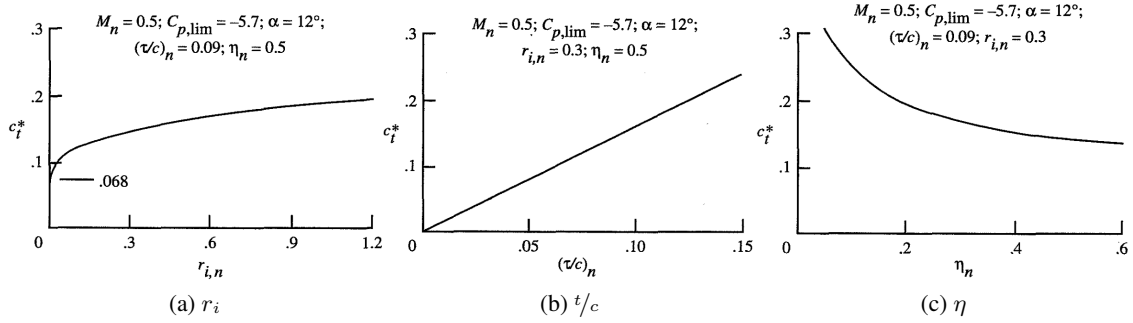


Figure 3.14: Effect on attained leading edge thrust  $C_t$  of various geometrical parameters[80]

for greater attained leading edge thrust. In each case, blunting / increasing the frontal area proves to be beneficial but may have a negative impact on the profile drag.

### 3.4.3 Equivalent Mach Number

Equation (3.119) can in fact be used to calculate attained thrust with arbitrary values of  $C_{p,lim}$  because it already contains all the required information. This is due to the fact that the aerofoil pressure distribution and the limiting pressure  $C_{p,lim}$  both have the same dependence on Mach number i.e. they change in accordance with the Prandtl-Glauert rule. This means that for the same aerofoil and angle of attack, the value of  $K_t$  is independent of Mach number. For this reason, we can simply define an equivalent Mach number  $M_e$  at which  $C_{p,lim} = C_{p,vac}$  and substitute this in equation (3.119) to calculate  $K_t$ . The equivalent Mach number is computed by equating the pressure coefficients  $C_{p,vac}$  at the equivalent Mach number and  $C_{p,lim}$  at the normal freestream Mach number

$$\frac{-2}{\gamma M_e^2} = C_{p,lim}(M_n) \frac{\sqrt{1 - M_n^2}}{\sqrt{1 - M_e^2}} \quad (3.121)$$

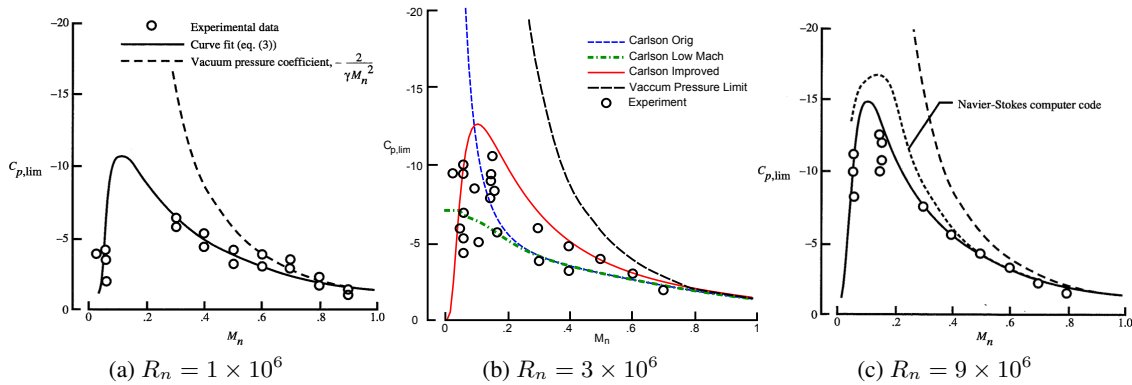
and rearranging to get the equivalent Mach number

$$M_e = \frac{-\sqrt{2}}{\gamma C_{p,lim} \sqrt{1 - M_n^2}} \sqrt{\sqrt{1 + (\gamma C_{p,lim} \sqrt{1 - M_n^2})^2} - 1} \quad (3.122)$$

### 3.4.4 Curve Fit Formulae for $C_{p,lim}$

The following curve fit relationships for  $C_{p,lim}$  were devised by applying Equations (3.119) and (3.122) to experimental cases where, by trial and error, a value of  $C_{p,lim}$  was found which reproduced the data. Particular attention was paid to the breakaway points, i.e. where the results deviate from the linear theory indicating the onset of flow separation. This was done for a large number of experimental cases from the literature at the time. The database had aerofoils ranging from  $t/c = 4\%$  to  $15\%$ ,  $\eta = 10$  to  $0.42$  with leading edge indices  $r_i = 0.24$  to  $0.33$ . Flow conditions were in the Mach number range  $M = 0.03$  to  $0.9$  and Reynolds numbers from  $Re = 1 \times 10^6$  to  $30 \times 10^6$ . As above, Carlson devised a curve fit equation to represent the experimentally determined

Original Method 1979 [82]	Low Mach Method 1983 [83]	Improved Method 1996 [80]
$K = 4 - 3M_n$	$K = 4 - 3M_n + 4(1 - M_n)^{15}$	$K = 8(1 - M_n)$
$e_4 = 0.05 + 0.35(1 - M_n)^2$	$e_4 = 0.05 + 0.35(1 - M_n)^2$ Note. $C_{p,lim}$ value for $M_n = 0.05$ held between $M_n = 0 - 0.05$	$e_4 = 0.028M_n^{-0.75}$

Table 3.4: Exponents for Carlson's  $C_{p,lim}$  FormulaeFigure 3.15:  $C_{p,lim}$  vs  $M_n$  [80]

values of  $C_{p,lim}$  which is of the form

$$C_{p,lim} = -\frac{2}{\gamma M_n^2} \left( \frac{Re_n \times 10^{-6}}{Re_n \times 10^{-6} + 10^K} \right)^{e_4} \quad (3.123)$$

In various publications and reports, several versions of the formula were presented with different expressions for the exponents  $e_4$  and  $K$ . These are summarised in Table 3.4. It should be noted that when compared with separated viscous flow pressure distributions,  $C_{p,lim}$  is not the minimum pressure coefficient found on the aerofoil surface but a representative average pressure for the separated region on the aerofoil so can not be directly compared. The purpose of this analogy is that rather than having a purely curve fit relationship for  $K_t$ , some physics is retained which should make the formulas more widely applicable.

The three sets of exponents for Equation (3.123) can give quite different results, especially at lower Mach numbers. Figure 3.15(a) and (c) show predictions using Carlson's improved method at Reynolds numbers of 1 and 9 million as well as some experimental results. For both these cases, the curve fits match the experimental data reasonably well. (b) shows all three predictions for a Reynolds number of 3 Million. This case shows significant scatter in the experimental results which is likely to be because at this Reynolds number, the results are sensitive to laminar to turbulent transition. All three curves approach the vacuum pressure limit at Mach numbers close to 1.0. At around Mach 0.5, the original and low Mach methods have very similar results but the improved method makes more optimistic estimates. This is thought to be because after significant experience using the method (17 years between publications) the estimates were thought to be too severe. Furthermore, the experimental database is larger for later versions of the formula. It is at low Mach

numbers that the formulae become really quite different. The original method predicts that as the Mach number approaches zero,  $C_{p,lim}$  becomes very large, following the trend set by the the vacuum pressure limit. This was obviously an oversight as the method was designed for use at higher normal Mach numbers. The improved method takes a different approach and the limiting pressure goes to zero as the Mach number approaches zero. This seems to at least partially match the experimental data although there is no physical explanation of this phenomenon and hence its validity is highly questionable. The low Mach approach seems the most appropriate in this region as it is not particularly sensitive to the Mach number as would be expected although is probably quite conservative. For the normal free-stream Mach number experienced by the 1303 UCAV at take-off;  $M_n = 0.25 \times \cos(47^\circ) = 0.17$ , the estimate from the original method is thought to be the most appropriate because (a) it seems to lie around the average of the experimental data points and (b) is it approximately mid-way between the other two formulae.

Figure 3.15(c) includes some results from computations performed using NASA's RANS code CFL3D with the Spalart-Allmaras turbulence model, treated in the same manner as the experimental results. The curve seems to follow the trend of Carlson's improved method (reducing  $C_{p,lim}$  at low Mach number) albeit with higher levels of suction. This could be evidence that the limiting pressure does in fact reduce with Mach number for  $M_n < 0.175$  although the results of a compressible CFD code at these low Mach numbers may be inaccurate. Also this points out the tendency of RANS codes to over-predict attained suctions, possibly due to inadequate turbulence modelling or lack of transition prediction.

The Reynolds number sensitivity is the same between all three versions of the method. From results presented in Reference [80], the relationship seems to be simpler and there is less scatter in the results. The exception to this is a  $Re = 3 \times 10^6$  when the results are thought to be sensitive to transition.

### 3.4.5 Application of Carlson's Procedure in the Constraint Function

For the high lift constraint function there are various practicalities in applying the procedure which have not yet been discussed. A summary of the process in the computer program is given below.

1. Determine basic QVLM grid
  - The original (planar wing) RANS mesh is read into memory. To save i/o time, a version of the mesh with no volume cells is used as they are not required here.
  - The mesh deformation subroutine is called which updates the surface mesh points to represent the current design.
  - Twist is removed from the wing and values of twist are stored for use later.
  - Spanwise vortex and control point spacing is determined based on the wing planform and QVLM requirements.
  - Local wing twist, chord and leading edge sweep are calculated at each leading edge control point.
  - Streamwise sections are extracted at each spanwise location by linear interpolation and normalised to the local chord.
  - Chordwise vortex and control point locations are calculated for each section.
2. Section normal parameters are calculated for each leading edge control point

- Decompose the aerofoil into camber line  $((y_u + y_l)/2)$  and thickness  $(y_u - y_l)$  distributions. For this the lower surface points are interpolated at the upper surface  $x$  locations using cubic spline interpolation.
  - Position of maximum thickness  $\eta(x)$  is determined through a search.
  - The thickness distribution is fitted to a 6<sup>th</sup> order polynomial of the form  $k_1x^{0.5} + k_2x^{1.5} + \dots + k_nx^{n-0.5}$  using a least squares fit. The constant  $k_1$  is related to the leading edge radius by  $r/c = \frac{k_1^2}{2}$ .
  - Equations (3.112–3.116) are then applied to calculate the section normal parameters.
3. The surface slopes  $\partial y/\partial x$  are calculated for each control point by interpolation of the camber line extracted in (2).
  4. The QVLM program is run, which calculates the local leading edge thrust  $C_t$  and hence  $C_{t,n}$  with (3.117) for each leading edge control point at the specified lift coefficient. Now all the necessary information is known for calculation of the attained thrust factor  $K_t$
  5. Calculate the equivalent Mach number  $M_e$  using Equation (3.122)
  6. Calculate the limiting pressure coefficient  $C_{p,lim}$  with Equation (3.123)
  7. Calculate the attained thrust factor  $K_t$  with Equation (3.119)

## 3.5 Adjoint Solver

This section gives some background on the adjoint method and justifies its use in this work. A derivation of the discrete adjoint method is then presented and the solver used in this work, ADJ-MERLIN, is described.

### 3.5.1 Background

There are various methods available for computation of the objective or constraint function gradients. The most obvious is approximating the derivative through finite differences. The sensitivity derivative could then be computed using a forward or backward difference

$$\frac{\partial F}{\partial \beta_k} = \frac{F(\boldsymbol{\beta} \pm \mathbf{e}_k \epsilon) - F(\boldsymbol{\beta})}{\pm \epsilon} \quad (3.124)$$

This technique is simple to implement although for large numbers of design variables is extremely expensive requiring  $ndv + 1$  evaluations of  $F$ . When the aerodynamic function is calculated using a Navier-Stokes CFD code, the computing requirement can easily become too high. Additionally, the method is only 1st order accurate and the accuracy depends on the step size  $\epsilon$ . If  $\epsilon$  is too large, higher order terms may become significant invalidating the linear approximation. If  $\epsilon$  is too small, this would cause noise and/or spurious results which affect the gradient accuracy. For improved (2nd order) accuracy a central difference could be used but this requires even more calls ( $2 \times ndv$ ) to the aerodynamic function. Various more involved methods have been developed over the years including complex variable methods and automatic differentiation methods. These offer benefits in accuracy although no significant reduction in the computational requirement can be obtained.

### 3.5.2 Quasi-Analytical Methods

A class of methods exist known as quasi-analytical methods. These arise from differentiating the objective function directly using the chain rule. The aerodynamic function  $F$  is a function of the converged flowfield variables  $\mathbf{Q}^*$  which in turn are a function of the design variables  $\boldsymbol{\beta}$ , the domain geometry  $\mathbf{X}$  which is also a function  $\boldsymbol{\beta}$  and the design variables  $\boldsymbol{\beta}$  themselves. The aerodynamic function can be written as

$$F = F(\mathbf{Q}^*(\boldsymbol{\beta}), \mathbf{X}(\boldsymbol{\beta}), \boldsymbol{\beta}) \quad (3.125)$$

If this function is differentiated with respect to the design variables we obtain

$$\frac{dF}{d\beta_k} = \left( \frac{\partial F}{\partial \mathbf{Q}} \right)^t \frac{d\mathbf{Q}^*}{d\beta_k} + \left( \frac{\partial F}{\partial \mathbf{X}} \right)^t \frac{d\mathbf{X}}{d\beta_k} + \frac{\partial F}{\partial \beta_k} \quad (3.126)$$

The aerodynamic objective with respect to flowfield variables, domain geometry and design variables,  $\frac{\partial F}{\partial \mathbf{Q}}$ ,  $\frac{\partial F}{\partial \mathbf{X}}$  and  $\frac{\partial F}{\partial \beta_k}$  respectively are relatively simple and cheap to evaluate. However the term  $\frac{d\mathbf{Q}^*}{d\beta_k}$  is somewhat more complex. Two main approaches exist for the solution of equation (3.126) which are direct differentiation and the adjoint method which is used in this work.

#### 3.5.2.1 Direct Differentiation

The direct differentiation approach attempts to obtain  $\frac{d\mathbf{Q}^*}{d\beta_k}$  through the solution of an additional equation. To obtain this equation the flow solver residual must be differentiated, similar to the

differentiation of the aerodynamic function (equation(3.136)) above in order to obtain an expression which can be solved for  $\frac{d\mathbf{Q}^*}{d\beta_k}$ .

$$\mathbf{R} = \mathbf{R}(\mathbf{Q}^*(\beta), \mathbf{X}(\beta), \beta) = 0 \quad (3.127)$$

$$\frac{d\mathbf{R}}{d\beta_k} = \frac{\partial \mathbf{R}}{\partial \mathbf{Q}} \frac{d\mathbf{Q}^*}{d\beta_k} + \frac{\partial \mathbf{R}}{\partial \mathbf{X}} \frac{d\mathbf{X}}{d\beta_k} + \frac{\partial \mathbf{R}}{\partial \beta_k} = 0 \quad (3.128)$$

This can then be rearranged and solved for  $\frac{d\mathbf{Q}^*}{d\beta_k}$ . Terms in equation (3.139) are again relatively simple to obtain,  $\frac{\partial \mathbf{R}}{\partial \mathbf{Q}}$  is the residual Jacobian, identical to what is found in the flow solver.

For the solution of equation (3.139) a linear system must be solved once for each design variable. Depending on the complexity of the residual Jacobian, this may be quite expensive and thus not offer any benefit as compared to the finite difference approach. Additionally the computational requirement still scales with  $ndv$  and therefore is not suitable for optimisation problems with many variables.

### 3.5.2.2 Adjoint Method

The adjoint approach circumvents having to calculate  $\frac{d\mathbf{Q}^*}{d\beta_k}$  by adding the differentiated residual equation (3.139) to the aerodynamic function (3.137) with the help of a Lagrange multiplier known as the adjoint vector  $\lambda$ . This gives

$$\frac{dF}{d\beta_k} = \left( \frac{\partial F}{\partial \mathbf{Q}} \right)^t \frac{d\mathbf{Q}^*}{d\beta_k} + \left( \frac{\partial F}{\partial \mathbf{X}} \right)^t \frac{d\mathbf{X}}{d\beta_k} + \frac{\partial F}{\partial \beta_k} + \lambda^t \left( \frac{\partial \mathbf{R}}{\partial \mathbf{Q}} \frac{d\mathbf{Q}^*}{d\beta_k} + \frac{\partial \mathbf{R}}{\partial \mathbf{X}} \frac{d\mathbf{X}}{d\beta_k} + \frac{\partial \mathbf{R}}{\partial \beta_k} \right) \quad (3.129)$$

which can then be rearranged to give

$$\frac{dF}{d\beta_k} = \left[ \left( \frac{\partial F}{\partial \mathbf{Q}} \right)^t + \lambda^t \frac{\partial \mathbf{R}}{\partial \mathbf{Q}} \right] \frac{d\mathbf{Q}^*}{d\beta_k} + \left[ \left( \frac{\partial F}{\partial \mathbf{X}} \right)^t + \lambda^t \frac{\partial \mathbf{R}}{\partial \mathbf{X}} \right] \frac{d\mathbf{X}}{d\beta_k} + \frac{\partial F}{\partial \beta_k} + \lambda^t \frac{\partial \mathbf{R}}{\partial \beta_k} \quad (3.130)$$

As the adjoint vector is as yet undefined, we can eliminate the term including  $\frac{d\mathbf{Q}^*}{d\beta_k}$  which is difficult to calculate by setting the multiplying bracket to zero. This yields the adjoint equation

$$\begin{aligned} \left[ \left( \frac{\partial F}{\partial \mathbf{Q}} \right)^t + \lambda^t \frac{\partial \mathbf{R}}{\partial \mathbf{Q}} \right] &= 0 \\ \text{or } \left( \frac{\partial \mathbf{R}}{\partial \mathbf{Q}} \right)^t \lambda &= - \frac{\partial F}{\partial \mathbf{Q}} \end{aligned} \quad (3.131)$$

which is solved once only for the adjoint vector  $\lambda$ . The sensitivity derivatives can then be calculated

$$\frac{dF}{d\beta_k} = \left[ \left( \frac{\partial F}{\partial \mathbf{X}} \right)^t + \lambda^t \frac{\partial \mathbf{R}}{\partial \mathbf{X}} \right] \frac{d\mathbf{X}}{d\beta_k} + \frac{\partial F}{\partial \beta_k} + \lambda^t \frac{\partial \mathbf{R}}{\partial \beta_k} \quad (3.132)$$

For a pure aerodynamic shape optimisation, i.e. the design variables affect only the shape of the vehicle through grid sensitivities and not the boundary conditions, the last two terms become zero. Better reflecting how the objective sensitivity is calculated in ADJ-MERLIN, Equation (3.143) then

becomes

$$\frac{dF}{d\beta_k} = \left( \frac{\partial F}{\partial \mathbf{X}} \right)^t \frac{d\mathbf{X}}{d\beta_k} + \boldsymbol{\lambda}^t \frac{\partial \mathbf{R}}{\partial \mathbf{X}} \frac{d\mathbf{X}}{d\beta_k} \quad (3.133)$$

The adjoint equation (3.142) is solved iteratively in the same manner as the flow equations with the implicit solver. The following iterative procedure is employed which contains a fictitious time term  $1/\Delta t$

$$\left[ \frac{1}{\Delta t} \frac{\partial \mathbf{Q}}{\partial \mathbf{P}} + \frac{\partial \tilde{\mathbf{R}}(\mathbf{Q}^*)}{\partial \mathbf{P}} \right]^t {}^n \Delta \boldsymbol{\lambda} = - \left\{ \frac{\partial F}{\partial \mathbf{P}} + \left[ \frac{\partial \mathbf{R}(\mathbf{Q}^*)}{\partial \mathbf{P}} \right]^t \boldsymbol{\lambda}^n \right\} \quad (3.134)$$

which is solved for  ${}^n \Delta \boldsymbol{\lambda}$  using the same BILU procedure as in the flow solver and then the adjoint vector is updated at the next iteration according to

$$\boldsymbol{\lambda}^{n+1} = \boldsymbol{\lambda}^n + {}^n \Delta \boldsymbol{\lambda} \quad (3.135)$$

In equation (3.145), as with the flow solver, approximations are made in the LHS residual Jacobian denoted by the ‘~’ symbol. The residual Jacobian on the RHS must be exact as in the limit of a converged solution, this term does not approach zero.

In order to save computational time, the terms  $\frac{\partial \tilde{\mathbf{R}}(\mathbf{Q}^*)}{\partial \mathbf{P}}$  and  $\frac{\partial F}{\partial \mathbf{P}}$  are only computed once and stored in memory. The exact RHS Jacobian is not stored but multiplied term by term with the adjoint vector after each iteration. This saves memory as the exact higher order Jacobian is quite large.

$$\frac{\partial \mathbf{R}}{\partial \mathbf{X}} \frac{\partial \mathbf{X}}{\partial \beta_k} = \frac{\partial \mathbf{R}}{\partial (\boldsymbol{\xi}, \boldsymbol{\eta}, \boldsymbol{\zeta})} \frac{\partial (\boldsymbol{\xi}, \boldsymbol{\eta}, \boldsymbol{\zeta})}{\partial \mathbf{X}} \frac{\partial \mathbf{X}}{\partial \beta_k} \quad (3.136)$$

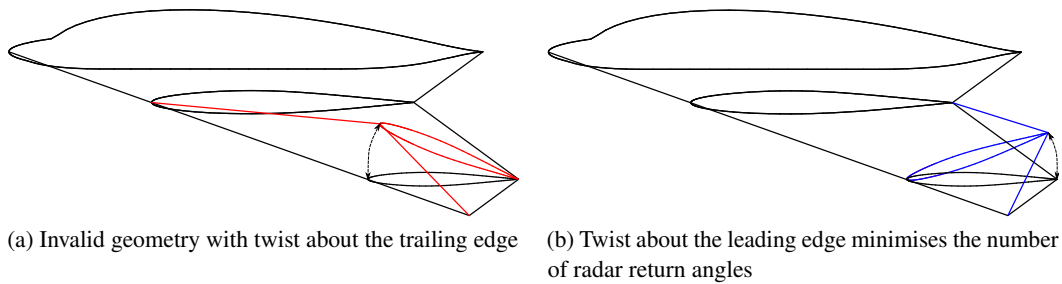


Figure 3.16: Twist applied at the second crank

### 3.6 Geometry Parametrisation

This section describes the geometry parameterisation used in this work as well as describing how the grid sensitivities are calculated for integration with the adjoint solver. Care has been taken to develop methods currently in the literature for use on this problem which has some special requirements.

Ensuring the wing remains low observable requires that both the leading and trailing edge remain straight between cranks in order to minimise the number of angles from which radar will be reflected. This is also an important requirement for control integration as the hinge line needs to remain straight. This dictates that for a Lambda wing UCAV, two twist variables are permitted with master sections located at each of the trailing edge crank  $y$  positions. The leading edge is kept straight by making it the origin for wing twists (see Figure 3.16). In order to gain improved control over wing loads, we require arbitrary aerofoil sections to be defined at many more stations along the wing so in this parameterisation scheme, the aerofoil master sections have been made independent of the twist sections. This allows for aerodynamic twist along the span through camber change between the geometric twist sections.

#### 3.6.1 Aerofoil Parameterisation

The aerofoil geometry is modified by increments to the original shape. This ensures that the scheme is simple to differentiate for integration into the adjoint solver. Changes are made to the original shape by adding basis function curves  $f(x)$  multiplied by weighting factors  $\beta$  which become the design variables. After an increment of one design variable, the new shape becomes

$$y_1 = y_0 + f(x)\Delta\beta \quad (3.137)$$

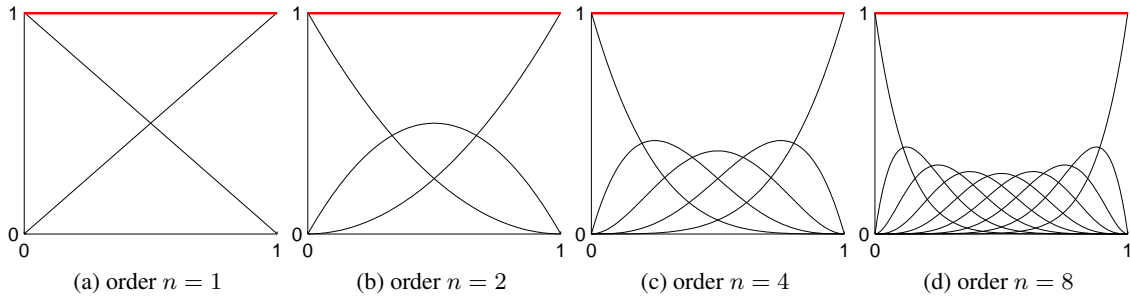
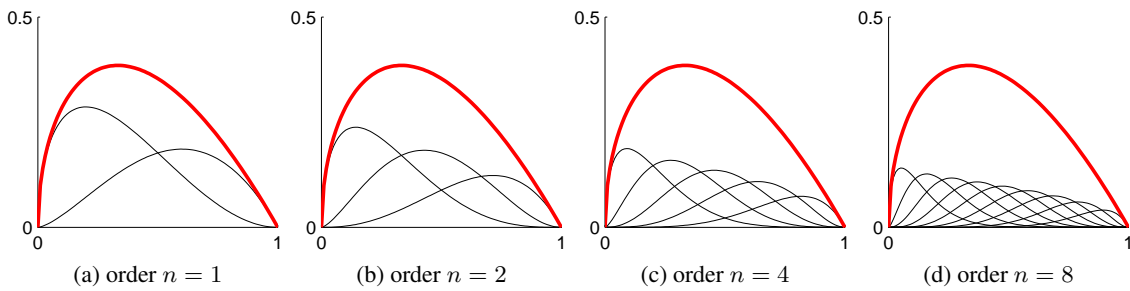
The grid sensitivity for this is simply

$$\frac{\partial y}{\partial \beta} = f(x) \quad (3.138)$$

##### 3.6.1.1 Bernstein Polynomial Basis Functions

The basis function curves used are Bernstein polynomials. These functions are popular choices for aerofoil design as their implementation is simple and they ensure that smooth geometries are




 Figure 3.17: Bernstein polynomial basis functions  $S_{r,n}$  with different values of  $n$ 

 Figure 3.18: Basis functions with class shape transformation  $CS_{r,n}$ 

always obtained. A set of curves of order  $n$  giving  $n + 1$  curves labeled  $r = 0, n$  is described by

$$S_{r,n}(x) = K_{r,n}x^r(1-x)^{n-r} \quad (3.139)$$

where

$$K_{r,n} = \frac{n!}{r!(n-r)!} \quad (3.140)$$

The increment to the aerofoil surface  $\Delta y$  is calculated by summing all the weighted basis function curves and adding to the original shape.

$$\Delta y = \sum_{r=0}^n S_{r,n} \Delta \beta_{n+1} \quad (3.141)$$

The basis function curves  $S_{r,n}(x)$  are shown graphically in Figure 3.17. At  $x = 0$ , the 1<sup>st</sup> design variable has complete control over the geometry because all the other curves go to zero. Similarly at the trailing edge the last variable controls the shape. The other design variables influence the shape for the whole aerofoil but have the greatest influence at a particular chord wise position. This ensures that the aerofoil geometry will always be smooth. It is worth noting that at any position, the total sum of all the basis function curves is 1.

The above basis functions can be directly used to control the aerofoil camberline by applying the same displacements to the upper and lower surfaces.

For full aerofoil design, the leading and trailing edge points must remain fixed at  $y = 0$  so gaps do

not open up in the geometry. Using the above method, this means that  $\beta_1$  and  $\beta_{n+1}$  have to remain zero. This approach gives relatively poor control over the leading edge shape which is crucial for both transonic and high lift design. One technique for improving this is to cluster the control points near the leading and/or trailing edge. For example leading edge clustering can be achieved by substituting  $\sqrt{x}$  for  $x$  in the above equations but this only partially alleviates the problem because the influence of these functions still tends to zero at the leading edge and hence the curvature is not particularly well controlled.

### 3.6.1.2 Class Shape Transformation (CST)

An extension to the above method is the use of class functions introduced by Kulfan [84]. This method has successfully been used for several optimisation problems including [85, 86]. The class functions denoted  $C$  are implemented simply by multiplying them with the weighted basis function curves in the parametrisation scheme. These functions could potentially take any form although for subsonic aerofoil design a simple function which ensures a blunt leading edge and sharp trailing edge is sufficient.

$$C(N1, N2) = x^{N1}(1-x)^{N2} \quad (3.142)$$

which for  $N1 = 0.5$  and  $N2 = 1$  gives

$$C = \sqrt{x}(1-x) \quad (3.143)$$

This transformation is shown graphically in Figure 3.18 and as shown, ensures  $y = 0$  at  $x = 0$  and  $x = 1$ . Other values for  $N1$  and  $N2$  could be used for example a supersonic aerofoil with sharp leading and trailing edges could use  $N1 = 1$  and  $N2 = 1$  or a rounded shape is obtained with  $N1 = 0.5$  and  $N2 = 0.5$ . The total aerofoil shape perturbation would be

$$\Delta y = C \sum_{r=0}^n S_{r,n} \Delta \beta_{r+1} \quad (3.144)$$

One advantage of this method is now the leading edge radius and trailing edge included angle is directly controlled by the first and last weighting factors  $\beta_1$  and  $\beta_{n+1}$  such that

$$\frac{r_{le}}{c} = \frac{\beta_0^2}{2} \quad (3.145)$$

and

$$\tan(\gamma_{te}) = \beta_{n+1} \quad (3.146)$$

This method can easily be extended to represent the entire wing as described in Kulfan's paper but this would not be appropriate for the UCAV design problem as it does not automatically ensure straight leading and trailing edges.

### 3.6.2 Aerofoil perturbation with constant area

A desirable property for the parametrisation scheme is the ability to modify the geometry without changing the cross sectional area of the wing. This ensures that internal volume and structural requirements can be met without the need for additional optimiser constraints. For any shape

modification  $y_1 = y_0 + \Delta y$ , the new aerofoil surface  $y_2$  is calculated which has been scaled to have the same area as the original aerofoil.

$$y_2 = y_1 \frac{A_0}{A_0 + \Delta A} \quad (3.147)$$

where the original area is given by

$$A_0 = \int_0^1 y_0 dx \quad (3.148)$$

Therefore the change in area is

$$\Delta A = \Delta \beta \int_0^1 f(x) dx \quad (3.149)$$

The change in area w.r.t the design variables (used for calculating the sensitivity) is

$$\frac{\partial \Delta A}{\partial \beta} = \int_0^1 f(x) dx \quad (3.150)$$

Substituting  $y_1$  into  $y_2$  and using the product and quotient rules to differentiate gives

$$\frac{\partial y_2}{\partial \beta} = \frac{A_0}{A_0 + \Delta A} \frac{\partial y_1}{\partial \beta} + y_1 \frac{\partial}{\partial \beta} \left( \frac{A_0}{A_0 + \Delta A} \right) \quad (3.151)$$

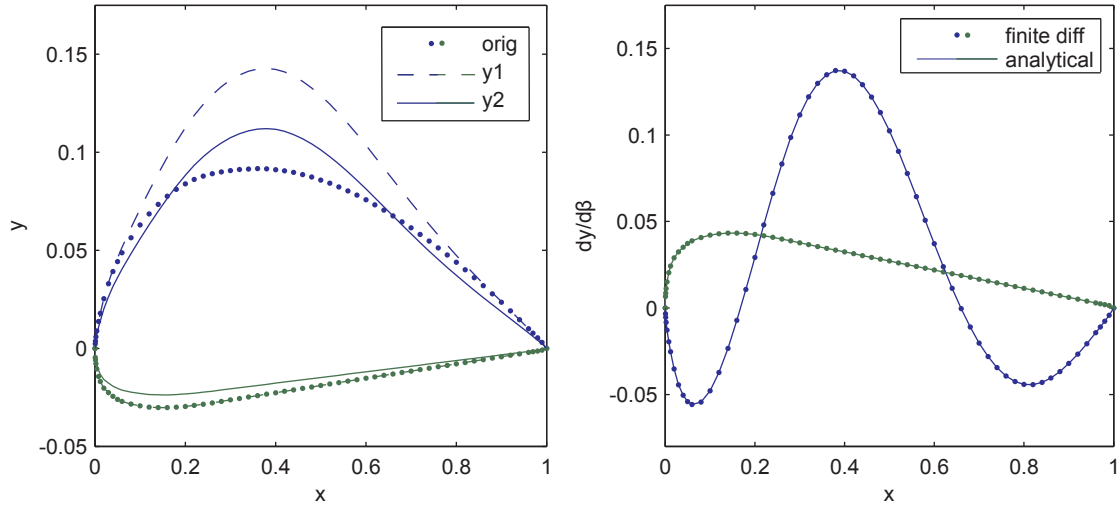
$$= \frac{A_0}{A_0 + \Delta A} \frac{\partial y_1}{\partial \beta} + y_1 \frac{-(A_0) \left( \frac{\partial}{\partial \beta} \Delta A \right)}{(A_0 + \Delta A)^2} \quad (3.152)$$

$$= \frac{A_0}{A_0 + \Delta A} \frac{\partial y_1}{\partial \beta} - \frac{A_0 y_1}{(A_0 + \Delta A)^2} \int_0^1 f(x) dx \quad (3.153)$$

removing terms in which  $\Delta A \rightarrow 0$  and simplifying

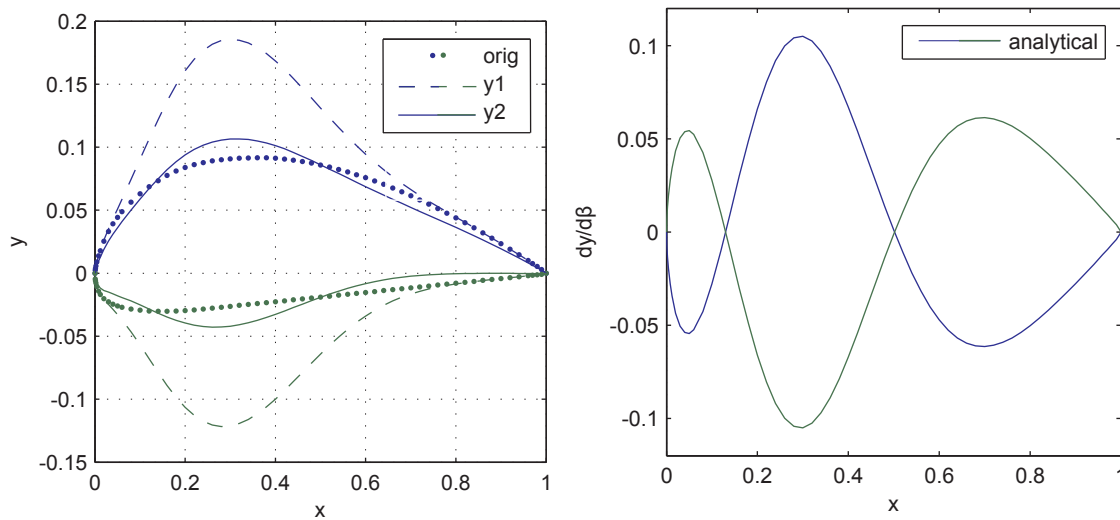
$$\frac{\partial y_2}{\partial \beta} \approx \underbrace{\frac{\partial y_1}{\partial \beta}}_{\text{original sensitivity}} - \frac{y_1}{A_0} \underbrace{\int_0^1 f(x) dx}_{\text{area under basis function curve}} \quad (3.154)$$

Figures 3.19,3.20 show examples of aerofoil modifications (a) using Bernstein polynomial basis functions with the class shape transformation and with the thickness scaled along with the corresponding grid sensitivities (b). In (a), the dotted line is the original Clark Y aerofoil, the dashed line shows a modification made using the  $3^{rd}$  of 8 design variables and solid line has been scaled so it has the same cross sectional area as the original. In (b) the grid sensitivities are shown calculated analytically (solid) and with a finite difference of  $\Delta \beta = 10^{-6}$  (dots). The two give the same results providing verification for Equation (3.154). Figure 3.19 is a modification to the upper surface. As shown, an increase in area by the design variable causes the lower surface to be scaled back to become smaller. Figure 3.20 shows a modification to the thickness distribution. This is done by first extracting the thickness distribution  $t(x) = y_u - y_l$  and camber line  $y_c(x) = (y_u + y_l)/2$  and applying the parametrisation to the thickness distribution. The modified thickness is then added back to the mean camber line. This method for controlling the thickness is combined with camber line deformation to give full control over the aerofoil shape.



(a) Aerofoil modification with 3<sup>rd</sup> upper surface variable      (b) Geometry sensitivity for 3<sup>rd</sup> upper surface variable

Figure 3.19: Example upper/lower surface movement for a Clark Y aerofoil with 8 design variables



(a) Thickness modification with 3<sup>rd</sup> variable      (b) Geometry sensitivity for 3<sup>rd</sup> variable

Figure 3.20: Example thickness distribution modification for a Clark Y aerofoil with 6 design variables

### 3.6.3 Wing Parametrisation

The three dimensional wing shape is controlled by applying the above aerofoil, camberline and thickness perturbations or wing twists at selected ‘master sections’ up the wing. Between master sections and specified spanwise extents for each variable, the grid point displacements are determined using linear interpolation in the spanwise ( $z$ ) coordinate. Due to the limited number of permitted twist sections, camber or aerofoil sections are defined independently and at more sections so there is improved control over the local loadings without invalidating platform constraints.

#### 3.6.3.1 Camber, Aerofoil or Thickness

The above techniques for 2D aerofoil parametrisation are applied to the 3D wing using the following technique. At the ( $z$ ) position where displacements are to be applied, the aerofoil surface points are extracted through interpolation along  $k$  direction grid lines. The section is then translated, rotated and normalised in the  $x,y$  plane so the leading and trailing edges fall at  $x = 0, y = 0$  and  $x = 0, y = 1$  respectively.  $\theta_{inc}$  is the local twist angle.

$$\begin{pmatrix} x' \\ y' \end{pmatrix} = \frac{1}{c} \begin{pmatrix} \cos\theta_{inc} & \sin\theta_{inc} \\ -\sin\theta_{inc} & \cos\theta_{inc} \end{pmatrix} \begin{pmatrix} x - x_{le} \\ y - y_{le} \end{pmatrix} \quad (3.155)$$

The shape perturbations and grid sensitivities are calculated for the 2D aerofoil as described above. Reverse transformations are then applied to the  $x$  and  $y$  coordinates and the grid sensitivities to put the aerofoil back to the original position.

$$\begin{pmatrix} x \\ y \end{pmatrix} = \begin{pmatrix} x_{le} \\ y_{le} \end{pmatrix} + c \begin{pmatrix} \cos\theta_{inc} & -\sin\theta_{inc} \\ \sin\theta_{inc} & \cos\theta_{inc} \end{pmatrix} \begin{pmatrix} x' \\ y' \end{pmatrix} \quad (3.156)$$

$$\begin{pmatrix} \partial x / \partial \beta \\ \partial y / \partial \beta \end{pmatrix} = \begin{pmatrix} \sin\theta_{inc} \\ \cos\theta_{inc} \end{pmatrix} \frac{\partial y}{\partial \beta} \quad (3.157)$$

#### 3.6.3.2 Twist

Twist is applied to a section about the point  $x_0, y_0$  with

$$\begin{pmatrix} \Delta x \\ \Delta y \end{pmatrix} = \begin{pmatrix} \cos\Delta\theta & \sin\Delta\theta \\ -\sin\Delta\theta & \cos\Delta\theta \end{pmatrix} \begin{pmatrix} x - x_0 \\ y - y_0 \end{pmatrix} + \begin{pmatrix} x_0 \\ y_0 \end{pmatrix} \quad (3.158)$$

for the UCAV optimisation, the origin for twists is the leading edge of that particular section. The grid sensitivities for twist are calculated by

$$\begin{pmatrix} \partial x / \partial \theta \\ \partial y / \partial \theta \end{pmatrix} = \begin{pmatrix} y - y_0 \\ x - x_0 \end{pmatrix} \quad (3.159)$$

#### 3.6.3.3 Interpolation

Once the displacements and sensitivities for the section of interest have been calculated, displacements between this section and the inboard and outboard sections are calculated according to the

non-dimensional distance in the  $z$  direction. Subscript  $i$  denotes the grid point where the displacement is calculated and  $j$  is for the master sections. For displacements ( $\Delta x, \Delta y$ ) or sensitivities ( $\partial x/\partial \beta, \partial y/\partial \beta$ ), inboard or outboard respectively, the variable of interest denoted  $\phi$  is

$$\phi_i = \phi_j \frac{z_i - z_{j-1}}{z_j - z_{j-1}} \quad \text{or} \quad \phi_i = \phi_j = \frac{z_i - z_j}{z_{j+1} - z_j} \quad (3.160)$$

If there are no sections defined inboard or outboard i.e. it is the first or last section, the root or tip are used respectively.

### 3.6.4 Volume grid

Once the displacements or sensitivities at the surface are known, the variables are calculated in the volume grid in the following manner. An arc length is defined which is the non dimensional distance along a grid line starting at the surface  $j = 1$  to the cell of interest at  $j$ .

$$A(j) = \frac{\sum_{l=2}^j L_l}{\sum_{l=2}^{j_n} L_l} \quad (3.161)$$

where

$$L_l = \sqrt{(x_l - x_{l-1})^2 + (y_l - y_{l-1})^2 + (z_l - z_{l-1})^2} \quad (3.162)$$

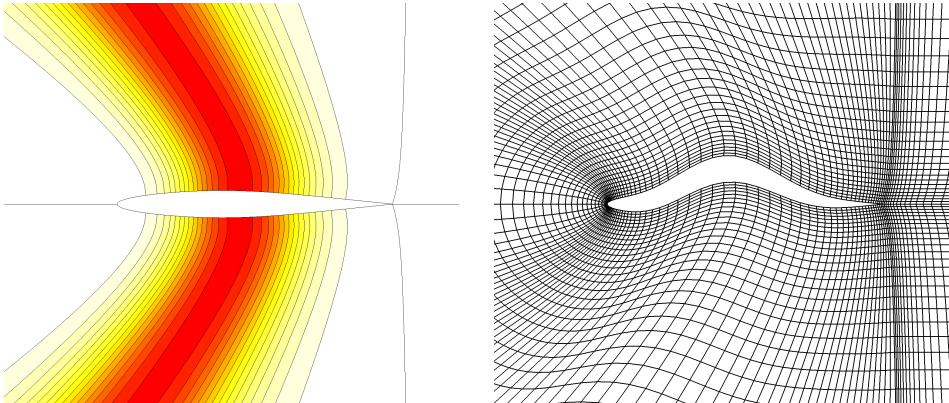
The variable of interest  $\phi$  is then calculated

$$\phi_j = (1 - A(j))\phi_{surface} \quad (3.163)$$

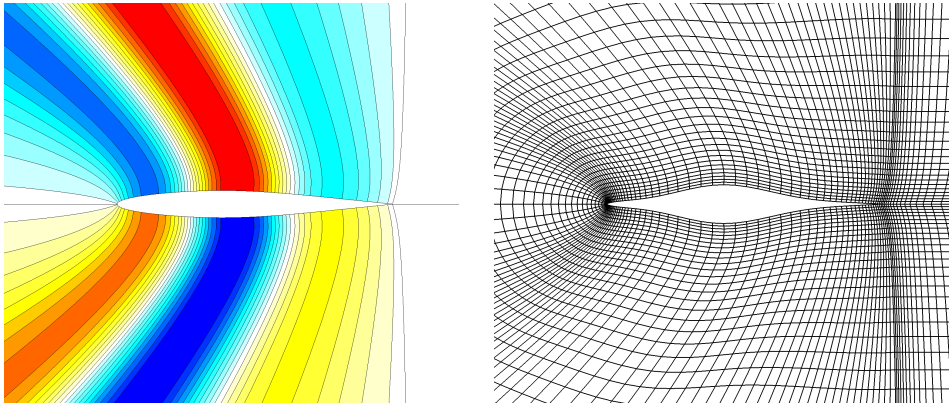
This formula is first applied to cells in the wake plane and then to all of the volume cells. Example volume grid sensitivities and displacements are shown in Figure 3.21

### 3.6.5 Angle of Incidence

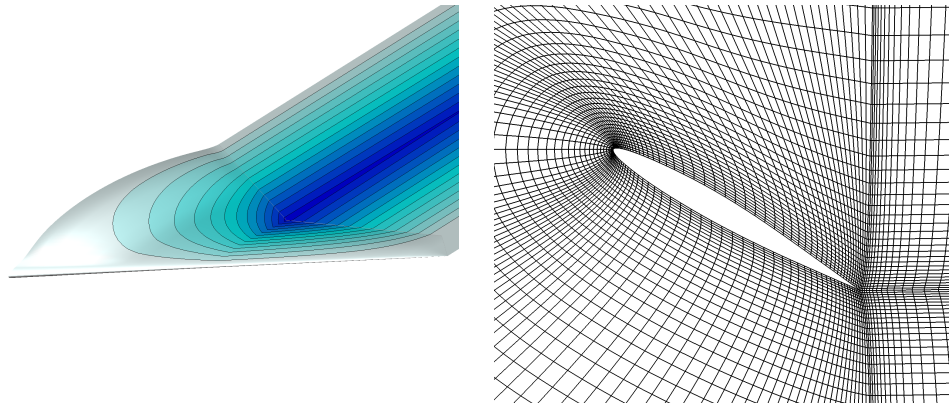
Wing twists are applied at various sections along the wing but the root incidence is controlled using the overall incidence angle. This is implemented by rotating the whole grid about the origin (0,0,0) in the  $x, y$  plane. This has benefits over modifying the root incidence because it minimises the relative movement of volume grid cells and hence helps preserve the mesh quality. It also has the benefit that there is a single variable that predominantly controls the lift. The expression used to update the incidence angle is the same as Equation (3.158) with the corresponding sensitivity calculated with Equation (3.159) where  $x_0 = 0, y_0 = 0$ . This is applied to all the cells in the domain and the moment reference point.



(a) Camber line increment 5<sup>th</sup> of 10 variables



(b) Thickness deformation 5<sup>th</sup> of 10 variables



(c) Twist applied at 1st crank location

Figure 3.21: Volume grid *y* sensitivity (red +*tive* blue -*tive*) and corresponding grid movement





## Chapter 4

# Aerodynamic Investigations

---

The flow physics of the 1303 UCAV concept have been investigated numerically using the MERLIN flow solver as well as the commercial flow solver Cobalt for further investigation into the lateral characteristics. Comparisons of the total forces, surface pressures and skin friction patterns are made with results from the QinetiQ 5m wind tunnel and ARA TWT tests.

The 1303 UCAV has several features which make it challenging to model accurately using CFD. Although not a particularly complex shape, large spanwise chord variations mean that mesh clustering is important to capture details of the flow near the leading edge, especially towards the wingtip. The sweep angle of  $\Lambda = 47^\circ$  combined with the blunt nosed aerofoil sections means that smooth surface separations and vortical flows are present making it challenging to obtain a mesh independent solution as well as being challenging for turbulence modelling. For the purposes of assessing wing designs, we are generally less interested in the post stall flowfield but concerned with predicting the onset of these flow separations accurately.

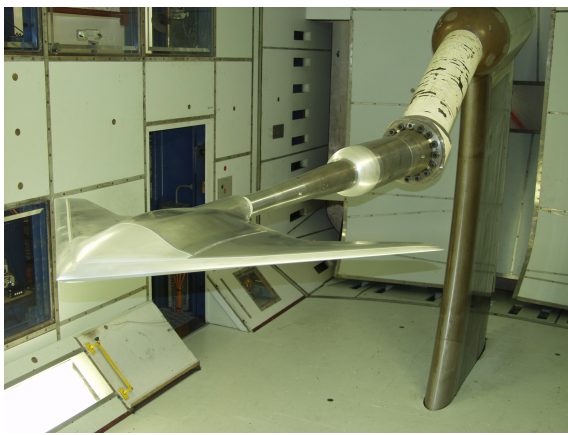
### 4.1 Geometry

The basic geometry, shown in Figure 4.1, was supplied in CAD format for the vehicle outer mould line shape. This does not include features such as an intake or control surfaces but it does have a small gap at the rear for the engine exhaust.

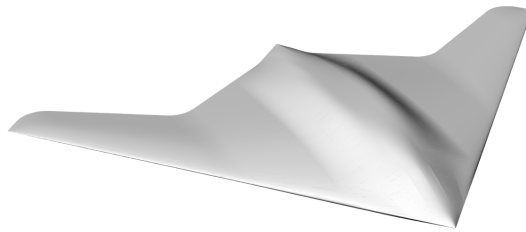
The basic planform shape has a leading edge sweep of  $\Lambda = 47^\circ$  and trailing edge sweeps of  $\Lambda = -30^\circ$  (root),  $+30^\circ$  and  $-47^\circ$  (tip). The crank locations are located at  $\eta = 0.46$  and  $\eta = 0.90$  but the trailing edge has been rounded off smoothing the chord distribution for continuous mouldline controls. The wing is comprised of a NACA 64A-0012 at the root, reducing in thickness linearly to a NACA 64A-008 aerofoil at the first crank which is continued for the rest of the wing. These are symmetrical aerofoils of 12% and 8% thickness respectively and have their position of maximum thickness located at 40% chord. They also include the A modification which increases thickness towards the trailing edge. The wing has been modified near the root with additional thickness, to give a fuselage. The leading edge is also modified at the root to be sharp. Spanwise distributions of leading edge radius, chord, thickness and position of maximum thickness are given in figure 4.2 which shows the leading edge radius reducing to zero at the root. We can also see that the body is 14% thick at the centre and the position of maximum thickness is located at approximately

Reference Area	$0.602149m^2$
Longitudinal ref length $\bar{c}$	$0.53975m$
Lateral ref length $b$	$1.5240m$
Aspect ratio $AR$	$3.857$
Moment reference point $x$	$0.45885m$
Moment reference point $y$	$-0.023m$

Table 4.1: 1303 wind tunnel model (1:10.8 scale) reference values



(a) QinetiQ Wind Tunnel Model



(b) CAD Geometry

Figure 4.1: 1303 Geometry

$x/c = 0.45$ ,  $5\%c$  behind that of the aerofoil sections which should slightly improve the transonic performance.

In the QinetiQ wind tunnel test, the model had interchangeable leading edges. Three leading edge geometries were tested, one rounded, one sharp and a baseline leading edge. The baseline leading edge is rounded for most of the span but sharp at the root, similar to that of other stealth aircraft e.g. B2. This investigation is limited to the baseline leading edge. The wind tunnel model also has a sting fairing at the rear, attached to the wing. In the initial computational studies, the sting was ignored because only the aerodynamics of the vehicle itself were of interest. It was previously unclear exactly what effect this has on the forces and moments but this is investigated here using the overset feature in Cobalt flow solver. Figure 4.3 shows the position of the pressure tappings used in the wind tunnel test. They are arranged in 7 streamwise rows at  $\eta = 0.3, 0.4, 0.5, 0.6, 0.7, 0.8$  and  $0.9$ . They are mostly located on the upper surface leading edge but there is one complete row located at  $\eta = 0.6$ . There are also a few pressure taps located on the lower surface near to the stagnation point. The reference values for the wind tunnel model are summarised in table 4.1.

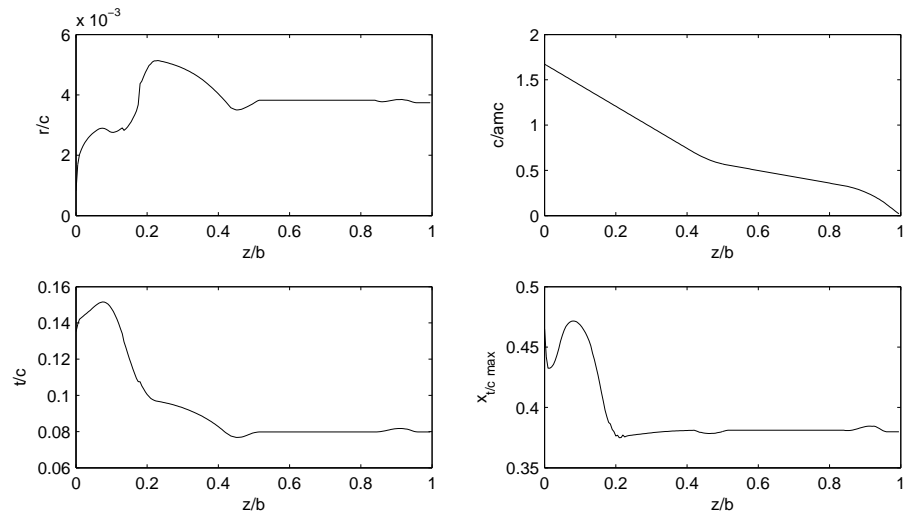


Figure 4.2: Various geometrical parameters for the 1303 UCAV

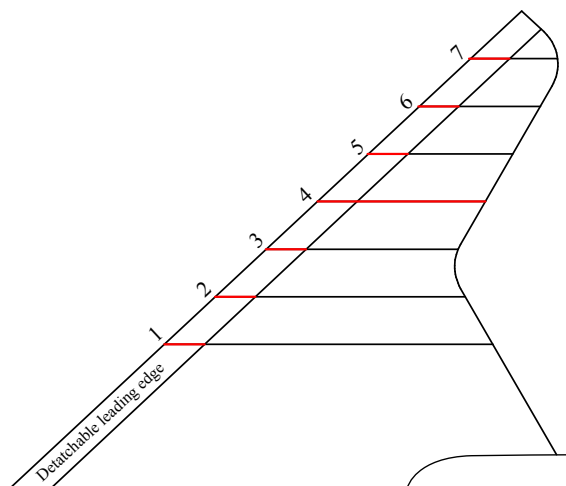


Figure 4.3: Pressure tap locations

$M_\infty$	$Re_{\infty M.A.C}$	$T_{static}(K)$	$\alpha(^{\circ})$
0.25	$5.6 \times 10^6$	294.5	$-2 \leq \alpha \leq 25$
0.8	$7.1 \times 10^6$	294.5	$0 \leq \alpha \leq 7.6$

Table 4.2: 1303 Flow conditions

## 4.2 CFD Procedure

### 4.2.1 Flow conditions

The freestream conditions for the low speed CFD calculations were set to match the QinetiQ wind tunnel experiment run 17. This was chosen as this test was the subject of a number of TTCP test cases and therefore there are several other CFD investigations for comparison. The Mach number for this test was  $M_\infty = 0.25$  which is close to the take-off/landing Mach number of a full scale vehicle. Some runs were also completed at tranonic cruise conditions ( $M_\infty = 0.8$ ) to match the ARA TWT test. The freestream conditions are summarised in Table 4.2.

### 4.2.2 Mesh

A structured multiblock mesh (shown in figure 4.4) was generated using GRIDGEN. The mesh is a C-H topology, C in the  $x - y$  plane. This gives a high quality hexahedral mesh with low skewness. For the exhaust gap at the back of the body an extra block was added which has a pole singularity down one edge. At the wingtip the mesh also reduces to a pole singularity and the grid lines run out in the spanwise direction to the boundary. The polar wingtip mesh caused problems for GRIDGEN due to undefined surface normal directions in cells at the wingtip resulting in skewed or negative volume elements. To resolve this, a Fortran program was used to check and repair problems due to grid lines crossing. In contrast to unstructured meshes, this mesh topology ensures that the geometry and flowfield are well resolved in the streamwise direction right up to the wingtip.

A 1<sup>st</sup> cell height of  $\Delta y = 5 \times 10^{-6}$  was used which gave a  $y^+$  of approximately 1 for the QinetiQ tunnel Reynolds number and slightly higher for the ARA test conditions. The initial mesh size was  $100 \times 100$  elements on the upper and lower surfaces of the wing and a growth rate of 1.25 gave a mesh size of approximately 2 million cells. To resolve the leading edge, the tangential mesh spacing is  $5 \times 10^{-4} c_{local}$  at the leading edge. The spanwise mesh spacing at the wingtip is  $2b \times 10^{-3}$ .

A mesh sensitivity study was conducted by checking the sensitivity of the total forces to chordwise refinement in the leading edge region as well as spanwise refinement. For the chordwise refinement, the number of mesh points for the first 25% of the chord (thought to be the most important region) was doubled. The spanwise refinement involved increasing the spanwise number of elements by a factor of 1.5 but clustering the points more towards the wingtip. This resulted in approximately double the spanwise resolution near the tip with little change at the root. An incidence angle of  $8.77^{\circ}$  was used as here there is a moderate flow separation present and this is approximately where pitch up occurs. The results of the study are presented in table 4.3. The results show that there was only a small change in the computed forces  $O(2\%)$  for lift and drag. A higher change of 5.34% was detected in the pitching moment with spanwise mesh refinement however this actually amounts to an extremely small change in the pitching moment as it is close to zero at this point. The 2 million cell baseline mesh is therefore regarded to be appropriate and affordable for this study. This

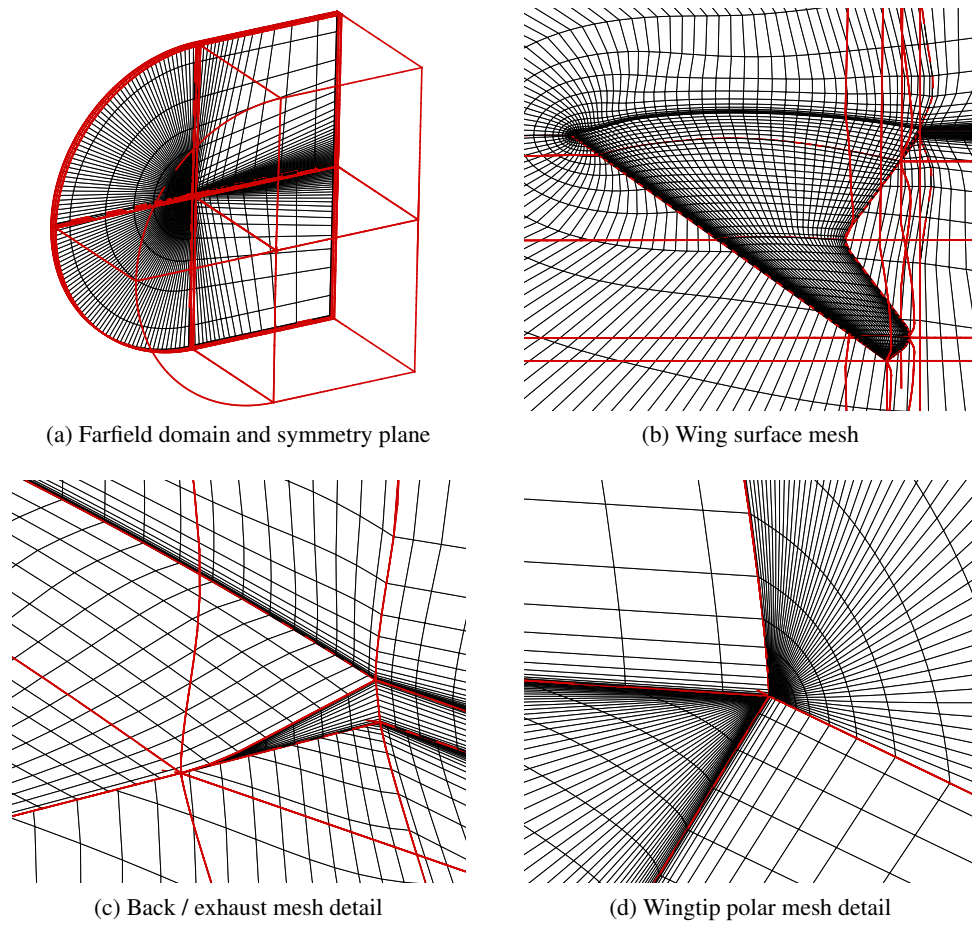
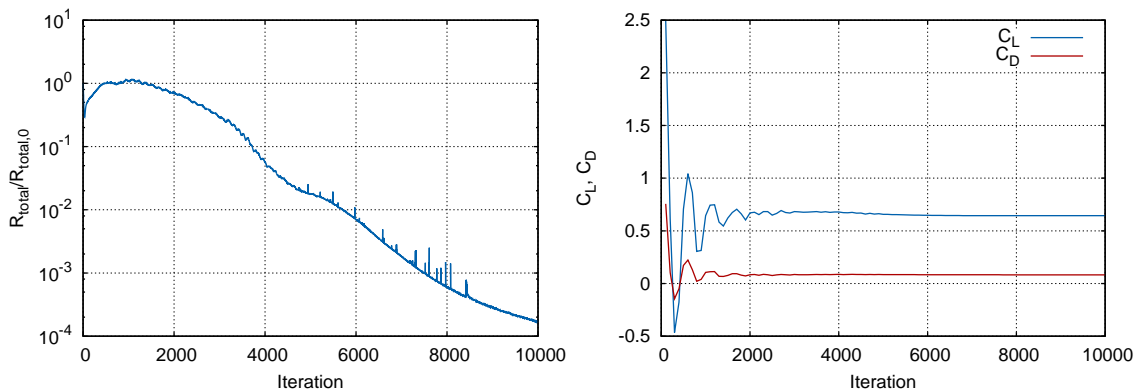


Figure 4.4: 1303 multiblock mesh. Red lines indicate block boundaries, every 2<sup>nd</sup> grid line shown.

Refinement	$C_L$	change	$C_D$	change	$C_M$	change
None	0.487		0.0401		-0.00670	
Chordwise	0.488	0.18%	0.0410	2.3%	-0.00677	1.08%
Spanwise	0.488	0.29%	0.0401	-0.16%	-0.00705	5.34%

Table 4.3: Mesh Refinement Results



(a) Residual convergence

(b) Lift and drag convergence

Figure 4.5: MERLIN convergence for 1303 UCAV at  $M = 0.25$ ,  $\alpha = 11.9^\circ$ 

does not guarantee mesh independence for all incidence angles but demonstrates that the current mesh should be sufficient to obtain meaningful results up until pitch up occurs.

### 4.2.3 Convergence

The calculations were run for 10,000 iterations with the CFL number starting at 1 and increasing as the residual reduces to 10. The residual reduced approximately 4 orders of magnitude (Figure 4.5) and the forces and moments converged to steady values. Some of the calculations may not have required this many iterations for convergence but were run to completion regardless.

## 4.3 Longitudinal Results

The change in forces and moments and analysis of flow separation are discussed with respect to the incidence angle.

### 4.3.1 Total Forces

The general trends in the RANS results compare well with the QinetiQ experimental data. The lift curve in Figure 4.6(a) follows the experimental data closely for angles of incidence below  $10^\circ$  although at a slightly lower lift. It is unclear exactly what the reason is for this although the wind tunnel test report [36] suggests there is a slight uncertainty as to the accuracy of the

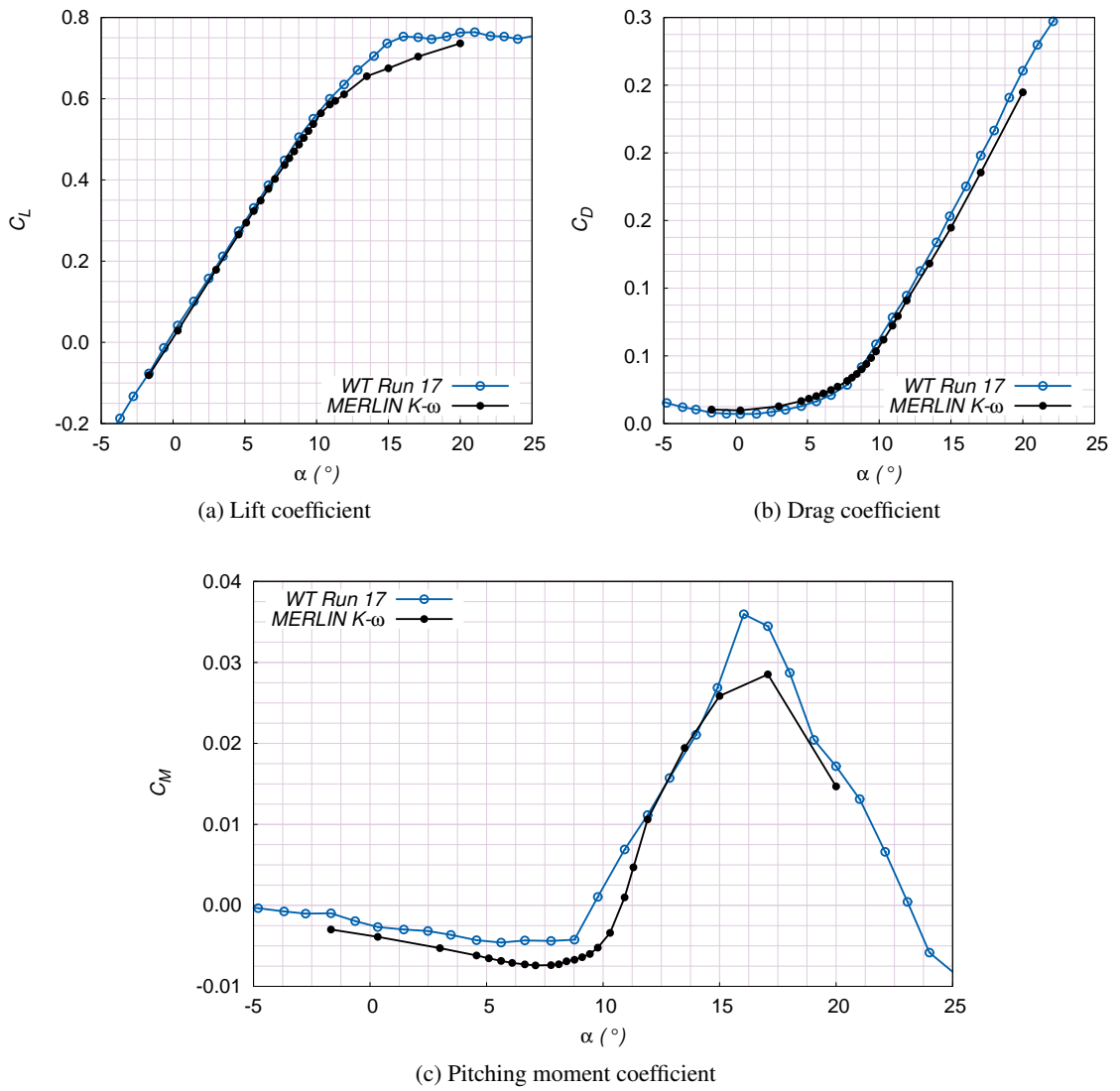
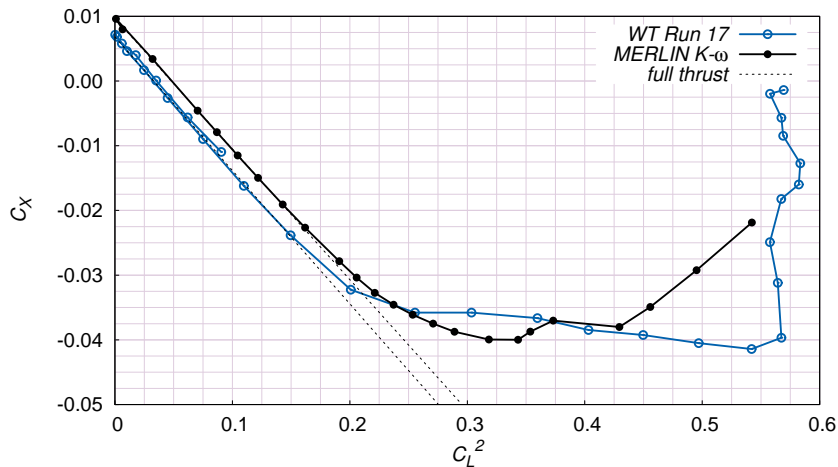


Figure 4.6: Mach 0.25 total forces

Figure 4.7: Axial force vs  $C_L^2$ 

absolute incidence measurement. For angles above  $10^\circ$  both the experimental and RANS curves show a reduction in the lift curve slope although the RANS results predict that this will be more severe. This could be due to the dissipative nature of the RANS method or inadequate turbulence modelling for prediction of vortical flows. The drag curve in Figure 4.6(b) shows that the RANS result matches the experimental curve reasonably well although at small angles of incidence the drag is substantially over predicted by 27%. Not modeling the sting may partially account for this discrepancy as well as an extent of laminar flow being present at low incidences. These issues are further discussed in a subsequent section. As the incidence is increased and separated flow regions become more prominent, the drag force becomes under predicted. As with the lift, this could be due to under prediction of the vortex strength or influence.

The pitching moment curve matches the experimental trends very well. At low incidence, when the flow is attached, there is an offset with  $C_M$  being over predicted. The low incidence  $C_M$  slope is also over predicted but the prediction seems to be better than many other CFD results discussed previously. Lawson and Barakos [87] suggested that the pitching moment agreement could be improved by moving the moment reference point rearwards by  $3.76\text{mm}$ . This change when applied to the current RANS result reduces the  $C_M$  slope too much and furthermore there is also no scientific basis for applying this correction. The incidence at which the slope of the pitching moment curve becomes positive in the RANS result is  $7.1^\circ$  whereas in the experiment it is initially observed at  $5.622^\circ$ . In the experiment, the pitching moment slope remains almost neutrally stable until  $8.77^\circ$  when a strong pitch break is observed. This pattern is somewhat smoothed out in the RANS result with the pitch break occurring more slowly over an incidence range of a few degrees. At high incidences  $> 16^\circ$ , the pitching moment curve returns to positive stability and this is also predicted in the RANS result.

The axial force coefficient ( $C_x$ ) gives an indication of when the attached leading edge flow breaks down and hence when the onset of flow separation occurs. Linear theory predicts that for attached flows  $C_x \propto C_L^2$  so when the curve deviates from this theoretical result, we can assume a significant flow separation has occurred. Figure 4.7 shows that in both cases, the low  $C_L$  axial



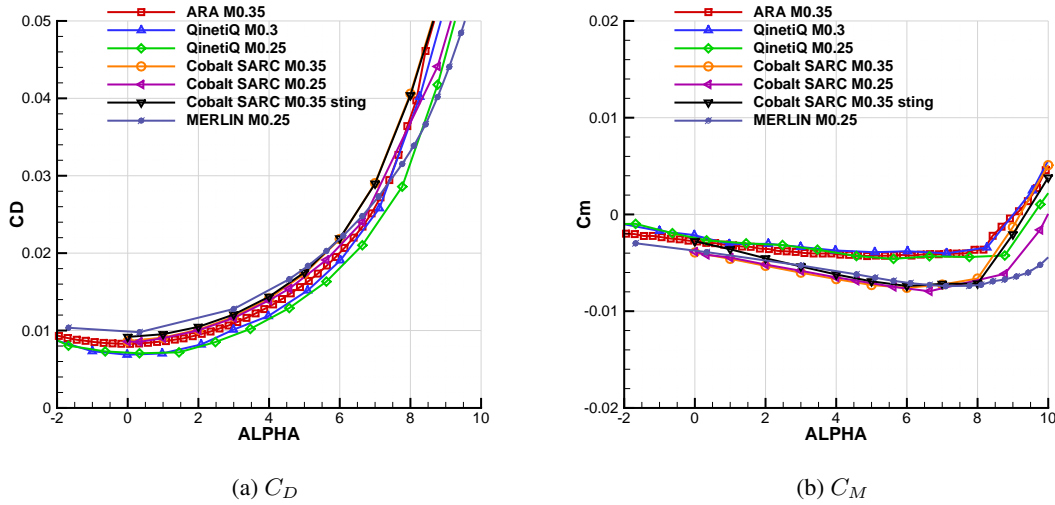


Figure 4.8: Various Wind Tunnel and Solver Comparisons

Result	$C_D$	Counts
ARA M0.35	0.00829	82.9
QinetiQ M0.3	0.00688	68.8
QinetiQ M0.25	0.00714	71.4
Cobalt SARC M0.35	0.00863	86.3
Cobalt SARC M0.25	0.00858	85.8
Cobalt SARC M0.35 sting	0.00978	97.8
MERLIN 0.25	0.00988	98.8

 Table 4.4:  $\alpha = 0^\circ$   $C_D$  various numerical and wind tunnel results

force is proportional to  $C_L^2$  and a best fit line is shown. The point at which the deviation from linear theory occurs in each case coincides with an angle of incidence in the range  $7.1 - 7.77^\circ$  (RANS) and  $6.64 - 7.77^\circ$  (experiment). In the case of the RANS result this is the same interval that the pitching moment slope changes sign and thus  $C_X$  departure is thought to be a good indicator of the onset of pitch divergence. The experimental  $C_X$  break occurs somewhere in the plateau region of the CM curve and close to the RANS result, within the resolution of the data points. The constant offset between the two lines is likely to be either due to the sting faring not being modeled or different skin friction drag, possibly due to laminar flow in the experiment.

### 4.3.2 QinetiQ and ARA Test Comparisons with Corresponding RANS results

#### 4.3.2.1 Drag

Drag on the 1303 UCAV has tended to be over predicted by RANS codes particularly at zero lift. This is thought to be due to laminar flow in the QinetiQ experiment where transition fixing was not employed. In the ARA test, transition strips were applied at approximately 5% chord. Although there is no cross over in the Mach number ranges between the two tests, they do get close. The

QinetiQ (low speed) test was run at a Mach number of 0.3 while the lowest Mach number in the ARA test was 0.35. By running CFD computations at both these conditions, we can assess the sensitivity to Mach and Reynolds numbers in this range as well as the importance of transition fixing. The effect on drag of the sting is also assessed numerically.

Figure 4.8(a) shows numerical and experimental results for  $C_D$ . In the QinetiQ test, the drag predicted at  $M = 0.25$  and  $M = 0.3$  is virtually identical at low incidence. As the incidence is increased, the drag becomes higher at Mach 0.3, presumably due to compressibility effects. The same conclusion is reached with the Cobalt results run at QinetiQ  $M = 0.25$  and ARA  $M = 0.35$  conditions, suggesting that the Mach and Reynolds number sensitivity is small at low incidence.

Between the ARA and QinetiQ test results there is a substantial difference in zero lift drag of 14 drag counts ( $C_D \times 10^{-4}$ ). As we expect the Mach and Reynolds number differences to have little effect, this is highly likely to be due to laminar flow in the QinetiQ experiment. The problem is complicated at higher incidences because compressibility does seem to have some effect. At  $\alpha = 7^\circ$  the QinetiQ (transition free)  $M = 0.3$  drag approaches the ARA  $M = 0.35$  result indicating transition may be less critical at high incidence.

Cobalt over predicts the zero lift drag by 14.4 counts at Mach 0.25 compared with the QinetiQ (transition free) test. At Mach 0.35 and comparing with the ARA test (transition fixed), the over prediction is significantly reduced to 3.4 counts. In the ARA test the 1<sup>st</sup> 5% of the chord may still be laminar giving a possible explanation of this over prediction.

MERLIN predicts that the zero lift drag is higher, 13 counts higher than the equivalent Cobalt solution and further from the experimental result. At higher incidence angles, MERLIN under predicts the drag. The reason for this discrepancy is not known but differences between codes of this magnitude are not uncommon.

Cobalt results at Mach 0.35 with and without the sting show that there is an 11 drag count penalty with the sting at  $\alpha = 0$ . This diminishes at incidence angles above 5 degrees.

#### 4.3.2.2 Pitching Moment

The pitching moment results in Figure 4.8(b) show that at incidence angles below  $5^\circ$ , the pitching moment slope is over predicted in all the RANS results and there is little difference between them. Likewise there is little difference between the various experimental results at low incidence.

The QinetiQ Mach 0.25 result pitches up a little later than the QinetiQ Mach 0.3 or ARA Mach 0.35 results, indicating compressibility has some effect. This trend is also captured in the corresponding Cobalt results. The Mach number in these calculations can become quite high locally although there was no supersonic flow present in the solution.

The sting faring has a small nose up effect pitching moment of  $\delta C_M = 0.0012$  at zero lift. As with drag, this also diminishes as the incidence is increased and there is nearly no effect on pitchup.

#### 4.3.3 Spanwise Forces

Local spanwise force coefficients help to gain an improved understanding of the flow physics causing non-linear behaviour to occur. Firstly a comparison between the quasi vortex lattice method and the RANS result is made and a discussion of how the QVLM aids our understanding for this problem.

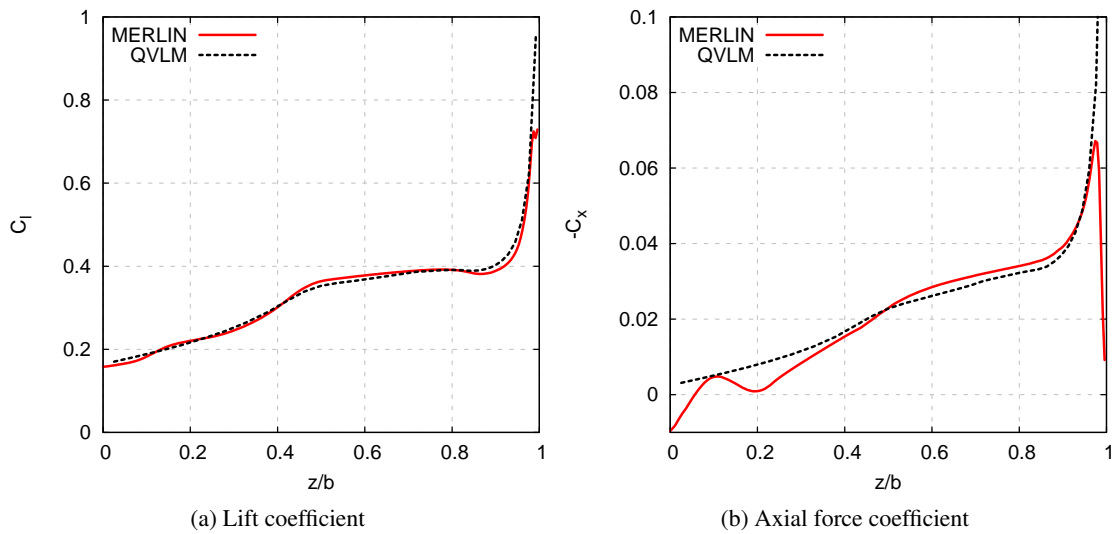


Figure 4.9: QVLM compared with MERLIN RANS result  $\alpha = 4.57^\circ$

Figure 4.9 shows the local lift and axial force coefficients plotted against the spanwise coordinate  $z/b$  at an incidence of  $\alpha = 4.57^\circ$ . There is only a small amount of flow separation present at the wingtip in the RANS result and the results match up very well, confirming that the wing is acting according to the linear theory. A large local  $C_l$  variation is observed with low local loading at the root, increasing towards the wingtip. In a viscous flow regime this will clearly cause local flow separations as observed with the RANS analysis at the tip. This variation can easily be explained in terms of changes in the strength of the bound vortex.

The combination of wing sweep and taper cause the wingtips to become highly loaded. Sweep causes the root to become relatively less loaded as each wing is in the downwash (behind the bound vortex) of the opposing wing. This effect is felt most strongly at the root as the downwash velocity diminishes with distance ( $x^{-1}$ ). This means that the tips experience less downwash and hence sustain a higher local lift. Taper causes parts of the wing to become highly loaded because the lift distribution is sustained over a reducing chord. With a reduced chord, local  $C_L$  is increased. As the wing tapers to a chord of zero, the local loading at the tip becomes extremely high causing flow separation. Furthermore the Reynolds number in the vicinity of the wingtip is relatively low which further promotes early flow separation.

The agreement between the quasi-vortex-lattice axial force integrated axial force from the RANS solution is reasonable. At the root the RANS result predicts a lower force due to the trailing edge gap at the centre span and a small local flow separation caused by the sharp leading edge. Towards the wingtip the agreement is reasonably good especially considering the QVLM result makes no attempt to model viscous or thickness effects. This confirms that the QVLM is a valid 'engineering approach' for design of this class of wing.

Figure 4.10 shows the force coefficients  $C_l$ ,  $C_x$ ,  $C_m$  and the minimum pressure peak  $C_{p,min}$  plotted against the non-dimensionalised spanwise distance  $z/b$ . The line colour indicates whether the flow has separated in the leading edge region with a black line representing attached flow and a blue line showing where the flow has separated. During post processing the leading edge flow is

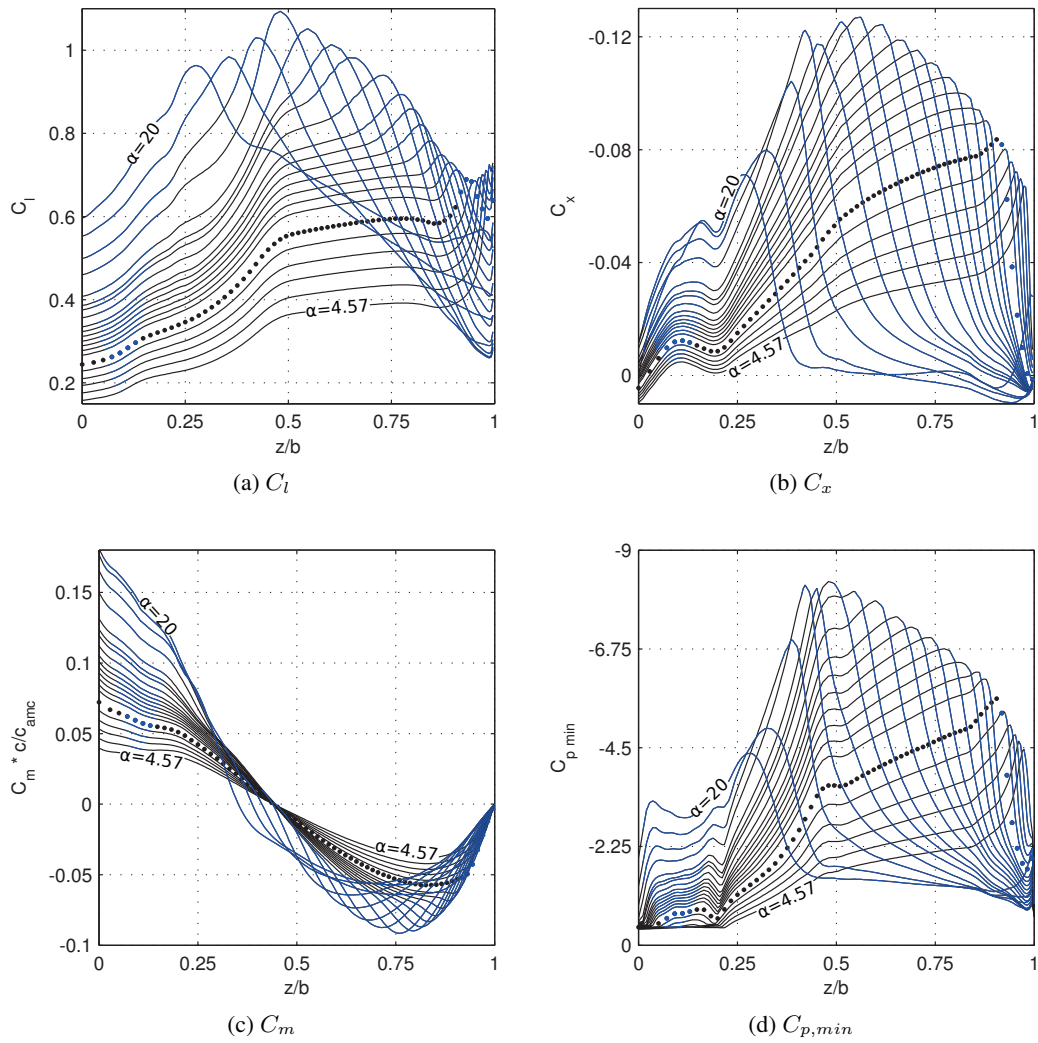


Figure 4.10:  $C_l$ ,  $C_x$ ,  $C_m$ ,  $C_{p,min}$  vs spanwise coordinate  $z/b$

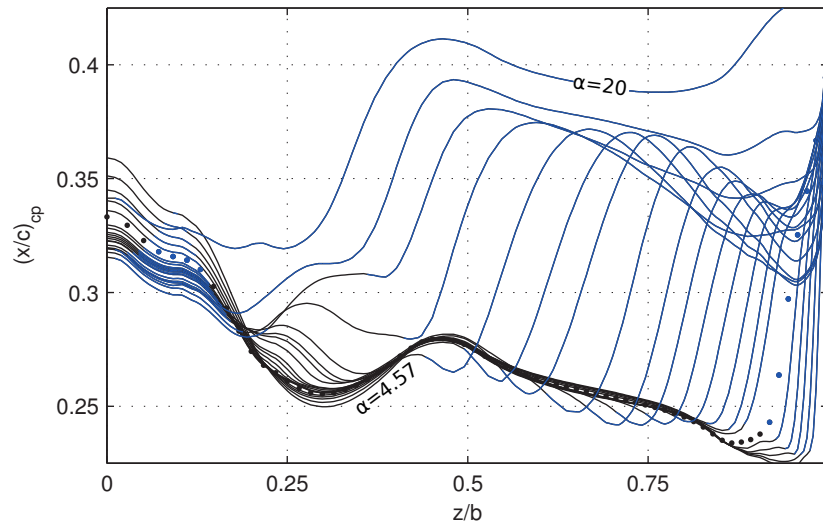


Figure 4.11: Chordwise centre of pressure location vs spanwise coordinate  $z/b$

assumed to have separated if a negative tangential skin friction is detected within  $10\%c_{local}$  from the leading edge on the upper surface of the wing. Each line on the plot corresponds to an angle of incidence computation although the first 3 solutions have been omitted to simplify the plots. The first line therefore corresponds to an angle of incidence of  $4.57^\circ$ . The  $\alpha = 7.1^\circ$  line which represents the onset of pitch divergence is bold and dotted.

Spanwise lift distributions (Figure 4.10(a)) for all the incidence angles show the flow development as the incidence angle is increased. Two sources of flow separation are apparent, one at the wingtip and another at the root. The root separation is due to the locally sharp leading edge resulting in a relatively small region of separated flow. The effect this has on the total forces is thought to be relatively small until high incidence as the lift distribution is not significantly changed from its attached flow shape.

The wingtip flow separation appears to dominate the high lift behaviour of the wing. The flow is unlike that seen on conventional slender wings where the separation point is fixed at the apex. This mixed flow type is due to the wing having moderate sweep and a large leading edge radius. As the angle of incidence is increased, the wingtip separation moves inboard. A region of enhanced vortex lift can be seen outboard of the separation point for a short spanwise distance and this grows as the incidence is increased. The enhanced lift is caused by a vortex emanating from the separation point. The vortex's trajectory initially follows a path, roughly parallel to the leading edge, acting similar to a slender wing vortex and creating additional lift. Further downstream the vortex lifts from the surface and is convected downstream. Its diameter appears to increase and the lift force diminishes.

The axial force coefficient  $C_x$ , indicates the onset of flow separation. As shown in Figure 4.10(b), contrary to the lift force, immediately as  $C_x$  reaches its maximum magnitude, flow separation occurs. The  $C_x$  peak increases as the separation point moves inboard, suggesting that the maximum sustainable axial force may be linked to the local Reynolds number. The shape of the spanwise leading edge suction peak curve,  $C_{p,min}$  shown in Figure 4.10(d), closely matches the shape of the

axial force curves, showing that the axial force is strongly dependent on the leading edge suction peak generated when the flow is attached.

The spanwise moment coefficients presented are calculated for a 2D section such that the curve represents the local contribution to the total pitching moment. For low angles of incidence when the flow is attached and the pitching moment slope is stable, the outboard portion of the wing creates a nose down contribution to pitching moment which is cancelled out by the nose up moment from the inboard portion of the wing. There is an additional nose down pitching moment created at the root due to the camber of the body. As the incidence is increased, initially the pitching moment slope remains negative (stable) because flow separations are small and the vortex flow still maintains suction near the tip. As the separation grows, the vortex moves inboard and therefore forward (due to wing sweep), contributing less to the total pitching moment due to a smaller moment arm. The wingtip lift force diminishes and the nose down contribution to pitching moment is reduced. The inboard sections continue to create increasing nose up moments and the overall pitching moment slope becomes positive. At the wingtip the greatest nose down force from approximately the last 10% of the span is seen as the pitching moment slope changes sign (indicated by dotted line).

Figure 4.11 shows that for sections experiencing enhanced vortex lift, the centre of pressure initially moves forward giving a nose up pitching moment contribution. Further outboard, when the lift is reduced, the centre of pressure moves back to  $40\%c$ . The strongest unstable pitching moments in both the computation and experiment are in the incidence range  $10^\circ > \alpha > 16^\circ$ . This occurs when the separation point approaches the spanwise position where the leading edge intersects the moment reference axis. The enhanced vortex lift now no longer offsets the reduction in pitching moment due separation due to a small moment arm.

At high incidences  $> 16^\circ$  when a pitching moment recovery is seen, we can see in the spanwise  $C_m$  result that movement of the separation point has caused the nose up pitching moment contribution to collapse. These sections are now producing a nose down moment due to a rearward movement of the centre of pressure to  $40\%c$ . The root and tip separations also join together, accelerating the movement of the outer separation point towards the root.

#### 4.3.4 Pressure Distributions

The computed pressure distributions are compared with the experimental pressure tap measurements as shown in Figure 4.12. The wind tunnel model had 88 pressure taps in 7 rows located as shown in Figure 4.3, the majority were located on the wing upper surface near the leading edge. At  $z/b = 0.6$  (section 4), there is one row which spans the whole chord.

Figure 4.12(a) shows pressure distributions for  $\alpha = 5.622^\circ$ . At this incidence the flow is largely attached apart from a small separation near the wing tip. The RANS and wind tunnel results match up extremely well in this case. (c) shows the pressure distributions at  $\alpha = 7.77^\circ$ , just after the pitching moment slope has become positive. The RANS result curve shows signs of flow separation in the last section (7) only, whereas the experimental data shows a slight deviation from the attached flow pattern in section 6 as well. The separation in the final section is also more developed in the experiment indicated by a smaller suction peak. This is typical in that the wind tunnel model shows flow separation at a slightly lower incidence than the RANS result. Although there is clearly separated flow in (b), the vortex lift contribution can be seen as there is still a reasonably large suction present at the tip sections. At section 7 the separation is more developed in the wind tunnel

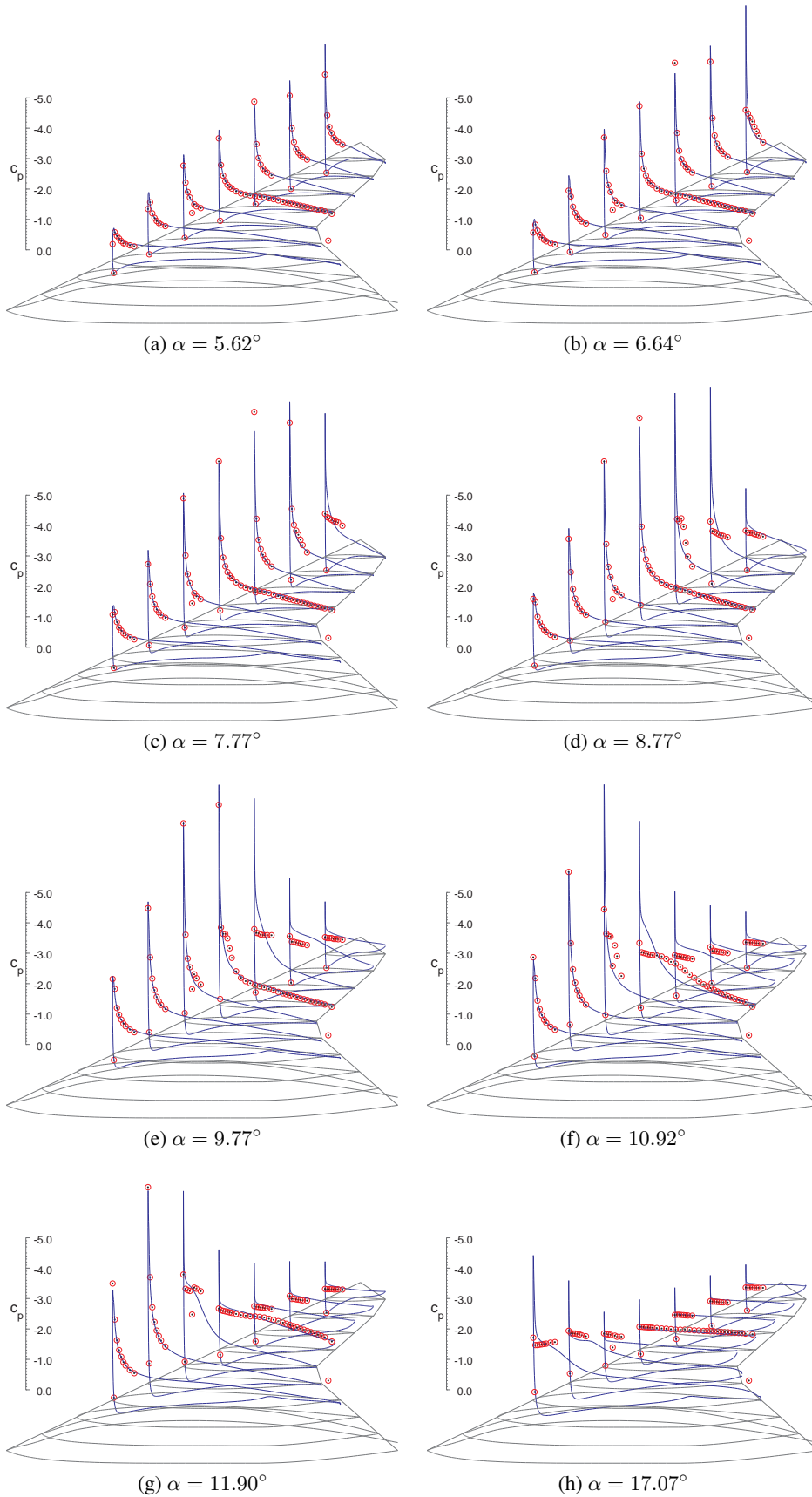


Figure 4.12: 1303 Pressure distributions: MERLIN (blue lines) and QinetiQ Run17 (red dots)

result but the RANS prediction underestimates the vortex lift. This means that although the onset of flow separation is predicted too late, the amount of additional vortex lift may also be underestimated which partially cancels out this effect in the overall forces. In (e) ( $\alpha = 9.77^\circ$ ) there are three sections (5-7) in the computational results with separated flow and 4 sections (4-7) in the experiment. Again as shown, sections 4 and 5 the flow separation is more developed in the experimental result but the vortex lift is underestimated. In sections 6 and 7 the flow is now fully separated and the RANS solution slightly overestimates the upper surface suction. Fig.4.12(g) shows that at  $\alpha = 11.9^\circ$ , sections 4-7 the lift force has largely diminished and the agreement between the experiment and the computation are good.

The pressure tap data gives the indication that the flow separates sooner in the experiment than in the RANS computation. For this reason it is suggested that for design, a slightly more conservative approach should be used when estimating the maximum attainable leading edge thrust such as Carlson's original or improved methods. In reality it is extremely difficult to reliably predict the limiting pressure even with the most advanced numerical methods which justifies the empirical approach.

#### 4.3.5 Flow Visualisation and Pitchup

Figure 4.13 shows the computed skin friction lines coloured by pressure coefficient. This gives an improved understanding of what happens to flow post separation and the effects that this has on the pitching moment. The pitch divergence is essentially caused by the early onset of flow separation towards the wingtips. As the wing is swept ( $47^\circ$ ) and the wingtips are positioned behind the aircraft's centre of gravity, a loss of lift in this region causes an imbalance in the nose up (from the inner wing) and nose down (from the wingtips) pitching moment contributions and hence the pitching moment slope becomes positive. A small amount of flow separation at the wingtips can be tolerated however as the separation moves inboard and more lift is lost, the pitching moment slope becomes positive. The severity of the change in pitching moment slope depends upon the shape of the spanwise lift distribution. Near the tip, the slope of the spanwise lift distribution  $\partial C_L / \partial \eta$  is high, this means that as incidence is increased, the separation point moves inboard fairly slowly. As the separation approaches the outer crank position, the slope  $\partial C_L / \partial \eta$  becomes much lower and hence the separation spreads inboard much more quickly.

Not all of the factors relating to the flow separation have a negative influence in the pitch divergence. As seen in Figure 4.11 when the flow separates, the centre of pressure actually moves forward due to the leading edge vortex which also creates some additional lift. Despite this small forward movement of the centre of pressure (which contributes to pitch divergence), this phenomenon tends to delay pitch divergence due to the additional lift created. As the separation point moves inboard, this forward shift in the centre of pressure becomes more significant because the chord is increased and the wing is sustaining a higher lift here.

Outboard from the separation point, the vortex lifts away from the surface and increases in diameter (Figure 4.13). This reduces its influence on the wing and the enhanced lift is lost. Now the centre of pressure moves rearwards which aids in the recovery of pitching stability at high incidence. For this reason, a wing designed to enhance the vortex lift effect near the tip may improve the pitch divergence properties of the wing. This could be achieved with a locally sharp leading edge to encourage a strong vortex flow in the tip region. Further inboard, the focus should be delaying flow



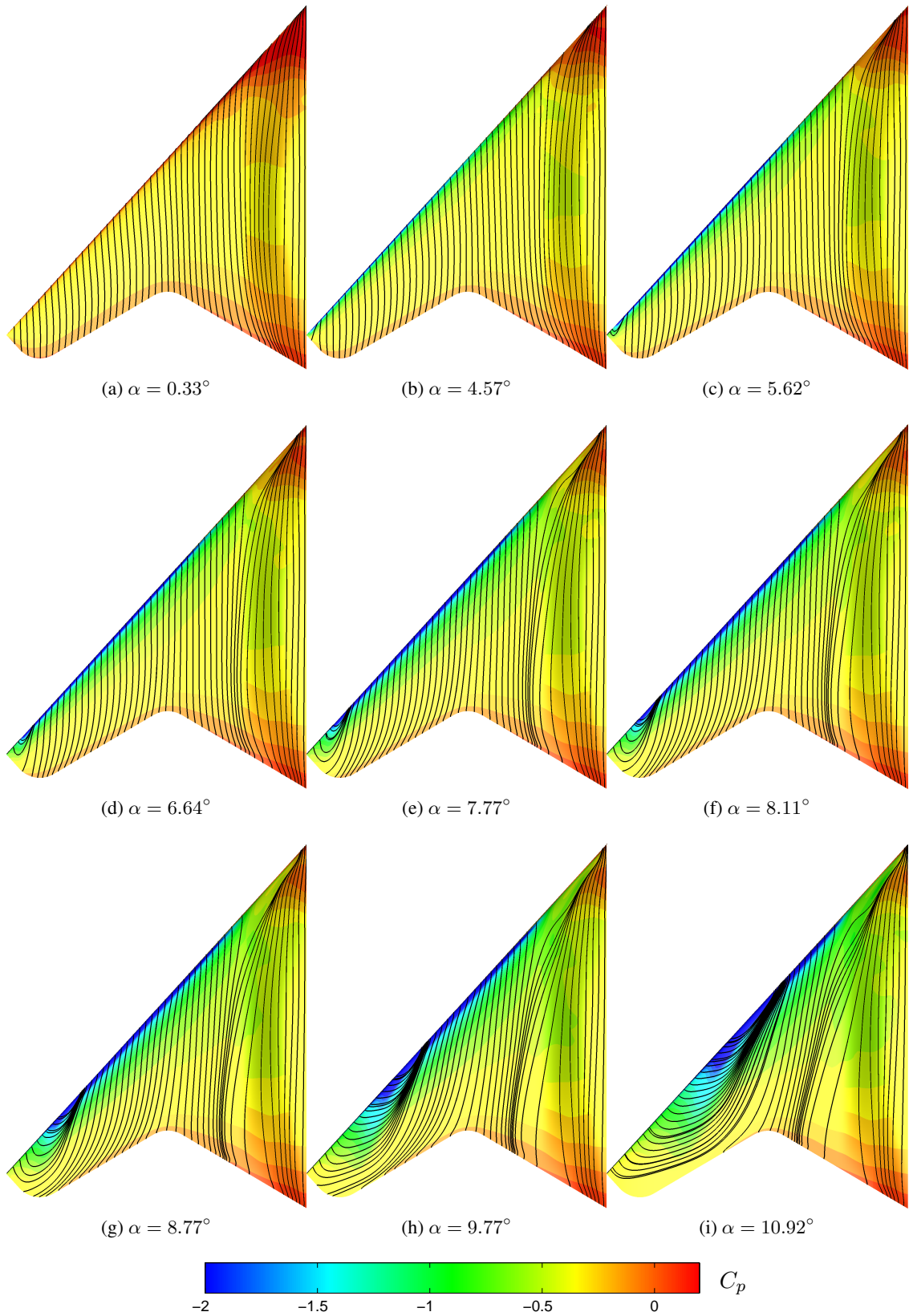


Figure 4.13: 1303 coloured  $C_p$  distributions and skin friction lines

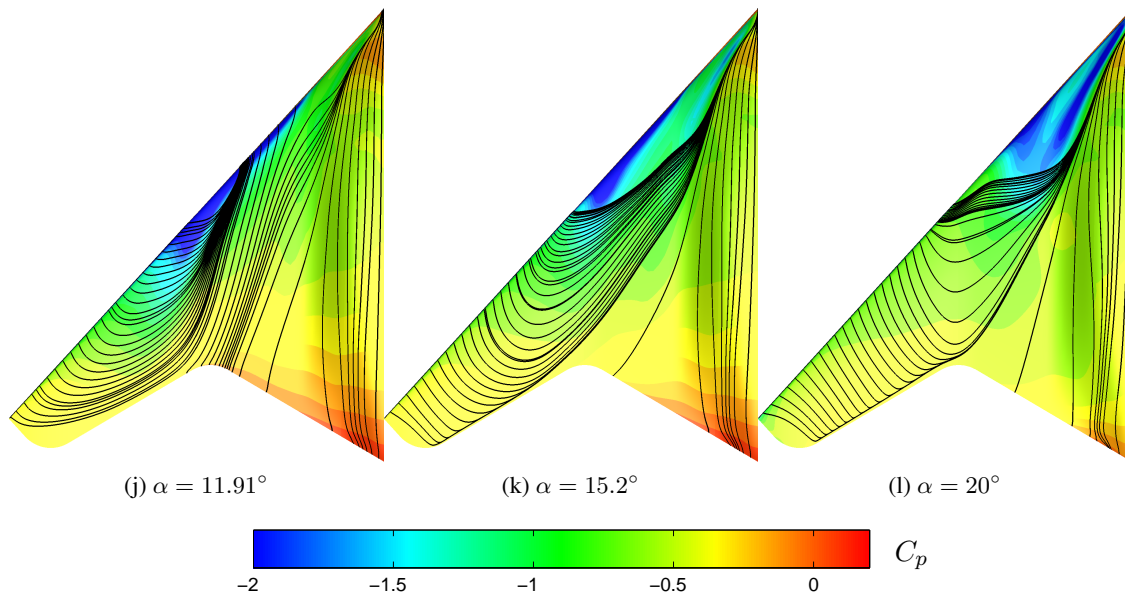


Figure 4.13: 1303 coloured  $C_p$  distributions and skin friction lines (*cont.*)

separation for as long as possible. Increasing the leading edge radius or adding additional camber would have this effect as well as the possibility of some form of boundary layer devices to help keep the flow attached.

#### 4.3.6 Comparisons with the Cobalt Solver

An analysis of 1303 QinetiQ test run 17 was also done with Cobalt for the same free-stream conditions and same structured mesh that was used for the MERLIN calculations. This allows an assessment of the sensitivity of the solution to the particular CFD code and turbulence model being used. The results for lift, drag and moment coefficients are shown in figure 4.15. The turbulence models used in Cobalt were  $k-\omega$ ,  $k-\omega SST$  and *SARC* (Spalart-Allmaras Rotational Correction [88, 89]). Most of these turbulence models are commonly seen for aeronautical applications but the *SARC* model is more uncommon.

The *SARC* model is a modification to the original SA model introduced by Shur, *et al.* [89] aiming to generalise more case specific vortex corrections used in previous models e.g. [90]. The Rotational Correction (RC) in the *SARC* model is a multiplying correction factor applied to the production term in the original SA model. The term has the effect of transforming the production term into a dissipation term in the vortex core region. This tends to reduce the eddy viscosity and reduce the tendency of the standard SA model to over damp vortex flows. The RC term detects vortex flow regions by comparing the relative magnitude of the strain and the vorticity. The term has a negligible effect in boundary and shear layers where strain dominates but is activated in vortex cores where the strain is small and vorticity magnitude is high.

The results from the QinetiQ wind tunnel test run 8 are also included which are at a higher Reynolds number ( $Re = 8.5 \times 10^6$ ) to demonstrate the effect of Reynolds number sensitivity in the experiment.

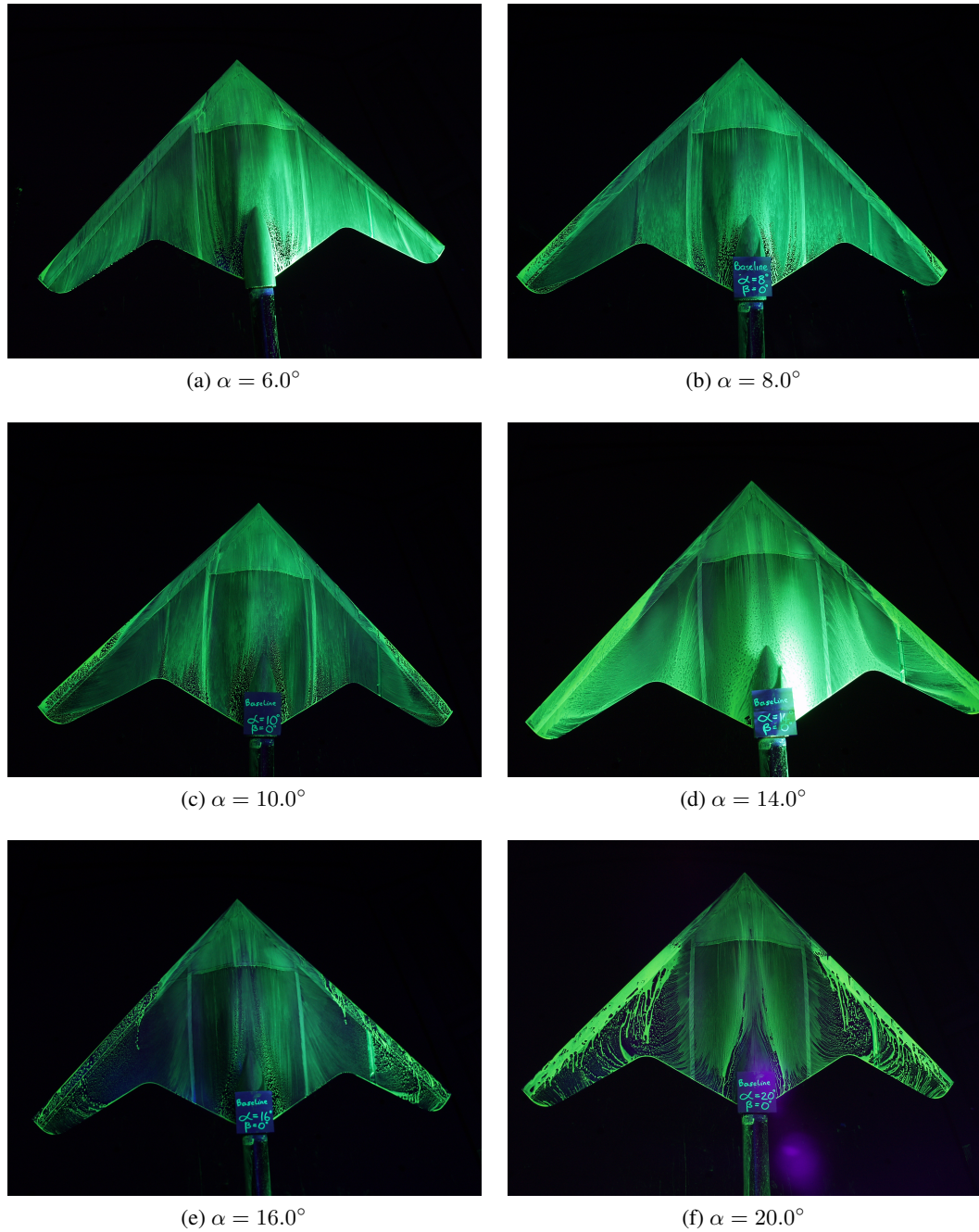


Figure 4.14: 1303 experimental oil flow visualisation  $\beta = 0^\circ$

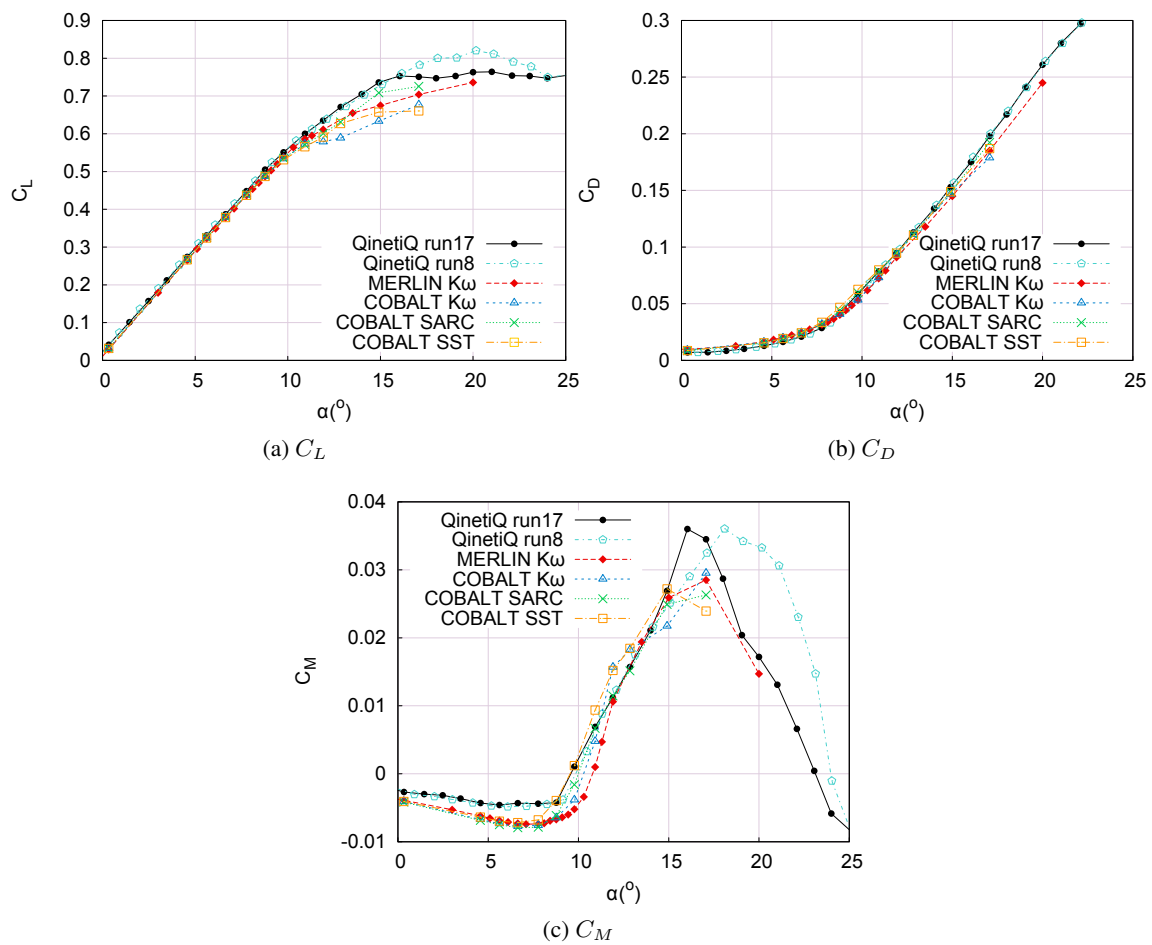


Figure 4.15: Code and turbulence model comparisons

Below  $\alpha = 8^\circ$  when the flow is predominantly attached, the lift drag and moment coefficients predictions are all very similar, indicating that little sensitivity exists here. The same conclusions as above are therefore reached.

At higher incidences when flow separation is present in the solutions there is a greater spread in the results. For lift, the Cobalt  $k - \omega$  model performs the worst compared with the experiment showing a premature reduction in lift curve slope at around  $\alpha = 11^\circ$ . The MERLIN  $k - \omega$ , Cobalt  $k - \omega$  SST and SARC all perform similarly in the range  $10 - 12^\circ$  but the SARC model is best compared with the experiment at incidences above this.

For drag, the results in each case are very similar indicating that there is little sensitivity to the turbulence model. At higher incidences where there is a small spread in the results, the Cobalt SARC model performs best compared with the experiment.

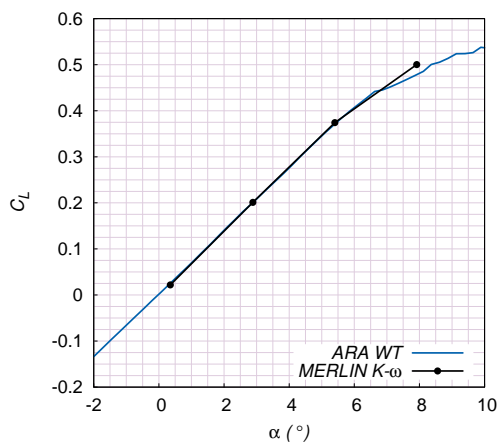
The moment coefficients show that the onset of pitch divergence between the different models has quite a spread of around  $1^\circ$ . It is difficult to say which is best compared with the experiment as the low incidence results are not close enough to make a proper judgement. The Cobalt  $k - \omega$  SST model shows pitchup first followed by Cobalt SARC, Cobalt  $k - \omega$  and lastly MERLIN  $k - \omega$ .

Overall, the results suggest that the Cobalt SARC model performs best, probably because the vortices are less damped than with other models and hence more vortex lift is seen. This is particularly evident in the lift curve slope in Figure 4.15(a). It is interesting to note the large differences between the MERLIN and Cobalt  $k - \omega$  results with MERLIN performing comparatively better. A possible explanation is that MERLIN is less dissipative on the current mesh because the numerical order of accuracy is higher.

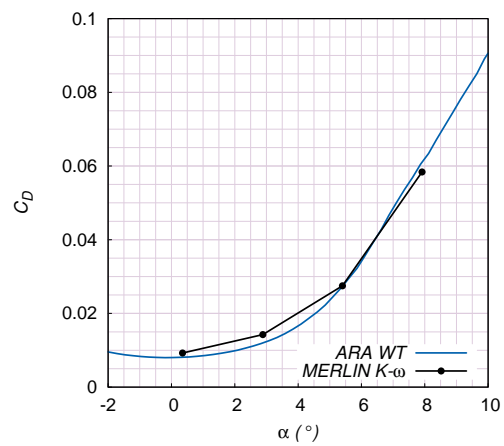
There seems to be two dominating phenomena that the flow solver and turbulence model needs to capture correctly in order to predict the total forces. The first is correct prediction of the onset of flow separation. The second is correctly predicting the amount of enhanced vortex lift that will be generated. Each turbulence model and code tested acts differently in these regards. When predicting the normal force for example, premature prediction of separation onset would cause a reduction in lift. Stronger vortex prediction would cause an increase in nonlinear vortex lift. For a model exhibiting both these deficiencies, normal force and pitching moment might appear to be predicted well because the two effects would cancel each other out. At this stage we are in no position to recommend a particular turbulence model for this task, further investigation needs to be done into the nature of each model for this class of flows, especially with regard to the onset of flow separation. A simpler test case would be invaluable for this purpose because our inability to numerically reproduce the results in the linear region prevents us from making a proper judgement of the results. A NATO working group [91] is currently in progress aiming to address some of these issues.

#### 4.3.7 Cruise Results

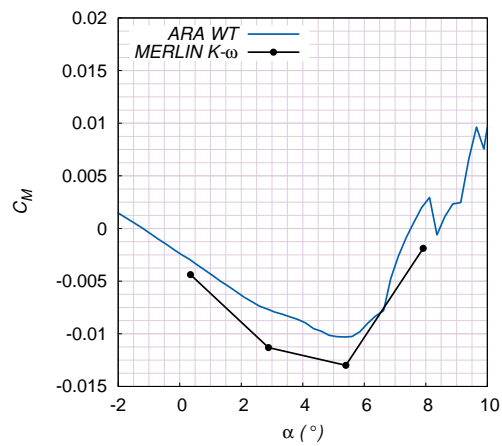
A limited number of computations were performed at freestream conditions to match the ARA Transonic wind tunnel results at the cruise Mach number ( $M = 0.8$ ). This demonstrates the ability to predict the cruise performance of the vehicle. The same physical wind tunnel model was used as in the QinetiQ test. Transition bands were applied at 5% chord which should help reduce errors due to regions of laminar flow. The tunnel conditions for this test are summarised in table 4.2.



(a) Lift coefficient



(b) Drag coefficient



(c) Pitching moment coefficient

Figure 4.16: Mach 0.8 total forces

The lift curve slope is accurately captured with only the final point ( $\alpha = 7.6$ ) showing an error. In contrast to the low speed results, when the lift curve slope reduces in the experiment, an over prediction is seen in the RANS result. As with the low speed comparisons, the RANS prediction over estimates the drag at low incidence although it is less severe than at low speed, possibly because of the transition bands. At higher incidences the drag is a little under predicted. The pitching moment slope is now steeper (more stable) than in the low speed test, this is due to the effects of compressibility moving the centre of pressure rearwards. The static margin again is over predicted and there is a small (negative) offset at zero lift. The wing now exhibits pitchup at a lower incidence of approximately  $\alpha = 5.5^\circ$ . This is caused by shock induced separation and appears to be reasonably accurately captured by the RANS results.

Overall the quality of the agreement between MERLIN and the experiment seems to be reasonable. Although there are differences in the drag and pitching moment predictions, the results should be adequate for assessing the effect of incremental design changes.

## 4.4 Lateral Results

The directional stability of the 1303 UCAV is assessed by making computations at sideslip angles of  $\beta = +5^\circ$ ,  $+10^\circ$  and some at  $+15^\circ$ . For these computations, the mesh was mirrored to represent both wings. This obviously doubles the mesh size to around 4 Million elements, increasing the computational requirement significantly. Due to unsatisfactory yawing moment predictions made by MERLIN for the wing without sting, Cobalt was used to model the wing, sting and fairing combination using overset mesh. Using overset has the benefit that exactly the same structured mesh can be used for the wing, eliminating uncertainties which which would otherwise be introduced by changing the mesh type and spacing. As well as looking at the yawing moment, the effect on the pitching moment and axial force can also be assessed.

The sting / fairing geometry used for these computations is a cylinder with its axis orientated in the  $x$  direction which for simplicity is terminated downstream with an ogive,  $4 \times c_{root}$  from the wing. The sting geometry was generated with a CAD package and intersected with the wing surface. The sting mesh outer boundary is located at twice the sting radius from the sting axis. An unstructured tetrahedral/prism mesh with spacing to match the structured background mesh was generated with ANSYS ICEM software. Various views of the mesh are shown in figure 4.17. The colours indicate the various boundary regions in the sting mesh, red is the wing, green is the sting fairing which is also included in the force integration and blue is the sting which is ignored. In the overset calculation, Cobalt automatically calculates which elements are blanked in each mesh at the beginning of the calculation. Unfortunately, due to limitations in the Cobalt method, some ‘double accounting’ of forces occurs for overlapping regions on the surface. An attempt to match the mesh spacing between the two meshes was made which minimises the size of the overlapping regions and hence the errors.

### 4.4.1 Directional Stability

The directional stability  $\frac{\partial C_n}{\partial \beta}$  or  $C_{n\beta}$  is calculated with central differences, for example

$$C_{n\beta}(\beta = 2.5) = \frac{C_n(\beta = 5) - C_n(\beta = 0)}{5(\pi/180)} \quad (4.1)$$

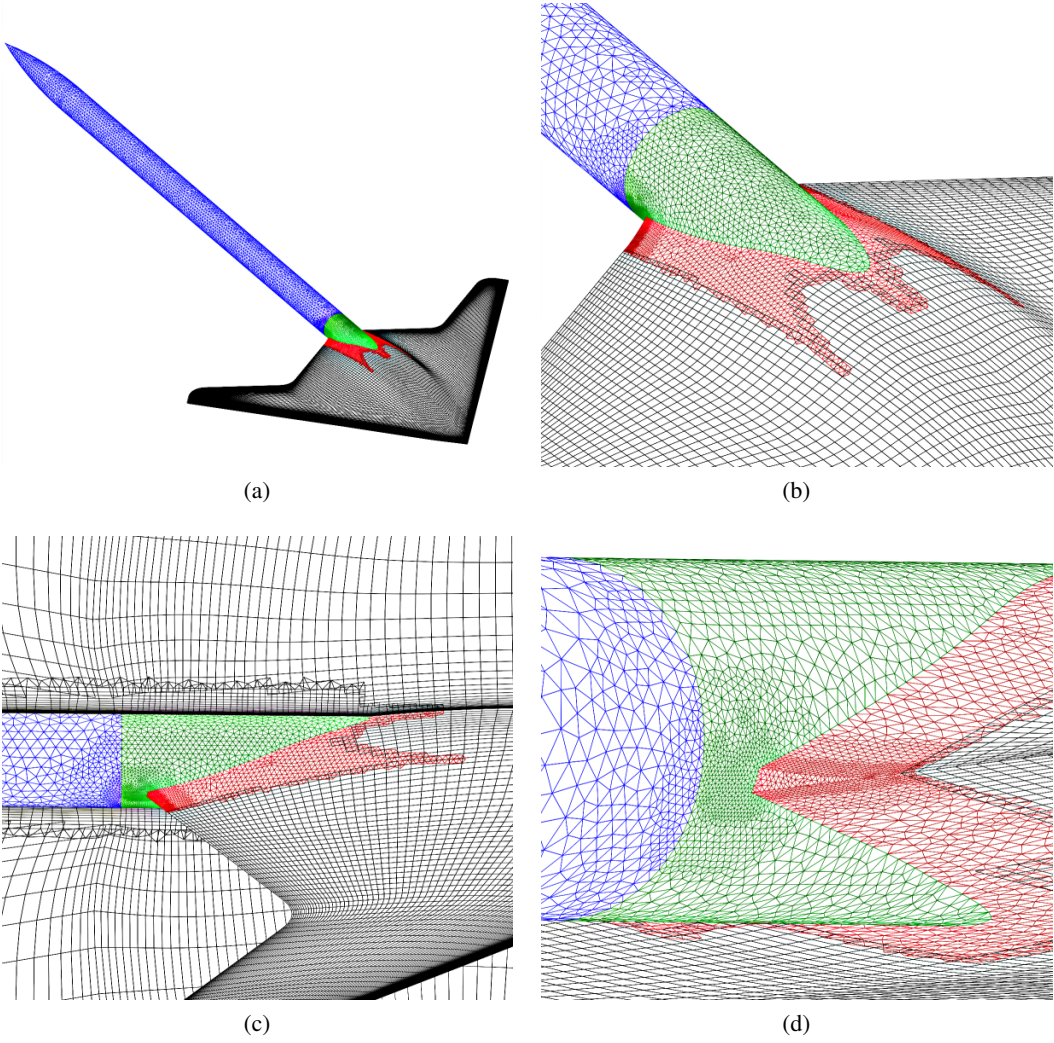


Figure 4.17: Overset mesh used in Cobalt



with  $\beta$  in degrees. In the QinetiQ wind tunnel test, the data was not collected at fixed incidence angles hence to calculate the stability derivatives, the data needed to be interpolated at distinct  $\alpha$  values. This was done in  $0.5^\circ$  increments by linear interpolation. Force and moment conventions dictate that the sideslip angle  $\beta$  and the yaw angle  $\psi$  are in fact opposite, i.e.  $\beta = -\psi$ . This means the condition for directional stability requires that for a positive disturbance in sideslip, a positive yawing moment is required to return the nose towards the wind or mathematically  $C_{n\beta} > 0$ .

The QinetiQ results (Figure 4.18(a)) show that at low incidence, the 1303 UCAV is directionally stable about the moment reference point. The stability level slightly increases with increasing incidence until around  $\alpha = 6^\circ$  at which point the stability level decreases rapidly, becoming unstable. For  $\beta = \pm 2.5$ , the wing becomes neutrally stable at  $\alpha = 7^\circ$ . At  $\alpha = 9^\circ$  the stability begins to improve again returning to positive stability around  $11^\circ$ . In the wind tunnel result, some asymmetry exists between the positive and negative sideslip cases indicating that the  $\beta$  measurement may have a small offset or other asymmetry such as tunnel swirl may exist. At the higher sideslip angles ( $\beta = \pm 7.5$ ), the wing becomes unstable in yaw slightly earlier by about  $\Delta\alpha = 0.5 - 1.0^\circ$ . This is thought to be due to the effect of the increased sweep on the trailing wing which reduces the incidence at which the flow begins to break down.

Figure 4.18(b) shows directional stability predictions from MERLIN. The shape of the curve is very similar to the wind tunnel results but an offset of approximately  $\Delta C_{n\beta} = -2.5 \times 10^{-3}$  is seen, making the wing directionally unstable throughout the incidence range. Aside from this offset, the shape and slopes match well although the reduction in  $C_{n\beta}$  is less sharp. This is analogous to the pitching moment with the early reduction in  $C_{n\beta}$  slope ( $\alpha \sim 3^\circ$ ) not captured but the later main break ( $\alpha \sim 6$ ) captured well. As with the wind tunnel results, as the sideslip angle is increased, the wing becomes unstable in yaw before it does in pitch. The reduction in directional stability with increasing sideslip angle appears to be slightly more severe than in the wind tunnel results.

The Cobalt results with the sting present (figure 4.18(c)) match the experiment much more closely with more or less the correct stability level predicted at low incidence. (d) shows a force breakdown of the contributions from the wing and the sting fairing shown separately. The sting fairing contribution to the directional stability is approximately constant. The isolated wing results are very similar to the MERLIN results confirming that the MERLIN results are likely to be correctly predicted. This shows that for the assessment of wing stability in the wind tunnel, the sting arrangement used in the 1303 test with the sting fairing attached to the wing is not satisfactory.

Figures (e) and (f) are show comparisons of the Cobalt predictions plotted alongside the QinetiQ test data with zoomed axes. These show how closely the results compare. In each case, the RANS results break a little earlier but the shape is very well captured, even after flow separation has occurred.

#### 4.4.2 Pitching Moment

In the experiment (Figure 4.19(a)), changes in the shape of the pitching moment curve are seen when  $\beta$  is changed. At  $\beta = \pm 5^\circ$  the curve is similar to  $\beta = 0$  except the low incidence slope is slightly reduced. At  $\beta = \pm 10^\circ$ , the low incidence slope is positive indicating that it has become unstable. At  $7^\circ$  there is a brief return to negative slope before pitchup occurs.

Figures 4.19(b) and (c) show that both MERLIN and Cobalt predictions exhibit the opposite trend to the experiment i.e. the stability improves with increasing sideslip angle. A MERLIN polar was

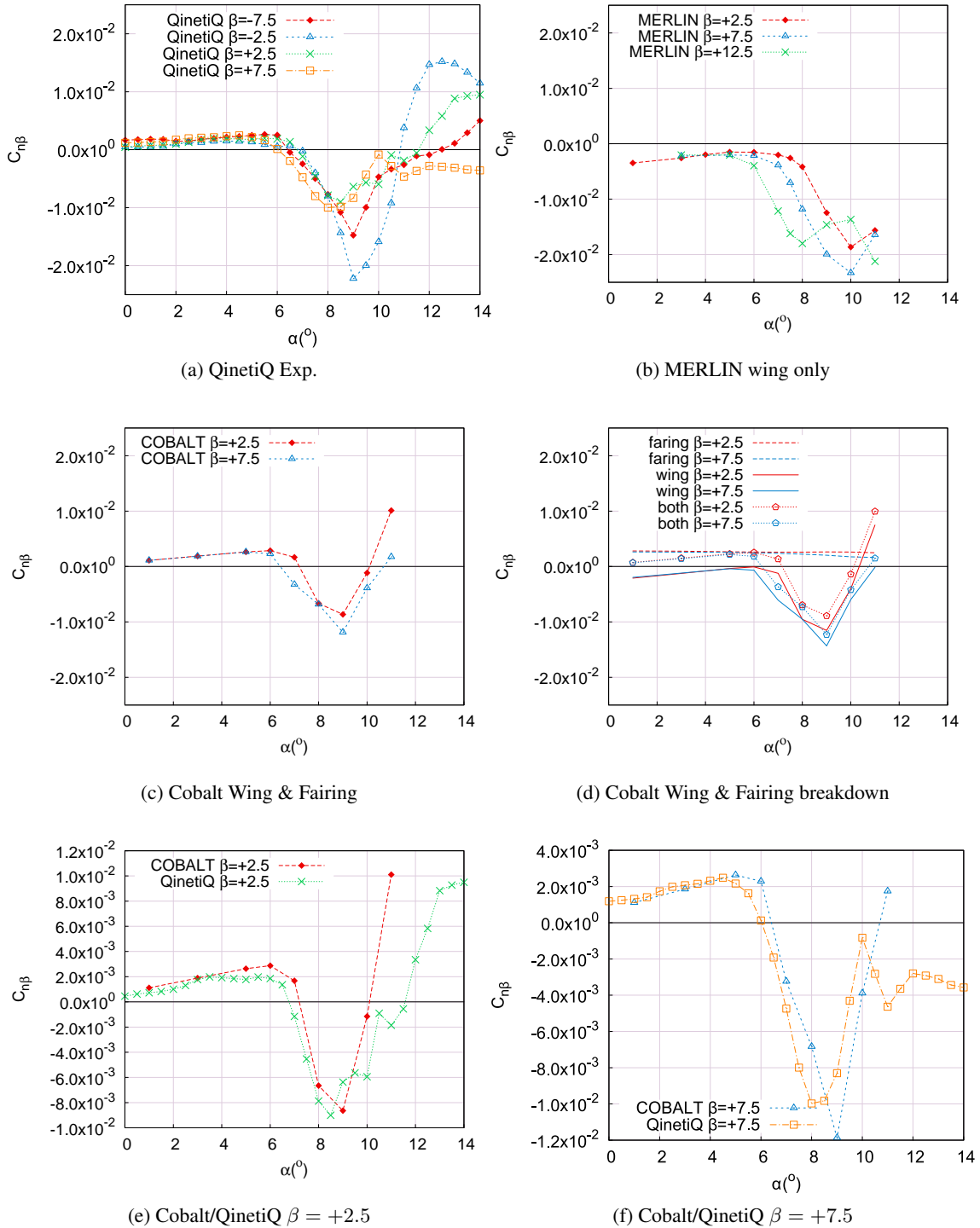


Figure 4.18: 1303 UCAV Directional Stability  $C_{n\beta}$  vs  $\alpha$

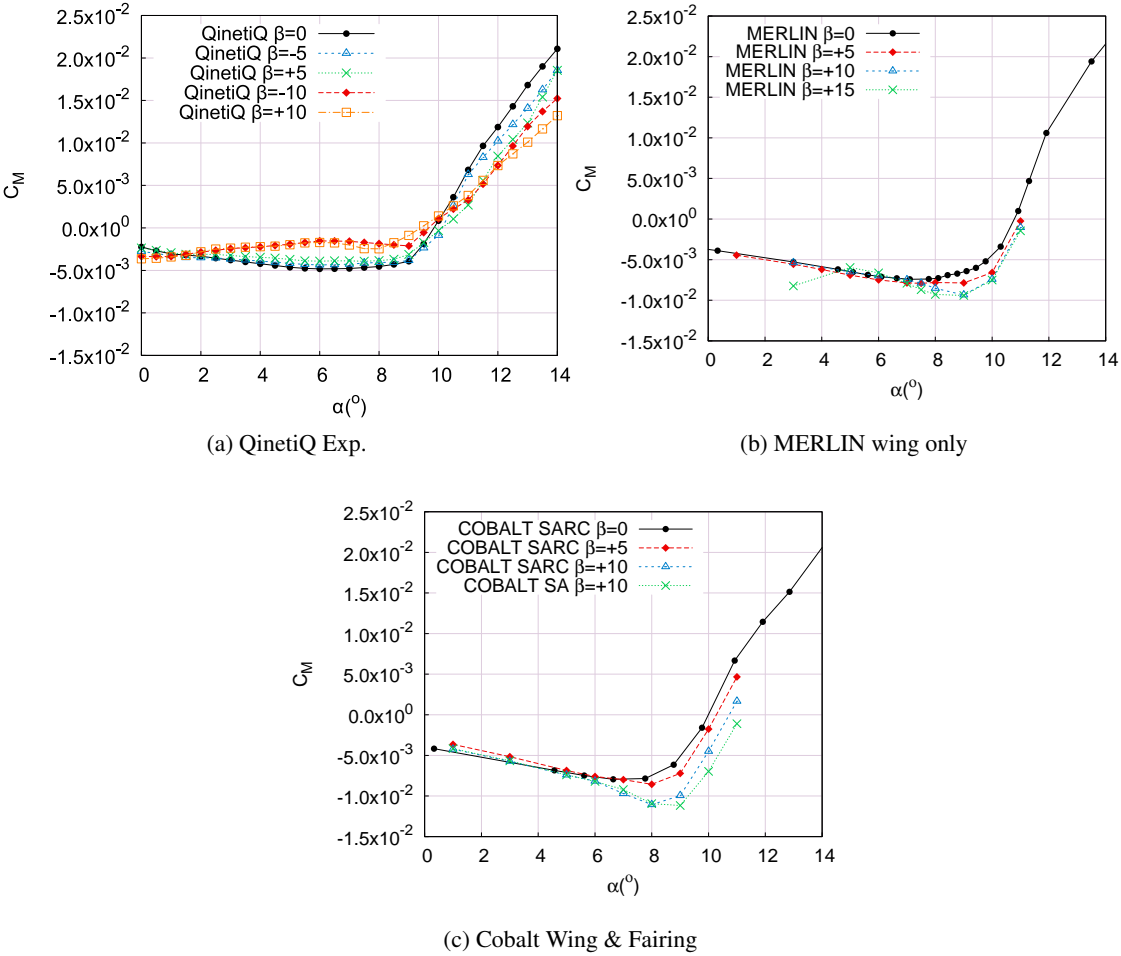


Figure 4.19: 1303 UCAV Pitching Moment  $C_M$  vs  $\alpha$  at different sideslip angles  $\beta$

also done with  $\beta = 15^\circ$  to see if the effect seen in the experiment could be reproduced at an higher sideslip angles but the stability actually increased further. No explanation for this can be offered.

#### 4.4.3 Spanwise Forces with Sideslip

The spanwise lift coefficient, axial force coefficient, yawing moment and pitching moment are shown for various incidence and sideslip angles in figs. 4.20 to 4.22. For the yawing moment, only the axial force components are considered. The leading and trailing wings are plotted together so differences in the force distributions can be seen. Thicker lines give an indication of whether flow separation has occurred at that location.

When the flow is predominately attached, the leading wing has a higher lift than the trailing wing. This is because they effectively have different sweeps which reduces the lift curve slope of the trailing wing. The leading wing also retains more attached flow than the trailing wing. When the flow separates, more additional nonlinear lift is generated on the trailing wing. It is greater in both magnitude (higher local  $C_l$ ) and in its spanwise influence. Between the  $\beta = 5$  and  $\beta = 10$  result, the differences become even larger.

For axial force, when there is attached flow, the trailing wing has a larger axial force contribution which has a stabilising effect in yaw. This leads us to believe that the side forces must have an unstable influence to make the wing directionally unstable in yaw at low incidence. As incidence is increased, but still in the linear range, the differences between the leading and trailing wings becomes larger, increasing the stability level. Above  $\alpha = 8$ , when the flow separates a sharp reduction in axial force is seen. This is more severe on the trailing wing and hence has a destabilising effect, causing the  $C_{n\beta}$  curve to become negative. As there is no increment in axial force due to the leading edge vortex, the wing becomes unstable in yaw before it does in pitch and hence this is likely to determine the maximum usable incidence.

The pitching moment is closely related to the lift coefficient and hence sees the benefit of the enhanced vortex lift for the trailing wing. At lower incidences when the flow is attached, the leading wing makes the greatest contribution to nose down pitching moment. At higher incidences, the trailing wing makes a larger contribution due to the additional non-linear vortex lift effect.

#### 4.4.4 Flow Visualisation

Figure 4.23 shows surface pressure distributions and skin friction lines for the 1303 UCAV at various incidence and sideslip angles from the Cobalt runs with the SARC turbulence model. This gives an intuitive understanding of the effect of sideslip on the leading and trailing wings. At low incidence angles there is very little difference in the flow topology other than the slight tilting of the streamlines towards the incoming flow. As incidence is increased, differences become apparent. The separation point on the leading wing remains further outboard than for the trailing wing. The nature of the separations are quite different. The leading wing exhibits a bubble type separation with a weak vortical flow that generates little additional lift. On the trailing wing, a stronger vortex is seen, having a much stronger influence than is seen on the leading wing or at zero sideslip. At  $\beta = 5^\circ$ , the flow topology on the trailing wing is similar to that at zero sideslip but on the  $\beta = 10^\circ$  the trailing wing shows a double vortex system, like what is commonly found on slender wings. This clearly generates more non-linear vortex lift and the vortex influence is felt further from the separation point than at lower or zero sideslip.

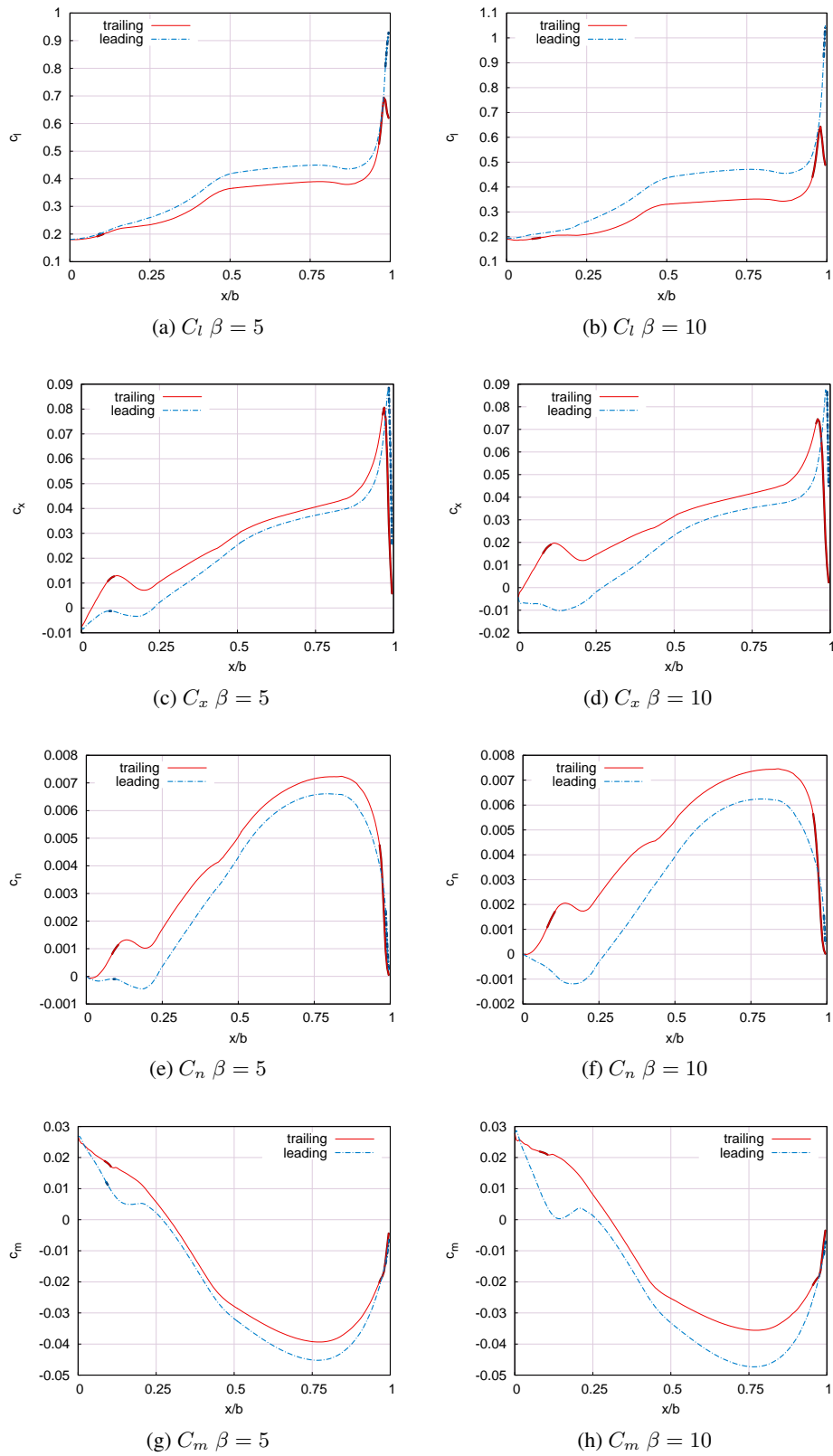


Figure 4.20: Spanwise forces for leading and trailing wings  $\alpha = 5$

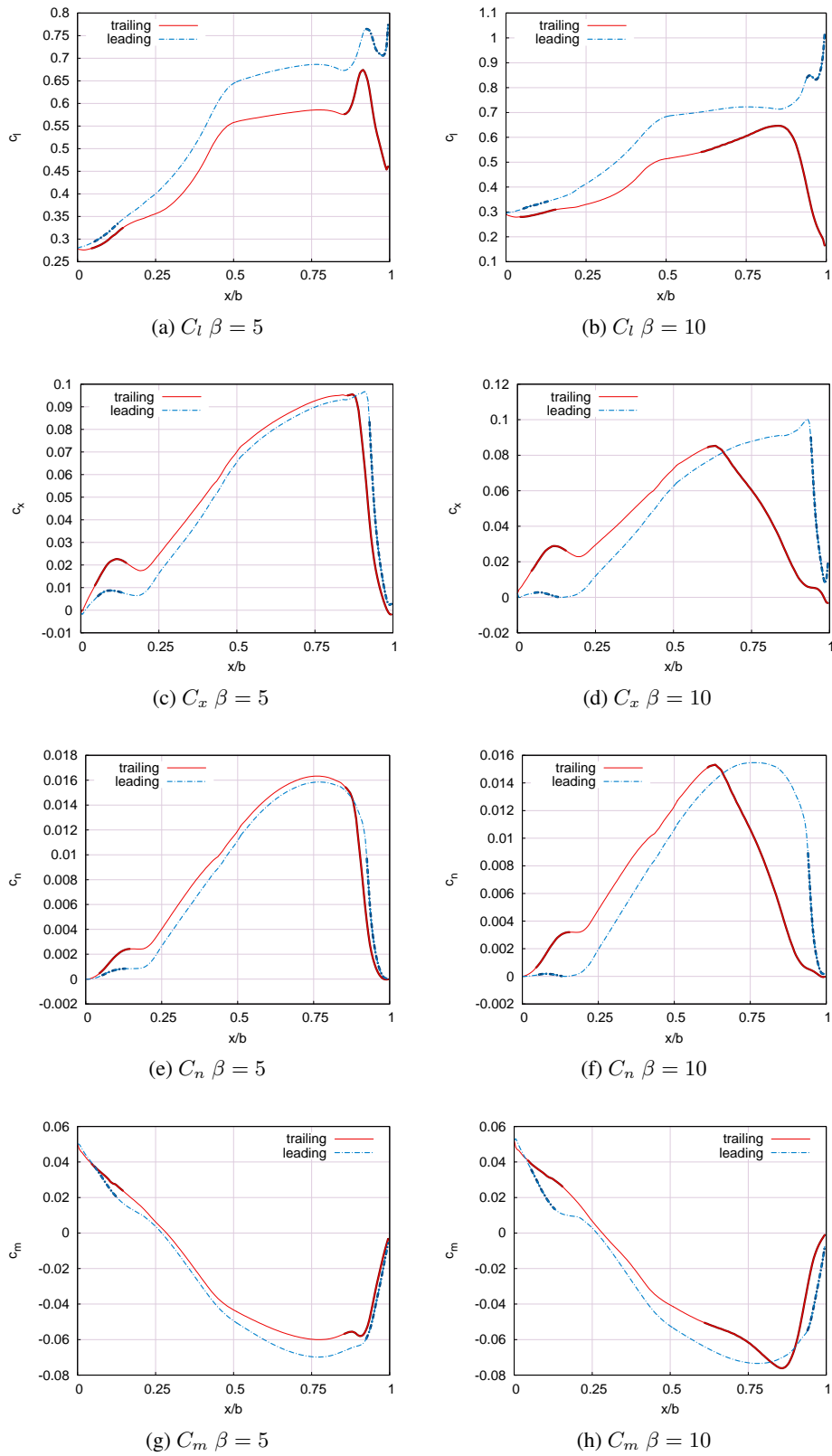


Figure 4.21: Spanwise forces for leading and trailing wings  $\alpha = 8$

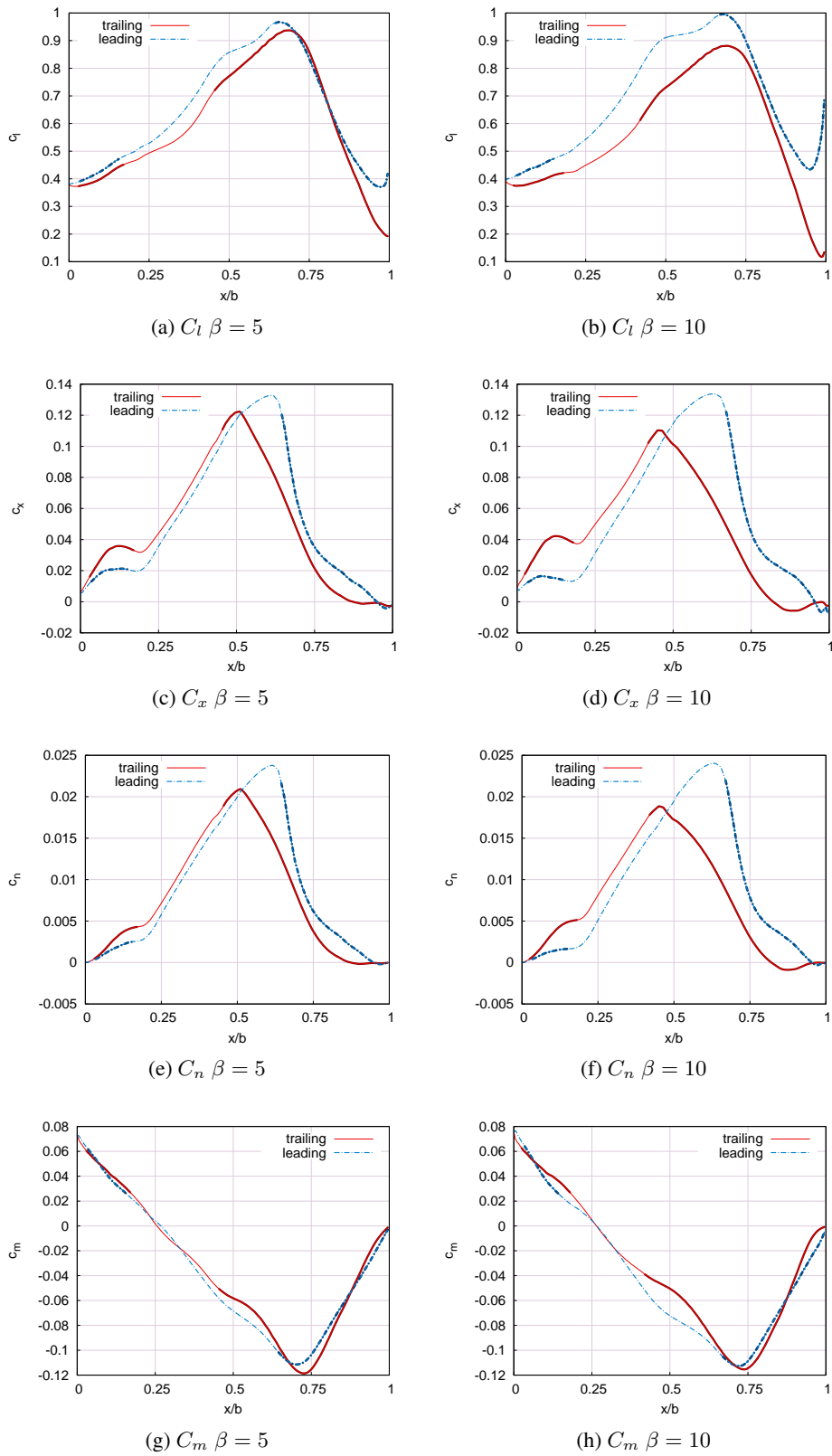


Figure 4.22: Spanwise forces for leading and trailing wings  $\alpha = 11$

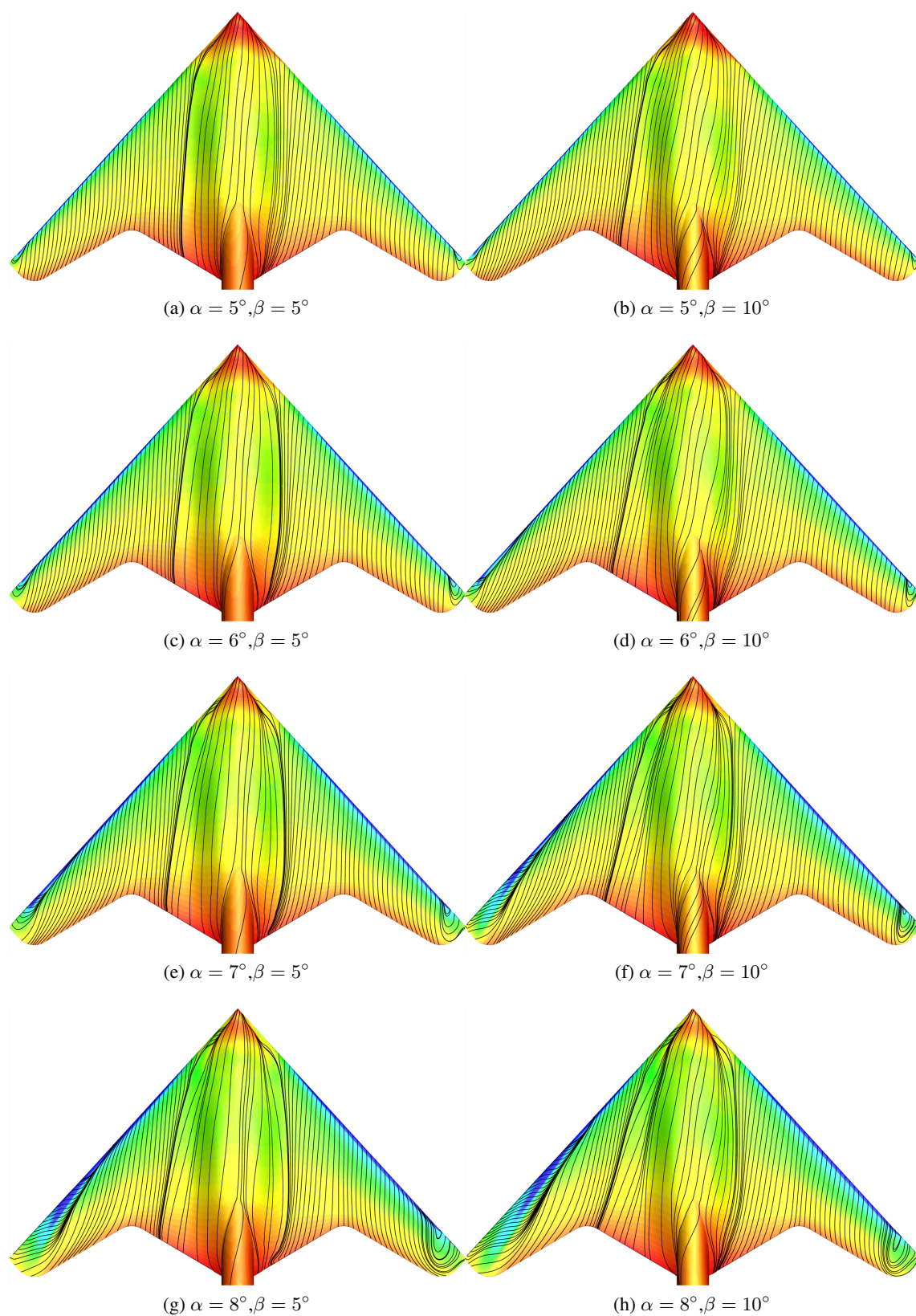


Figure 4.23: Coloured  $C_p$  distribution and skin friction lines at various incidence and sideslip angles



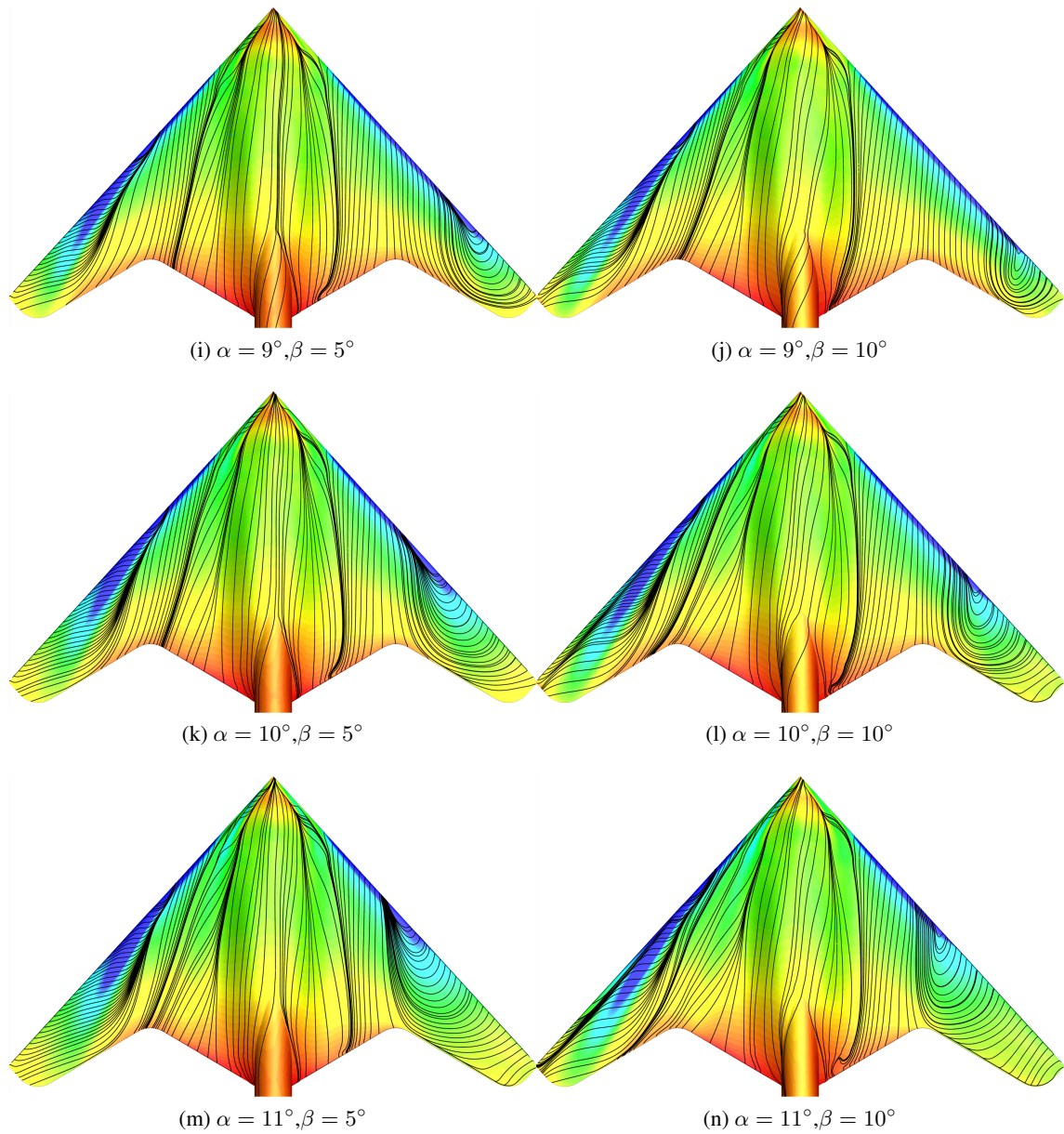


Figure 4.23: Coloured  $C_p$  distribution and skin friction lines at various incidence and sideslip angles (*cont.*)

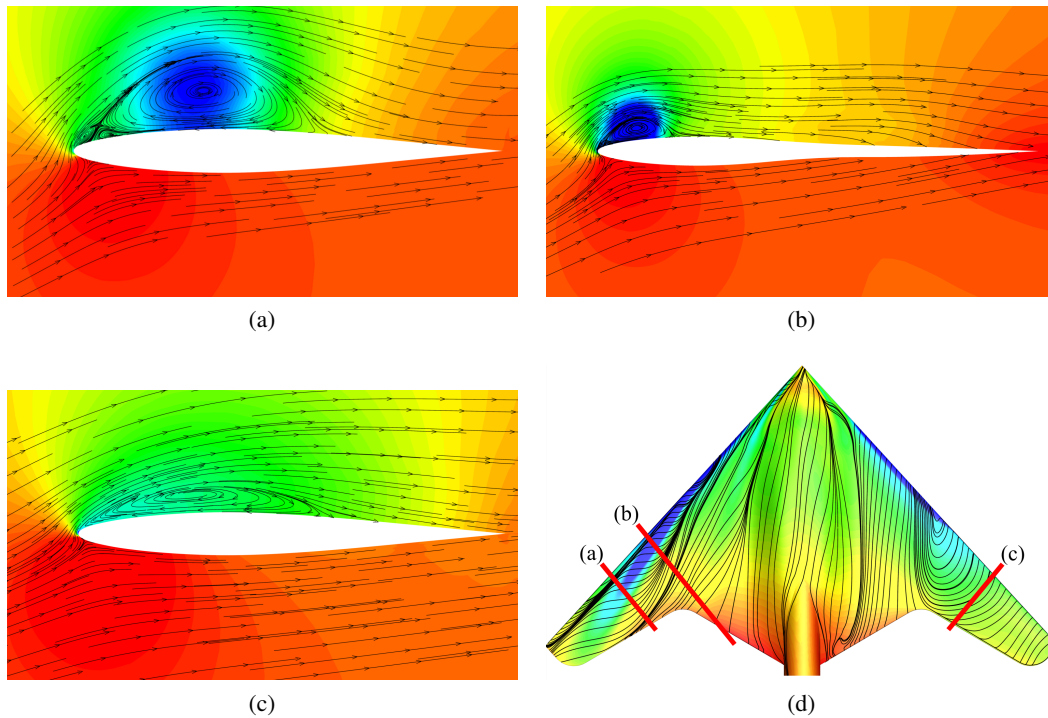


Figure 4.24: Coloured  $C_p$  distribution and streamlines at slices normal to the leading edge  $\alpha = 11^\circ, \beta = 10^\circ$

Slices normal to the leading edge (Figure 4.24) show the flow topology off the wing surface. On the leading wing, reduction in the effective sweep causes the leading edge vortex to become much weaker. The separation resembles a bubble type separation and it does not penetrate the freestream flow very much. On the trailing wing, the increase in sweep causes a strong vortical flow to occur. The double primary / secondary vortex topology can be seen and a strong suction is indicated by the deep blue colour. This vortex pair is much more persistent, staying near the surface and generates more vortex lift than before.

## 4.5 Discussion

The aerodynamics of the 1303 UCAV were previously investigated by several groups with the aim of understanding the performance of RANS solvers for making high lift predictions for this type of planform. Due to the wide range of mesh types, flow solvers and geometrical differences relating to the sting, it was difficult to draw meaningful conclusions about the effect of each of these parameters on the resulting forces, moments and flowfields. In the current investigation, a high quality structured mesh was used to conduct calculations with two different flow solvers (MERLIN and Cobalt), various turbulence models as well as overset mesh calculations to assess the effect of the sting fairing.

Using the MERLIN solver, a detailed investigation has been made into the 1303 UCAV flowfields, analysing spanwise force coefficients, pressure slices as well as skin friction patterns. These indicate that although two sources of flow separation are apparent, pitch divergence is essentially due to

leading edge separation and loss in lift near the wingtip. The vortex from the apex only has an effect at much higher incidences, long after pitch divergence has occurred. Looking at the centre of pressure locations and local pitching moment contributions throughout the incidence range shows that when the flow initially separates, the leading edge vortex has a beneficial (stabilising) effect. This is despite a slight forward movement in centre of pressure that was observed. The influence of this tip vortex is relatively short-lived on this wing and it moves away from the surface and the suction is lost. This leads to a reduction in normal force and hence pitch divergence occurs. Once the separation has passed the moment reference position, the wing returns to positive stability. This is further accelerated by the combining of the wing tip vortex with the vortex emanating from the apex.

With the same computational mesh, freestream conditions and turbulence model (only  $k - \omega$  was common between the codes), some sensitivity can be attributed to the particular flow solver, appearing to have an effect on the resulting forces and moments. There may be many reasons for these discrepancies but they appear to be largely due to the amount of vortex lift predicted which primarily depends on the levels of numerical dissipation in the code and the turbulence modelling. The flow solvers MERLIN and Cobalt are fundamentally quite different in the way that the fluxes are calculated at the cell boundaries and hence are expected to behave slightly differently on the same mesh. Good comparisons of the results is important for confidence in the codes.

Comparing the various wind tunnel results where possible as well as considering corresponding numerical results, it seems that experimentally controlling or predicting transition is extremely important to obtain the correct drag. The numerical results confirm that there is little Mach and Reynolds number sensitivity in the QinetiQ and ARA tests however the drag in the different experiments is very different. This can only be attributed to the large extent of laminar flow present in the QinetiQ experiment which is consistent with Authur's predictions. The sting fairing has also been shown to effect on the computed forces. With the sting, the low incidence drag is increased although this diminishes with increasing incidence. The pitching moment also shows a nose up increment which also diminishes with increasing incidence and there is almost no effect on pitchup.

The directional stability of the 1303 UCAV has also been investigated by performing calculations on the full wing at different sideslip angles. Initially the MERLIN flow solver was used, but the directional stability at low incidence was predicted differently to the experiment. This was due to the omission of the sting fairing in the geometry. To remedy this, the overset mesh feature in Cobalt was used to model the wing and sting combination with the same structured wing mesh, giving much better results compared with the experiment. The effect of the sting fairing was stabilising in yaw and changes only slightly with incidence. The MERLIN results obtained previously were in fact very similar to the Cobalt results when the forces on the sting fairing were omitted. This indicates a good agreement between the codes and suggests little interference with the sting and fairing was present.

The directional stability of the wing changes significantly with incidence. The wing initially displays a benign  $C_{n\beta}$  curve, increasing slightly with incidence angle until a break occurs, making the wing directionally unstable. This was well predicted by both the MERLIN and Cobalt solvers but at an incidence approximately  $1^\circ$  later than in the experiment. Sideslip also affects the pitching moment in both the experiment and the RANS calculation but now with contradictory effects. In the RANS calculation, the pitch stability increases with increasing side-slip angle due to stronger

vortical flows and more nonlinear lift on the trailing wing. With sideslip, the leading wing experiences less enhanced vortex lift than before. In the experimental results the opposite effect is seen with a reduction in pitch stability when the sideslip angle is increased. Little is known about the flowfield or force breakdown in the experiment so the reasons for this are unknown.

Overall the RANS investigation has shown that the trends in the experimental data can be well captured although flow separation and the associated non-linearities happen a little later than in the experiment. An investigation into the effect of the sting has shown that its effects are mainly seen to the directional stability with only a small effect on the pitching moment, and drag at low incidence.

There remain several issues with some aspects of the 1303 predictions, especially with the prediction of drag which is probably attributable to laminar flow, particularly on the lower surface of the wing. This could be further investigated with a transition prediction model although it may be more beneficial to fix transition in future experiments as this would likely be more representative of a full scale aircraft.

## Chapter 5

# UCAV Wing Optimisation

---

An optimisation study for the 1303 UCAV has been conducted attempting to minimise drag in the cruise configuration subject to constraints designed to avoid flow separation at take-off. The methodology combines the flow solver MERLIN to calculate the aerodynamic forces and moments at cruise conditions and the quasi-vortex-lattice method to apply constraints to the design in order to avoid flow separation at take-off. These are combined with an SQP gradient based optimiser to iteratively converge upon a final designed wing.

### 5.1 Geometry and Mesh

#### 5.1.1 Geometry

There are several reasons why the original 1303 geometry is not used for this wing optimisation. The primary reason is that the rounded trailing edge does not represent a typical low observable UCAV. Secondly the trailing edge gap at the root causes unnecessary complications for the geometry parametrisation. The sharp leading edge at the root, while being a likely feature of a realistic UCAV configuration is not properly modelled anyway due to the lack of engine intake and hence a rounded leading edge is preferred.

A new idealised wing geometry was created for the wing optimisation. This wing is based on the original planform but the straight trailing edge sections were extended to give defined trailing edge cranks. The dimensions of the new wing are given in Table 5.1. A NACA 64A008 aerofoil was then applied to this to give the basic wing shape. A representative body was added to the wing which has the same thickness and a similar position of maximum thickness as the original design. The body was blended into the wing using spline functions. A comparison of the two wings is shown in Figure 5.1.

#### 5.1.2 Mesh

The two MERLIN meshes are shown in Figure 5.2. The first (a) was created for the Euler analysis in the optimisation process. The surface mesh has 80 chordwise  $\times$  50 spanwise elements on the upper and lower surfaces. A first cell height of  $10^{-3}$  was used so that near the tip, the normal spacing did not become excessively large compared with the local chord. This results in a mesh size

	$Z(m)$	$c(m)$	$\Lambda_{LE}(\circ)$	$\Lambda_{TE}(\circ)$
root	0.0	0.903	47	-30
C1	0.353	0.320	47	30
C2	0.69	0.153	47	-47
tip	0.762	0.0		

Table 5.1: Squared 1303 planform dimensions

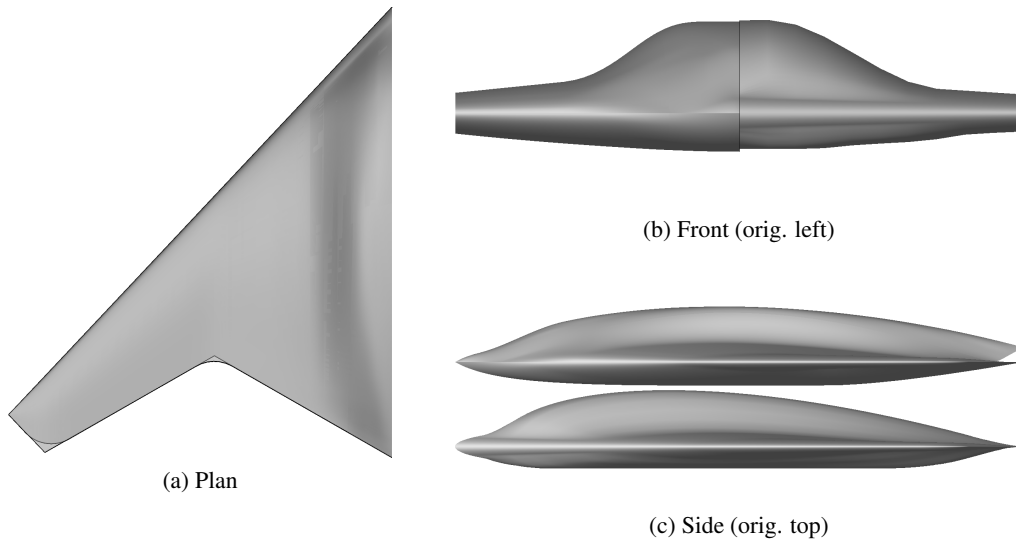


Figure 5.1: Original and optimisation geometry comparison

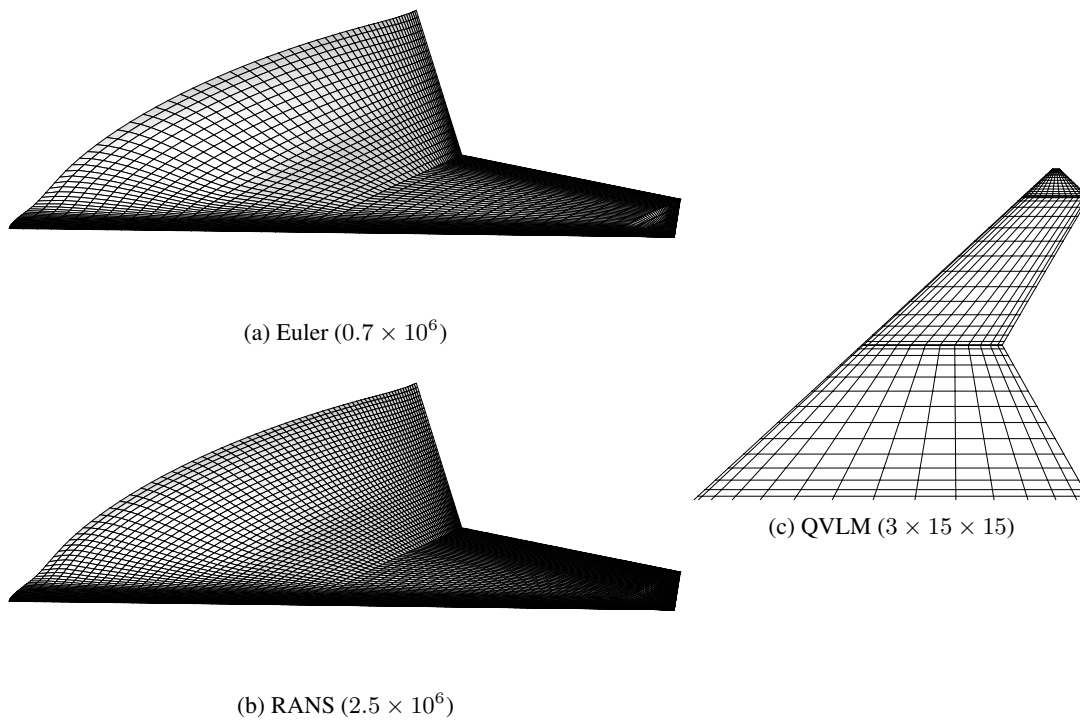


Figure 5.2: Computational meshes

$h(m)$	$T_\infty(K)$	$\rho(kg/m^3)$	$a(m/s)$	$M_\infty$	$v(m/s)$	$v(mph)$	$Re \times 10^{-6}$
0	288.2	1.225	340.3	0.2	68.1	152	25.2
0	288.2	1.225	340.3	0.25	85.1	190	31.5
11,000	216.7	0.364	295.0	0.8	236.0	528	32.6

Table 5.2: 1303 Vehicle scale flow conditions ( $\bar{c} = 5.4m$ )

of around 700,000 elements which was chosen to give reasonable accuracy and a reasonably short solution time. When setting up the optimisation, it is important to consider the turnaround time for designs, especially when computational resource is limited. This encourages experimentation and hence further exploration of the design space and will ultimately result in improved designs.

The second mesh (b) is used for the RANS assessment of the designs. It has 100 chordwise  $\times$  100 spanwise elements on the upper and lower surfaces. The 1<sup>st</sup> cell height was  $5 \times 10^{-7} c_{bar}$  which gives a  $y^+ O(1)$  for the vehicle scale Reynolds number. The mesh size is approximately 2.5 Million elements.

The third mesh (c) is used for the quasi-vortex-lattice analysis. The QVLM becomes mesh independent for very low numbers of elements but it is important that the geometry is adequately represented. A mesh size of  $15 \times 15$  elements is used on each of the three spanwise sections. This gives a solution time of around 1 second so a complete set of constraint gradients for a large number of variables takes in the order of 1-2 minutes.

## 5.2 Design Points

The design lift coefficients for cruise and take-off/landing will be determined by the relative dynamic pressure at each of the points. The take-off speed will be in the range  $M_\infty = 0.2 - 0.25$  at sea level. The cruise speed will nominally be  $M_\infty = 0.8$  at an altitude of 11,000m. Table 5.2 summarises the ISA conditions at these altitudes.

At each of the design points, the lift must equal the weight hence

$$L = W = (1/2\rho v^2 SC_L)_{takeoff} = (1/2\rho v^2 SC_L)_{cruise} \quad (5.1)$$

The ratio of lift coefficients at the two points is given by

$$\frac{C_{L,takeoff}}{C_{L,cruise}} = \frac{(\rho v^2)_{cruise}}{(\rho v^2)_{takeoff}} \quad (5.2)$$

Assuming the lowest (worst case) take-off speed of  $M_\infty = 0.2$  this ratio is 3.57. At the higher take-off speed of  $M_\infty = 0.25$  the ratio is 2.29. Previous work by Nangia [92] suggested that a take-off lift coefficient of around  $C_L = 0.7$  would be the highest you could reasonably expect without excessive twist and camber. Assuming this can be achieved at Mach 0.2, the resulting cruise lift coefficient would be  $C_L = 0.2$ . For a higher speed take-off at  $M_\infty = 0.25$ , and using the same cruise lift coefficient, the take-off lift requirement would be  $C_L = 0.45$ . This gives a range of possible useful take-off lift coefficients and the aim here is to investigate the effect on cruise performance of designing the wing for different high lift capabilities.

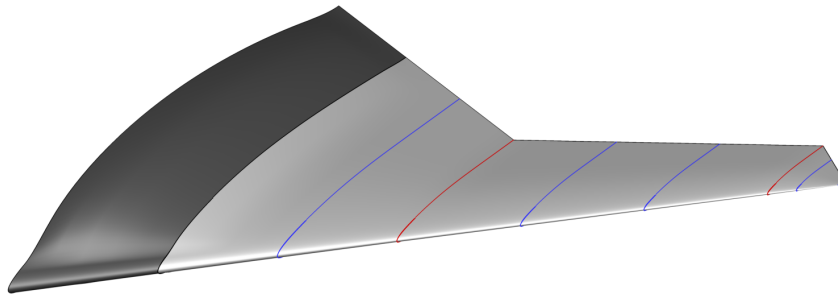


Figure 5.3: Design variable sections

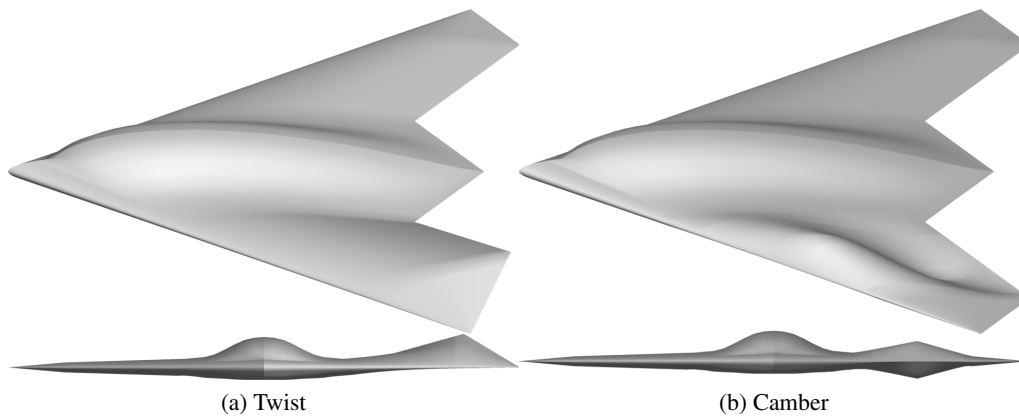


Figure 5.4: Design Variable Examples

### 5.3 Design Variables

Two design variable combinations have been used during the design process, one where the camber and twist is allowed to deform, and one where the camber, twist and thickness are allowed to deform. The first set of design variables (camber and twist) were used for initial design and sensitivity studies. Later the thickness was allowed to attempt to overcome some problems with the design and gain further improvements at cruise. In each case, the master sections (highlighted in Figure 5.3) remain the same. In the figure, red lines indicate sections where wing twist are applied (section rotated about spanwise coordinate). Aerofoil/camber deformations are applied at the sections marked in red and in blue. Near the root, the wing is shaded darker grey to indicate that no camber or aerofoil displacements occur here. This is to avoid making large displacements to the body geometry and hence causing packaging problems. This region does get modified by the first twist variable but displacements are small for modest twist angles and reduce to zero at the root. For camber or aerofoil displacements, Bernstein polynomials of order 9 (10 variables) are used. For camber sections, this results in 8 design variables per section (leading and trailing edge are fixed), and for thickness modifications there are 10 variables per section. The design variables used are summarised in Table 5.3.



Design Variable	Number of sections	Number per section	Total
incidence angle $\alpha$	1	1	1
twist	2	1	2
camber	8	8	64
thickness	8	10	80
<b>total camber</b>			<b>67</b>
<b>total camber+thickness</b>			<b>147</b>

Table 5.3: Summary of design variables

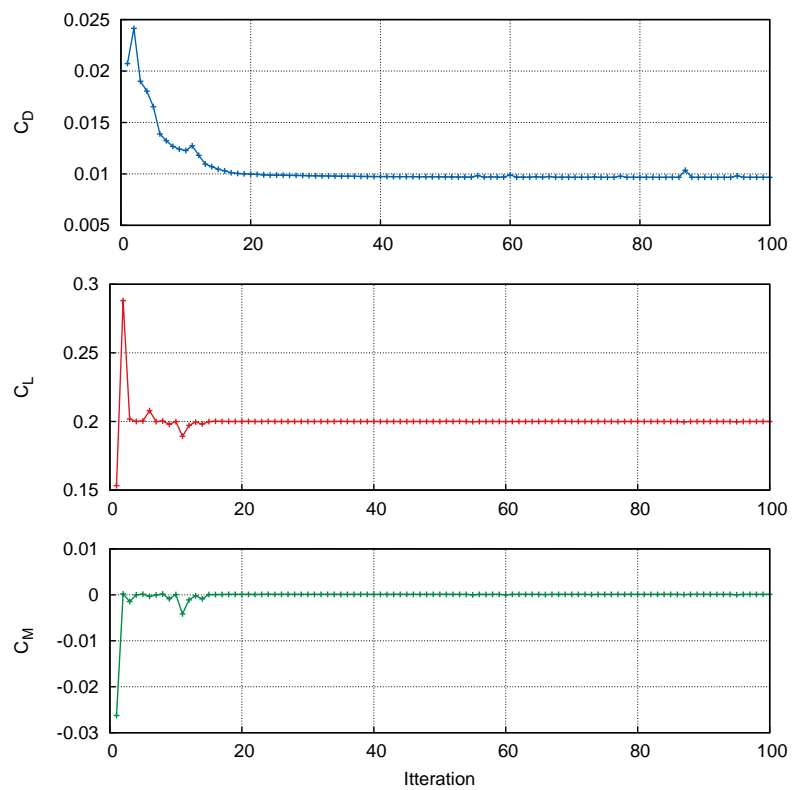


Figure 5.5: Optimiser convergence

Naming System	Take-off $C_L$	Design Variables	Notes
$C_L0.0C$	N/A	Twist,Camber	Cruise design
$C_L0.4C$	0.4	Twist,Camber	
$C_L0.5C$	0.5	Twist,Camber	
$C_L0.5CT$	0.5	Twist,Camber,Thickness	
$C_L0.6C$	0.6	Twist,Camber	

Table 5.4: Designed wings

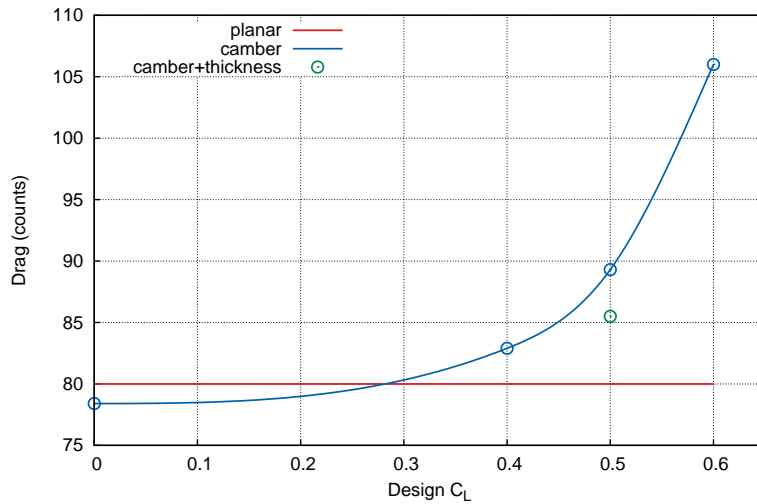


Figure 5.6: Objective vs constants for various designs

## 5.4 Optimiser convergence

A summary of the different designs produced with assigned names is given in Table 5.4. They are labelled according to the design lift coefficient and the design variables used. The optimisations were run on a small HPC cluster over 16 Processors. With the current mesh size, the procedure took an average of 0.8 hours (clock time) per design iteration so could typically be run overnight.

Figure 5.5 shows the objective and constraint history for the  $C_L 0.6C$  design run for 100 iterations. The design was initialised with some nominal camber and twist to avoid start-up problems. The objective function (drag) reduces significantly over the first 20 optimiser iterations when relatively large changes occur in the design variables. The initial lift is well below the design lift coefficient ( $C_L = 0.2$ ) due to initial washout and after 1 iteration it overshoots above the design lift. The lift and pitching moment then oscillates in the first 20 or so iterations before settling at the final value. The design has more or less converged after 40 iterations although was run for 100 steps in total to see if any further improvements could be made. Subsequent runs used this first design as a starting point which reduces the start-up oscillations giving estimated saving equivalent 5 iterations. Upon completion, in each case, the optimiser has converged, not being able to reduce the objective any more, and all the constraints are satisfied to within the specified tolerance.

The following sections will discuss the final objective functions and the impact of the high lift constraint, the shape of the designs produced and an evaluation of the designs using the previously described RANS method on a much finer computational mesh.

## 5.5 Designed wings

A summary of of the final objective function values for each of the designed wings is shown in Figure 5.6. This shows a small improvement over the planar wing for the  $C_L 0.0C$  design of around 2 drag counts ( $10^{-4}C_D$ ). Limiting the improvement that can be gained, is the trim constraint ( $C_M$ ), which will give a drag penalty compared with an untrimmed wing. As the design lift is increased, a drag penalty becomes apparent due to the increased amount of of twist and camber required to

obtain the specified high lift performance. For the  $C_L 0.6C$  design, this penalty becomes quite large (over 25 counts more than the planar wing). Allowing the thickness to change partially alleviates this drag rise for the  $C_L 0.5CT$  design showing a 4-5 drag count reduction over the camber only design.

### 5.5.1 Geometry

Figures 5.7 and 5.8 show the geometry and aerofoils for each of the designed wings. A discussion will be made about how the optimiser has achieved the above improvements.

#### 5.5.1.1 Cruise Design

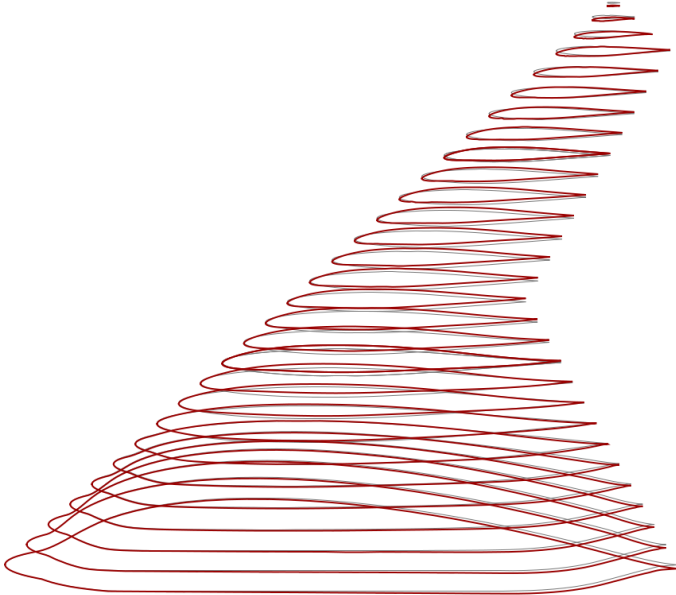
As shown in Figure 5.7(a), the cruise design (no high lift constraint) has only very subtle changes compared with the original planar wing. The aerofoils have been slightly cambered near the leading edge which has the effect of unloading this region slightly. Furthermore, a small amount of washout has been applied at the first and second cranks ( $2^\circ$ ) which helps to trim the wing as well as slightly modifying the lift distribution.

#### 5.5.1.2 High Lift Camber Designs

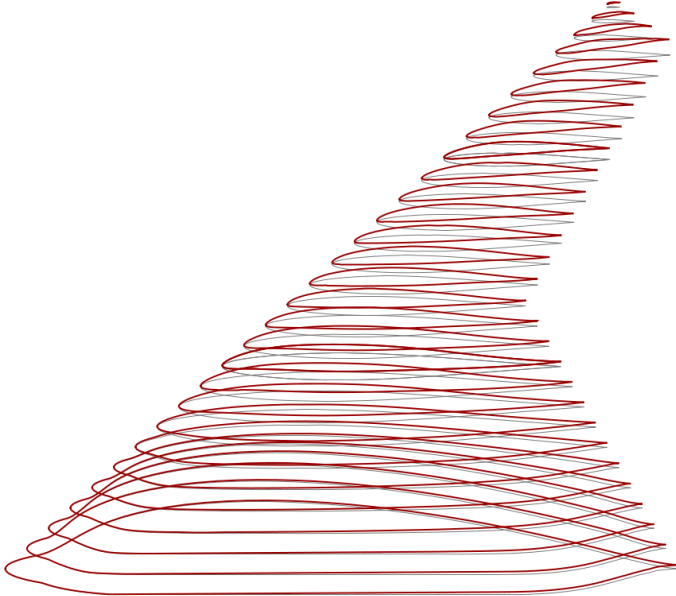
The high lift cambered wing designs (b,c,e) show much larger geometrical changes. A significant amount of twist and camber has been added in order to sufficiently unload the wing leading edge at the take-off incidence, especially towards the wingtip. As shown in Figure 5.8, at the first crank ( $\eta = 0.46$ ), the aerofoil sections for the three designs are all very similar, with a small amount of leading edge droop to keep the leading edge flow attached as well as a slight reflex to bring the aircraft back in trim. Similar aerofoil shapes indicate that this area is not critical for the high lift performance and hence the geometry is chosen for cruise requirements. The section at  $\eta = 0.68$  is located mid way between the first and second cranks. Here the aerofoils are again quite similar between the designs but the washout is increased with increasing high lift constraint. At  $\eta = 0.91$  (second crank), again the twist increases with increasing high lift constraint, this time the change is more pronounced. Interestingly, the leading edge droop actually reduces with increasing high lift constraint. This is because this section is locally over twisted in order to obtain sufficient washout outboard of this point. This is a consequence of having just two sections where the wing is allowed to twist and will clearly will have an associated drag penalty. The problem could be alleviated with an additional twist section further outboard but this may affect the RCS and/or control integration. Near the trailing edge, the optimiser has also added additional camber. This looks to be akin to the aft loaded supercritical aerofoil sections where additional lift is generated on the lower surface. At  $\eta = 0.95$ , mid way between the second crank and the tip, the aerofoils become even more cambered. The twist here is the same as at the second crank they are intrinsically linked.

#### 5.5.1.3 High Lift Camber and Thickness Design

The last design (5.7(d)) is for a take-off lift coefficient of  $C_L = 0.5$  but this time the thickness distribution was allowed to change. At the first crank, the leading edge region became thinner with thickness being moved rearwards presumably to improve its transonic performance. Other than this, the camberline is very similar to the camber only design. At  $\eta = 0.68$  the thickness distribution is very similar to the original NACA64A008 aerofoil. At the second crank ( $\eta = 0.91$ ) and outboard

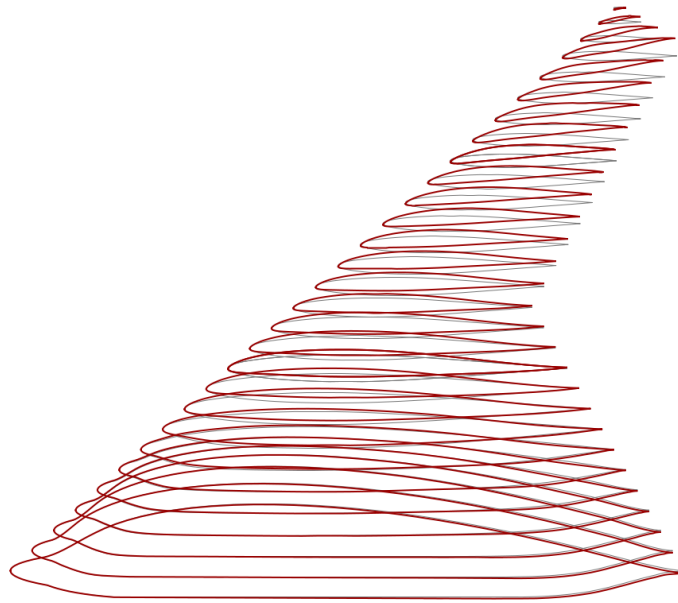


(a)  $C_L 0.0C$  Design

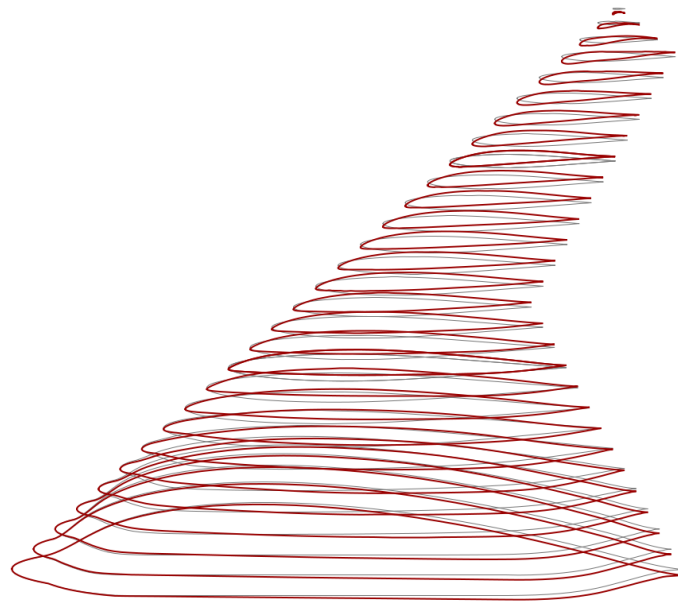


(b)  $C_L 0.4C$  Design

Figure 5.7: Designed wings

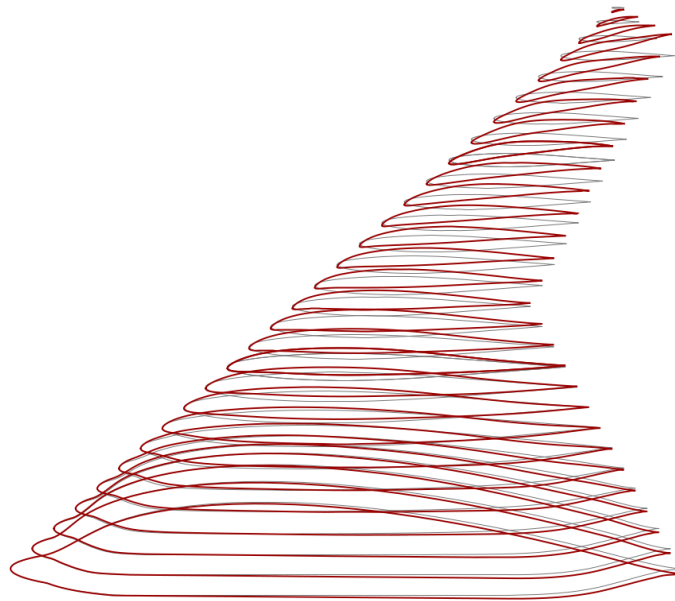


(c)  $C_L 0.5C$  Design



(d)  $C_L 0.5TC$  Design

Figure 5.7: Designed wings *Cont.*

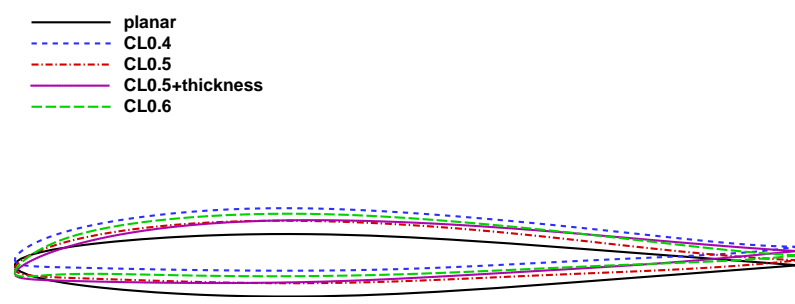
(e)  $C_L 0.6C$  DesignFigure 5.7: Designed wings *Cont.*

of this point, the leading edge became noticeably thicker. This has allowed there to be less twist and hence the section can sustain a higher lift at both cruise and take-off. This will improve the cruise lift distribution and hence reduce the drag.

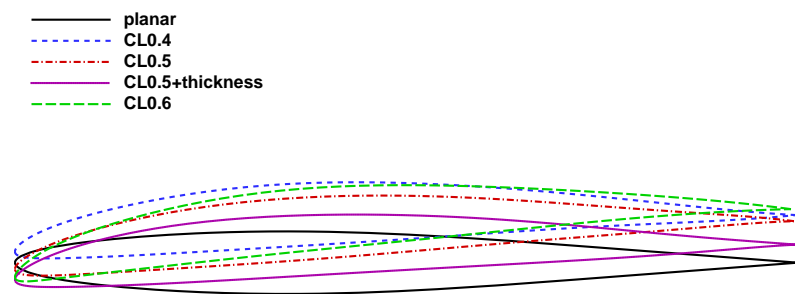
Modifying the camber and twist is thought to have a relatively small effect on the vehicle RCS. Changing the leading edge radius however may have a larger effect. In-service stealth aircraft e.g. B2 have sharp leading edges particularly towards the tip in order to reduce RCS but this is in direct contradiction to aerodynamic requirements to keep the flow attached. Another stealth platform F-117 has a sharp leading edge along the whole span. This however is on a highly swept wing  $> 60^\circ$  which allows additional non-linear vortex lift for take-off and landing. It does however mean that the aspect ratio will be low and hence the aircraft will have a low range. When designing the outer shape of a low observable aircraft, changing parameters that have a large effect on the RCS is not really advised unless the effects are well understood. Ultimately a combined aerodynamic / radar signature optimisation may provide improved designs although it may be difficult to formulate sensible objectives or constraints. Considering the leading edge radius, there will essentially be a trade-off between observability and high lift capability, which will ultimately drive the size / cost of the resulting vehicle.

#### 5.5.1.4 Euler $C_p$ Slices: Cruise

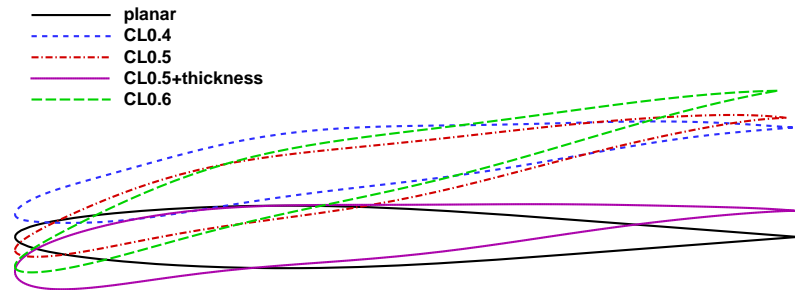
Figure 5.9 shows the final design pressure distributions from the Euler calculations ( $C_L = 0.2$ ). This is useful for looking at the relative chordwise and spanwise loadings as well as identifying shockwaves near the leading edge, not so obvious on the coloured  $C_p$  contour plots. The planar wing, from approximately the mid span outwards, has a peaky pressure distribution with increasingly large suction peaks. These peaks are quickly terminated by a strong shock near the leading edge.



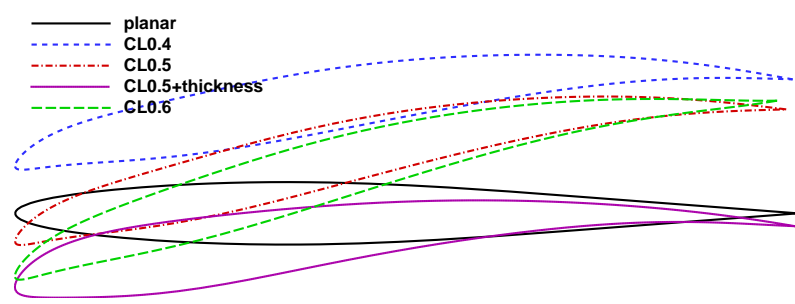
(a)  $\eta = 0.46$



(b)  $\eta = 0.68$

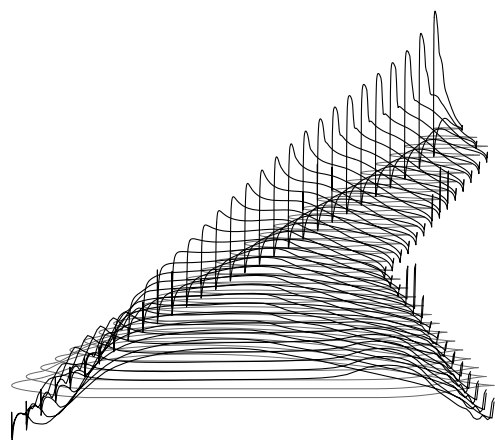


(c)  $\eta = 0.91$

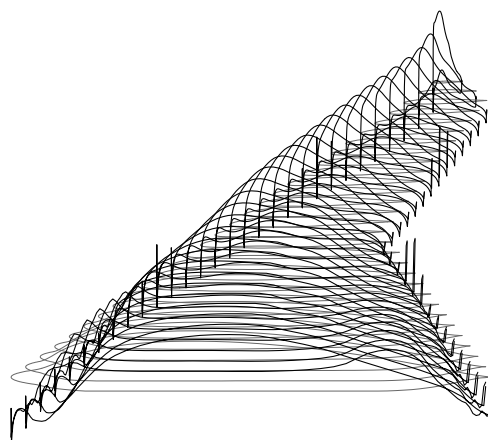


(d)  $\eta = 0.95$

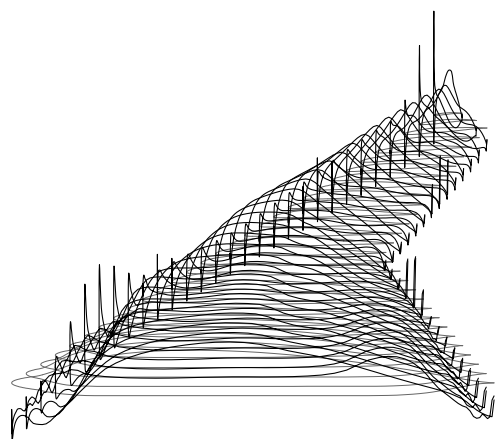
Figure 5.8: Aerofoils



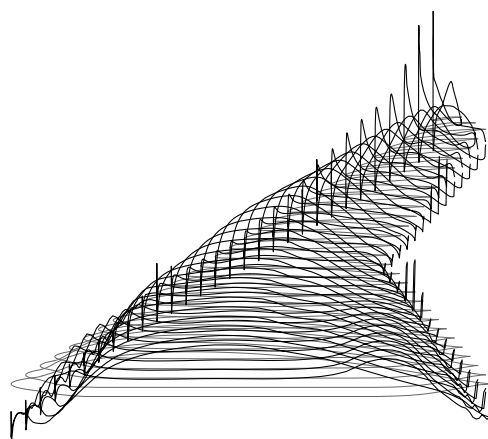
(a) planar



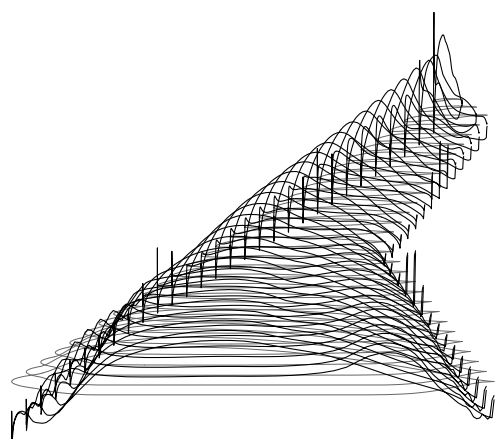
(b)  $C_L 0.0C$



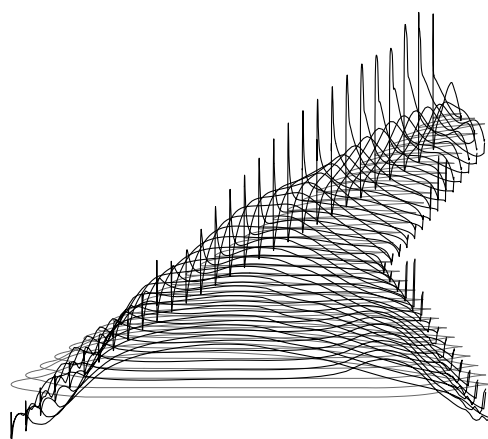
(c)  $C_L 0.4C$



(d)  $C_L 0.5C$



(e)  $C_L 0.5CT$



(f)  $C_L 0.6C$

Figure 5.9: Euler  $C_p$  distributions at cruise



For the cruise design ( $C_L 0.0C$ ), these pressure peaks have been eliminated. Now the highest  $C_p$  is found at approximately 1/3 of the chord with a shallower compression. The wing is now shock free apart from the very wingtip where the local loading remains high.

With the high lift designs, due to the degree of twist and camber applied, the wing now has negative loadings at the leading edge, indicated by suction on the lower surface and higher pressure on the upper surface. This becomes worse as the high lift constraint is increased. For the  $C_L 0.4C$  design, the region of negative loading is small and hence the drag penalty will be relatively small. For the  $C_L 0.5C$  and  $C_L 0.6C$  designs, the region becomes larger and there are shockwaves present on the lower surface. The design with modification of the thickness distribution was primarily intended to remedy this problem. As seen for the  $C_L 0.5CT$  design, the negative leading edge loadings are significantly reduced when the thickness is allowed to change.

Other changes visible in the pressure distributions are that for high lift constrained wings, more use is made of the lower surface for generation of lift. This helps to preserve the span loading of the planar or cruise wings (close to elliptical) when a high degree of washout is applied, otherwise these outboard sections would generate very little lift, only serving to reduce the effective aspect ratio of the wing giving a drag penalty.

An important consideration with the current method is that these designs were formed for a low drag in an Euler flow regime. In choosing an Euler objective function we have assumed that the improved designs will also be improved for viscous flows. This assumption will become invalid for wings which have a lot of twist and camber because they may experience early flow separation, resulting in a degradation in performance. This is seen with the higher lift designs in the RANS evaluation.

### 5.5.2 RANS evaluation

A RANS evaluation of the designed wings was conducted using the MERLIN flow solver and a similar mesh to that used in the 1303 test case investigation. The mesh size is now larger because a smaller 1<sup>st</sup> cell was required in order to resolve boundary layer at the higher Reynolds number. Analysis of the total forces and flowfields are given for both take-off and cruise conditions.

#### 5.5.2.1 Total Forces

Lift drag and moment coefficients are plotted against  $\alpha$  in Figure 5.10 for take-off conditions and Figure 5.11 for cruise. At cruise, each of the designs retains a linear lift curve slope for longer by at least  $2^\circ$ . The lift curve is shifted slightly lower due to the addition of washout in the designs. The lift curve indicates that the designed  $C_L 0.5CT$  wing now manages to sustain the most lift before stall. The cruise  $C_L$  is found at approximately  $\alpha = 3^\circ$ . The drag at this point is quite close between the designs with an increasing penalty for higher high lift constraints. With the exception of the  $C_L 0.6C$  design, at  $3^\circ$  the drag is actually lower than that of the planar wing. In contrast to the invicid analysis used in the optimisation loop, now the  $C_L 0.5CT$  wing actually has the lowest drag. Off design, at higher lift coefficients, the designed wings all have a lower drag than the planar wing due a reduction in the tip separation. Below the design  $C_L$ , the drag penalty of designed wings is higher, mainly due to flow separation on the lower surface of the wing.

For pitching moment, the planar wing is untrimmed with a nose down pitching moment generated at cruise. The  $C_L 0.4C$  design is now in trim at the design lift. The  $C_L 0.5C$  and  $C_L 0.6C$  designs

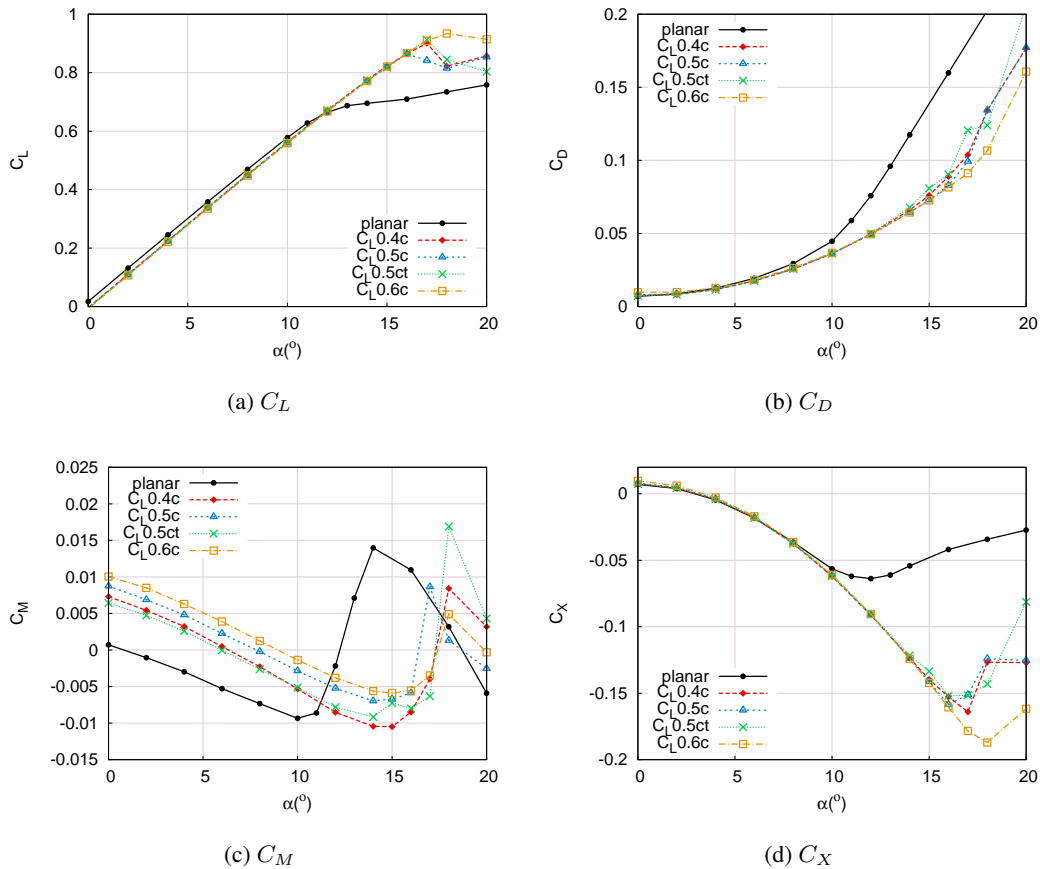
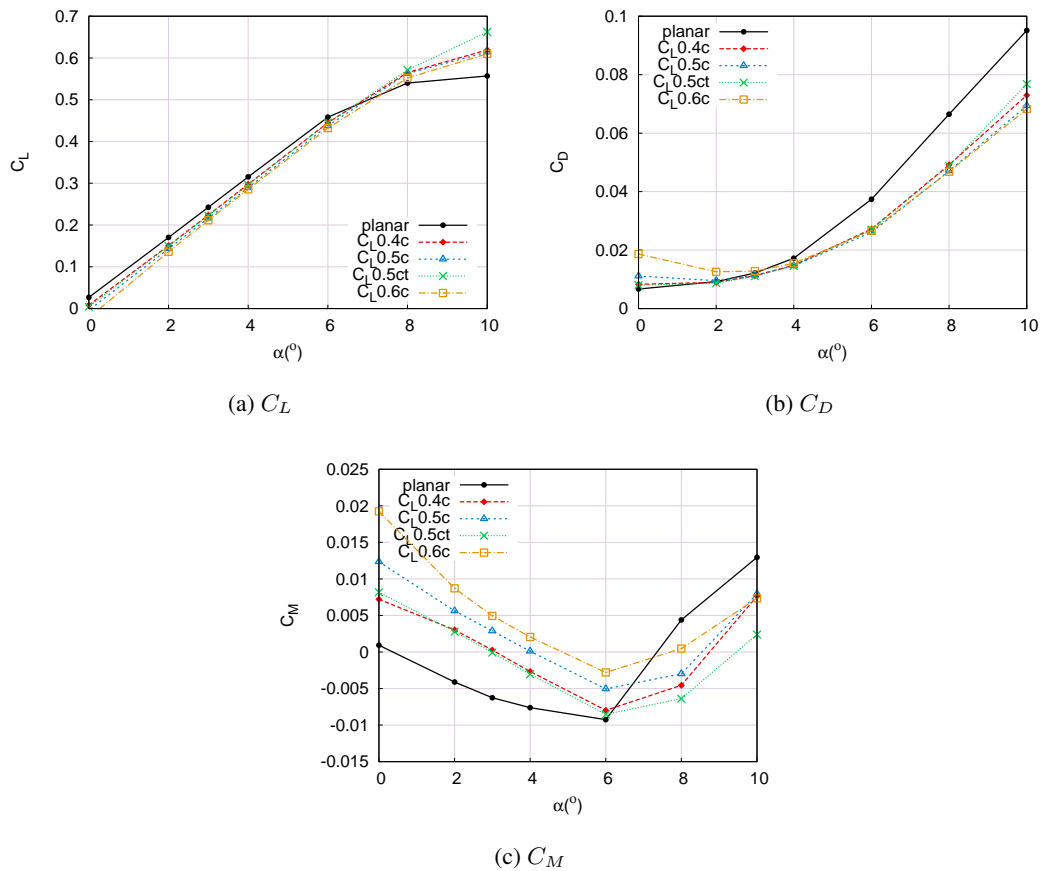


Figure 5.10: Designed wings total forces  $M = 0.25$

however have a small nose up pitching moment generated. Figure 5.12 shows that these wings experience leading edge flow separation and therefore enhanced suction due to the resulting vortex on the lower surface near the tips. Being behind the centre of gravity, this generates a nose up moment. This highlights a deficiency in the current methodology in that the Euler analysis does not capture the lower surface separation phenomenon. Using a viscous flow and adjoint solver for design may remedy the trim problem even if the flow separation could not be eliminated. A wing with leading edge separation on either the upper or lower surface may have undesirable directional stability characteristics which should be investigated. The lower surface flow separation has been eliminated on the  $C_L 0.5CT$  design and hence it is also in trim at the design lift. This is due to a larger leading edge radius at the wingtips and reduced washout. With a larger leading edge radius, the aerofoils can perform adequately over wider  $C_L$  range.

At take-off we are mainly interested in the high lift capability of the wings, determined by the lowest  $\alpha$  for  $C_{L,max}$ , pitchup or directional instability constraints but here only the longitudinal (lift,pitch) constraints are considered. The wings were not designed to be in trim at take-off so once trimmed, a small lift and/or drag penalty can be expected due to the trailing edge flap ‘up’ control deflections that would be required. The lift curve slope indicates that for the designed wings, the linear region now is extended by  $6^\circ$  with an abrupt stall rather than a reduction in slope as seen for

Figure 5.11: Designed wings total forces  $M = 0.8$ 

the planar wing. The drag is also reduced for the designed wings at higher lift coefficients ( $> 4^\circ$ ) due to a reduction in the amount of flow separation. This has the additional benefit of reducing the power requirement for take-off.

For the designed wings, the pitchup incidence has been increased from  $10^\circ$  to  $14 - 16^\circ$ , approximately  $2^\circ$  before the maximum lift occurs. The wings with higher high lift constraints perform better in this regard. All of the wings actually perform better than intended, reaching a lift coefficient of around  $C_L = 0.8$  before pitch up, giving an indicating that they may be over constrained. This will be discussed further in regard to the resulting flowfields where details of the flow separation can be analysed. This exceeds the estimate of  $C_{L,max} = 0.7$  given by Nangia [69] during a previous design attempt.

Another important indicator of the onset of flow separation and pitch divergence is the axial force. The deviation of axial force from the attached flow curve indicates loss of leading edge suction and hence stall. The  $C_L 0.4C$  and  $C_L 0.5C$  wings begin to deviate from the attached flow curve at  $14^\circ$ . The  $C_L 0.6C$  wing keeps predominantly attached leading edge flow up to  $17^\circ$ . This indicates that when a higher  $C_L$  is specified in the constraint, the flow separation moves away from leading edge and hence the current high lift constraint is no longer completely valid.

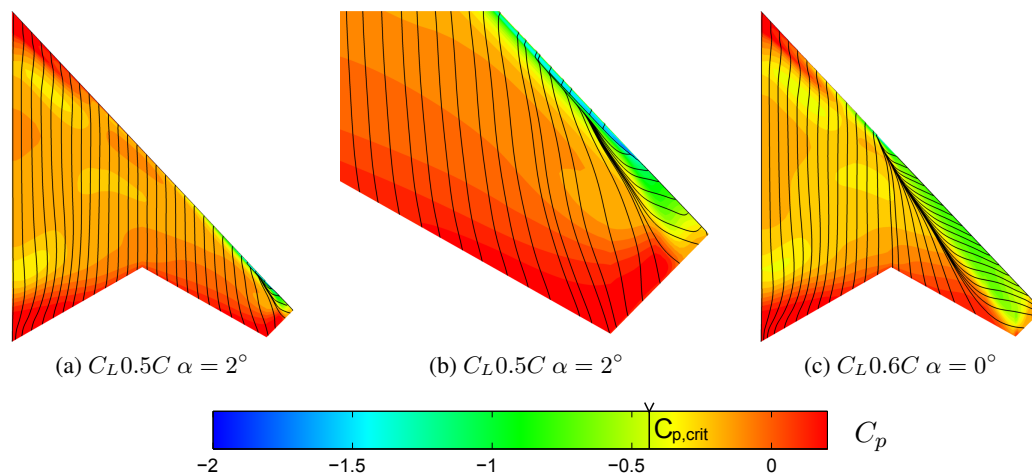


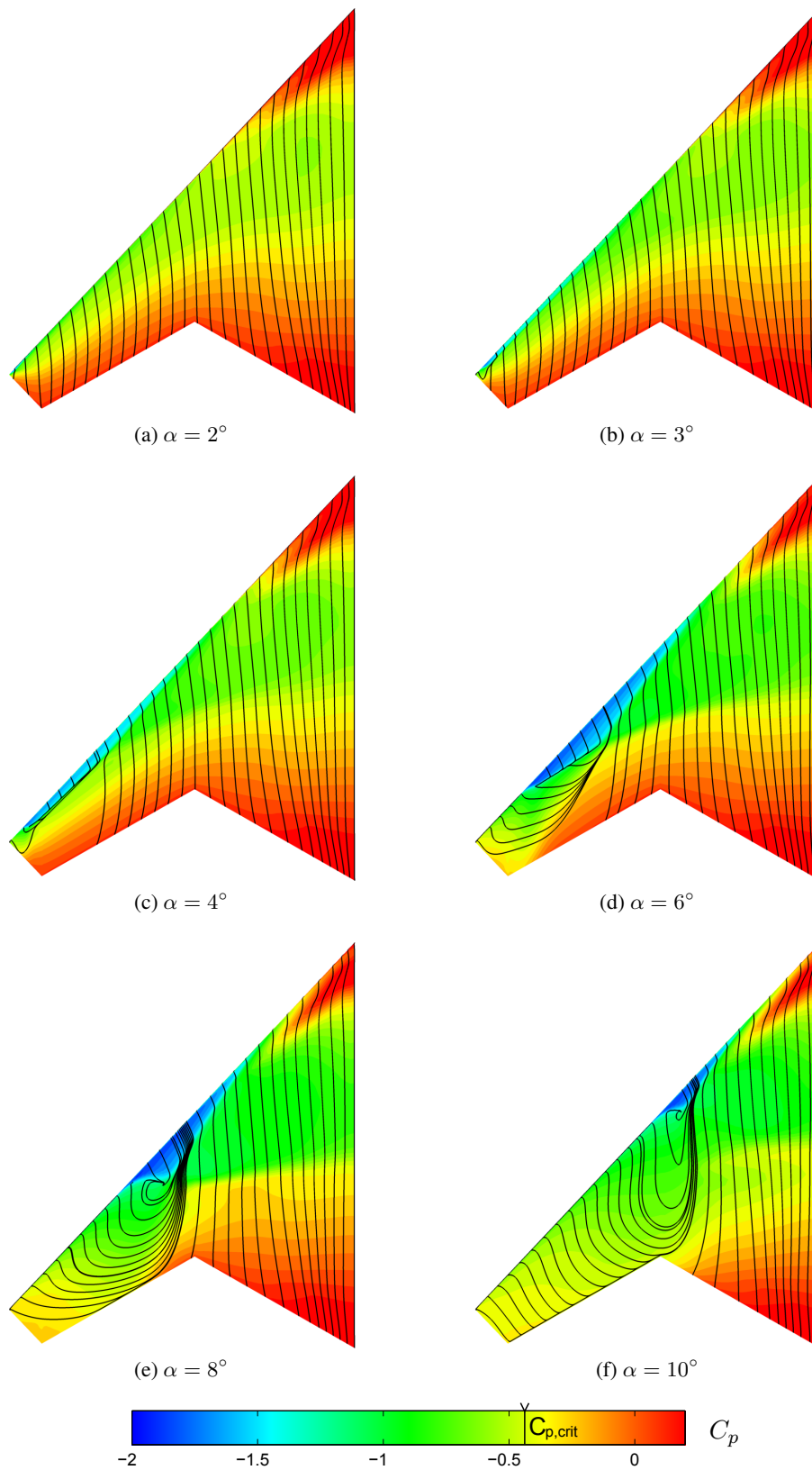
Figure 5.12: Lower surface separation on designed wings at low incidence,  $M = 0.8$

#### 5.5.2.2 $M = 0.8$ Flowfields

At cruise, the planar wing has flowfield characteristics quite different from those at low speed. As shown in Figure 5.13 at lower incidences  $< 6^\circ$  before flow separation occurs, there are normal shockwaves present close to the leading edge on the wing upper surface. These are referred to as the leading edge shocks. As the incidence is increased, a small wingtip separation begins to develop in a similar manner to the low speed case. When the incidence reaches  $6^\circ$ , a much larger separation suddenly occurs which begins at the junction of a newly formed normal shock originating from the body region and the leading edge shocks mentioned previously. This occurs at  $6^\circ$ , which is also the pitch up incidence. This second shock is normal to the flow at the wing root and begins to curve backwards, following the wing sweep further outboard. The shock is initially present due to the ‘middle effect’ where the wings join and the effective sweep is zero. It is exacerbated by the additional thickness of the fuselage.

The designed wing  $C_L 0.4C$  (Figure 5.14) displays similar behaviour although now the leading edge shocks are either eliminated or weakened through the addition of leading edge camber. Separation is now caused simply due to the strength of the normal shock. In each case pitchup still occurs at around  $6^\circ$  although  $C_L$  is actually lower than that for the planar wings. Addition of washout and camber towards the tips does little to delay the onset of this separation so the designed wings do not really have improved high lift performance at cruise. This may not be of particular concern as the ability to perform high g manoeuvres at cruise is unlikely to be an important requirement.

For the designed wings with higher design lift coefficients, a slight delay to the flow separation is observed but this makes little difference to the total forces with pitchup happening shortly after. We see that in some cases, at  $6^\circ$  or  $8^\circ$ , when a shock induced separation occurs near the inner crank, the wingtip actually retains attached flow.

Figure 5.13: Planar wing  $M = 0.8$  coloured  $C_p$  distributions and skin friction lines

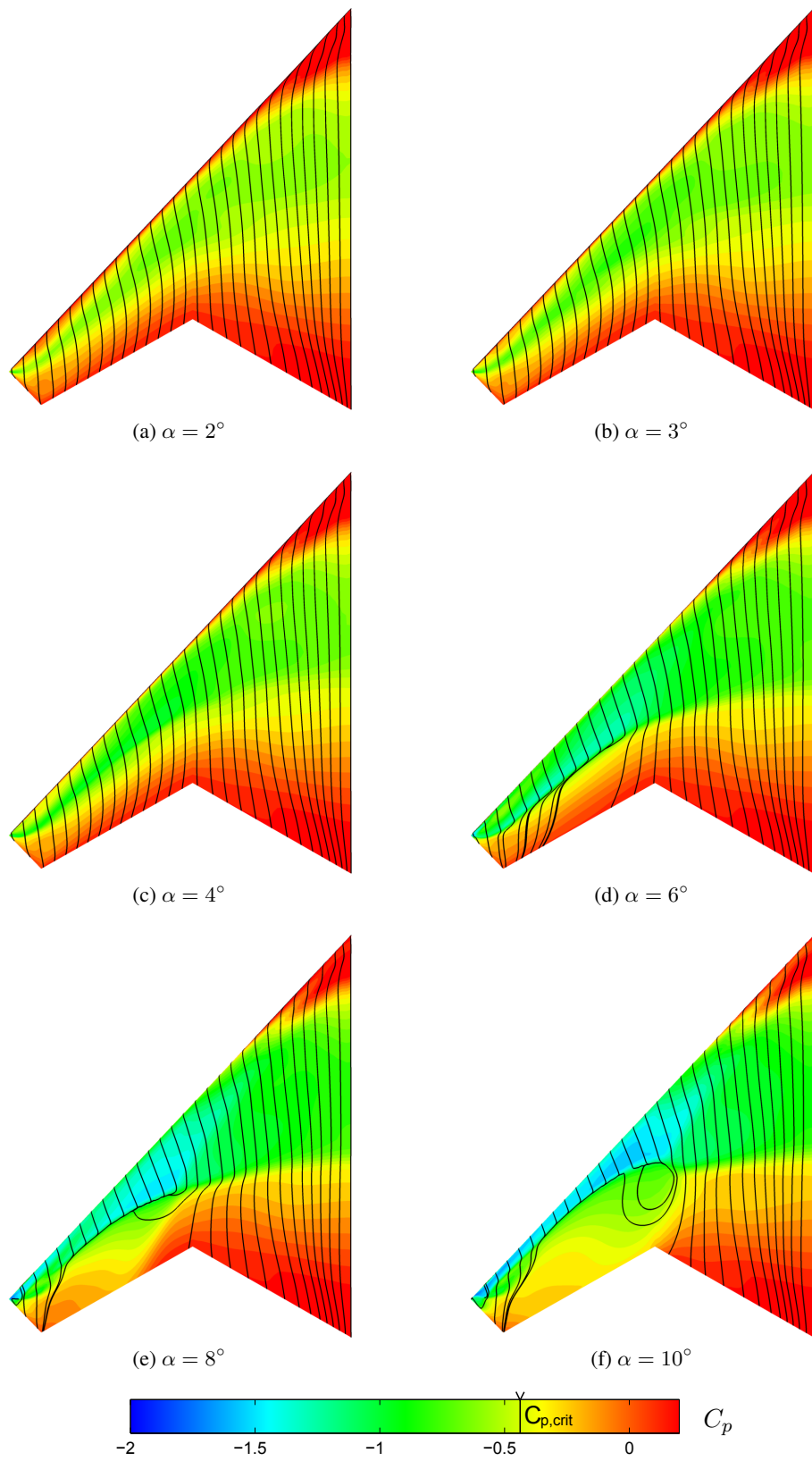


Figure 5.14:  $C_L 0.4C$   $M = 0.8$  coloured  $C_p$  distributions and skin friction lines

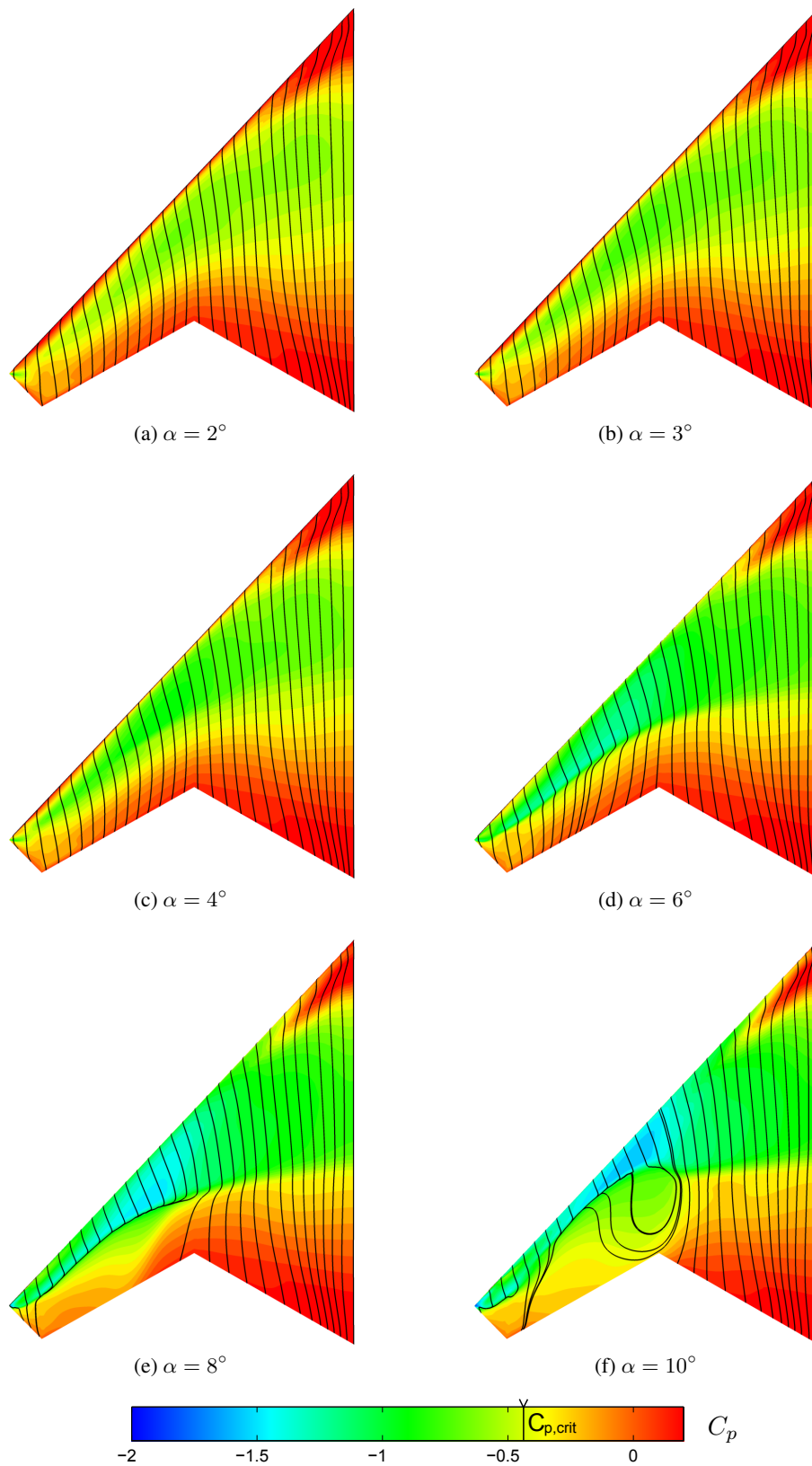


Figure 5.15:  $C_L 0.5C$   $M = 0.8$  coloured  $C_p$  distributions and skin friction lines

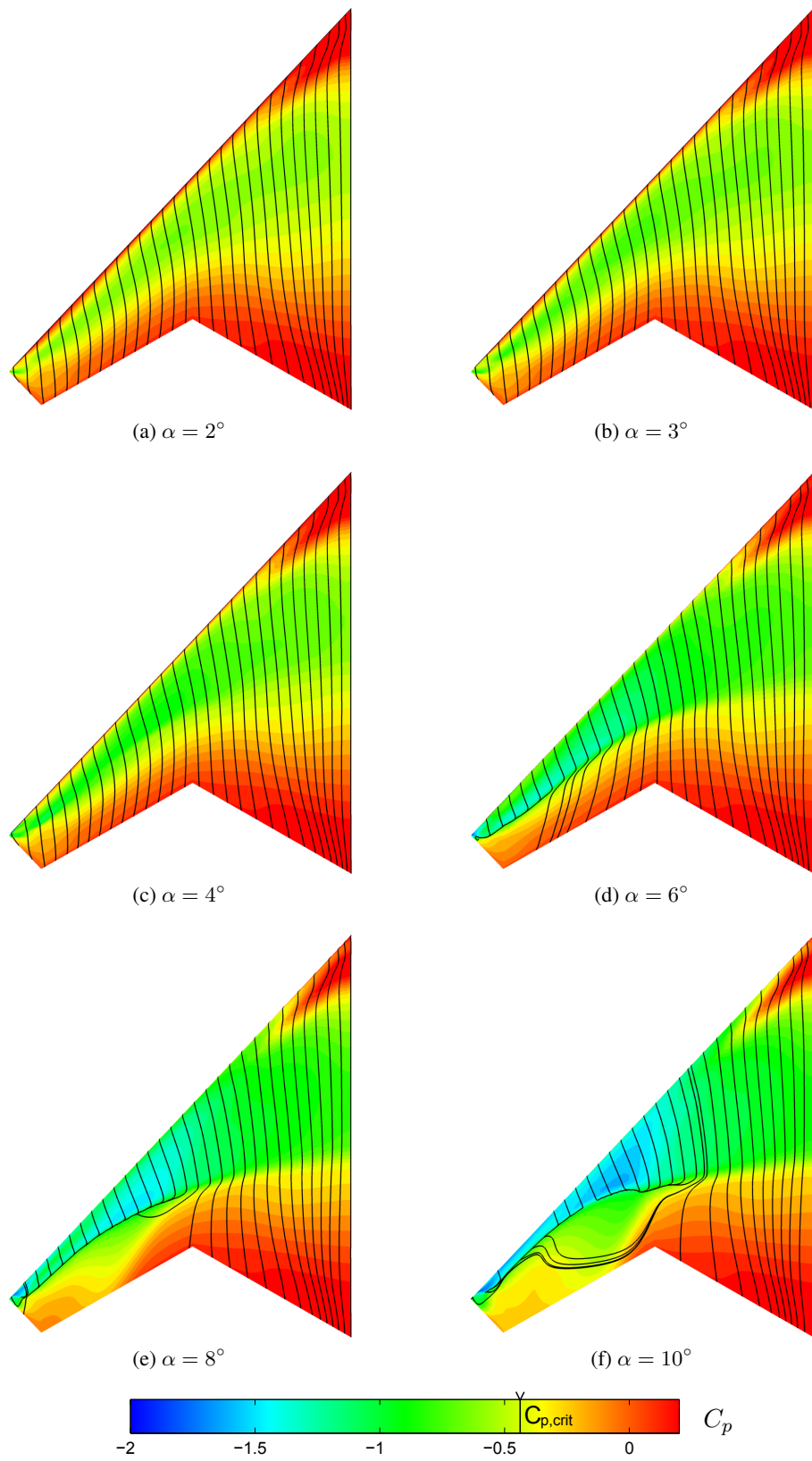


Figure 5.16:  $C_L 0.5CT$   $M = 0.8$  coloured  $C_p$  distributions and skin friction lines



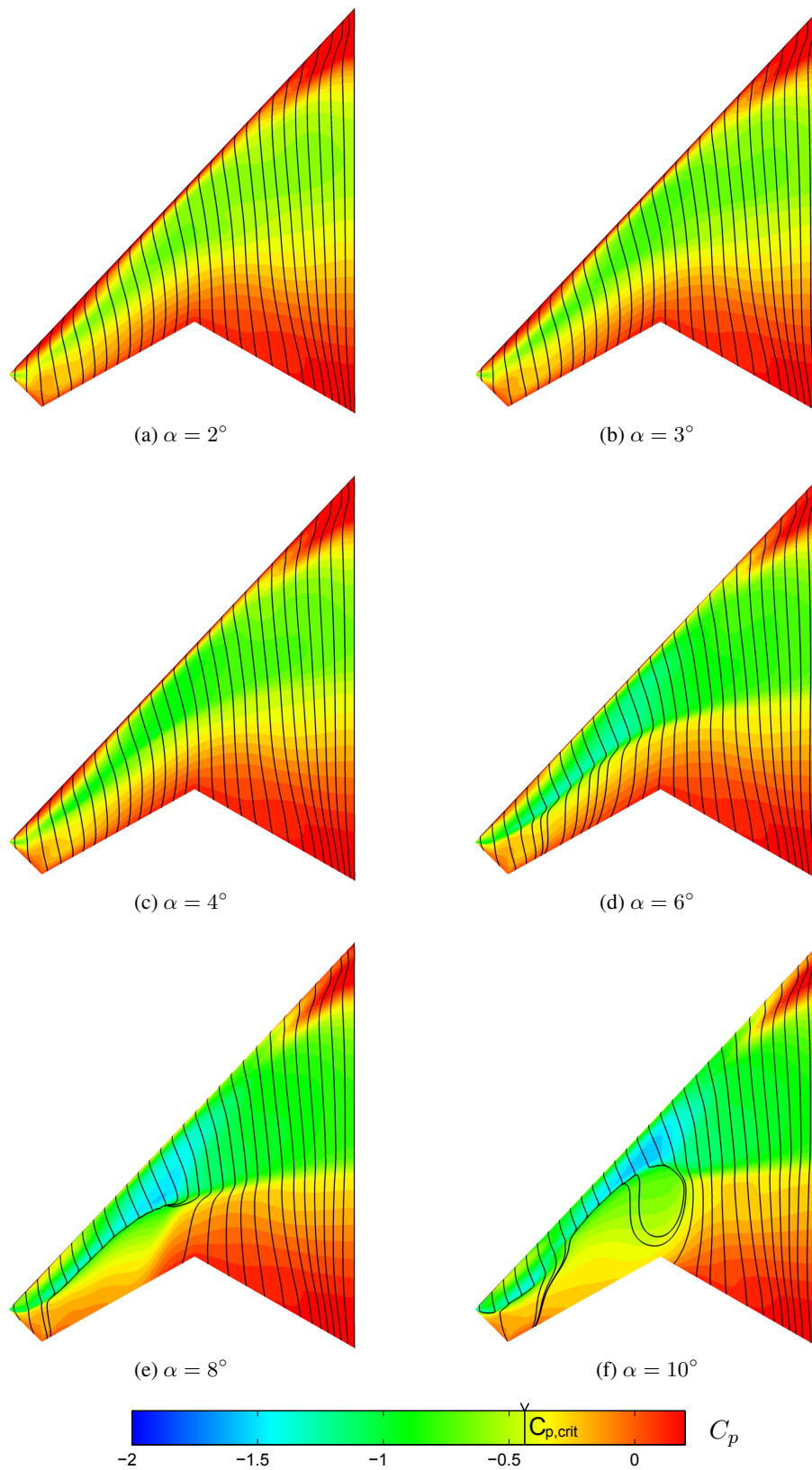


Figure 5.17:  $C_L 0.6C$   $M = 0.8$  coloured  $C_p$  distributions and skin friction lines

### 5.5.2.3 $M = 0.25$ Flowfields

The planar wing at  $M = 0.25$  behaves similarly to the original 1303 wind tunnel model. As the incidence is increased, the flow separation at the wingtip begins to spread up the wing, moving inboard more quickly once the separation position passes the 2<sup>nd</sup> crank. This time there is no flow separation at the apex below  $16^\circ$ , which actually appears to slow the pitch recovery at high incidence. This is of little relevance as the aircraft would have likely have lost control by this stage anyway.

In each case the designed wings initially show a small flow separation at the wingtip, which grows more slowly than in the planar wing case. At higher incidences, flow separation occurs elsewhere on the wing, away from the leading edge. With the  $C_L0.4C$  wing, initially spanwise flow is seen towards the trailing edge near the mid span, which then spreads forwards to the leading edge extremely quickly. The onset of pitchup actually coincides with the onset of this spanwise flow. On the  $C_L0.4C$  wing the flow separation causes the whole outer wing to become separated but on the higher lift designs, which have more twist and camber, there remains some attached flow between the two separated regions.

The spanwise flow described is in the location where trailing edge flaps would likely be placed and hence this would be likely reduce the control power of these devices, placing more severe limits on the controllable flight envelope. Large control deflections (especially trailing edge down) at some incidence before pitchup would be likely to cause the flow to separate earlier due to the addition of camber locally. Conversely trailing edge up deflections may be used to delay the onset of spanwise flow and pitchup, although this would require deflection of other surfaces to trim the aircraft.

The spanwise flow problem is somewhat reduced on the camber-thickness design which acts similarly to the planar wing. This indicates that there may be no other option but to increase leading edge radius for high lift performance as there are limited gains to be made from additional camber, due to control power requirements. This will have to be traded off against increased radar signature. This highlights a direction for further work in establishing control power for these configurations across the flight envelope.

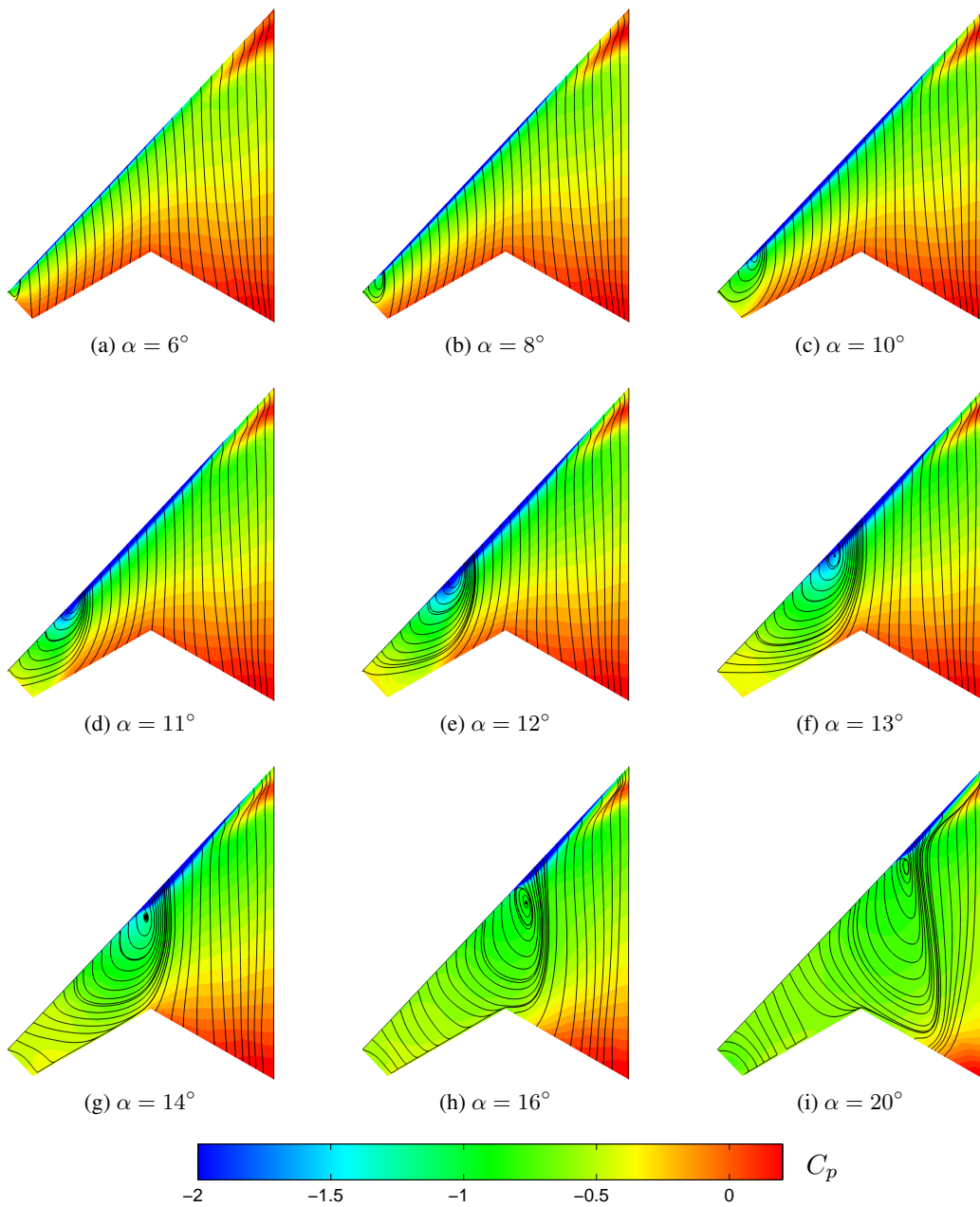


Figure 5.18: Planar wing  $M = 0.25$  coloured  $C_p$  distributions and skin friction lines

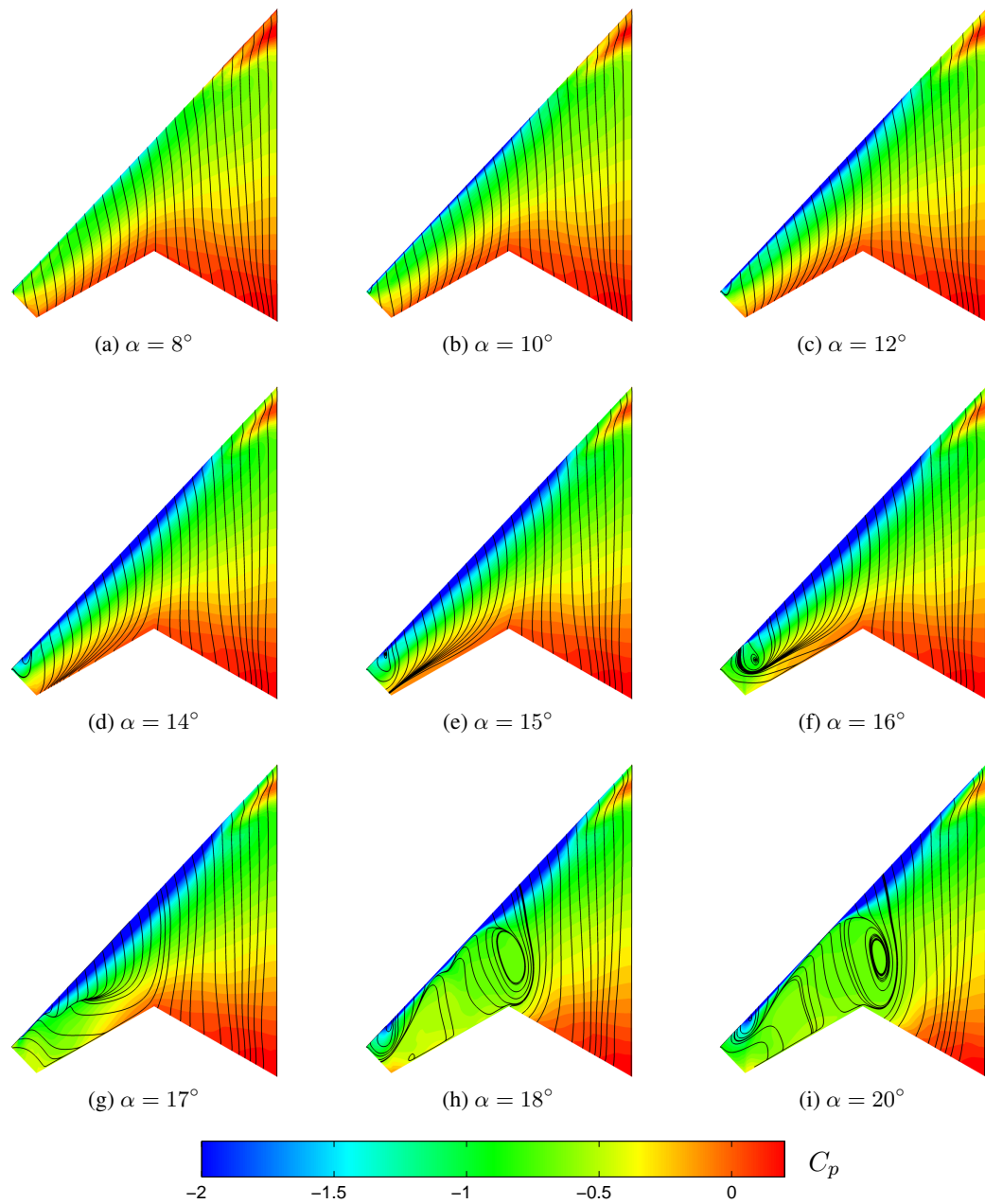


Figure 5.19:  $C_{L0.4C}$   $M = 0.25$  coloured  $C_p$  distributions and skin friction lines

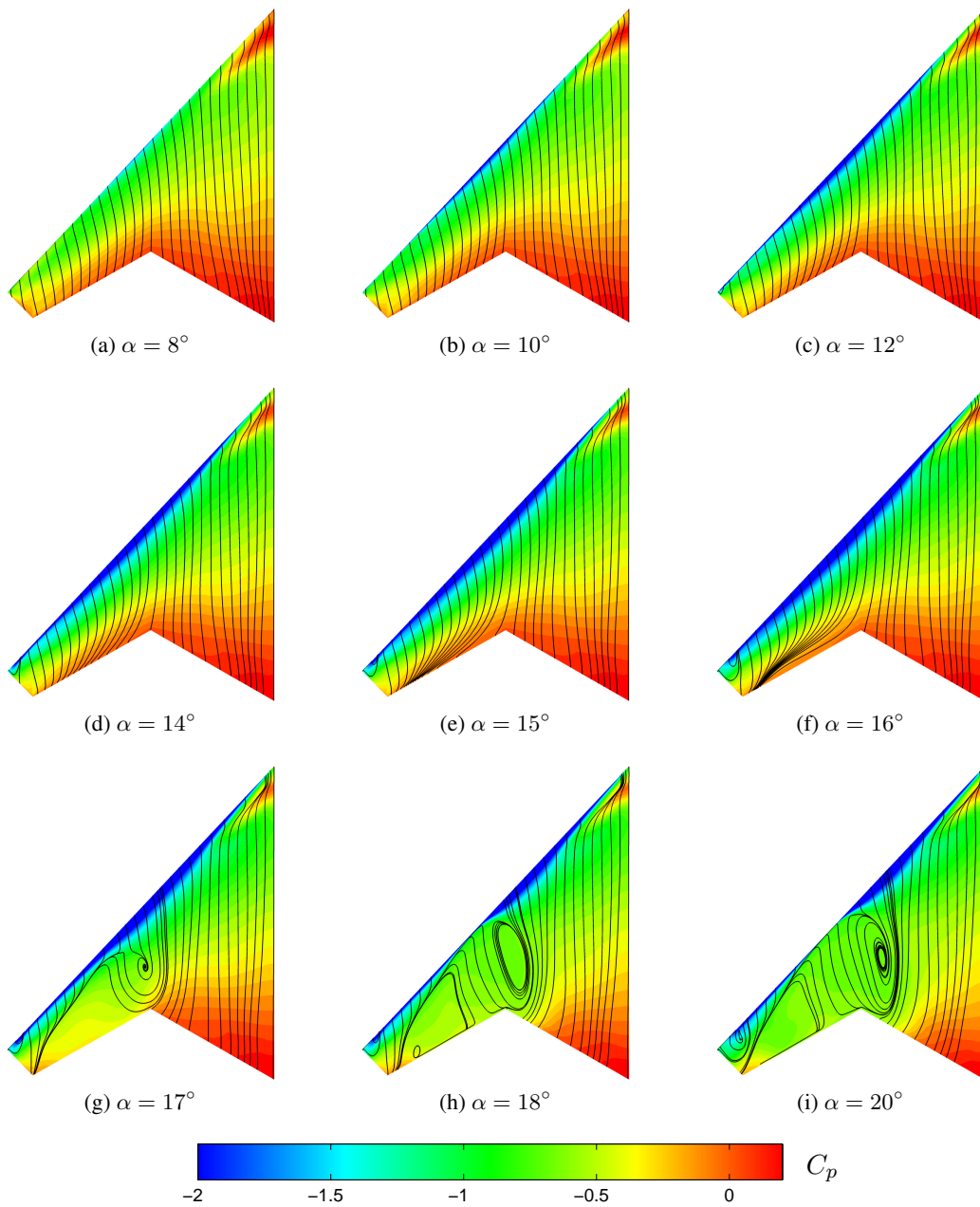


Figure 5.20:  $C_L 0.5C$   $M = 0.25$  coloured  $C_p$  distributions and skin friction lines

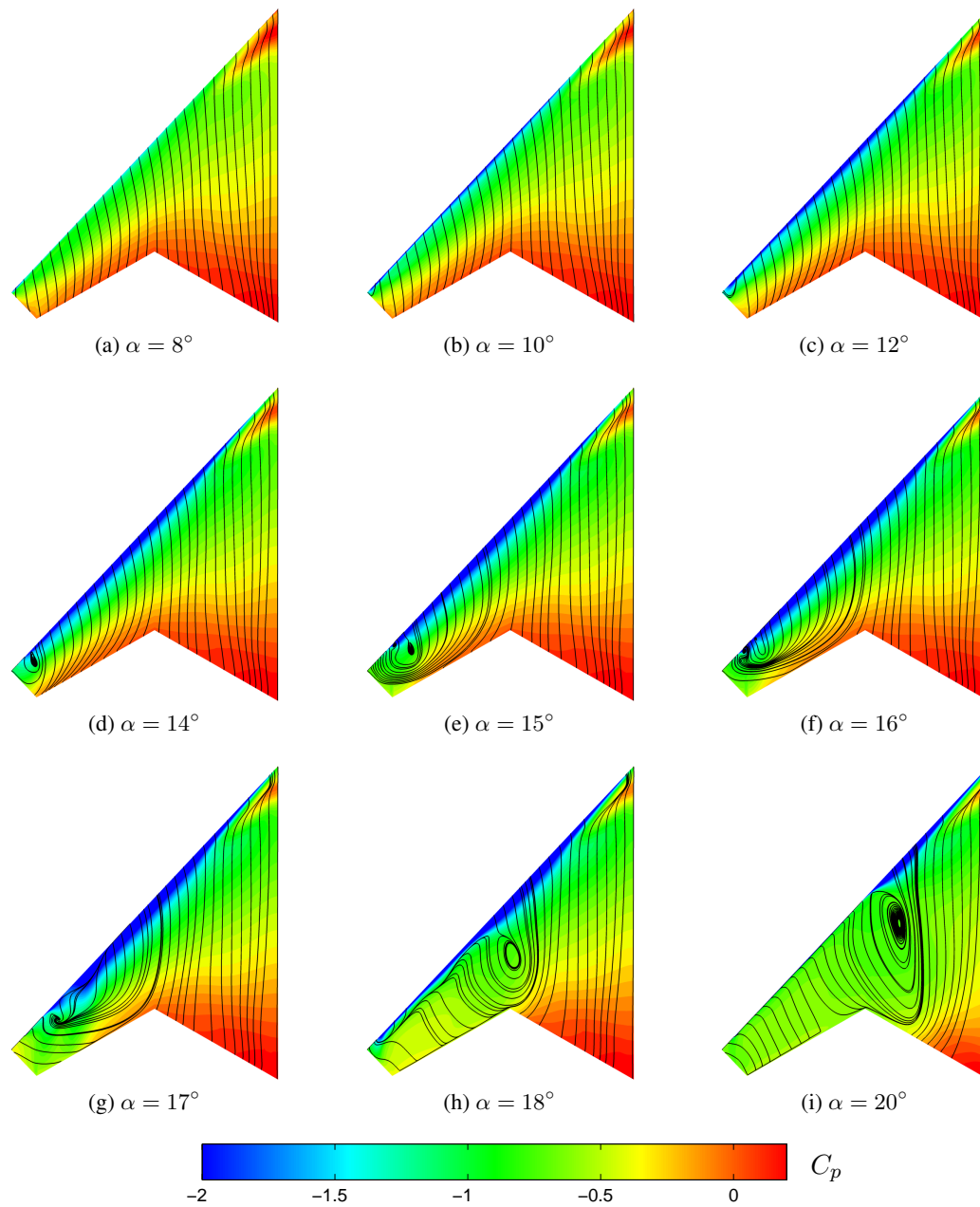


Figure 5.21:  $C_{L0.5CT}$   $M = 0.25$  coloured  $C_p$  distributions and skin friction lines

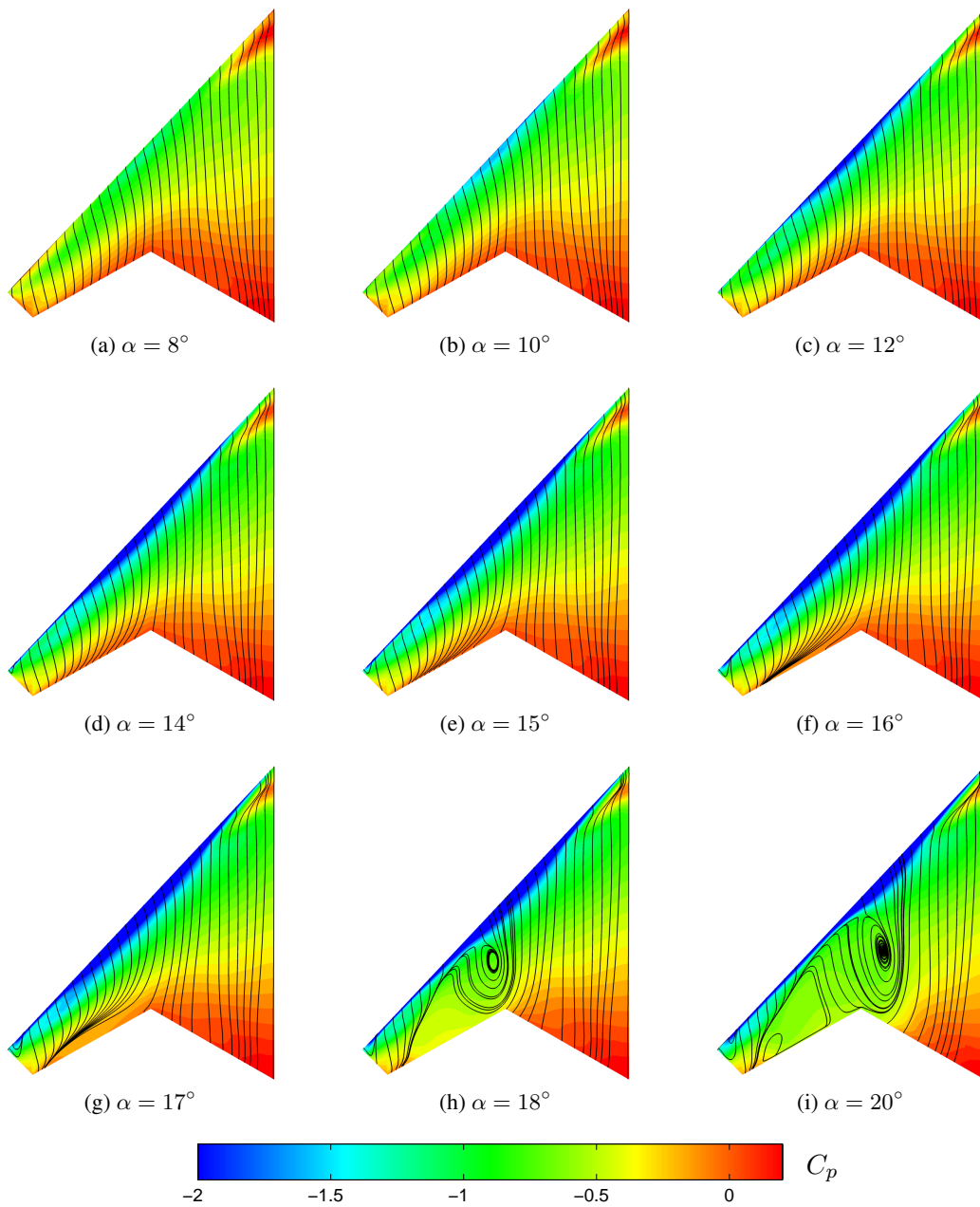


Figure 5.22:  $C_L 0.6C$   $M = 0.25$  coloured  $C_p$  distributions and skin friction lines

## 5.6 Discussion

The current method incorporates an iterative gradient based optimiser with the MERLIN flow solver to calculate the objective function ( $C_D$ ) at cruise. The optimisation was also subject to various constraints to ensure the correct lift and pitching moment at cruise, as well as a constraint designed to avoid flow separation and hence non-linear aerodynamics at take-off. This high lift constraint is based on Lan's quasi-vortex-lattice method and some auxiliary relationships from Carlson which place empirical limits on the amount of attainable leading edge thrust. Gradients of the Euler objective functions were calculated using an adjoint solver that for large numbers of variables can calculate the gradients efficiently.

In initial investigations, the standard vortex lattice method was used for the high lift constraint although it became clear after some experimentation that the gradients calculated by finite differences were extremely inaccurate often causing optimiser to divergence. This was due to errors in the leading edge thrust calculation in the standard method resulting from integration of the vortex distribution which contains a singularity at the leading edge. The quasi-vortex-lattice method eliminates this problem through a change in variables allowing exact computation of the theoretical leading edge thrust and hence accurate gradients can be obtained.

Parametrisation of the geometry also proved to be important for producing credible designs. Camber deformations were made using Bernstein polynomials which guarantees smooth geometries are always obtained. The thickness distribution was controlled with the same Bernstein polynomials combined with Kulfan's class shape transformation method which allows control over the leading edge radius and boat tail angle. In order to maintain a constant volume and therefore space for the wing structure and fuel, a novel method was used where the aerofoil thickness distributions were scaled to maintain the cross sectional area. This was also differentiated for integration into the adjoint solver. The benefit of this is that no explicit geometrical constraints are required in the optimiser, simplifying the process. For the wing on a UCAV, it is important the leading and trailing edges remain straight between cranks for both RCS and control surface integration. This constraint means only two twist sections were permitted with rotations made about the leading edges. This proved to be quite restrictive with high levels of twist required at the outer crank to sufficiently unload the wingtip region. Aerodynamically superior designs could likely be obtained if additional twist sections were permitted although the effect of this on RCS is unknown.

The optimisation method has succeeded in improving the high lift performance of the wing while keeping the overall drag in the cruise configuration similar to that of the planar wing. Carlson's leading edge thrust constraint has tended to over constrain the designs as indicated by the better than expected high lift performance. This will undoubtedly give a drag penalty as the resulting designs may have more twist and camber or a larger leading edge radius than a design designed purely for cruise. This highlights another area for future work in establishing more realistic limitations on leading edge thrust for this Mach and Reynolds number range.

Producing wing designs for different lift coefficients has given some indication of the trade-off between cruise and take-off performance. The wing designed purely for cruise gives a moderate reduction in drag. As the design lift is increased, there is initially a small drag increase and then the drag penalty appears to diverge at higher design lift coefficients. This becomes worse in the viscous regime due to lower surface flow separation which also causes the wing to become out of trim.



A design that allowed the thickness distribution to be modified showed that for aerodynamics, a very large leading edge radius is preferred towards the wingtip. This allows less twist and thus a more ‘optimal’ lift distribution for cruise. A large leading edge radius however is likely to compromise the low observable properties of the wing and therefore a maximum allowable value for the leading edge radius should be determined from a signature perspective prior to aerodynamically designing the wing. For the sections where the thickness was shifted towards the leading edge, or excessive camber is required, it may be beneficial to increase the overall cross sectional area, helping to achieve smoother aerofoil profiles giving improved performance over a wider  $C_L$  range. This might also alleviate the low incidence flow separation on the lower surface of the wing.

The viscous analysis has showed that the current method produces wing designs successful at delaying pitch divergence, although significant amounts of spanwise flow now occur towards the trailing edge before pitch up occurs. To obtain designed wings with higher maximum lift, a more sophisticated high lift constraint (considering the whole boundary layer) would be required. This would be numerically complex and possibly unsuitable for gradient based optimisation. The current constraint is thought to be good for producing ‘balanced’ designs with a compromise between take-off and high lift performance. It is also simple and numerically well behaved making it suitable for gradient based optimisation.



## Chapter 6

# Conclusions

---

In this thesis, there are two main research topics. The first is a detailed aerodynamic investigation into the 1303 UCAV at low speeds, aiming to better understand the non-linear aerodynamics of this class of lambda wing UCAV at high lift as well as our ability to predict the aerodynamics using RANS flow solvers and turbulence models. It has been shown that reasonable predictions can be made using these methods and much of the flow physics is generally well captured. There are some unresolved issues which have been highlighted and recommendations made for future experiments and modelling.

The second topic is the development and application of a design method for these wings, aiming to address issues highlighted in previous conceptual design studies, that both the low speed high lift and transonic behaviour are important. A novel optimisation approach has been developed and used to generate improved designs for the 1303 configuration. The approach has proved to be successful in producing balanced designs with better than expected high lift performance and good transonic characteristics.

### 6.1 Achievements

The main achievements in the current work have been

- An in depth numerical analysis has been completed for the 1303 UCAV configuration
  - Good agreement with experimental data including prediction of pitchup
  - Flow physics for pitch-up, lateral and yaw instabilities has been revealed
  - Axial force ( $C_X$ ) shown to be a good indicator of pitchup
  - Various turbulence models tested
  - Sting faring investigated using overset and shown to be important for yaw stability
- A novel optimisation methodology for UCAV wing design has been developed
  - Adjoint method has been coupled with a vortex lattice code and empirically based high lift constraint
  - Unique parameterisation scheme which maintains LO shape and internal volume
- Several high lift UCAVs have been designed

- Maximum lift  $C_{L,max} \geq 0.8$  (exceeds previous estimates)
- Good transonic performance

## 6.2 Further Work

The current work has improved understanding of various aspects of UCAV wing aerodynamics as well as aspects specific to the 1303 wind tunnel tests but the predictions could still be improved. The aerodynamic phenomena present are complicated and sensitive to mesh resolution and turbulence modelling. Furthermore in the QinetiQ experiment regions of laminar flow are thought to be present that are not accounted for in the current numerical analysis. In order to draw more meaningful conclusions about the performance of RANS codes for this type of wing, simpler cases should be studied with reduced geometric complexity and the uncertainties due to transition eliminated by experimentally fixing transition. Transition should be fixed at the stagnation line because much of the important flow physics occurs around this region. This would help to reduce the computational burden and permit a more in-depth computational investigation. Improved data for comparison including surface and off surface data would benefit this investigation greatly such as high quality oil flow patterns, PSP and PIV data for CFD comparisons.

Investigation into transition at full scale Reynolds numbers would be invaluable to ensure that meaningful results can actually be obtained from low Reynolds number wind tunnels. This would have to involve either high Reynolds number testing in a facility such as the European Transonic Wind Tunnel or Flight testing. Both of these activities are extremely expensive.

The wing design method has been successful with significant improvements to the design but there are still improvements that could be made. These fall into two main categories: improving the quality of the designs obtained with the same objectives and constraints or increasing the scope of the design method by including other disciplines such as stealth or structural design and allowing for greater freedom in the design.

The former could be achieved by increasing the fidelity of both the cruise and high lift analysis. In principle viscous flow solvers could be used in both of these areas although it is likely that difficulties may arise. There would be a much larger computational cost involved in producing a single design with greatly increased turn around time. Also additional non-linearities arising from viscous flow may make it challenging for a gradient based optimiser to find improved designs, especially if large flow separations are present. For the high lift constraint, formulation of a suitable constraint which avoids flow separation may also be very difficult as there is no single criterion that guarantees this. If many constraints are required (as with the current method) the benefit of using the adjoint solution to calculate gradients is lost and the process becomes very inefficient.

In the shorter term, it may be possible to use a viscous solution for the objective if either improvements are made to adjoint-MERLIN to permit viscous solutions on large meshes or if another adjoint solver was utilised. Additionally, the current high lift constraint could be improved to be more accurate for the current Mach and Reynolds number range by adjusting the empirical constants to better represent current experimental data.

In the author's opinion, greater improvements could be realised by addressing the second category of improvements; increasing the scope of the optimisation. Integrating an RCS objective or constraint would allow for more freedom for design variable changes which may include planform

topology, sweep angles, crank positions and thickness or leading edge radius. Allowing greater freedom in this way would likely yield greater benefits.



# Bibliography

---

- [1] *Joint Doctrine Note 2/11 The UK Approach to Unmanned Aircraft Systems*. The Development, Concepts and Doctrine Centre - Ministry of Defence, 2011.
- [2] D. P. Raymer et al. *Aircraft design: a conceptual approach*. Vol. 3. Washington: American Institute of Aeronautics and Astronautics, 1999.
- [3] L. Johnston. “High-Lift Aerodynamics of Uninhabited Combat Air Vehicle Configurations with Reduced Radar Cross-Section Characteristics”. *Conference*. Presented at RAES Applied Aerodynamics Conference, Bristol 17-19 July, 2012.
- [4] F. J. Hale. *Introduction to Aircraft Performance, Selection and Design*. New York: John Wiley & Sons, 1984.
- [5] *MIL-C-5011-A Charts; Standard Aircraft Characteristics and Performance, Piloted Aircraft*. US Air Force, 1951.
- [6] N. Qin, A. Vavalle and A. L. Moigne. “Spanwise Lift Distribution for Blended Wing Body Aircraft”. *Journal of aircraft* vol. 42, no. 2 (2005), pp. 356–365.
- [7] E. Lan and J. Roskam. *Airplane Aerodynamics and Performance*. Darcorporation, 2000.
- [8] *Predator Image*. Accessed 20 Oct 2013. URL: [http://commons.wikimedia.org/wiki/File:MQ-1\\_Predator\\_unmanned\\_aircraft.jpg](http://commons.wikimedia.org/wiki/File:MQ-1_Predator_unmanned_aircraft.jpg).
- [9] *BAE Systems Mantis Image*. Accessed 20 Oct 2013. URL: [http://www.hitechweb.genezis.eu/UCAV02.files/bae\\_mantis\\_uav\\_3.jpg](http://www.hitechweb.genezis.eu/UCAV02.files/bae_mantis_uav_3.jpg).
- [10] *BAE Systems Corax Image*. Accessed 20 Oct 2013. URL: [http://www.hitechweb.genezis.eu/UCAV02.files/bae\\_corax\\_uav\\_1\\_big.jpg](http://www.hitechweb.genezis.eu/UCAV02.files/bae_corax_uav_1_big.jpg).
- [11] *Tarranis Image*. Accessed 20 Oct 2013. URL: <http://media.aerosociety.com/aerospace-insight/files/2012/06/Taranis.jpg>.
- [12] *nEUROn Image*. Accessed 20 Oct 2013. URL: <http://theaviationist.com/wp-content/uploads/2012/12/nEUROn.jpg>.
- [13] *X47a Image*. Accessed 20 Oct 2013. URL: [http://upload.wikimedia.org/wikipedia/commons/8/8f/X-47A\\_rollout.jpg](http://upload.wikimedia.org/wikipedia/commons/8/8f/X-47A_rollout.jpg).
- [14] *X47b Image*. Accessed 20 Oct 2013. URL: <http://www.navair.navy.mil/img/uploads/111029-f-em261-011.jpg>.
- [15] *X45a Image*. Accessed 20 Oct 2013. URL: [http://www.airforce-technology.com/projects/x-45-ucav/images/x45ucav\\_10.jpg](http://www.airforce-technology.com/projects/x-45-ucav/images/x45ucav_10.jpg).
- [16] *Lockheed Martin F117 Image*. Accessed 20 Oct 2013. URL: [http://www.fas.org/man/dod-101/sys/ac/f-117\\_13-front.jpg](http://www.fas.org/man/dod-101/sys/ac/f-117_13-front.jpg).

- [17] *Northrop Grumman B2 Image*. Accessed 20 Oct 2013. URL: [http://upload.wikimedia.org/wikipedia/commons/d/dc/US\\_Air\\_Force\\_B-2\\_Spirit.jpg](http://upload.wikimedia.org/wikipedia/commons/d/dc/US_Air_Force_B-2_Spirit.jpg).
- [18] I. Whitmore, K. Weatherill, K. Stevens, J. Green, J.-J. Vallée, M. Bourasseau, E. Garnier and J.-M. Massonnat. *The Application of Flow Control To A Highly Convoluted Air Intake Duct for a Combat UAV*. Tech. rep. BAE SYSTEMS, Military Air & Information, Warton Aerodrome, Lancashire, UK, 2012.
- [19] A. M. O. Smith. “High-Lift Aerodynamics”. *Journal of Aircraft* vol. 12, no. 6 (1975), pp. 501–530.
- [20] L. K. Loftin Jr and A. E. Von Doenhoff. *Exploratory Investigation at High and Low Subsonic Mach Numbers of Two Experimental 6-Percent Thick Airfoil Sections Designed to Have High Maximum Lift Coefficients*. Research Memorandum L51F06. NACA, 1951.
- [21] B. S. Stratford. “The Prediction of Separation of the Turbulent Boundary Layer”. *Journal of Fluid Mechanics* vol. 5 (1959), pp. 1–16.
- [22] R. H. Liebeck. “A Class of Airfoils Designed for High Lift in Incompressible Flow”. *Journal of Aircraft* vol. 10 (1973), pp. 610–617.
- [23] C. D. Harris. *NASA supercritical airfoils: a matrix of family-related airfoils*. NASA Technical Paper 2969, 1990.
- [24] M. Nemec, D. W. Zingg and T. H. Pulliam. “Multipoint and multi-objective aerodynamic shape optimization”. *AIAA journal* vol. 42, no. 6 (2004), pp. 1057–1065.
- [25] J. J. Reuther, A. Jameson, J. J. Alonso, M. J. Rimlinger and D. Saunders. “Constrained Multipoint Aerodynamic Shape Optimization using an Adjoint Formulation and Parallel Computers, part 1”. *Journal of Aircraft* vol. 36, no. 1 (1999), pp. 51–60.
- [26] L. Huyse, S. L. Padula, R. M. Lewis and W. Li. “Probabilistic approach to free-form airfoil shape optimization under uncertainty”. *AIAA journal* vol. 40, no. 9 (2002), pp. 1764–1772.
- [27] E. C. Polhamus. *Vortex lift research: Early contributions and some current challenges*. NASA Conference Publication 2416. NASA, 1986, p. 1.
- [28] D. Hummel. *On Vortex Formation over a Slender Wing at Large Incidence*. CP-247 Paper 15. AGRAD, 1965, pp. 247–252.
- [29] E. Polhamus. *A Concept of the Vortex Lift of Sharp-Edged Delta Wings Based on a Leading-Edge Suction Analogy*. Technical Note D-3767. NASA, 1966.
- [30] J. M. Luckring. “Reynolds number, compressibility, and leading-edge bluntness effects on delta-wing aerodynamics”. *ICAS 24th International Congress of the Aeronautical Sciences*. 2004.
- [31] W. Fritz. “Numerical simulation of the peculiar subsonic flow-field about the VFE-2 delta wing with rounded leading edge”. *Aerospace Science and Technology* vol. 24, no. 1 (2013), pp. 45–55.
- [32] J. Luckring. “Compressibility and leading-edge bluntness effects for a 65 delta wing”. *42nd AIAA Aerospace Sciences Meeting and Exhibit, Reno, Nv*. AIAA 2004-765. 2004.
- [33] D. I. A. Poll. “Transition in the infinite swept attachment line boundary layer”. *Aeronautical Quarterly* vol. 30 (1979), pp. 607–629.
- [34] S. J. Woolvin. “UCAV Configuration & Performance Trade-Offs”. *44th AIAA Aerospace Sciences Meeting and Exhibit*. AIAA 2006-1264. Defence Science & Technology Laboratory, Farnborough, GU14 0LX, UK. 2006.



- 
- [35] S. Woolvin. "A Conceptual Design Study of the 1303 UCAV Configuration". *24th AIAA applied aerodynamic conference, San Francisco, CA*. AIAA 2006-2991. Defence Science & Technology Laboratory, Farnborough, GU14 0LX, UK. 2006.
- [36] R. J. Bruce. *Low speed wind tunnel tests on the 1303 UCAV concept*. Tech. rep. QINETIQ/FST/TR025502/1.0. QinetiQ, 2003.
- [37] D.-S. Lee, L. F. Gonzalez, K. Srinivas and J. Periaux. "Robust evolutionary algorithms for UAV/UCAV aerodynamic and RCS design optimisation". *Computers & Fluids* vol. 37, no. 5 (2008), pp. 547–564.
- [38] L. González, E. Whitney, J. Périaux and K. Srinivas. "Practical Aerodynamic Design for UAVs using Multicriteria Evolutionary Algorithms." *VKI lecture series on Optimization Methods & Tools for Multicriteria/Multidisciplinary Design*. 2004.
- [39] D. Lee, L. F. Gonzalez, J. Periaux and G. Bugada. "Multi-objective design optimization of morphing UAV aerofoil/wing using hybridised MOGA". *Congress on Evolutionary Computation (CEC)*. IEEE. 2012, pp. 1–8.
- [40] K. Park and B.-S. Kim. "Optimal Design of Airfoil Platform Shapes with High Aspect Ratio Using Genetic Algorithm". *World Academy of Science, Engineering and Technology* vol. 76 (2013), p. 443.
- [41] A. Vavalle and N. Qin. "Iterative response surface based optimization scheme for transonic airfoil design". *Journal of aircraft* vol. 44, no. 2 (2007), pp. 365–376.
- [42] A. Keane. "Wing optimization using design of experiment, response surface, and data fusion methods". *Journal of Aircraft* vol. 40, no. 4 (2003), pp. 741–750.
- [43] A. Jameson. "Aerodynamic design via control theory". *Journal of Scientific Computing* vol. 3, no. 3 (1988), pp. 233–260.
- [44] E. Ahlstrom, R. Gregg, J. Vassberg and A. Jameson. "G-force: The Design of an Unlimited Class Reno Racer". *18th AIAA Applied Aerodynamics Conference, Denver, CO*. AIAA 2000-4341. 2000.
- [45] B. Soemarwoto, A. Jameson, A. Martins, B. Oskam and M. Laban. "Adaptive aerodynamic optimization of regional jet aircraft". *40th AIAA Aerospace Sciences Meeting & Exhibit*. AIAA 2002-260. AIAA. 2002.
- [46] A. Jameson, J. Reuther and J. Alonso. "Aerodynamic Shape Optimization of Supersonic Aircraft Configurations via an Adjoint Formulation on Distributed Memory Parallel Computers". *6th AIAA/USAF/NASA/ISSMO Symposium on Multidisciplinary Analysis and Optimization, Bellevue*. AIAA Paper-96- 4045. 1996.
- [47] A. Le Moigne. "A Discrete Navier-Stokes Adjoint Method for Aerodynamic Optimisation of Blended Wing Body Configurations". PhD thesis. Cranfield University, 2002/2003.
- [48] A. L. Moigne and N. Qin. "Variable-fidelity aerodynamic optimization for turbulent flows using a discrete adjoint formulation". *AIAA journal* vol. 42, no. 7 (2004), pp. 1281–1292.
- [49] A. Le Moigne and N. Qin. "Aerofoil profile and sweep optimisation for a blended wing-body aircraft using a discrete adjoint method". *Aeronautical Journal* vol. 110, no. 1111 (2006), pp. 589–604.
- [50] W. Wong, A. Le Moigne and N. Qin. "Parallel adjoint-based optimisation of a blended wing body aircraft with shock control bumps". *Aeronautical Journal* vol. 111, no. 1117 (2007), pp. 165–174.

- [51] M. Förster and A. Pal. “AMG in TAU: Adjoint Equations and Mesh Deformation”. *Computational Flight Testing* vol. 123 (2013), pp. 1–15.
- [52] J. Brezillon, R. Dwight and M. Widhalm. “Aerodynamic Optimization for Cruise and High-Lift Configurations”. *MEGADESIGN and MegaOpt - German Initiatives for Aerodynamic Simulation and Optimization in Aircraft Design*. Vol. 107. Springer Berlin Heidelberg, 2009, pp. 249–262.
- [53] S. Kirn, J. Alonso and A. Jameson. “Design optimization of high-lift configurations using a viscous continuous adjoint method”. *40th AIAA Aerospace Sciences Meeting and Exhibit, Reno, Nv*. AIAA-2002-0844. 2002.
- [54] G. Billman and O. B.A. *High L/D Extended Range/Payload Fighter Aircraft Technology*. Tech. rep. Boeing Phantom Works: AFRL, 1998.
- [55] R. J. Bruce. *High speed wind tunnel tests on the 1303 UCAV concept*. Tech. rep. QINETIQ/FST/TR030214/1.0. QinetiQ, 2003.
- [56] M. D. Wong, G. J. McKenzie, M. V. Ol, K. Petterson and S. Zhang. “Joint TTCP CFD studies into the 1303 UCAV performance: first year results”. *24th Applied Aerodynamics Conference, San Francisco, CA*. AIAA 2006-2984. 2006.
- [57] K. Petterson. “CFD analysis of the low-speed aerodynamic characteristics of a UCAV”. *44th AIAA Aerospace Sciences Meeting and Exhibit, Reno*. AIAA 2006-1259. 2006.
- [58] K. Petterson. “Low-Speed Aerodynamic and Flowfield Characteristics of a UCAV”. *24th Applied Aerodynamics Conference, San Francisco*. AIAA 2006-2986. AIAA. 2006.
- [59] M. D. Wong and J. Flores. “Application of OVERFLOW-MLP to the Analysis of the 1303 UCAV”. *24th AIAA Applied Aerodynamics Conference*. AIAA 2006-2987. 2006.
- [60] F. Zhang, M. Khalid and N. Ball. “A CFD based study of UCAV 1303 model”. *23rd AIAA Applied Aerodynamics Conference, Ontario Canada*. AIAA 2005-4615. 2005.
- [61] M. Arthur and C. Atkin. “Transition Modelling for Viscous Flow Prediction”. *36th AIAA fluid dynamics conference and exhibit, San Francisco*. AIAA-2006-3052. 2006.
- [62] M. Arthur and K. Petterson. “A computational study of the low-speed flow over the 1303 UCAV configuration”. *25th AIAA Applied Aerodynamics Conference, Miami, FL*. AIAA 2007-4568. 2007.
- [63] M. T. Arthur, H. P. Horton and M. S. Mughal. “Modeling of Natural Transition in Properly Three-Dimensional Flows”. *39th AIAA Fluid Dynamics Conference, Texas*. AIAA 2009-3556. 2009.
- [64] S. E. Sherer, M. R. Visbal and R. E. Gordnier. “Computational study of Reynolds number and angle-of-attack effects on a 1303 UCAV configuration with a high-order overset-grid algorithm”. *27th AIAA Applied Aerodynamics Conference, San Antonio, Texas*. AIAA 2009-751. 2009.
- [65] M. E. Milne. *CFD Analysis of the 1303 UCAV*. Tech. rep. QINETIQ/FST/AVS/TR046449. Unclassified. QinetiQ, 2005.
- [66] G. J. McKenzie. *A Computational Fluid Dynamics Investigation of the Unmanned Combat Air Vehicle 1303 Blended Wing Body Configuration*. Tech. rep. DSTO, 2005.
- [67] M. T. Arthur, R. M. Ashworth and D. A. Peshkin. *Developments in Viscous Flow Calculation for UCAV Configurations*. Tech. rep. QinetiQ/08/00740. UK Restricted. QinetiQ, 2008.

- 
- [68] M. E. Milne and C. L. Wooding. *Aerodynamic Optimisation of the 1303 UCAV*. Tech. rep. QINETIQ/06/02045/1.0. UK Restricted. QinetiQ, 2006.
- [69] M. Palmer and R. Nangia. *A Tolerant Wing Design for UCAV*. Tech. rep. Nangia Aero Research Associates, 2011.
- [70] M. D. Atkinson and F. Ferguson. “A Computational Fluid Dynamic Investigation of the 1303 UCAV Configuration with Deployable RAO Vortex Flaps”. PhD thesis. North Carolina Agricultural and Technical State University, 2005.
- [71] J. J. Chung and T. Ghee. “Numerical Investigation of the UCAV 1303 Configuration With and Without Simple Deployable Vortex Flaps”. *Proceedings of the 24th AIAA Applied Aerodynamic Conference, San Francisco, CA*. AIAA 2006-2989. 2006.
- [72] *NAG Fortran Library Routine Document E04UCF/E04UCA*. [NP3657/21]. National Algorithms Group.
- [73] B. Zhong, S. Shaw and N. Qin. “BILU implicit multiblock Euler/Navier Stokes simulation for rotor tip vortex and wake convection”. *International Journal for Numerical Methods in Fluids* vol. 55 (Oct. 2007), pp. 509–536. DOI: 10.1002/flid.1455.
- [74] N. Qin, A. Vavalle, A. L. Moigne, M. Laban, K. Hackett and P. Weinerfelt. “Aerodynamic considerations of blended wing body aircraft”. *Progress in Aerospace Sciences* vol. 40, no. 6 (2004), pp. 321–343. ISSN: 0376-0421. DOI: 10.1016/j.paerosci.2004.08.001.
- [75] D. C. Wilcox. *Turbulence modeling for CFD*. Vol. 3. DCW industries La Canada, CA, 2006.
- [76] S. Osher and F. Solomon. “Upwind difference schemes for hyperbolic systems of conservation laws”. *Mathematics of computation* vol. 38, no. 158 (1982), pp. 339–374.
- [77] J. Katz and A. Plotkin. *Low-Speed Aerodynamics*. Cambridge Aerospace Series. Cambridge University Press, 2001. ISBN: 9780521665520.
- [78] E. Lan and J. Roskam. “Leading-edge force features of the aerodynamic finite element method”. *Journal of Aircraft* vol. 9 (1972), pp. 864–867.
- [79] C. E. Lan. “A Quasi-Vortex-Lattice Method in Thin Wing Theory”. *Journal of Aircraft* vol. 11, no. 9 (1974), pp. 518–527. DOI: 10.2514/3.60381.
- [80] H. W. Carlson, M. O. McElroy, W. B. Lessard and L. A. McCullers. *Improved Method for Prediction of Attainable Wing Leading-Edge Thrust*. NASA Technical Paper 3557. NASA, 1996.
- [81] I. Kroo. *Applied Aerodynamics: A Digital Textbook*. Desktop Aeronautics, Inc., 2007.
- [82] H. W. Carlson, J. M. Robert and L. B. Reymond. *Estimation of Attainable Leading-Edge Thrust for wings at Subsonic and Supersonic Speeds*. NASA Technical Paper 1500. NASA, 1979.
- [83] H. W. Carlson. *An Aerodynamic Analysis Computer Program and Design Notes for Low Speed Wing Flap Systems*. Tech. rep. NASA Technical Report CR-3675. NASA, 1983.
- [84] B. M. Kulfan. “Universal parametric geometry representation method”. *Journal of Aircraft* vol. 45, no. 1 (2008), pp. 142–158.
- [85] A. Mousavi, P. Castonguay and S. Nadarajah. “Survey of shape parameterization techniques and its effect on three-dimensional aerodynamic shape optimization”. *AIAA 37th Fluid Dynamics Conference and Exhibit, Miami, Florida*. AIAA 2007-3837. 2007.
- [86] M. H. Straathof, M. J. Van Tooren, M. Voskuil and B. Koren. “Aerodynamic shape parameterisation and optimisation of novel configurations”. *Proceedings of the RAeS Aerodynamic*

- Shape Parameterisation and Optimisation of Novel Configurations Conference, London.* 2008.
- [87] S. Lawson and G. Barakos. “DES for UCAV Weapon Bay Flow”. *Progress in Hybrid RANS-LES Modelling*. Springer, 2010, pp. 123–135.
- [88] *Cobalt Version 6.0 User’s Manual*. 2013.
- [89] M. L. Shur, M. K. Strelets, A. K. Travin and P. R. Spalart. “Turbulence modeling in rotating and curved channels: Assessing the Spalart-Shur correction”. *AIAA journal* vol. 38, no. 5 (2000), pp. 784–792.
- [90] N. Qin and C. Jayatunga. “Algebraic turbulence modelling for vortical flows around slender bodies”. *Proceedings of the AGARD 82nd Fluid Dynamics Panel Symposium on Missile Aerodynamics*. 1998.
- [91] *RTO Task Group AVT-183 Website*. Accessed 20 Oct 2013. NATO. URL: [http://www.cso.nato.int/ACTIVITY\\_META.asp?ACT=1765](http://www.cso.nato.int/ACTIVITY_META.asp?ACT=1765).
- [92] D. M. Nangia R.K. Palmer. “A "Tolerant" Wing Design for UCAV”. *49th AIAA Aerospace Sciences Meeting and Exhibit*. AIAA 2011-548. Consulting Aeronautical Engineers, Nangia Aero Research Associates. 2011.